EXPERIMENTAL AND NUMERICAL STUDY ON PSEUDO-SHOCK STRUCTURES IN A MIXED COMPRESSION RECTANGULAR SUPERSONIC INTAKE

A THESIS SUBMITTED TO
THE GRADUATE SCHOOL OF NATURAL AND APPLIED SCIENCES
OF
MIDDLE EAST TECHNICAL UNIVERSITY

BY

ALİ CAN ÖZER

IN PARTIAL FULFILLMENT OF THE REQUIREMENTS
FOR
THE DEGREE OF DOCTOR OF PHILOSOPHY
IN
AEROSPACE ENGINEERING

JULY 2023

Approval of the thesis:

EXPERIMENTAL AND NUMERICAL STUDY ON PSEUDO-SHOCK STRUCTURES IN A MIXED COMPRESSION RECTANGULAR SUPERSONIC INTAKE

submitted by **ALİ CAN ÖZER** in partial fulfillment of the requirements for the degree of **Doctor of Philosophy** in **Aerospace Engineering, Middle East Technical University** by,

Prof. Dr. Halil Kalıpçılar
Dean, Graduate School of **Natural and Applied Sciences** _____

Prof. Dr. Serkan Özgen
Head of Department, **Aerospace Engineering** _____

Prof. Dr. Yusuf Özyörük
Supervisor, **Aerospace Engineering, METU** _____

Examining Committee Members:

Prof. Dr. Oğuz Uzol
Aerospace Engineering, METU _____

Prof. Dr. Yusuf Özyörük
Aerospace Engineering, METU _____

Prof. Dr. Sinan Eyi
Aerospace Engineering, METU _____

Prof. Dr. Nafiz Alemdaroğlu
Aerospace Engineering, Atılım University _____

Dr. Sıtkı Uslu
Mechanical Engineering, TOBB ETU _____

Date: 24.07.2023

I hereby declare that all information in this document has been obtained and presented in accordance with academic rules and ethical conduct. I also declare that, as required by these rules and conduct, I have fully cited and referenced all material and results that are not original to this work.

Name Last name : Özer, Ali Can

Signature :

ABSTRACT

EXPERIMENTAL AND NUMERICAL STUDY ON PSEUDO-SHOCK STRUCTURES IN A MIXED COMPRESSION RECTANGULAR SUPERSONIC INTAKE

Özer, Ali Can
Doctor of Philosophy, Aerospace Engineering
Supervisor: Prof. Dr. Yusuf Özyörük

July 2023, 241 pages

This study investigates the characteristics of pseudo-shocks, which are complex flow structures related to shock wave boundary layer interactions (SWBLI) in a mixed compression, rectangular, supersonic intake. Wind tunnel experiments and numerical simulations are conducted to examine the pseudo-shock structures under different conditions, including variations in Mach number and bleed configurations. The experiment approach involves measuring pressure distribution along and at the exit of the intake and visualizing the pseudo-shocks using the high-speed shadowgraphy technique at various levels of back pressure throttling, generated with a back pressure valve. The oscillatory behaviour of the pseudo-shocks during the dwell time of the back pressure valve is analyzed, and the effects of back pressure throttling transition on shock structures and pressure distribution are examined. Moreover, the hysteresis behaviour, resulting from the throttling direction of the back pressure valve, is examined. Further, characteristics diagrams are obtained, and the performance of the air intake test items and the modes of operations are examined. The numerical simulations utilize Menter's Shear Stress Transport (SST) and Baseline (BSL) k-ω turbulence models, with a focus on investigating the models' predictive capabilities for pseudo-shocks and examining the flow field within the

intake. Moreover, the effect of a parameter related to the stress-limiter of the SST model is also investigated. Comparison with the experimental data is done using both the shadowgraph images and the pressure measurement data. The experimental results show that, as the back pressure valve proceeds, some transitions lead abrupt changes in the shock structures such as sudden change of the orientation of the shock-train and separation or attachment of sonic lines on the ramp and cowl surfaces. Furthermore, those points of abrupt changes are also prone to exhibit hysteresis behaviour. The oscillatory nature of the pseudo-shocks can cause the first shock of the pseudo-shock to oscillate with a displacement amplitude of 45% of the throat height of the intake. As the pseudo-shock structures start to interact with the bleed region, the maximum amount of displacement of the shocks during oscillations decreases. The numerical simulations show that the relative sizes of the separation bubbles on the cowl and ramp side are important in determining the orientation of the shock-train. Additionally, the comparison between the simulation results and the experimental data revealed that there are noticeable differences between the SST and BSL models at lower throttled conditions. The stress-limiter parameter was also found to have an apparent impact on the simulation results. However, as the throttling increases and the mode of operation approaches the critical, the disparity between the results decreases.

Keywords: Supersonic Intake, Shock Wave Boundary Layer Interaction, Pseudo-Shock, Wind Tunnel Tests, Computational Fluid Dynamics

ÖZ

KARMA SIKIŞTIRMALI DİKDÖRTGEN SES-ÜSTÜ BİR HAVA ALIĞINDA BENZETİK ŞOK YAPILARI ÜZERİNE DENEYSEL VE SAYISAL ÇALIŞMA

Özer, Ali Can
Doktora, Havacılık ve Uzay Mühendisliği
Tez Yöneticisi: Prof. Dr. Yusuf Özyörük

Temmuz 2023, 241 sayfa

Bu çalışma, karma sıkıştırmalı, dikdörtgen, ses-üstü bir hava alığında, şok dalgası sınır tabakası etkileşimi ile ilişkili karmaşık akış yapıları olan benzetik şokların karakteristiklerini araştırmaktadır. Farklı Mach sayıları ve sızma havası uygulamaları için benzetik şok yapılarını incelemek üzere rüzgar tüneli deneyleri ve sayısal benzetimler gerçekleştirilmiştir. Deneysel yaklaşım, hava alığı boyunca ve çıkışında basınç dağılımının ölçülmesi ve yüksek hızlı gölge ölçümü tekniği kullanılarak elde edilen görüntülerle benzetik şokların görselleştirilmesini içerir. Farklı arka basınç kısılması için benzetik şokların salınımlı davranışı analiz edilmiş ve arka basınç kısılmasındaki geçişlerin şok yapıları ve basınç dağılımı üzerindeki etkileri incelenmiştir. Ayrıca, arka basınç kısma yönüne göre, şok yapılarının histerez davranışı, hava alığı boyunca alınan basınç ölçümleri üzerinden incelenmiştir. Dahası, karakteristik diyagramlar elde edilmiş ve hava alığı konfigürasyonlarının performansı ve çalışma modları incelenmiştir. Sayısal benzetimlerde, Menter'in Kesme Gerilimi Taşıma ve Temel k-ω türbülans modelleri kullanılmış ve benzetik şoklar için modellerin kestirim yeteneklerinin araştırılması ve hava alığı içerisindeki akışın incelenmesi hedeflenmiştir. Ayrıca, Kesme Gerilimi

Taşıma modelinde bulunan gerilim sınırlayıcı katsayının etkisi de incelenmiştir. Deneysel verilerle karşılaştırma, hem gölge ölçümü görüntüleri hem de basınç verileri kullanılarak yapılmıştır. Deneysel sonuçlar, benzetik şokların salınımlı davranışının benzetik şokun ilk şokunda, hava alığı boğazına oranla %45 mertebesinde yerdeğişim salınımına neden olabileceğini göstermiştir. Benzetik şok yapıları sızma havası kanalı ile etkileşime girdikçe salınım miktarı azalmaktadır. Ayrıca, arka basınç vanası kısıldıkça, bazı geçişlerin, şok yapılarında ani değişikliklere, şok treninin yöneliminin aniden değişmesine, rampa ve davlumbaz yüzeylerindeki sonik hatların ayrılmasına veya yüzeye bağlanmasına neden olduğu gözlenmiştir. Dahası, ani değişiklik noktalarının histerez davranış sergileme eğiliminde olduğu gözlenmiştir. Sayısal benzetimler, davlumbaz ve rampa tarafındaki ayrılma kabarcıklarının, şok treninin yönelimini belirlemede önemli olduğunu göstermektedir. Ayrıca, benzetim sonuçları ile deneysel veriler arasındaki karşılaştırma, Kesme Gerilimi Taşıma ve Temel modelleri arasında, özellikle görece düşük arka basınç koşullarında dikkate değer bir fark olduğunu ortaya koymaktadır. Gerilim sınırlayıcı katsayının da benzetim sonuçları üzerinde önemli bir etkiye sahip olduğu görülmüştür. Ancak, arka basınç arttıkça ve hava alığı çalışma modu kritik moda yaklaştıkça, sonuçlar arasındaki fark azalmaktadır.

Anahtar Kelimeler: Ses-üstü Hava Alığı, Şok Dalgası Sınır Tabaka Etkileşimi, Benzetik Şok, Rüzgar Tüneli Testleri, Hesaplamalı Akışkanlar Dinamiği

“Ars longa, vita brevis.”

ACKNOWLEDGMENTS

I am deeply grateful for the unwavering support and guidance provided by my supervisor, Prof. Dr. Yusuf Özyörük who has been my advisor since my Master's studies. He always made time for me whenever I needed assistance, attentively listening to my concerns, and offering technical expertise and encouragement. Furthermore, he has been diligent in reviewing my thesis, providing invaluable feedback that has greatly enriched the quality of my work. I truly appreciate his dedication and contribution to my academic journey. Thank you Yusuf Hocam, for being an exceptional mentor and making a significant impact on my research and personal growth.

I would like to express my sincere gratitude Prof. Dr. Sinan Eyi and Assist. Prof. Dr. Sıtkı Uslu, the members of the Thesis Monitoring Committee (TİK), for their support and valuable insights throughout my thesis studies. Their active engagement in all TİK meetings and their guidance, expertise and significant contributions have been instrumental in shaping the research and I sincerely thank them for their invaluable contributions. I extend my thanks to the thesis jury members, Prof. Dr. Nafiz Alemdaroğlu and Prof. Dr. Oğuz Uzol, for their interest in my research and the valuable contributions they made during the thesis presentation. Their feedback, particularly regarding the organization of the thesis, has significantly improved its clarity.

I would like to express my gratitude to Dr. Bülent Sümer, the Assistant Manager of TÜBİTAK SAGE, for his thorough examination of the thesis and providing valuable comments and recommendations that improved the quality of the work. His insightful suggestions on the organization of the thesis have made it more comprehensible. I also express my gratitude to Bora Yazıcı, the Coordinator of the Air Breathing Propulsion Systems Group at TÜBİTAK SAGE, for his valuable feedback on experimental and numerical methods. His support has been instrumental in enhancing the quality of my work.

I want to express my deep gratitude to the late Asst. Prof. Dr. Bülent Yüceil for his wholehearted assistance in refining the experimental method and conducting trial experiments. His unwavering dedication and selfless support, day and night, have been crucial. May he rest in peace, and I will always cherish the memories of working with Bülent Hocam with immense respect and gratitude.

I am deeply thankful to Prof. Dr. Okşan Çetiner Yıldırım, Asst. Prof. Hayri Acar, and Oğuz Özdoğan for their invaluable contributions in conducting the wind tunnel experiments. Their relentless dedication and technical support have played a vital role in the success of this research. Their willingness to go above and beyond, sacrificing their time and effort day and night, has been truly remarkable and has greatly influenced the completion of this thesis. I am truly grateful for their significant role in making this research possible.

I am truly fortunate to have had Dilay Kılavuz as a collaborator during this period of my academic pursuits. Dilay's skills and dedication were instrumental in several crucial aspects of my research, including the mechanical design and assembly of the test item, data processing, and performing the wind tunnel tests. Her meticulous attention to detail ensured the successful development and construction of the test item, while her efforts in data processing enabled the extraction of meaningful insights from complex datasets. Apart from her technical contributions, Dilay's support and encouragement were invaluable to me during the highs and lows of this challenging academic journey. Her willingness to lend an ear, provide insightful feedback, and offer constructive suggestions greatly enriched my research experience.

I am grateful to Ilgaz Doğa Okcu for being a steadfast supporter of my work right from the beginning. As my academic confidant and companion, his presence has significantly enriched the overall experience of my academic journey. Our discussions on scientific methodologies, sharing our thoughts and worries, our lighthearted chats and “long lasting confabulations” have been invaluable sources of

motivation and inspiration throughout this process. I cannot thank him enough for his contributions.

I would like to say thank you to Merve Özkan, Muharrem Özgün, Ali İzzet Alkılıç, and Ali İhsan Akbaş for their efforts during the wind tunnel experiments.

Special thanks go to my mother, Gülseren Özer, my father, Baki Özer, and my big brother, Doğukan Özer, for their presence and constant motivation throughout my academic journey. From my childhood, they have been there to support and encourage my academic studies, and their belief in me has been a driving force. I am deeply grateful for their support and the positive impact they have had on my education.

The present research was supported by TÜBİTAK-SAGE.

TABLE OF CONTENTS

ABSTRACT v

ÖZ vii

ACKNOWLEDGMENTS x

TABLE OF CONTENTS xiii

LIST OF TABLES xvii

LIST OF FIGURES xviii

LIST OF ABBREVIATIONS xxxii

CHAPTERS

1 INTRODUCTION 1

1.1 Background 1

1.2 Objective of the Thesis 3

1.3 Detailed Physics of Supersonic Intake Flows 3

1.3.1 Working Principles of Supersonic Intakes 3

1.3.2 Shock Wave Boundary Layer Interaction and Pseudo-Shock 11

1.3.3 Catastrophe, Hysteresis and Bifurcation Effects 19

1.4 Literature Review 21

1.5 Scope of the Work 27

1.6 The Outline of the Thesis 28

2 EXPERIMENTAL TECHNIQUE AND DATA PROCESSING 29

2.1 Trisonic Wind Tunnel 29

2.2 Test Configuration 30

2.3 Test Item and Instrumentation 32

2.4 Motion Profile for the Back Pressure Valve 36
2.5 Test Conditions 38
2.6 Pressure Measurement 39
2.7 Calculation of Pressure Recovery and Mass Flow Ratio 42
2.8 Response Analysis for the Pressure Measurement Tubing 43
2.9 Shadowgraph Images and Edge Detection 45
3 EXPERIMENTAL RESULTS 51
3.1 Shock Structures 51
3.1.1 Mach = 3 with Bleed (Test 4331) 51
3.1.1.1 Average Images 51
3.1.1.2 Transitions and Change in The Shock Structures 54
3.1.1.3 Shock Oscillations 59
3.1.2 Mach = 2.63 with Bleed (Test 4340) 74
3.1.2.1 Average Images 74
3.1.2.2 Transitions and Change in the Shock Structures 76
3.1.2.3 Shock Oscillations 79
3.1.3 Mach = 3 without Bleed (Test 4372) 90
3.1.3.1 Average Images 90
3.1.3.2 Transitions and the Change in the Shock Structure 92
3.1.3.3 Shock Oscillations 93
3.1.4 Mach = 2.63 without Bleed (Test 4373) 101
3.1.4.1 Average Images 101
3.1.4.2 Transitions and the Change in the Shock Structures 103
3.2 Pressure Measurements 105

3.2.1 Overall Behavior and Repeatability Tests....105
3.2.2 Change of Pressure Along the Intake and Hysteresis....108
3.2.2.1 Mach = 3 with Bleed (Test 4331)....108
3.2.2.2 Mach = 2.63 with Bleed (Test 4340)....115
3.2.2.3 Mach = 3 without Bleed (Test 4372)....119
3.2.2.4 Mach = 2.63 without Bleed (Test 4373)....124
3.2.3 Characteristics Diagrams....128
4 NUMERICAL SIMULATIONS AND COMPARISONS WITH THE EXPERIMENTS....131
4.1 Geometry, Grid, Boundary Conditions and Method....131
4.2 Turbulence Models....135
4.3 Grid Sensitivity Study....138
4.4 Matrix of Simulations....139
4.5 Results and Comparison with The Experimental Data....140
4.5.1 Simulations at VPN 1....140
4.5.1.1 Simulations at Mach = 3....140
4.5.1.2 Simulations for Mach = 2.63....146
4.5.1.3 Examination of Pre-Shock Mach Number....151
4.5.2 Simulations at Different Back Throttling....155
4.5.2.1 Mach = 3 with Bleed (Test 4331)....155
4.5.2.2 Mach = 3 without Bleed (Test 4372)....169
4.5.2.3 Mach = 2.63 with Bleed (Test 4340)....178
4.5.2.4 Mach = 2.63 without Bleed (Test 4373)....185
5 SUMMARY AND CONCLUDING REMARKS....193

REFERENCES 199

APPENDICES

A. Calculated Distances Using the Tracer Lines for Different Tests and VPNs 211

B. Oscillation of Shock Patterns for Different Tests and VPNs 217

C. Change in the Shock Structures During Back Pressure Transitions..... 223

D. Change of Shock Structures During Buzz..... 225

E. Pressure Data of the Repatability Tests..... 227

F. Change of Pressure Along the Intake for Different Tests and VPNs 229

G. Mach Number Contour Plots and Pressure Data Obtained from the Numerical Simulations..... 234

CURRICULUM VITAE 241

LIST OF TABLES

TABLES

Table 2-1. Locations of pressure measurement taps in millimeters..... 36
Table 2-2. Details of the valve motion profile. 37
Table 2-3. Test conditions..... 39
Table 2-4. Pressure measurement taps connected to the respective pressure scanners. 40
Table 3-1. Summary of changes in shock positions for Mach = 3 with bleed (Test 4331). 72
Table 3-2. Summary of changes in shock positions for Mach = 2.63 with bleed (Test 4340). 88
Table 3-3. Summary of change in shock positions for Mach = 3 without bleed (Test 4372). 99
Table 4-1. Pressure far-field boundary conditions. 134
Table 4-2. Matrix of simulations. 139

LIST OF FIGURES

FIGURES

Figure 1-1. Typical rectangular (or two-dimensional) mixed compression supersonic intake section view (reproduced from [6]). 5
Figure 1-2. Two-dimensional mixed compression supersonic intake elements and idealized representation of shock systems (reproduced from [21]). 6
Figure 1-3. Throat (minimum area) locations for external and mixed compression intakes. 7
Figure 1-4. Operating modes for external compression supersonic intakes (reproduced from [25]). 8
Figure 1-5. Intake characteristic diagram and operating conditions (reproduced from [26], [27]). 9
Figure 1-6. Operating condition definitions with bleed (adapted and reproduced from [29]). 9
Figure 1-7. Idealized shock trap effect of bleed (reproduced from [29]). 10
Figure 1-8. Representation of SWBLI in a supersonic intake (reproduced from [33]). 12
Figure 1-9. Oblique shock boundary layer interaction for attached (top) and separated (bottom) conditions [34] (reproduced sketches). 12
Figure 1-10. Edney's [35] classification of shock interference (reproduced from [34]). 14
Figure 1-11. Schematic for normal shock wave – turbulent boundary layer interactions [24] (reproduced from [7], [39]). 15
Figure 1-12. Representation of pseudo-shock and change of pressure along it (reproduced from [24]). 16
Figure 1-13. Typical terminal shock patterns for supersonic intakes (reproduced from [24] and [9]) 17
Figure 1-14. Schematic of pseudo-shock for λ-type (top) and X-type (bottom) shock structures in a constant area channel (reproduced from [42]). 18

Figure 1-15. Catastrophe, hysteresis and bifurcation (reproduced from [54]) 20
Figure 2-1. Schematic of the Wind Tunnel. 30
Figure 2-2. Schematic for the test configuration (reproduced and adapted from [80]) 31
Figure 2-3. Isometric view of the air intake test item. 32
Figure 2-4. Section view of the air intake test item. 33
Figure 2-5. Dimensions of the air intake test items. 34
Figure 2-6. The measurement pipe and the back pressure valve. 34
Figure 2-7. Air intake station numbering, ramp side, cowl side and the intake entrance height. 35
Figure 2-8. Change of the position of the back pressure valve, full profile (left), close-up view (right). 37
Figure 2-9. Change of the throttling area and the area ratio with the valve position (left) and the VPN (right). 38
Figure 2-10. Variation of test section Mach number and total pressure with time. 39
Figure 2-11. Change of the pressure with time at V1 for Test 4331 (Top: complete data, middle: close-up view-1, bottom: close-up view-2) 41
Figure 2-12. Pressure response of the tubing for the step rise input and linear rise input. 44
Figure 2-13. Pressure response of the tubing for the oscillatory input. 45
Figure 2-14. Comparison of the raw image and the edge detection map 46
Figure 2-15. Comparison of the raw image and the edge detection map for Test 4331 at different VPNs. 47
Figure 2-16. Calibration images 47
Figure 2-17. The tracer line (a), edge detection map (b), intersection point (c). 49
Figure 2-18. Tracer Lines. 49
Figure 3-1. Average images for Mach = 3 with bleed (Test 4331) at VPNs 11 to 16. 52
Figure 3-2. Average images for Mach = 3 with bleed (Test 4331) at VPNs 17 to 22. 53

Figure 3-3. Closer view of the average images for Mach = 3 with bleed (Test 4331) at VPNs 18 to 21 54
Figure 3-4. Variation of the position of the valve and change of shock structures between VPNs 11 and 12 for Mach = 3 with bleed (Test 4331). 55
Figure 3-5. Change of the shock structures between VPNs 11 and 12 for Mach = 3 with bleed (Test 4331). 56
Figure 3-6. Variation of the position of the valve and change of the shock structures between VPNs 16 and 17 for Mach = 3 with bleed (Test 4331). 57
Figure 3-7. Change of the shock structures between VPNs 16 and 17 for Mach = 3 with bleed (Test 4331). 57
Figure 3-8. Variation of position of valve and change of shock structures between VPNs 17 and 18 for Mach = 3 with bleed (Test 4331). 58
Figure 3-9. Change of shock structures between VPNs 17 and 18 for Mach = 3 with bleed (Test 4331). 59
Figure 3-10. Calculated distances using tracer line 1 and corresponding valve positions for Mach = 3 with bleed (Test 4331). 60
Figure 3-11. Histogram plots for VPNs 15 to 17 (Mach = 3, with bleed, Test 4331). 61
Figure 3-12. Calculated distances using tracer line 2 and corresponding valve positions for Mach = 3 with bleed (Test 4331). 62
Figure 3-13. Histogram plots for VPNs 19 to 21 (Mach = 3, with bleed, Test 4331). 62
Figure 3-14. Oscillation of shock patterns at VPN 13 for Mach = 3 with bleed (Test 4331). 63
Figure 3-15. Comparison of shock positions at VPN 13 for Mach = 3 with bleed (Test 4331). 64
Figure 3-16. Comparison of shock positions at VPN 14 for Mach = 3 with bleed (Test 4331). 64
Figure 3-17. Comparison of shock positions at VPN 15 for Mach = 3 with bleed (Test 4331). 65

Figure 3-18. Comparison of shock positions at VPN 16 for Mach = 3 with bleed (Test 4331). 65
Figure 3-19. Oscillation of shock patterns at VPN 17 for Mach = 3 with bleed (Test 4331). 66
Figure 3-20. Comparison of shock positions at VPN 17 for Mach = 3 with bleed (Test 4331). 66
Figure 3-21. Oscillation of shock patterns at VPN 18 for Mach = 3 with bleed (Test 4331). 67
Figure 3-22. Comparison of shock positions at VPN 18 for Mach = 3 with bleed (Test 4331). 68
Figure 3-23. Oscillation of shock patterns at VPN 19 for Mach = 3 with bleed (Test 4331). 69
Figure 3-24. Comparison of shock positions at VPN 19 for Mach = 3 with bleed (Test 4331). 69
Figure 3-25. Oscillation of shock patterns at VPN 20 for Mach = 3 with bleed (Test 4331). 70
Figure 3-26. Comparison of shock positions at VPN 20 for Mach = 3 with bleed (Test 4331). 70
Figure 3-27. Comparison of shock positions at VPN 21 for Mach = 3 with bleed (Test 4331). 71
Figure 3-28. Comparison of shock positions at VPN 22 for Mach = 3 with bleed (Test 4331). 71
Figure 3-29. Comparison of shock positions at VPNs 13 and 14 for Mach = 3 with bleed (Test 4331). 73
Figure 3-30. Comparison of shock positions at VPNs 15, 16 and 17 for Mach = 3 with bleed (Test 4331). 73
Figure 3-31. Comparison of shock positions at VPNs 18, 19 and 20 for Mach = 3 with bleed (Test 4331). 74
Figure 3-32. Average images for Mach = 2.63 with bleed (Test 4340) at VPNs 11 to 16. 75

Figure 3-33. Average images for Mach = 2.63 with bleed (Test 4340) at VPNs 17 to 22. 75
Figure 3-34. Comparison of shock structures between the Mach = 2.63 (Test 4340) and Mach = 3 (Test 4331) with bleed for VPN 11. 76
Figure 3-35. Variation of the position of the valve and change of shock structures between VPNs 11 and 12 for Mach = 2.63 with bleed (Test 4340). 77
Figure 3-36. Variation of the position of the valve and change of shock structures between VPNs 16 and 17 for Mach = 2.63 with bleed (Test 4340). 78
Figure 3-37. Change of the shock structures between VPNs 16 and 17 for Mach = 2.63 with bleed (Test 4340). 79
Figure 3-38. Calculated distances using tracer line 1 and corresponding valve positions for Mach = 2.63 with bleed (Test 4340). 80
Figure 3-39. Histogram plots for VPNs 15 and 16 (Mach = 2.63, with bleed, Test 4340). 80
Figure 3-40. Calculated distances using tracer line 2 and corresponding valve positions for Mach = 2.63 with bleed (Test 4340). 81
Figure 3-41. Histogram plots for VPNs 17 to 19 (Mach = 2.63, with bleed, Test 4340). 81
Figure 3-42. Comparison of shock positions at VPN 13 for Mach = 2.63 with bleed (Test 4340) 82
Figure 3-43. Comparison of shock positions at VPN 14 for Mach = 2.63 with bleed (Test 4340) 82
Figure 3-44. Comparison of shock positions at VPN 15 for Mach = 2.63 with bleed (Test 4340) 82
Figure 3-45. Oscillation of shock patterns at VPN 16 for Mach = 2.63 with bleed (Test 4340) 83
Figure 3-46. Comparison of shock positions at VPN 16 for Mach = 2.63 with bleed (Test 4340) 84
Figure 3-47. Comparison of shock positions at VPN 17 for Mach = 2.63 with bleed (Test 4340) 84

Figure 3-48. Comparison of Mach stems at VPNs 17 and 18 for Mach = 2.63 with bleed (Test 4340). 85
Figure 3-49. Comparison of shock positions at VPN 18 for Mach = 2.63 with bleed (Test 4340). 85
Figure 3-50. Oscillation of shock patterns at VPN 19 for Mach = 2.63 with bleed (Test 4340). 86
Figure 3-51. Comparison of shock positions at VPN 19 for Mach = 2.63 with bleed (Test 4340). 86
Figure 3-52. Comparison of shock positions at VPN 20 for Mach = 2.63 with bleed (Test 4340). 87
Figure 3-53. Comparison of shock positions at VPN 21 for Mach = 2.63 with bleed (Test 4340). 88
Figure 3-54. Comparison of shock positions at VPNs 14, 15 and 16 for Mach = 2.63 with bleed (Test 4340). 89
Figure 3-55. Comparison of shock positions at VPNs 17, 18 and 19 for Mach = 2.63 with bleed (Test 4340). 89
Figure 3-56. Average images for Mach = 3 without bleed (Test 4372) at VPNs 11 to 15. 91
Figure 3-57. Average images for Mach = 3 without bleed (Test 4372) at VPNs 16 to 19. 92
Figure 3-58. Variation of the position of the valve and change of shock structures between VPNs 10 and 11 for Mach = 3 without bleed (Test 4372). 93
Figure 3-59. Calculated distances using tracer line and corresponding valve positions for Mach = 3 without bleed (Test 4372). 94
Figure 3-60. Histogram plots for VPNs 13 and 15 (Mach = 3, without bleed, Test 4372). 94
Figure 3-61. Oscillation of shock patterns at VPN 11 for Mach = 3 without bleed (Test 4372). 95
Figure 3-62. Comparison of shock positions at VPN 11 for Mach = 3 without bleed (Test 4372). 95

Figure 3-63. Comparison of shock positions at VPN 12 for Mach = 3 without bleed (Test 4372).....96
Figure 3-64. Comparison of shock positions at VPN 13 for Mach = 3 without bleed (Test 4372).....96
Figure 3-65. Comparison of shock positions at VPN 14 for Mach = 3 without bleed (Test 4372).....97
Figure 3-66. Oscillation of shock patterns at VPN 15 for Mach = 3 without bleed (Test 4372).....98
Figure 3-67. Comparison of shock positions at VPN 15 for Mach = 3 without bleed (Test 4372).....98
Figure 3-68. Comparison of shock positions at VPN 16 for Mach = 3 without bleed (Test 4372).....98
Figure 3-69. Comparison of shock positions at VPNs 11, 12 and 13 for Mach = 3 without bleed (Test 4372).....99
Figure 3-70. Comparison of shock positions at VPNs 14, 15 and 16 for Mach = 3 without bleed (Test 4372).....100
Figure 3-71. Oscillation of shock patterns at VPN 17 for Mach = 3 without bleed (Test 4372).....101
Figure 3-72. Average images for Mach = 2.63 without bleed (Test 4373) at VPNs 10 to 15.....102
Figure 3-73. Average images for Mach = 2.63 without bleed (Test 4373) at VPNs 16 to 19.....102
Figure 3-74. Variation of the position of the valve and change of shock structures between VPNs 13 and 14 for Mach = 2.63 without bleed (Test 4373).....103
Figure 3-75. Variation of the position of the valve and change of shock structures between VPNs 17 and 18 for Mach = 2.63 without bleed (Test 4373).....104
Figure 3-76. Variation of V1 pressure and valve position with respect to time for Mach = 3 (Test 4331) and for Mach = 2.63 (Test 4340) with bleed.....105
Figure 3-77. Variation of V1 pressure and valve position with respect to time for Mach = 3 (Test 4372) and for Mach = 2.63 (Test 4373) without bleed.....106

Figure 3-78. Variation of pressures with respect to valve position for Mach = 3, with bleed (Test 4331 and 4331-rep). 107
Figure 3-79. Variation of pressure with respect to VPN for Mach = 3, with bleed (Test 4331 and 4331-rep). 108
Figure 3-80. Change of pressure along the intake at VPNs between 9 and 13 for Mach = 3 with bleed (Test 4331). 110
Figure 3-81. Change of pressure along the intake at VPNs between 14 and 18 for Mach = 3 with bleed (Test 4331). 111
Figure 3-82. Change of pressure along the intake at VPNs between 18 and 22 for Mach = 3 with bleed (Test 4331). 112
Figure 3-83. Change of pressure along the intake at VPNs between 23 and 30 for Mach = 3 with bleed (Test 4331). 112
Figure 3-84. Variation of pressure with respect to VPN and comparison of throttling direction for Mach = 3 with bleed (Test 4331). 113
Figure 3-85. Change of pressure along the intake and comparison of throttling direction at VPNs 15 and 16 for Mach = 3 with bleed (Test 4331). 114
Figure 3-86. Change of pressure along the intake and comparison of throttling direction at VPNs 17 and 18 for Mach = 3 with bleed (Test 4331). 115
Figure 3-87. Change of pressure along the intake at VPNs between 9 and 13 for Mach = 2.63 with bleed (Test 4340). 116
Figure 3-88. Change of pressure along the intake at VPNs between 14 and 18 for Mach = 2.63 with bleed (Test 4340). 117
Figure 3-89. Variation of pressure with respect to VPN and comparison of throttling direction for Mach = 2.63 with bleed (Test 4340). 118
Figure 3-90. Change of pressure along the intake and comparison of throttling direction at VPNs 14, 16 and 18 for Mach = 2.63 with bleed (Test 4340). 119
Figure 3-91. Change of pressure along the intake at VPNs between 9 and 13 for Mach = 3 without bleed (Test 4372). 120
Figure 3-92. Change of pressure along the intake at VPNs between 14 and 18 for Mach = 3 without bleed (Test 4372). 121

Figure 3-93. Change of pressure along the intake at VPNs between 18 and 20 for Mach = 3 without bleed (Test 4372). 121
Figure 3-94. Variation of pressure with respect to VPN and comparison of throttling direction for Mach = 3 without bleed (Test 4372)..... 122
Figure 3-95. Change of pressure along the intake and comparison of throttling direction at VPNs 16 and 17 for Mach = 3 without bleed (Test 4372). 123
Figure 3-96. Change of pressure along the intake and comparison of throttling direction at VPNs 19 and 20 for Mach = 3 without bleed (Test 4372). 124
Figure 3-97. Change of pressure along the intake at VPNs between 9 and 13 for Mach = 2.63 without bleed (Test 4373). 125
Figure 3-98. Change of pressure along the intake at VPNs between 13 and 17 for Mach = 2.63 without bleed (Test 4373). 125
Figure 3-99. Change of pressure along the intake at VPNs between 17 and 19 for Mach = 2.63 without bleed (Test 4373). 126
Figure 3-100. Variation of pressure with respect to VPN and comparison of throttling direction for Mach = 2.63 without bleed (Test 4373)..... 127
Figure 3-101. Change of pressure along the intake and comparison of throttling direction at VPNs 16 and 17 for Mach = 2.63 without bleed (Test 4373). 128
Figure 3-102. Change of pressure along the intake and comparison of throttling direction at VPNs 17 and 18 for Mach = 2.63 without bleed (Test 4373). 128
Figure 3-103. Characteristic diagrams for the tests. 129
Figure 3-104. Variation of mass flow ratio with respect to the VPN. 130
Figure 3-105. Variation of the bleed pressure with the VPN. 130
Figure 4-1. CFD geometry and definition of boundary conditions for the test item with bleed. 133
Figure 4-2. Isometric view of the generated grid for the test item with bleed. 134
Figure 4-3. Change of pressure along the intake for different grid sizes. 138
Figure 4-4. Mach number contour for the numerical simulation corresponding to Mach = 3 with bleed (Test 4331) at VPN 1..... 141

Figure 4-5. Comparison of pressure distribution along the intake between numerical and experimental data for Mach = 3 with bleed (Test 4331) at VPN 1. 142
Figure 4-6. Comparison between the numerical density gradient magnitude contour and experimental shadowgraph image for Mach = 3 with bleed (Test 4331) at VPN 1..... 143
Figure 4-7. Density gradient magnitude contour with velocity vectors and zero velocity line for the numerical simulation corresponding to Mach = 3 with bleed (Test 4331) at VPN 1. 143
Figure 4-8. Mach number contour for the numerical simulation corresponding to Mach = 3 without bleed (Test 4372) at VPN 1. 144
Figure 4-9. Comparison of pressure distribution along the intake between numerical and experimental data for Mach = 3 without bleed (Test 4372) with fully open valve. 145
Figure 4-10. Comparison of the density gradient magnitude contours of numerical simulations for the corresponding condition to Mach = 3 without bleed (Test 4372) at VPN 1..... 145
Figure 4-11. Comparison of the numerical density gradient magnitude contour (with velocity vectors) and experimental shadowgraph images for Mach = 3 without bleed (Test 4372) at VPN 1. 146
Figure 4-12. Mach number contours for the numerical simulations corresponding to Mach = 2.63 with bleed (Test 4340) at VPN 1. 148
Figure 4-13. Comparison of pressure distribution along the intake between numerical and experimental data for Mach = 2.63 with bleed (Test 4340) at VPN 1. 149
Figure 4-14. Mach number contours for the numerical simulations corresponding to Mach = 2.63 without bleed (Test 4373) at VPN 1. 150
Figure 4-15. Comparison of pressure distribution along the intake between numerical and experimental data for Mach = 2.63 without bleed (Test 4373) at VPN 1..... 150

Figure 4-16. Comparison of the density gradient magnitude contours of numerical simulations for the corresponding condition to Mach = 2.63 without bleed (Test 4373) at VPN 1. 151
Figure 4-17. Placed lines. 152
Figure 4-18. Variation of Mach number distribution along placed lines obtained from the numerical simulations corresponding to Mach = 2.63 and Mach = 3 with bleed at VPN 1. 153
Figure 4-19. Comparison of Mach number distribution along L1-L6 obtained from the numerical simulations corresponding to Mach = 2.63 and Mach = 3 with bleed at VPN 1. 154
Figure 4-20. Comparison of Mach number distribution along L7-L10 obtained from the numerical simulations corresponding to Mach = 2.63 and Mach = 3 with bleed at VPN 1. 155
Figure 4-21. Mach number contours for the numerical simulations corresponding to Mach = 3 with bleed (Test 4331) at VPN 15. 157
Figure 4-22. Comparison of pressure distribution along the intake between numerical and experimental data for Mach = 3 with bleed (Test 4331) at VPN 15. 158
Figure 4-23. Numerical density gradient magnitude contours and experimental shadowgraph image for Mach = 3 with bleed (Test 4331) at VPN 15. 159
Figure 4-24. Density gradient magnitude contour with velocity vectors and zero velocity line for the numerical simulation corresponding to Mach = 3 with bleed (Test 4331) at VPN 15. 160
Figure 4-25. Comparison of pressure distribution and Mach number at the exit of the intake for Mach = 3 with bleed (Test 4331) at VPN 15. 160
Figure 4-26. Mach number contours for the numerical simulations corresponding to Mach = 3 with bleed (Test 4331) at VPN 18. 162
Figure 4-27. Comparison of pressure distribution along the intake between numerical and experimental data for Mach = 3 with bleed (Test 4331) at VPN 18. 163

Figure 4-28. Numerical density gradient magnitude contours and experimental shadowgraph image for Mach = 3 with bleed (Test 4331) at VPN 18. 164
Figure 4-29. Density gradient magnitude contours with velocity vectors and zero velocity line for the numerical simulation corresponding to Mach = 3 with bleed (Test 4331) at VPN 18. 164
Figure 4-30. Comparison of pressure distribution and Mach number at the exit of the intake for Mach = 3 with bleed (Test 4331) at VPN 18. 165
Figure 4-31. Mach number contours for the numerical simulations corresponding to Mach = 3 with bleed (Test 4331) at VPN 20. 166
Figure 4-32. Comparison of pressure distribution along the intake between numerical and experimental data for Mach = 3 with bleed (Test 4331) at VPN 20. 167
Figure 4-33. Density gradient magnitude contours with velocity vectors and zero velocity line for the numerical simulations corresponding to Mach = 3 with bleed (Test 4331) and shadowgraph image at VPN 20. 168
Figure 4-34. Comparison of pressure distribution and Mach number at the exit of the intake for Mach = 3 with bleed (Test 4331) at VPN 20. 169
Figure 4-35. Mach number contours for the numerical simulations corresponding to Mach = 3 without bleed (Test 4372) at VPN 15. 170
Figure 4-36. Comparison of pressure distribution along the intake between numerical and experimental data for Mach = 3 without bleed (Test 4372) at VPN 15. 171
Figure 4-37. Density gradient magnitude contours with velocity vectors and zero velocity line for the numerical simulation and the shadowgraph image corresponding to Mach = 3 without bleed (Test 4372) at VPN 15. 172
Figure 4-38. Comparison of pressure distribution and Mach number at the exit of the intake for Mach = 3 without bleed (Test 4372) at VPN 15. 173
Figure 4-39. Mach number contours for the numerical simulations corresponding to Mach = 3 without bleed (Test 4372) at VPN 18. 174

Figure 4-40. Comparison of pressure distribution along the intake between numerical and experimental data for Mach = 3 without bleed (Test 4372) at VPN 18. 175
Figure 4-41. Comparison of pressure distribution and Mach number at the exit of the intake Mach = 3 without bleed (Test 4372) at VPN 18. 175
Figure 4-42. Density gradient magnitude contours with velocity vectors and zero velocity lines for the numerical simulation and the shadowgraph image corresponding to Mach = 3 without bleed (Test 4372) at VPN 18. 177
Figure 4-43. Mach number contours for the numerical simulations corresponding to Mach = 2.63 with bleed (Test 4340) at VPN 18. 179
Figure 4-44. Comparison of pressure distribution along the intake between numerical and experimental data for Mach = 2.63 with bleed (Test 4340) at VPN 18. 180
Figure 4-45. Numerical density gradient magnitude contour and experimental shadowgraph image for Mach = 2.63 with bleed (Test 4340) at VPN 18. 181
Figure 4-46. Density gradient magnitude contour with velocity vectors and zero velocity line for the numerical simulation corresponding to Mach = 2.63 with bleed (Test 4340) at VPN 18. 181
Figure 4-47. Comparison of pressure distribution and Mach number at the exit of the intake for Mach = 2.63 with bleed (Test 4340) at VPN 18. 182
Figure 4-48. Mach number contours for the numerical simulations corresponding to Mach = 2.63 with bleed (Test 4340) at VPN 20. 183
Figure 4-49. Comparison of pressure distribution along the intake between numerical and experimental data for Mach = 2.63 with bleed (Test 4340) at VPN 20. 184
Figure 4-50. Comparison of pressure distribution and Mach number at the exit of the intake for Mach = 2.63 with bleed (Test 4340) at VPN 20. 184
Figure 4-51. Numerical density gradient magnitude contour with velocity vectors and experimental shadowgraph image for Mach = 2.63 with bleed (Test 4340) at VPN 20. 185

Figure 4-52. Mach number contours for the numerical simulations corresponding to Mach = 2.63 without bleed (Test 4373) at VPN 15. 187
Figure 4-53. Comparison of pressure distribution along the intake between numerical and experimental data for Mach = 2.63 without bleed (Test 4373) at VPN 15..... 188
Figure 4-54. Numerical density gradient magnitude contour and experimental shadowgraph image for Mach = 2.63 without bleed (Test 4373) at VPN 15. 188
Figure 4-55. Comparison of pressure distribution and Mach number at the exit of the intake for Mach = 2.63 without bleed (Test 4373) at valve position 15. 189
Figure 4-56. Mach number contours for the numerical simulations corresponding to Mach = 2.63 without bleed (Test 4373) at VPN 18. 190
Figure 4-57. Density gradient magnitude contours with velocity vectors and zero velocity line for the numerical simulation and the shadowgraph image corresponding to Mach = 2.63 without bleed (Test 4373) at VPN 18. 191
Figure 4-58. Comparison of pressure distribution along the intake between numerical and experimental data for Mach = 2.63 without bleed (Test 4373) at VPN 18..... 192
Figure 4-59. Comparison of pressure distribution and Mach number at the exit of the intake for Mach = 2.63 without bleed (Test 4373) at VPN 18..... 192

LIST OF ABBREVIATIONS

2-D	Two Dimensional
3-D	Three Dimensional
BSL	Baseline
CFD	Computational Fluid Dynamics
DAQ	Data Acquisition
DC	Direct Current
EARSM	Explicit Algebraic Reynolds Stress Model
Exp	Experiment
IRR	Integral Rocket Ramjet
ITU	Istanbul Technical University
LED	Light Emitting Diode
LDV	Laser Doppler Velocimetry
MFR	Mass Flow Ratio
RANS	Reynolds-Averaged Navier-Stokes
Rep	Repeatability
SST	Shear Stress Transport
SWBLI	Shock Wave Boundary Layer Interaction
VPN	Valve Position Number

CHAPTER 1

INTRODUCTION

1.1 Background

The concept of ramjet has been studied since the beginning of the 1900s, and its actual operation was achieved in the 1930s. During and after World War II, the interest in ramjet technology increased, and several operational systems, particularly missiles, were developed. The application of the Integral Rocket Ramjet (IRR) concept further increased the development activity of supersonic missile systems, resulting in a high interest in developing supersonic tactical missile systems propelled by IRR. When a solid rocket motor is integrated inside a ramjet engine, the resulting propulsion system is called an IRR type of propulsion system. This concept is widely utilized in modern ramjet missiles [1].

Ramjets are conceptually simple as they do not have any rotating parts. Air compression is achieved through the "ram" effect, where compression depends on the free stream velocity [2]. As a ramjet engine compresses and slows down the air along the intake, the air intake can be considered the key subcomponent of a ramjet that characterizes the engine's overall performance [3]–[6].

Along the supersonic air intakes for IRR systems, the majority of the incoming flow is compressed and slowed down through the aid of shocks, oblique and terminal. Due to viscosity, shock wave-boundary layer interactions (SWBLI) result in complex flow structures. Moreover, back pressure due to combustion results in the generation of a terminal shock, and its interaction with the boundary layer leads to the formation of a pseudo-shock.

In supersonic intakes, the presence of Shock Wave Boundary Layer Interactions (SWBLIs) results in the formation of a complex shock system instead of a single

terminal shock wave with idealized characteristics of a normal shock wave, particularly at high Mach numbers [7]. This shock system is commonly referred to as a pseudo-shock and it consists of successive shocks. Total pressure drop for an idealized normal shock and the pseudo-shock system are different. The maximum pressure recovery obtained with the pseudo-shock is less than the value obtained with normal shock wave[7]. Moreover, the pseudo-shock structures generate uneven velocity distribution at the exit of the intake, which is generally critical for the engine design. Furthermore, oscillatory behavior of the pseudo-shock is important for the engine performance. Thus, characterization of the pseudo-shock structures is important in terms of the performance characterization as well. Although, there are technological advances in the last fifty years, shock structures, shock wave boundary layer interactions and the pseudo-shock phenomena are extremely complex and still not well understood [8]. Studies are ongoing on the shock structures in supersonic intakes and both additional experimental and numerical data is needed to understand the physics of the flow.

For the characterization of the pseudo-shock system, as will be discussed in Section 1.4, there are experimental and numerical studies presented in the open literature. However, experimental examination, using both the high-speed shadowgraph images and the pressure measurements, regarding the pseudo-shocks in a mixed compression intake with different bleed configurations and several back pressures for different Mach numbers, is very limited. Oscillatory behaviour of the pseudo-shocks in a *duct* has been quantified by several studies. However, in a *supersonic intake*, although some studies [9]–[16] have focused on the interaction between the terminal shock and boundary layer and the oscillatory behaviour of the pseudo-shock has been acknowledged, the magnitude of these oscillations has not been quantified. Additionally, for the supercritical operation, the occurrence of abrupt changes in the shock structures as the back pressure changes and the examination of hysteresis behavior at related operational points are missing in the open literature. The open literature offers limited numerical studies specifically focusing on the pseudo-shock structures in supersonic intakes. The intake geometry of this study is based on the

work of Herrmann et al. [10]–[12], but their focus was primarily on the global performance of the intake and buzzing phenomena and no detailed examination of pseudo-shock structures was carried out. Furthermore, there is a lack of numerical research addressing the intake geometry employed in this study.

1.2 Objective of the Thesis

The objective of this thesis is to examine the following aspects related to pseudo-shock structures in a mixed compression rectangular supersonic intake:

i. the effects of back pressure on pseudo-shock structures,
ii. the effects of bleed on pseudo-shock structures,
iii. the magnitude of the fluctuations in the first shock of the pseudo-shock,
iv. hysteresis behaviour of the pseudo-shock,
v. numerical prediction capability of the SST and BSL turbulence models for pseudo-shock structures.

1.3 Detailed Physics of Supersonic Intake Flows

1.3.1 Working Principles of Supersonic Intakes

In this section, working principles of supersonic intakes are explained using information from various studies including [2], [4]–[10]. To clarify, most of the discussions in this section will focus on inviscid flow and idealized representations of shock waves.

In a ramjet engine, air is compressed and slowed down through the air intake, heated or combusted within the combustion chamber, and then discharged through the converging diverging nozzle. Assuming constant free stream conditions for air entering the ramjet, if the intake operates in a supercritical mode mass flow rate of

inflowing air remains constant. Downstream of the combustion chamber, the combustion gases enter the nozzle and are choked at the nozzle throat.

The mass flow rate through a choked nozzle can be calculated using Equation (1-1), where A_t, P_t, and T_t represent the throat area, total pressure, and total temperature at the nozzle throat, respectively. γ and R are the specific heat capacity ratio and gas constant, respectively.

$$\dot{m} = A_t \frac{p_t}{\sqrt{T_t}} \sqrt{\frac{\gamma}{R}} \left(\frac{\gamma+1}{2}\right)^{-\left(\frac{\gamma+1}{2(\gamma-1)}\right)} \tag{1-1}$$

Increasing the fuel flow rate, increases the T_t and subsequently increase the thrust. Assuming constant combustion efficiency and negligible heat losses, an increase in the fuel-air ratio will lead to an increase in the T_t due to the constant mass flow rate of inflowing air. To satisfy the continuity, an increase in the thrust demand or the fuel-air ratio requires an increase in the total pressure at the nozzle throat, assuming the γ and R are constant for different fuel-air ratios. The adjustment of the total pressure is expected to be achieved along the supersonic intake, where the total pressure drop changes according to the back pressure.

A significant amount of compression through the intake is achieved through the aid of shock waves, which naturally results in a drop in the total pressure. Viscosity is another source of the total pressure loss. To decrease the total pressure losses, a series of oblique waves are generally preferred. Supersonic flow must go through a normal shock wave to slow down to subsonic speeds.

A sectional view to define the parts of the intake is shown in Figure 1-1. The normal shock is generally located inside the "Internal Compression" part of the intake and it is sometimes called as terminal shock. For most of the operation, the terminal shock is expected to be located inside the subsonic diffuser. If the internal geometry downstream of the intake's throat is examined, a diverging shape can be observed. It should be noted that the given shape is for "mixed compression" type intakes.

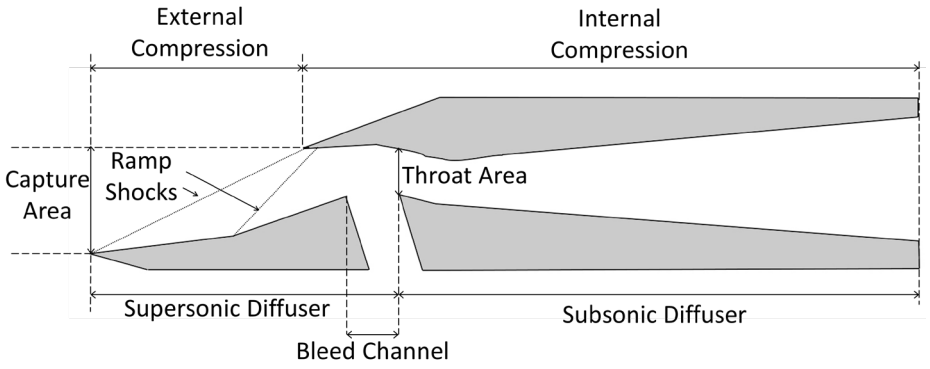


Figure 1-1. Typical rectangular (or two-dimensional) mixed compression supersonic intake section view (reproduced from [6]).

Figure 1-2 illustrates an idealized representation of the internal shock systems and the normal shock for a mixed compression intake. The flow is decelerated through the oblique shock waves and the internal shock systems upstream of the "throat area". From the capture area to the engine face, the intake's throat section has the smallest area. Although this section is referred to as the "throat," a choked flow or sonic condition at this section is not desired and can result in unstart of the intake [17]–[20]. Therefore, to account for operational conditions, the minimum Mach number at the throat is generally selected to be between 1.2-1.3 [20]. It's important to note that as the free stream Mach number increases, the Mach number at the throat also increases. Thus, for a fixed geometry intake, the throat Mach number is typically between 1.2-1.3 for the "lowest operational Mach number" of the ramjet. For instance, if the intake's operational free stream Mach number range is between 2-3, the throat Mach number at Mach = 2 is approximately 1.25, but at Mach = 3, the throat Mach number may exceed 2.

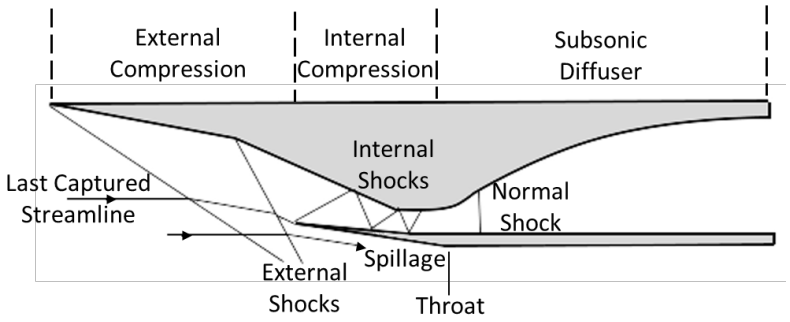


Figure 1-2. Two-dimensional mixed compression supersonic intake elements and idealized representation of shock systems (reproduced from [21]).

It is important to underline that the internal geometry downstream of the throat is diverging. Considering that the Mach number at the intake throat is greater than unity and the subsonic diffuser has a diverging shape, it is expected that the Mach number of the flow will increase along the subsonic diffuser. However, due to the influence of the back pressure from the combustion chamber and the requirement to match the total pressure at the intake exit, the formation of a terminal shock inside the subsonic diffuser becomes necessary. Consequently, the flow is not completely subsonic in the subsonic diffuser section; it slows down from supersonic to subsonic in this part of the intake. If there is no back pressure effect, a normal shock inside the diffuser is not anticipated [22]. In other words, the pressure inside the combustion chamber supports the formation of normal shock and determines its location [23]. Additionally, in the absence of sufficient back pressure, the flow may exit the air intake at supersonic velocities [24].

Before delving into the possible locations of the terminal shock, it should be noted that the air intake throat location definition varies between external and mixed compression intakes. The main difference between mixed compression and external compression intakes is the location of the throat or minimum area (See Figure 1-3). The location of the throat area usually identifies the operational point before transitioning to subcritical mode.

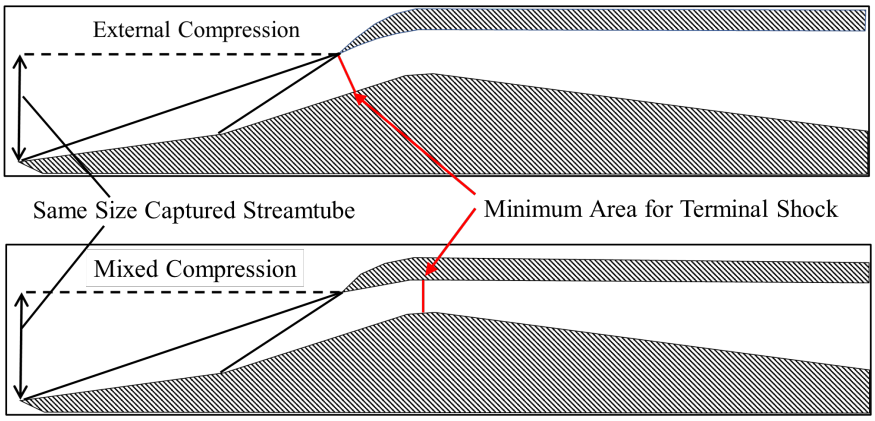


Figure 1-3. Throat (minimum area) locations for external and mixed compression intakes.

The idealized definitions of subcritical, critical, and supercritical for external compression intake are shown in Figure 1-4. As observed, as the back pressure increases or the required total pressure increases due to an increase in the thrust rating, the normal shock moves toward the intake throat. The operation point at which the terminal shock is located on the throat is referred to as "critical" operation point. If the back pressure continues to increase, the mass flow rate flowing into the intake decreases due to the spillage of the terminal shock or an increase in the bleed mass flow rate. As the operating Mach number changes, the oblique shock structures and internal shock system (see Figure 1-4) also change. For Mach numbers below the design value, the captured stream tube area decreases. In other words, spillage due to oblique shock occurs, and the capture ratio (defined as the ratio of the captured flow area, A_c, to the intake's cross-sectional area, A_0) becomes less than one.

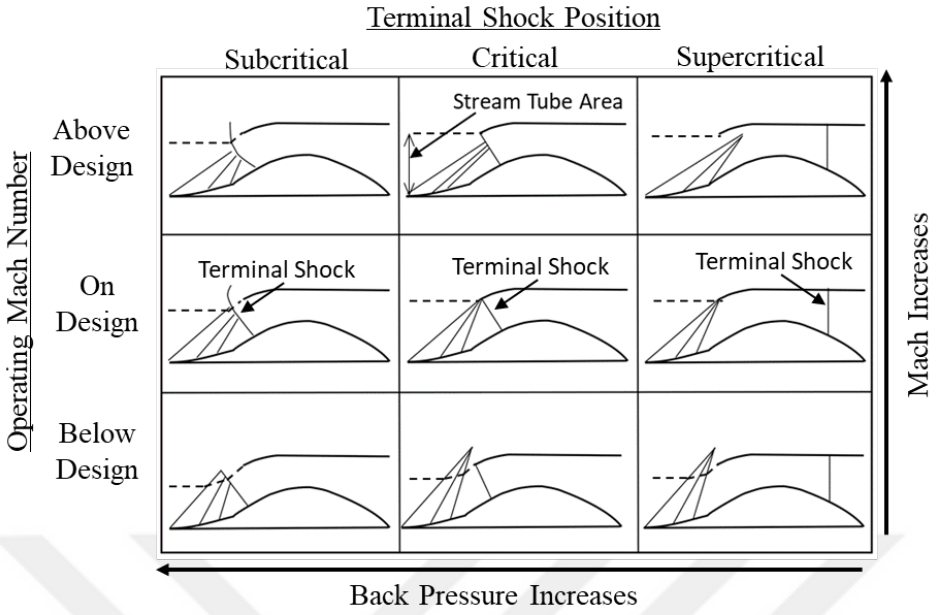


Figure 1-4. Operating modes for external compression supersonic intakes (reproduced from [25]).

In a mixed compression intake without bleed, the idealized spillage effect of the terminal shock (normal shock or bow shock) and the decrease in mass flow ratio can be seen in Figure 1-5, along with the intake performance curve or characteristic diagram. At the critical condition, the normal shock is located at the throat of the intake. In the subcritical condition, the normal shock is located upstream of the throat, while in the supercritical condition, it is located downstream of the throat. When the required exit total pressure is low or the back pressure is relatively low, a stronger shock is required. Due to the diverging shape of the diffuser and the presence of supersonic flow at the throat, the flow accelerates along the diffuser, and the terminal shock is located at far downstream of the diffuser. Thus, the Mach number of the incoming flow of the normal shock increases, and the shock strength increases as well, resulting in a higher total pressure loss. As the back pressure increases, the terminal shock forms at a location closer to the throat, and the Mach number of the flow entering the normal shock decreases, resulting in a weakened shock wave strength [26], [27]. If the characteristic diagram is examined, it can be seen that in the subcritical region, if the back pressure increases more, the region where the buzz phenomenon is seen starts. Inlet buzz can be defined as self-sustained

oscillations of the shock system that appear in almost every type of supersonic inlets and are characterized by high amplitude variations of the air mass flow and exit pressure [28]. It is a highly undesirable phenomenon that can result in thrust loss, flameout, and even structural damages to the engine.

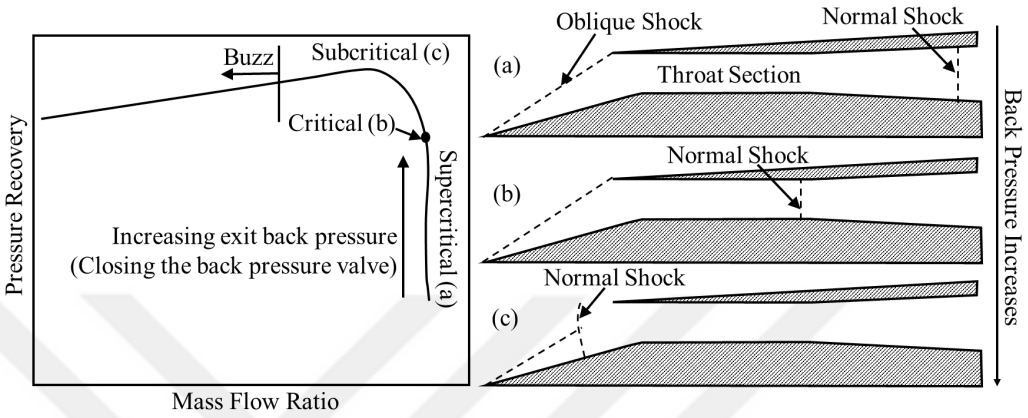


Figure 1-5. Intake characteristic diagram and operating conditions (reproduced from [26], [27]).

The presence of bleed can affect the definition of operating conditions. When the bleed is positioned at the intake throat, an increase in back pressure causes the terminal shock to approach the bleed area, as seen in Figure 1-6.

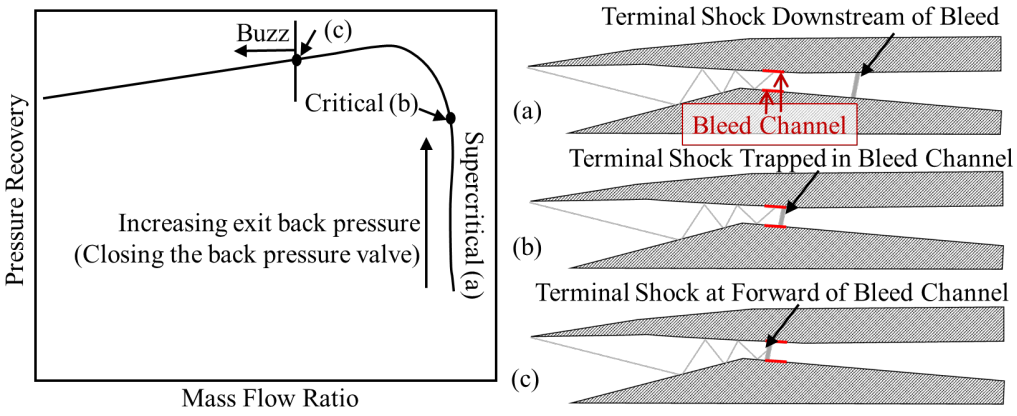


Figure 1-6. Operating condition definitions with bleed (adapted and reproduced from [29]).

Figure 1-6 shows that, when the "idealized" terminal shock is located downstream of the edge of the bleed slot, the operating point is defined as supercritical. However,

as the terminal shock moves to the downstream edge of the bleed slot due to increasing back pressure, the operating point transitions to critical. As the back pressure continues to increase, the terminal shock begins to influence the mass flow rate through the bleed, leading to a phenomenon known as "trapping" of the shock at the bleed slot. The term "trapped" is used because as more flow is discharged through the bleed slot, the change in the location of the terminal shock becomes relatively small. Additionally, when the normal shock positions itself within the shock trap region, the bleed flow generates an aerodynamic divergence effect, which intensifies as the normal shock moves upstream [29]. Figure 1-7 provides an idealized representation of a constant area channel with bleed slots on the upper and lower walls. In summary, unlike an air intake without bleed, as the back pressure increases and the terminal shock reaches the bleed slot, the mass flow rate starts to decrease at the critical operating point. If the back pressure exceeds the subcritical limit, buzzing phenomena are mostly observed.

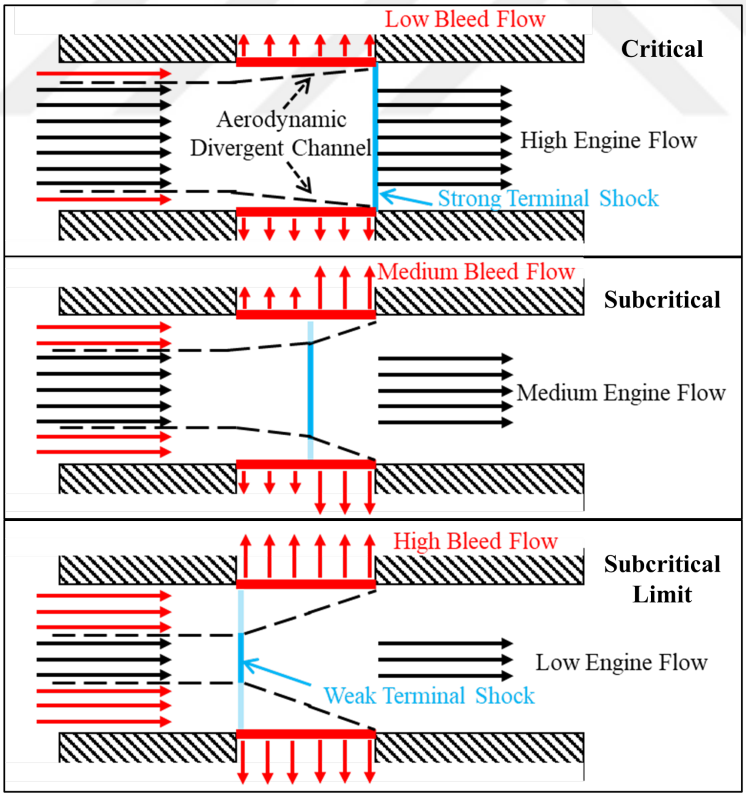


Figure 1-7. Idealized shock trap effect of bleed (reproduced from [29]).

As indicated in this section, the overall flow structure and the location of the terminal shock or normal shock are highly influenced by the back pressure. In subcritical operations, the presence of the terminal shock can also affect oblique shocks and internal shock systems. However, in contrast to the idealized representation of shocks, the interaction between shock waves and boundary layers, known as shock wave boundary layer interactions (SWBLI), gives rise to different flow structures. Due to the adverse pressure gradients, flow separations occur in relation to oblique shocks and normal shocks, accompanied by additional shocks resulting from these separations. Furthermore, the terminal shock inside the diffuser section has the potential to transform into a shock system with series of shocks and associated separations, often referred to as "pseudo-shock". In the subsequent section, various possible flow structures that can exist within a supersonic intake due to SWBLI and pseudo-shock are discussed.

1.3.2 Shock Wave Boundary Layer Interaction and Pseudo-Shock

In supersonic intake flows, formation of shock waves occurs when the flow encounters a change in surface slope, an obstacle downstream, or back pressure that forces the flow to transition from supersonic to subsonic. The interaction between a boundary layer and a shock wave results in complex flow features due to the rapid deceleration of the flow within the boundary layer and the propagation of the shock wave in a multi-layered structure [30]. SWBLI is classified as a flow with an adverse pressure gradient from the perspective of the boundary layer [31]. This is due to the localized increase in pressure caused by the presence of a shock wave. In intake flows, especially at supercritical conditions, SWBLIs, particularly those related to the terminal shock, dominate the flow field [14], [32].

Figure 1-8 depicts SWBLIs in a supersonic intake. The boundary layer develops along the surfaces of the intake, including the internal bottom and top surfaces starting from the leading edge of the ramp and the lip of the cowl, respectively. The cowl shock interacts with the relatively thick boundary layer over the bottom surface,

indicated as "Junction" in the figure. Additionally, multiple shock wave reflections within the throat section interact with the boundary layer. In supercritical operation, shock reflections can also be observed within the subsonic diffuser. Finally, the strong interaction between the terminal shock and the boundary layer leads to the formation of pseudo-shocks and shock-trains [8], [24].

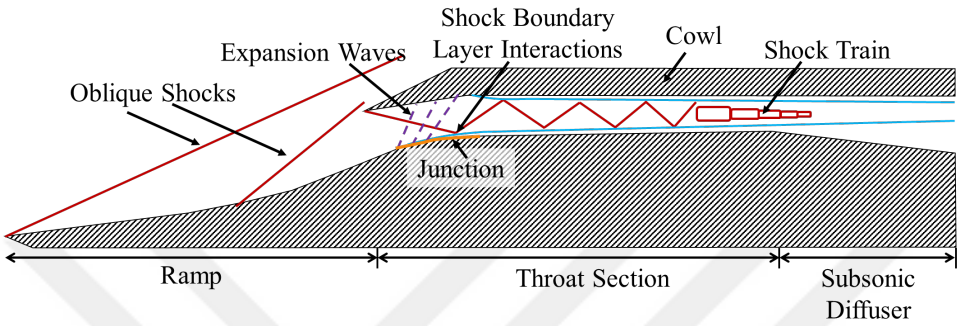


Figure 1-8. Representation of SWBLI in a supersonic intake (reproduced from [33]).

The interaction of the cowl shock with the boundary layer is known as oblique shock boundary layer interaction [33]. Figure 1-9 provides schlieren images and sketches illustrating this type of interaction.

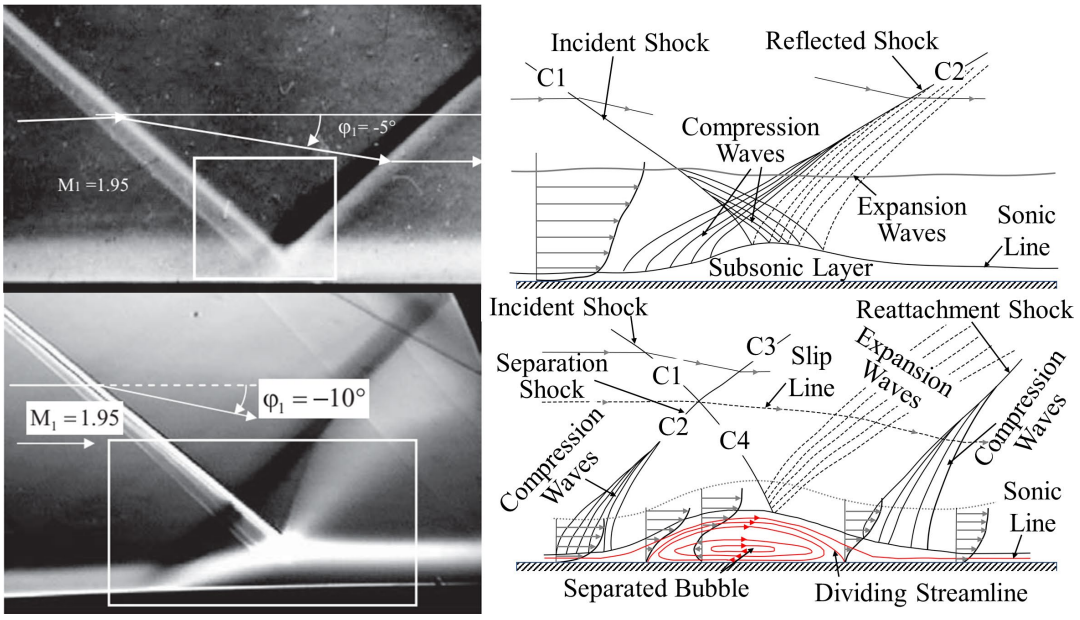


Figure 1-9. Oblique shock boundary layer interaction for attached (top) and separated (bottom) conditions [34] (reproduced sketches).

As seen in Figure 1-9, in the case of attached flow, the incident shock penetrates the subsonic layer and gradually bends as the local Mach number decreases. Consequently, the strength of the shock weakens and eventually disappears at the sonic line. Additionally, the pressure rise caused by the C1 shock is observed upstream of the corresponding inviscid impact location on the wall. This pressure rise is actually transmitted upstream with the aid of the subsonic section of the boundary layer. In conditions where separation occurs, the adverse pressure gradient imposed by the oblique shock is sufficiently high to cause stagnation or reversal of the flow in the vicinity of the wall, leading to flow separation. The formation of a separation bubble results in a curved surface for the flow, which is named as "dividing streamline" in the figure. The separation bubble plays a role in the generation of the C2 shock. As the incident shock (C1) interacts with the C2 shock, it penetrates into the separation bubble as a transmitted shock, named as C4 shock. Due to the shape of the bubble and the presence of the dividing streamline, the C4 shock is reflected as expansion waves, diverting the flow towards the wall and causing reattachment. Subsequently, the compression wave sequence combines and forms a reattachment shock.

Another type of SWBLI commonly observed in supersonic intake flows involves the terminal shock. It is suggested by [9], [24] that the realization of a terminal shock as a single normal shock wave, which would appear as a nearly planar discontinuity perpendicular to the flow direction, rarely occurs under typical operating conditions. The presence of walls, boundary layers, and their interactions with shocks lead to significant modifications of both the boundary layer and shock structures, as well as the overall flow field. The extent of these modifications depends greatly on the condition of the flow just prior to the terminal shock [8], [9], [24].

It is important to note that the occurrence of a terminal shock is primarily influenced by the back pressure for internal flows. In fact, it has been suggested by [34] that the formation of separation shocks in the subsonic diffusers of supersonic intakes is analogous to the flow separation in overexpanded nozzles due to this back pressure effect.

According to the findings of [24] and [9], as the Mach number downstream of the terminal shock increases, the shock structure transitions from a single attached shock to a shock-train consisting of oblique shocks with separations. Furthermore, the shock structures become more similar to Type I, rather than Type II, according to Edney's classification [35] of shock-shock interactions illustrated in Figure 1-10. That is, the Mach stem portion of the shocks becomes smaller as the incoming Mach number increases. Type I and Type II interactions are typically observed in the subsonic diffusers, while Type VI interactions occur in configurations with multiple ramps where the ramp shocks interfere with each other, particularly at below-design Mach numbers.

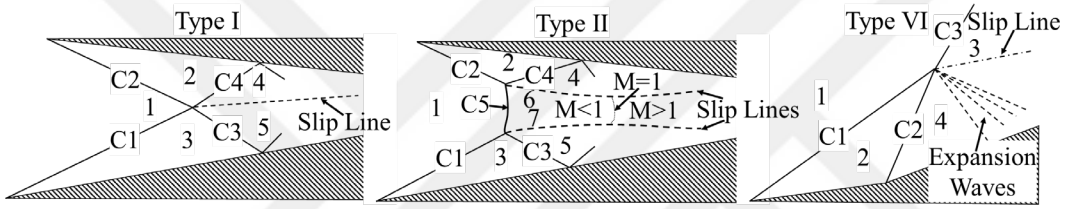


Figure 1-10. Edney's [35] classification of shock interference (reproduced from [34]).

For Type I and Type II interactions, the formation of C1 and C2 shocks is attributed to oblique ramps. However, for duct flows with back pressure, the presence of these shocks depends on the occurrence of flow separation due to the back pressure. The main difference between the two types lies in the formation of a "Mach Disc" or "Mach Stem". The Mach stem part of the structure behaves as a normal shock. Furthermore, the presence of two different interaction points at the edges of the Mach stem results in formation of the two distinct slip lines.

The characteristics of separation and shock structures in the subsonic diffusers of supersonic intakes vary depending on flow conditions and back pressure. The shock formed inside the diffuser due to the back pressure are referred to as "terminal shock". The terminal shock, when considered in conjunction with the boundary layer interactions, gives rise to different shock and flow structures depending on the flow conditions just before the onset of the terminal shock. Figure 1-11 illustrates the

typical terminal shock wave structures for a supersonic constant channel flow with back pressure. It can be observed that for Mach numbers below 1.2, an attached boundary layer shock wave interaction is present. However, as the Mach number increases, a curved shock is first formed, followed by bifurcated shock structures where boundary layer separation is extensive and reattachment tendencies are low. When the Mach number exceeds 1.5, multiple shocks appear downstream of the bifurcated shock. Furthermore, the Mach stem portion of the shocks becomes smaller as the incoming Mach number increases. Additionally, higher Mach number upstream of the pseudo-shock (pre-shock Mach number) results in thicker and wider separation bubbles, and the thickness of the boundary layer downstream of the first shock increases while the confinement effect due to the boundary layer becomes more pronounced. The sequence of bifurcated shocks is commonly referred to as a "shock-train". Beyond the shock-train, there is a region where static pressure continues to increase over a certain distance, and this entire pressure recovery zone is known commonly as the "pseudo-shock" [36]–[38].

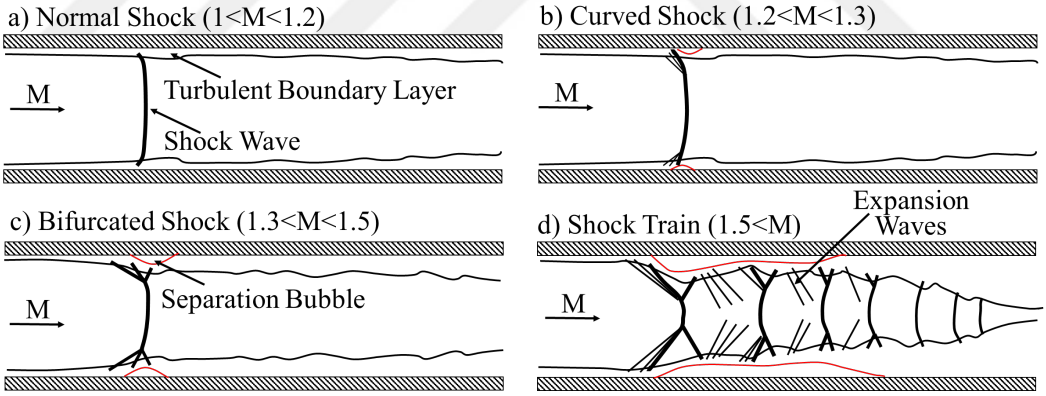


Figure 1-11. Schematic for normal shock wave – turbulent boundary layer interactions [24] (reproduced from [7], [39]).

Figure 1-12 provides a depiction of the pseudo-shock, shock-train region, mixing region, and the corresponding change in pressure along the pseudo-shock.

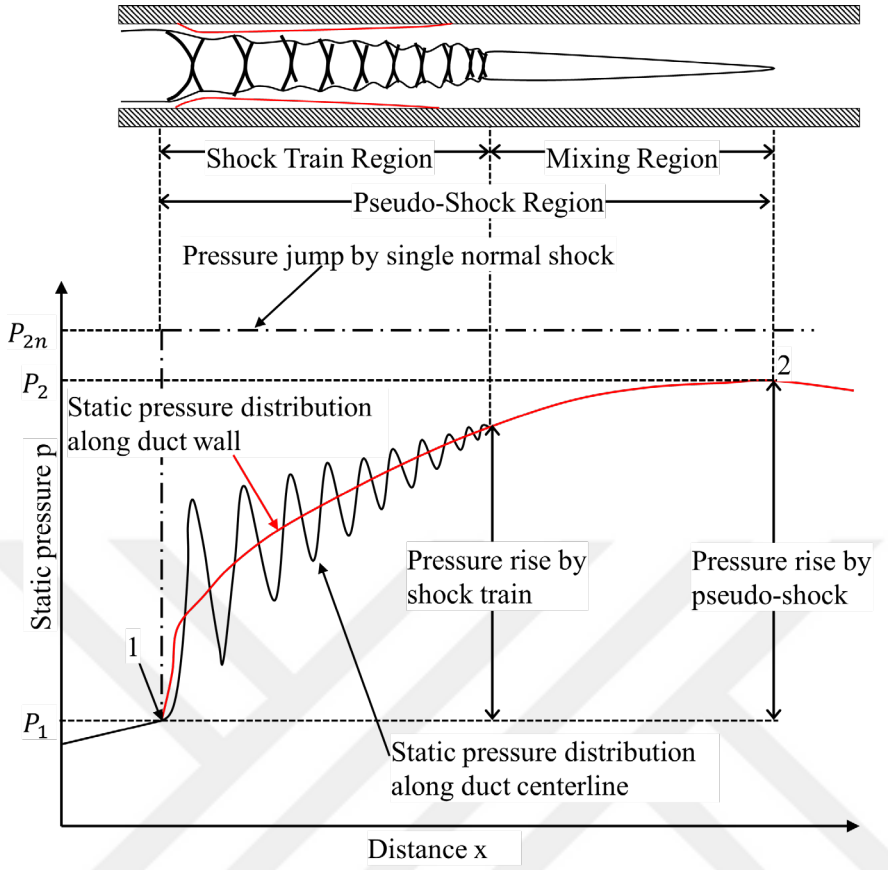


Figure 1-12. Representation of pseudo-shock and change of pressure along it (reproduced from [24]).

In Figure 1-12, it can be observed that the pressure rises in both the shock-train region and the mixing regions. Furthermore, the resulting pressure at the end of the pseudo-shock is lower than the theoretical pressure jump caused by a single normal shock. Additionally, along the centerline of the shock-train, the pressure profile fluctuates due to the successive shocks and expansion regions. However, the change in wall pressure along the duct remains monotonic in both the shock-train region and the mixing region. The existence of differences between the pressure distributions along the duct wall and centerline are noted also by Tamati et al. [40], [41].

The bifurcated shock structures without a Mach stem are sometimes referred to as "X-type," while the bifurcated shocks with a Mach stem are known as "λ-type." Research conducted by [37] has shown that as the Mach number increases, even in a constant area channel, X-type shock structures can be observed. In their

experiments, X-type shocks were observed after a pre-shock Mach number of 1.8. Furthermore, it has been suggested by [9], [24] that for a subsonic diffuser in a supersonic intake, the shock structure changes from a normal shock to a pseudo-shock as the Mach number at the upstream of the pseudo-shock (pre-shock Mach number, M_{1e}) increases. Figure 1-13 provides conceptual schematics illustrating the change in pseudo-shock structure for a supersonic intake diffuser. In the figure, M_∞ represents the free stream Mach number, M_{1e} represents the Mach number at the upstream of the pseudo-shock. The asymmetrical orientation of the pseudo-shock can be seen due to the non-symmetric nature of the diffuser. λ-type pseudo-shock waves are observed for relatively small incoming Mach numbers (M_{1e}), while X-type shocks are seen for higher Mach numbers [36]. In comparison to Edney's classification, λ-type is similar to Edney's Type II, and X-type is similar to Type I. It should be noted that actual shock patterns may differ from those presented in the figure, depending on the type and design of the air intake.

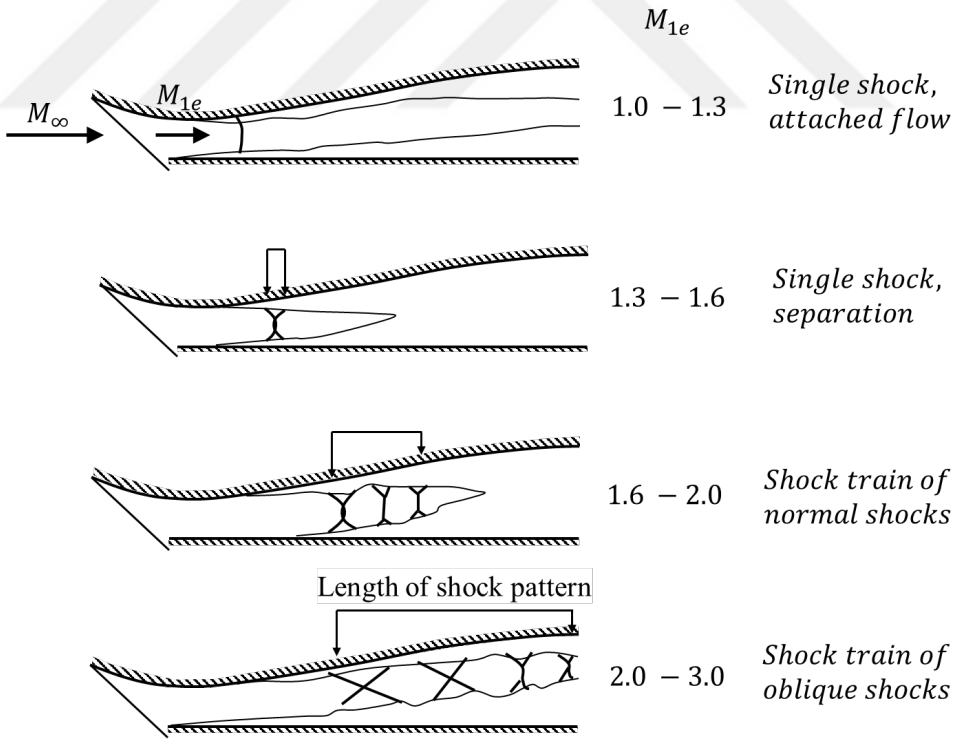


Figure 1-13. Typical terminal shock patterns for supersonic intakes (reproduced from [24] and [9])

When examining the pseudo-shock structures in Figure 1-11 and Figure 1-13, it is seen that the shock-train portion of the pseudo-shock becomes narrower towards the downstream. This narrowing is attributed to the thickening of the boundary layer, which confines the shock-train and gives rise to a phenomenon known as the "virtual nozzle [14]. Within the shock-train, the flow is decelerated by the shocks but then accelerates due to the virtual nozzle effect. The arrangement of shock waves within the pseudo-shock can vary depending on the flow confinement and Mach number, leading to the presence of both normal and oblique shock structures.

Following the shocks, there exists a mixing region. If the diffuser of the intake is sufficiently long, the flow can become relatively uniform and completely subsonic. The representation of X-type and λ-type pseudo-shock structures, including the shock-train and mixing regions, can be seen in Figure 1-14. Conceptually, apart from the specific shock types, both pseudo-shock structures can be considered similar.

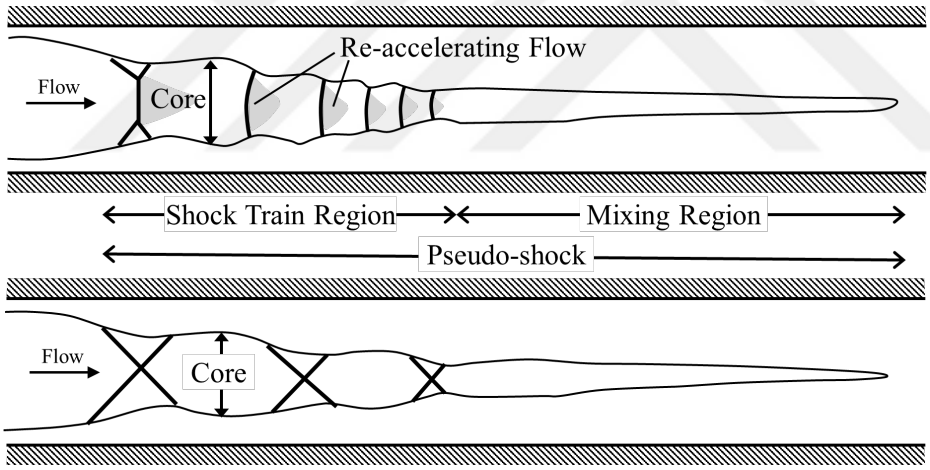


Figure 1-14. Schematic of pseudo-shock for λ-type (top) and X-type (bottom) shock structures in a constant area channel (reproduced from [42]).

The desired condition for the diffuser of a supersonic inlet is to have transonic SWBLIs occurring. However, in practice, termination shock waves are typically stronger than the transonic shock waves. Consequently, the goal of achieving weaker termination shocks is limited by constraints imposed by the overall system size and specific requirements [34]. Thus, as the strength of the terminal shock increases, formation of pseudo-shock is expected to occur. Therefore, it is anticipated that the

emergence of a pseudo-shock will transpire as the strength of the terminal shock increases.

1.3.3 Catastrophe, Hysteresis and Bifurcation Effects

Another interestingly observed features of the supersonic intakes are the hysteresis and catastrophe. This section begins by providing an explanation of the term "hysteresis." Subsequently, the hysteresis phenomena observed for shock interactions and supersonic intakes, as documented in previous studies [43]–[53], are presented and discussed. The concept of hysteresis is often discussed in conjunction with phenomena such as catastrophes and bifurcations, as highlighted in the cited sources. Zeeman [54] provides one of the earliest explanations of these phenomena. While Zeeman's work does not specifically focus on supersonic intakes, subsequent studies on supersonic intakes draw upon the theory expounded by Zeeman. The theory, known as "catastrophe theory," utilizes the mathematical branch of topology to represent relevant problems. The underlying idea of this theory is to describe natural events as smooth equilibrium surfaces that undergo breakdown when catastrophes occur, leading to significant changes in the system's behavior.

Figure 1-15 illustrates the behavior surface and response of behavior to variations in Variable 1 and Variable 2. In an ideal scenario, a smooth change in these variables would correspond to a smooth change in the system's behavior. However, due to the shape of the behavior surface and the presence of a fold curve, there exists a region where a single set of variables can lead to two distinct behaviors. This means that for fixed control parameters, multiple solutions are possible, resulting in bistable operation of the system, including supersonic intakes [46]. The specific behavior exhibited in this region depends on the path followed. For instance, the projection points of B and C from the behavior surface onto the control surface coincide, indicating that they result from the same set of variables. However, according to the behavior surface itself, they represent different behaviors. Moreover, starting from behavior A and changing the variables along different paths can lead to different

final behaviors, such as B or C, even if the final values of the variables are the same. This phenomenon, characterized by a bifurcated solution domain and the dependence of the solution on the path of variable changes, is known as "hysteresis." The shape of the behavior surface also gives rise to another phenomenon known as "catastrophe." When transitioning from point F to G or from D to E, there is a particular set of variables where a sudden and dramatic change in behavior occurs. This abrupt transition is referred to as a "catastrophe."

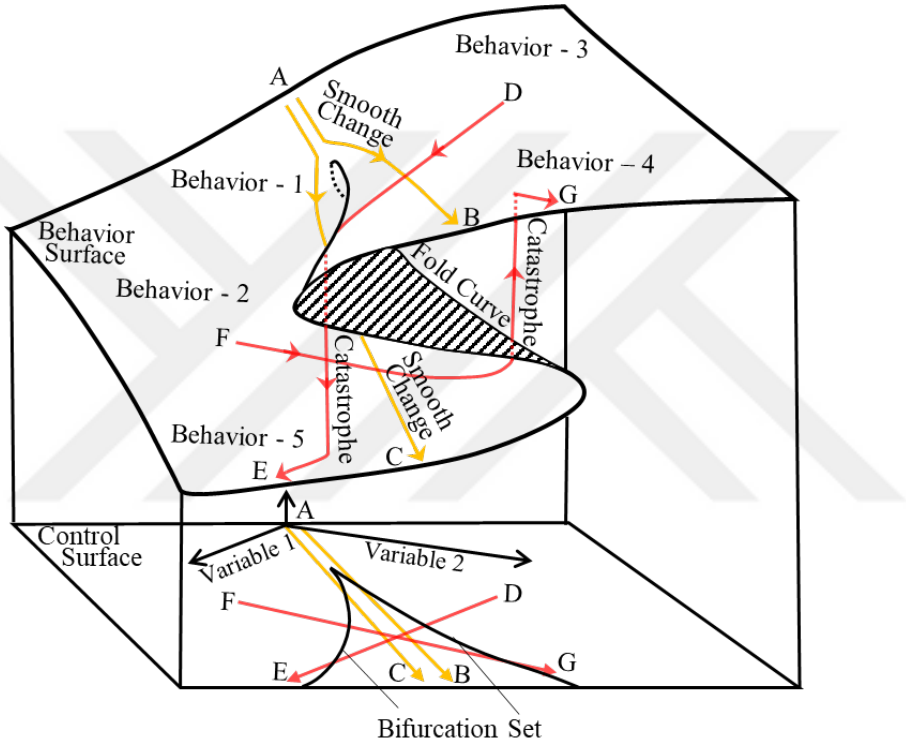


Figure 1-15. Catastrophe, hysteresis and bifurcation (reproduced from [54]).

Cui et al. [45], [46], [52], [53] worked on mentioned nonlinear hysteresis phenomenon related to start/unstart of ramjet and change of operation mode regarding to having terminal shock (ramjet mode) or not (scramjet mode). As discussed in the previous sections, if the back pressure applied to the ramjet intake is sufficiently low, formation of terminal shock is not seen and this mode is named as “scramjet mod”. Supersonic intakes might exhibit hysteresis features with the change of flight Mach number and angle of attack as well [52]. Ben-dor [55] provided a summary of hysteresis phenomena in simple shock wave reflections. The

study concluded that shock wave reflections exhibit hysteresis behavior between regular reflection and Mach reflection. References [43] and [56] present numerical studies that investigate the hysteresis behavior of the intake. Specifically, they explore the effect of cowl deflection on the shock structures and starting-unstarting characteristics of the intake.

As explained in this section, supersonic intakes prone to exhibit bifurcated performance although the operational conditions are the same. In other words, it is possible to observe hysteresis and catastrophe.

1.4 Literature Review

With the consideration of importance of SWBLIs in supersonic intake flows, there are several studies presented in the open literature. The most complex structure related to SWBLIs is noted to be “pseudo-shock” phenomena. When the supersonic flow is slowed down to subsonic in a duct surrounded by walls, such as supersonic intake’s subsonic diffuser, with sufficiently high back pressures, pseudo-shock is known to occur instead of a single normal shock wave [40], [57]. Moreover, even today, pseudo-shock and shock-train structures are very complicated and poorly understood, even in constant area ducts which is relatively simple case [8], [58].

In the context of internal flows with back pressure, studies on the pseudo-shocks can be classified into two categories; isolated constant area or divergent ducts and complete supersonic intakes.

Isolated Ducts

Tamati et al. [40], [41] conducted experimental studies on a constant area channel to investigate λ-type and X-type pseudo-shocks at different freestream Mach numbers and back pressures. Their findings revealed that the wall static pressure increases continuously throughout the pseudo-shock region. However, the static pressure within the mainstream section or inside the shock experiences alternating changes, with peak values coinciding with the observed shock positions using Schlieren

imaging. Additionally, immediately after the shock-train, the total pressure at the duct center is relatively low, indicating a difference in total pressure loss between the nearly normal shock wave portion and the bifurcated shock wave portion of the λ shocks. The authors proposed an explanation for the pseudo-shock mechanism, stating that separation from the wall, caused by an adverse pressure gradient, leads to the formation of a relatively low-speed region near the wall. The interaction between this layer and the shock waves in the core flow generates a series of shock waves, decelerating the flow to sonic speed. Subsequently, the mixing between the main flow and the low-speed region reduces distortion in the velocity profile, resulting in a more homogeneous flow after the mixing region. The authors also noted that λ-type and X-type pseudo-shock structures vary with the main flow Mach number or pre-shock Mach number. Furthermore, they observed that X-type shock structures are longer and contain more shocks.

Carroll et al. [57], [59], [60] conducted a series of experimental studies in a constant area rectangular duct, focusing on the effect of confinement level, defined as the ratio of boundary layer thickness to channel height, on pseudo-shock structures. Interestingly, even in a symmetric duct, they observed asymmetric flow features at a high pre-shock Mach number of 2.45. The level of confinement did not significantly affect the length of pseudo-shocks in high Mach number experiments. However, at a pre-shock Mach number of 1.6, increasing the confinement level led to longer and more stable and symmetric shock structures. The researchers also noted the aerodynamic nozzle effect of the pseudo-shock core flow. Laser Doppler Velocimetry (LDV) measurements showed a significant amplification of turbulent kinetic energy along the shock-train, particularly near the wall. The second shock downstream maintained the amplified turbulence level, which gradually decreased and diffused towards the pseudo-shock centerline. Additionally, the first shock of the pseudo-shock generated anisotropic turbulence, suggesting that modeling the pseudo-shock flow with isotropic turbulence models could be challenging.

Sugiyama et al. [61], [62] conducted experiments using Schlieren photography and wall pressure measurement to investigate the effect of flow confinement and pre-

shock Mach number on pseudo-shock length and type (λ or X type). Their findings were consistent with previous studies. They also observed asymmetric behavior of X-type pseudo-shocks in a symmetrical duct, which aligns with the observations in [63].

Matsuo et al. [64], [65] conducted experimental research on the oscillatory behavior of pseudo-shocks in a constant area rectangular duct. They found that as the pre-shock Mach number approaches 3, the amplitude of oscillation in the flow direction exceeds the equivalent duct diameter. Sugiyama et al. [66] investigated the effect of back pressure in a constant area channel at a pre-shock Mach number of approximately 1.6. They observed a transition from X-type to λ-type shock-train as the pressure ratio along the pseudo-shock decreases. The amplitude of oscillations for X-type pseudo-shocks was found to be 30% of the duct height, while for λ-type pseudo-shocks, it was 23% of the height. In [63], experimental results conducted at a Mach number of 2.7 were presented. The average amplitude of self-sustained oscillations of the pseudo-shock was found to be 6 mm, corresponding to approximately 11 percent of the duct height. Another study at a Mach number of 2 [42] reported a maximum fluctuation amplitude of 17 mm, equivalent to 25% of the duct height. It was also noted that increasing back pressure leads to a transition from X to λ-type for the leading shock of the pseudo-shock, and the height of the Mach stem increases after the appearance of the λ-type leading shock. Numerical studies [67]–[70] have also observed the self-sustained oscillatory behavior of the pseudo-shock within a duct.

Another numerical study on pseudo-shock structures in a constant area cylindrical duct were conducted by Kim et al. [71]. They utilized the k-ω SST turbulence model and compared their results with reference experimental data. The findings demonstrated compatibility in terms of the pressure change along the duct. However, it is important to note that the maximum duct Mach number or pre-shock Mach number for the pseudo-shock was 1.7, effectively 1.6. The numerical simulations revealed that an increase in the confinement ratio, or boundary layer blockage ratio, led to an increase in the length of the pseudo-shock. Additionally, the aspect ratio of

the duct was found to influence the characteristics and structures of the pseudo-shock. In another publication by the same authors [72], they presented results from their unsteady simulations using the k-ω SST model. The findings were considered to be compatible with the experimental data, showing an oscillation amplitude of ±5 mm around a mean value for the first shock of the pseudo-shock. Although the explicit dimension of the duct height was not provided, it was approximately 10 mm.

Supersonic Intake

According to the Schlieren images presented in reference [9], it is evident that for pre-shock Mach numbers up to 1.6, a single normal shock is observed. As the Mach number increases, the appearance of multiple shocks with a λ-shaped pattern becomes prominent. With further increases in the pre-shock Mach number, the bifurcation point moves away from the walls. Consequently, the patterns originating from the walls converge, leading to the formation of an X-shaped shock pattern. It is also noted that the X-type shock pattern has a tendency to become asymmetric.

Experimental studies on a rectangular, mixed compression supersonic ramjet intake were conducted by Herrmann et al. [10]–[12]. The experiments were carried out at three different Mach numbers: 2.5, 3, and 3.5, with varying bleed configurations. Measurements of pressure changes along the intake, static pressure at the intake exit, and Schlieren images at the intake's throat were obtained. However, the provided data on pressure changes along the intake is limited. Although their focus was primarily on the global performance of the intake and buzzing phenomena, pseudo-shock structures were observed in their Schlieren images. The results clearly demonstrate that changes in the bleed configuration significantly affect the pseudo-shock structures.

Zhang et al. [73] conducted both 3-D numerical with Reynolds-Averaged Navier-Stokes (RANS) approach and experimental studies on a mixed compression two-dimensional intake with variable geometrical features, focusing on different Mach numbers and back pressures. A sensitivity analysis of different turbulence models, including k-ε, k-ω, and Spalart-Allmaras, was conducted, and the Spalart-Allmaras

model was chosen for the numerical simulations. As the back pressure ratio increased, the structure of the first shock of the pseudo-shock changed from X type to λ-type. A comparison between the numerical and experimental results was provided for Mach numbers 1.5, 2, 3, and 4, focusing on the change of pressure along the intake under the highest back pressure condition or the weakest terminal/pseudo-shock condition. Due to the variable features of their intake, the contraction ratio of the intake was relatively high for each operating Mach number, and the study did not examine strong pseudo-shocks. The authors concluded that the results of the experiments and computational fluid dynamics (CFD) were consistent in terms of the change of pressure along the intake. The authors also investigated the effect of wall suction on critical pressure recovery and determined that wall suction increased the critical pressure recovery.

Soltani et al. [13] conducted experimental and numerical investigations on an axisymmetric mixed compression supersonic intake without bleed, focusing primarily on normal SWBLIs under subcritical conditions and in buzz phenomena. Both the experiments and numerical simulations were conducted for a free stream Mach number of 2. The numerical simulations involved 2-D axisymmetric RANS simulations, utilizing Menter's Shear Stress Transport (SST) turbulence model. A comparison between the numerical and experimental results was made in terms of the change of pressure along the intake. The comparison focused on the near-critical condition, where the strength of the pseudo-shock is relatively low. The results revealed some deviation between the CFD and experimental results in the immediate vicinity of the starting point of the pseudo-shock. Specifically, the CFD underpredicted the pressure rise due to the pseudo-shock near the intake's throat. However, better agreement was observed downstream, closer to the intake exit. Another comparison was made for the radial total pressure distribution at the intake's exit, using total pressure rakes. The results showed good compatibility between the numerical and experimental data. In conclusion, the authors observed that the interaction of the normal shock with the boundary layer led to the formation of a pseudo-shock, which was responsible for the reduction of pressure recovery and flow

distortion at the intake's exit. Numerical density gradient magnitude contour plots (numerical Schlieren) demonstrated the formation of the pseudo-shock, where the first shock of the shock-train exhibited a λ-type structure, while the successive shocks were categorized as normal shock-train. Although Mach number contours were not presented, and the pre-shock Mach number of the pseudo-shock was not explicitly mentioned, it can be inferred from the measured pressure values along the intake that it was likely below 1.4, approximately around 1.35. Moreover, the experimental measurements revealed the unsteady and oscillatory nature of the pseudo-shock.

Experimental observations of pseudo-shock structures in a supersonic mixed compression intake for different back pressures are presented in references [14] and [15]. These experiments were carried out at a freestream Mach number of 3, with the main objective of studying the unstarting behavior of the intake under various design features. The starting shocks of the pseudo-shock predominantly exhibit an X-type pattern, although there may be λ-type structures that are not clearly visible due to the image quality. It is observed that as the back pressure increases, the pseudo-shock structures move upstream.

Lee et al. [16] conducted a numerical and experimental study on a mixed compression intake with a freestream Mach number of 2.5. They observed asymmetric pseudo-shock structures. The asymmetric distribution of the boundary layer resulted in asymmetric deflection of the pseudo-shock. As the back pressure increased, the pseudo-shock waves moved upstream and formed shock structures similar to λ-shocks. The distance between successive shocks in the shock-train decreased. They noted that initially, as the terminal shock moved toward the inlet throat, a single normal shock was observed. However, the interaction between the oblique shock originating from the cowl lip and the normal shock led to thickening of the boundary layer. As a result, the effective aerodynamic area for the flow decreased, and the flow accelerated to supersonic velocities again, generating a shock-train.

The survey conducted in this section reveals that the length and type of a pseudo-shock structures are dependent on the level of back pressure and flow conditions upstream of the pseudo-shock. Different types of shock structures, such as X and λ shocks, can be observed. Additionally, the pseudo-shock exhibits self-sustained oscillatory behavior, and the magnitude of oscillation varies with the back pressure and flow conditions upstream of the shock. This asymmetric behavior is observed in both symmetric ducts and asymmetric diffusers of intakes. Experimental observations in this field are primarily conducted using schlieren or shadowgraph photography techniques. These methods allow visualization of the shock structures and their movement. Pressure measurements along the intake geometry are also performed, often in conjunction with variations in back pressure using a movable back pressure valve or nozzle. Numerical modeling of the flow through a pseudo-shock with isotropic turbulence models can pose a challenge. However, some studies utilizing the RANS approach with isotropic turbulence models have shown promising results. It should be noted that the comparison of these models with experimental data has been conducted for only a limited number of operational conditions. Among the isotropic turbulence models, Menter's Shear Stress Transport (SST) model is commonly preferred by several researchers in the field.

1.5 Scope of the Work

This thesis aims to examine pseudo-shock structures in mixed compression, rectangular supersonic intakes. Examination includes the change of shock-structures with respect to back throttling and oscillatory behavior of the pseudo-shock for during the constant back throttling. Moreover, hysteresis behavior is also examined. Both the experiments and numerical simulations are done for 2 different Mach numbers and 2 different bleed configurations. Wind tunnel experiments are conducted to measure change of pressure along the intake. Moreover, shadowgraph images are taken to visualize the pseudo-shock structures. CFD simulations using the RANS approach are conducted for the corresponding conditions and the results

of the numerical simulations are utilized to gain further insights into the flow characteristics within the intake. For the modeling of turbulence, well-established turbulence models for flows featuring adverse pressure gradients and separation, namely the Shear Stress Transport (SST) and Baseline (BSL) k-ω models are employed.

1.6 The Outline of the Thesis

The subsequent sections starts with a chapter on the experimental technique and the data processing. This chapter describes the specific methodology employed for conducting the wind tunnel tests and outlines the procedures for data acquisition and processing. Following, the thesis proceeds with the presentation of results obtained from the experiments. Moving forward, a chapter that presents the numerical simulation method utilized in the study and describes the numerical approach employed to model and simulate the flow within the supersonic intake. The obtained results from the numerical simulations are then presented and analyzed together with the comparison between the numerical results and the experimental data. The thesis concludes with a chapter dedicated to summarizing the key findings and drawing conclusions based on the experimental and numerical investigations conducted throughout the study.

CHAPTER 2

EXPERIMENTAL TECHNIQUE AND DATA PROCESSING

In this section, the Supersonic Wind Tunnel Tests conducted for the Air Intake Test Item are described in detail. The experimental setup and methodology used in the wind tunnel tests are presented, providing an overview of the test configuration. The instrumentation and measurement techniques employed to collect the necessary data during the wind tunnel tests are described including the pressure measurement and flow visualization techniques used to monitor and analyze the flow characteristics. The test procedure, including the process followed during the wind tunnel tests, is explained. Moreover, the test conditions are specified. The post-processing methods employed for the analysis of shadowgraph images and pressure measurement data are also presented.

2.1 Trisonic Wind Tunnel

The wind tunnel tests were conducted at the Trisonic Research Laboratory located at Istanbul Technical University (ITU). The wind tunnel has two test sections, one for conducting the experiments at Mach numbers below 2 and the other at Mach numbers between 2.6 and 4. The cross-sectional area of the test section is 15 cm x 15 cm. The tunnel is capable of operating within a range of 5 to 12 bars total pressure. A schematic of the wind tunnel is provided in Figure 2-1. The pressurized air is stored in tanks using compressors. The total pressure in the test section is controlled by a control valve. The airflow passes through the settling chamber before being accelerated through the variable Laval nozzle to achieve the desired Mach number within the test section. The test item is mounted inside the test section for experimentation. Downstream of the test section, the airflow is decelerated and

compressed through a diffuser before being exhausted to the atmosphere through an exhaust tower and a silencer.

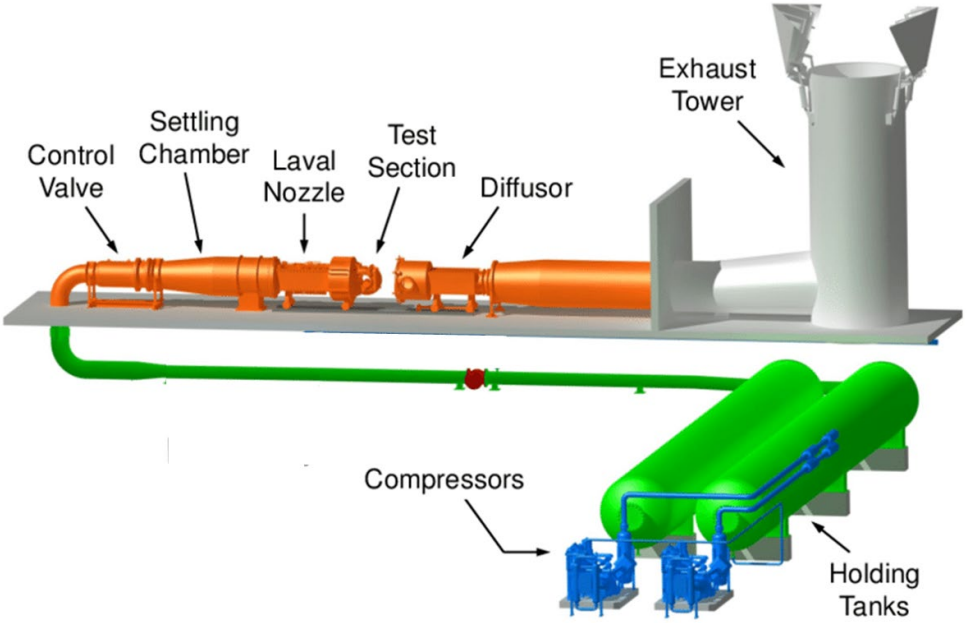


Figure 2-1. Schematic of the Wind Tunnel.

2.2 Test Configuration

The test configuration consists of a Test Item, a Back Pressure Valve, Pressure Scanners, a Flow Visualization System, and a Control System. Schematic for the configuration is given in Figure 2-2.

The Test Item is instrumented with the pressure taps to characterize the flow field inside the intake. The taps are connected to pressure scanners (Scanivalve DSA-3217) using special pneumatic pressure measurement tubes. The pressure is measured using two different pressure scanners with a measurement range of 4 bar and 10 bar.

The Back Pressure Valve is used to simulate the effect of an increase in pressure due to combustion. Several studies [74]–[79] have used a back pressure valve (plug) or a variable back nozzle to conduct experiments at various levels of back pressure. The

pressure is changed by moving the valve, in other words, changing the critical throttle cross-section.

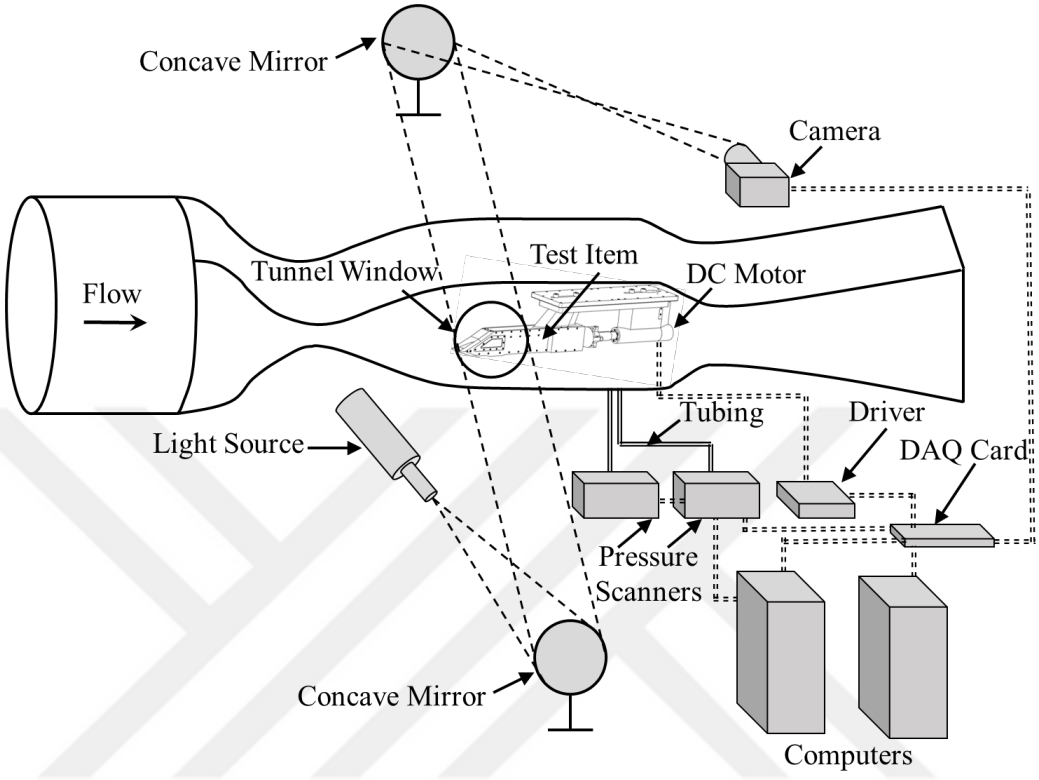


Figure 2-2. Schematic for the test configuration (reproduced and adapted from [80]).

The valve is driven by a brushless DC motor (Maxon EC-I 30) equipped with an integrated hall sensor and encoder. To investigate the flow field inside the intake, Shadowgraph Images are captured using the Flow Visualization System. It consists of a LED light source, convergent lens, concave mirrors, and a high-speed camera (Photron FASTCAM Mini). The high-speed camera was set to capture images at 8000 fps with a 768 x 432 resolution with a record duration of 8.628 seconds.

The Control System is used to control the back pressure valve movement and synchronization of the whole system. The system consists of computer, controller or driver (EPOS4) for the DC motor and a Data Aqcuisition (DAQ) card. The system operates at 32 kHz. After the wind tunnel flow conditions are stabilized, the High-Speed Camera starts to capture images and sends a 5V trigger signal to the DAQ

card. The Control System then starts the back pressure valve motion according to a predefined profile, measures the valve position using an integrated encoder and records. Moreover, the Control System sends 5V signals at 800 Hz to the Pressure Scanners. The Pressure Scanners capture the pressure data at each arrival of the signal. Furthermore, the high-speed camera sends a signal for each captured image. This high-speed camera signal data is recorded to check the duration between each image.

2.3 Test Item and Instrumentation

The Air Intake Test Item geometry was based on references [10]–[12], although the precise details were not provided. As a result, only key features such as ramp angles, design point Mach number, and diffuser angle were incorporated into the reference geometry. Furthermore, the dimensions of the wind tunnel necessitated scaling down the baseline geometry by 54%. An isometric view of the solid model of the air intake test item is shown in Figure 2-3, with the air intake at the front and the back pressure valve and DC motor at the back. Shadowgraph windows were used to visualize the shock structure within the intake, which were made from schlieren-quality high purity fused silica glass. The blockage ratio of the Test Item, excluding the mounts, is approximately 12%. However, when considering the mounts as well, the blockage ratio increases to 17%. It is worth noting that these values result in no problems in starting the tunnel.

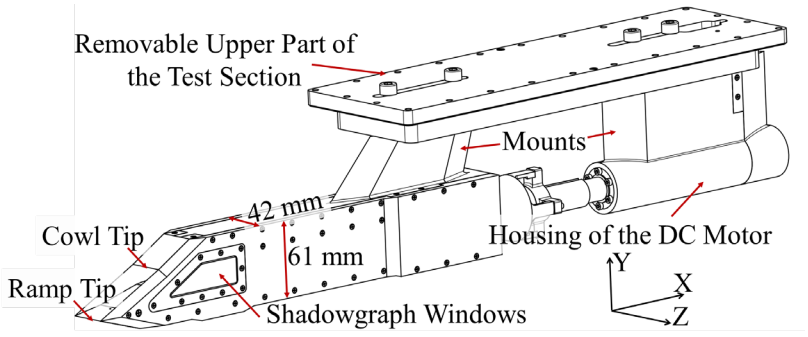


Figure 2-3. Isometric view of the air intake test item.

The experiments conducted in this study use two different test items, one with bleed and one without. The outer dimensions of both test items are identical with an overall length of 691 mm. The vertical distance between the cowl tip and ramp tip is 30 mm, which is same with the distance between parallel internal sidewalls.

The cross section view from the symmetry plane of the air intake, as well as the dimensions of the air intake and the layout of the pressure measurement taps, can be found in Figure 2-4 and Figure 2-5.

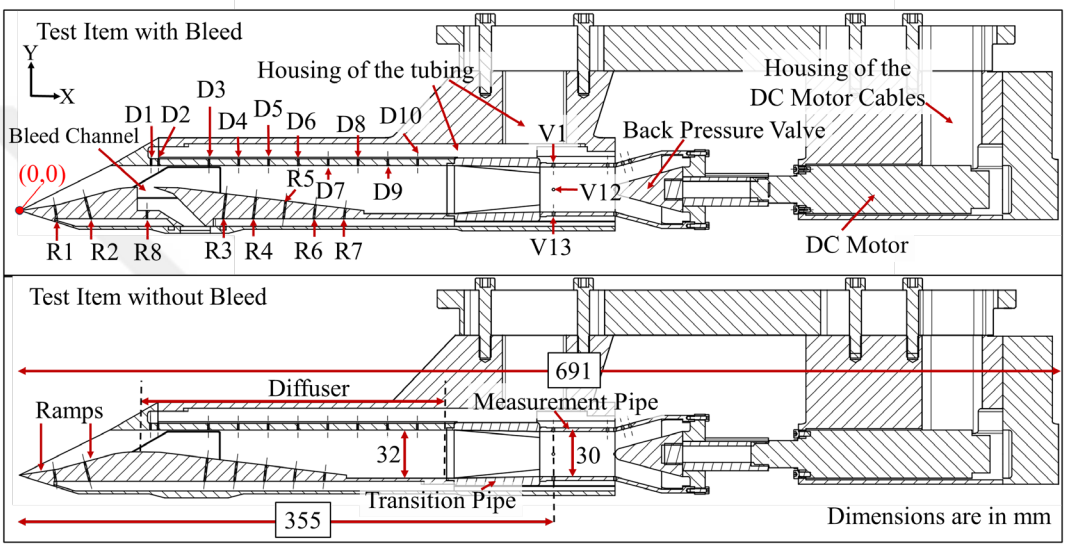


Figure 2-4. Section view of the air intake test item.

The test items feature two ramps at the front with angles of 9 and 15.1 degrees, followed by a circular arc with a radius of 80 mm. Design point Mach number of the intake is 3. The throat height of both intake test items are same, measuring 14.5 mm. For the test item with bleed, a bleed gap with a length of 11.4 mm is followed by a diffuser surface with -1 degrees and a length of 15.5 mm. On the other hand, the test item without bleed, its diffuser part starts at the end of the circular arc, followed by a -7 degrees part with a length of 125 mm. The internal height of the diffuser at the downstream end is 32 mm. A transition pipe converts the rectangular cross-section to a circular one with a diameter of 30 mm, followed by the measurement pipe where the pressure measurements are taken and the back pressure valve is located. The

pressure taps D1 to D10 are located on the cowl side (top side), while taps R1 to R7 are on the ramp side (bottom side).

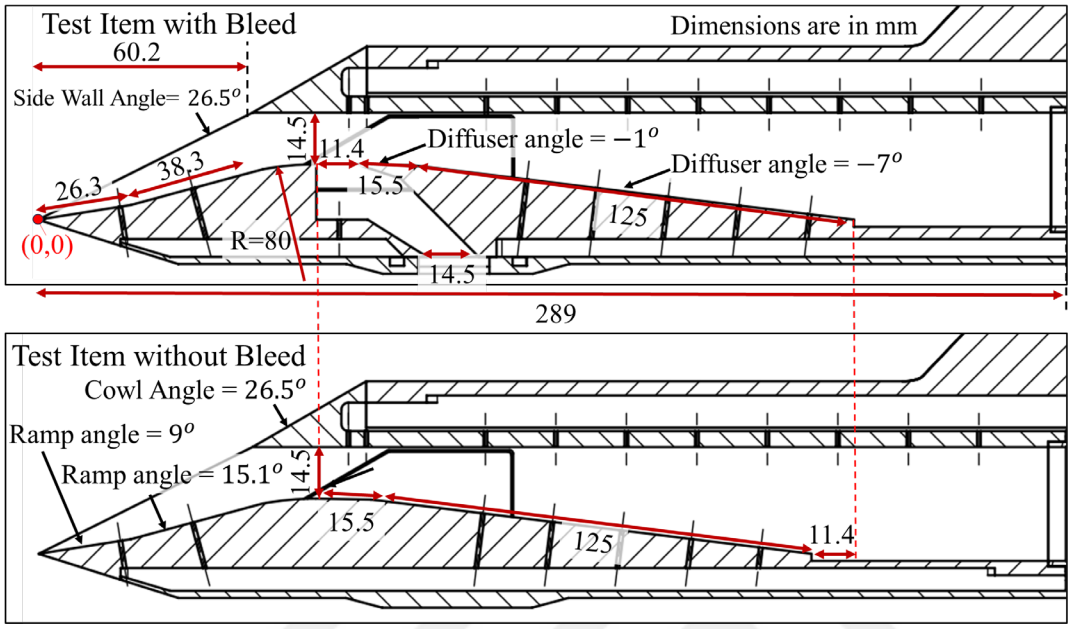


Figure 2-5. Dimensions of the air intake test items.

V1, V12, V13, and V14 taps are located at the exit of the intake on the measurement pipe section for pressure measurement in both intake geometry. V14 is situated on the opposite side of V12, with all V taps located 355 mm downstream from the ramp tip. An isometric view and an isometric section view of the measurement pipe and the back pressure valve are given in Figure 2-6. V1, V12, V13, and V14 pressure measurement taps are also highlighted in the figure.

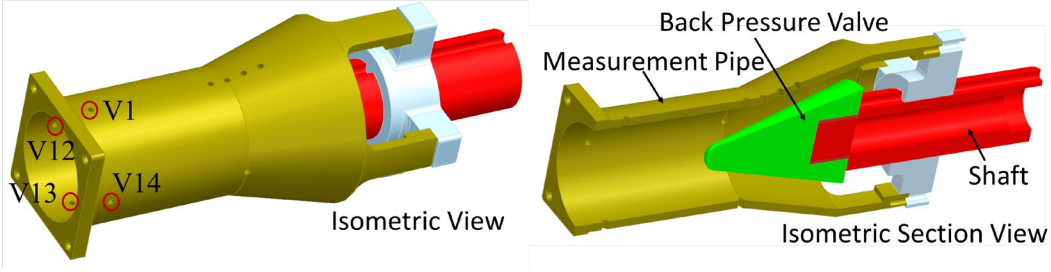


Figure 2-6. The measurement pipe and the back pressure valve.

In Figure 2-7 definitions are provided for the station numbering, ramp side, cowl side and the intake entrance height (h_0) . Station 3 is designated as the exit of the intake, where pressure taps V1, V12, V13 and V14 are positioned. Station 4 corresponds to the location where the flow area is minimum upstream of the station 3. The bottom internal surface of the intake, indicated by the blue line, are named as the ramp side where the top internal surface of the intake, highlighted in red, is named as the cowl side. The intake entrance height, denoted as h_0, represents the vertical distance between the ramp tip and the cowl, measuring 30 mm. By multiplying the h_0 with the internal width of the intake, which is also 30 mm, the effective flow area for the freestream flow entering the intake with a capture ratio of unity can be determined. The area is denoted as A_0.

The pressure measurement taps on the ramp side of the two test items are located at different horizontal distances from the ramp tip due to the presence of bleed in one of the test items. The locations of the pressure taps on the cowl side and measurement pipe are the same for both intake test items. Details on the horizontal distances between the pressure taps and ramp tip can be found in Table 2-1.

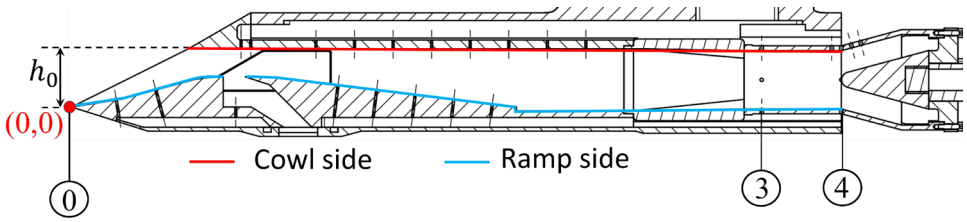


Figure 2-7. Air intake station numbering, ramp side, cowl side and the intake entrance height.

Table 2-1. Locations of pressure measurement taps in millimeters.

Tap Name	Axial Location [mm]	
	With Bleed	Without Bleed
R1	23	23
R2	43	43
R3	137	125
R4	157	144
R5	177	164
R6	196	184
R7	216	203

Tap Name	Axial Location [mm]
D1	87
D2	92
D3	126
D4	145
D5	165
D6	185
D7	205
D8	225
D9	245
D10	264

2.4 Motion Profile for the Back Pressure Valve

The motion profiles for the back pressure valve set for the valve follow a ladder-type pattern in which the back pressure valve is moved such that decreasing the exit area first and then downstream increasing the area during each test, except for Test 4331 – Rep, where the exit throat area is continuously decreased. Once the tunnel operating conditions are met, data acquisition and valve motion begin. The valve initially remains at its starting position for 0.1 seconds. In a direction of the valve motion, either forward or backward, it is moved 1.11 mm and then dwelled for 0.1 seconds before moving again to the next dwelling position. This process is repeated for 75 dwell points during the tests. For Test 4331 – Rep, the increments are half of the other profiles. The position profile is provided in Figure 2-8, and additional details regarding the profiles are included in Table 2-2. $\Delta \boldsymbol{x}$ represents the valve travel distance between each dwell point positions while $\Delta \boldsymbol{t_2}$ denotes the duration of motion between each dwell point. $\Delta \boldsymbol{t_1}$ represents the dwell time, during which the back pressure valve remains at a dwell point.

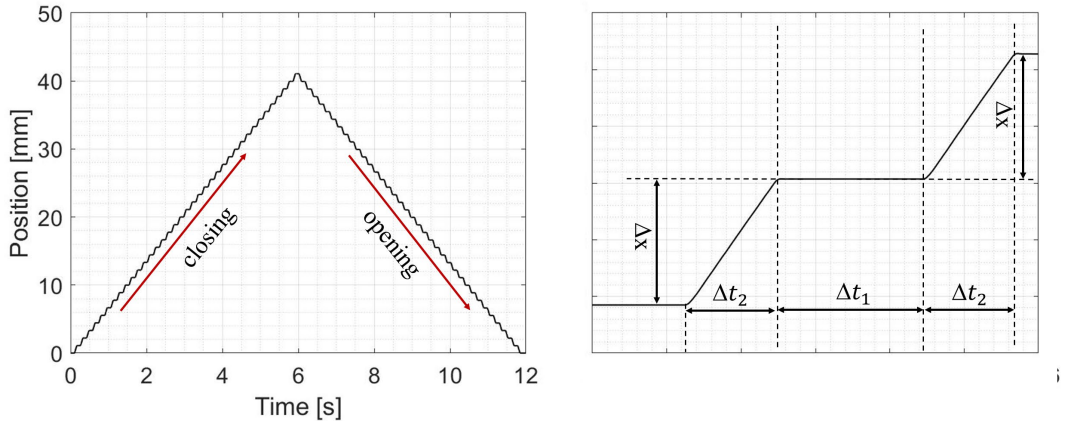


Figure 2-8. Change of the position of the back pressure valve, full profile (left), close-up view (right).

Table 2-2. Details of the valve motion profile.

$\Delta t_1\ [s]$	$\Delta t_2 [s]$	$\Delta x\ [mm]$
0.1	0.06	1.11

For the following sections, the valve position will be referred to as its dwell point. Valve Position Number 1 (VPN 1) represents the starting point, and VPN 2 corresponds to the position after the valve has moved forward one step. Up to VPN 38, the valve moves forward, resulting in a decrease in the throttling area. After VPN 38, the valve begins to open and dwells at the same positions as during the opening. To differentiate between the valve positions during the opening and closing phases, the ones during the opening are referred to as "VPN-opening," while the ones during the closing are referred to as "VPN-closing." This approach allows for a comparison of the experimental pressure data at the same VPNs, with one corresponding to the closing phase and the other corresponding to the opening phase, facilitating an investigation into the hysteresis behavior.

The repositioning of the valve brings about changes in the back throttling area (A_4), which can be assessed through geometric calculations and measurements derived from the solid model. Figure 2-9 shows the change in the throttling area and its

percentage relative to the inlet's capture area for a capture ratio of 1 (corresponds to A_0) with respect to the valve position.

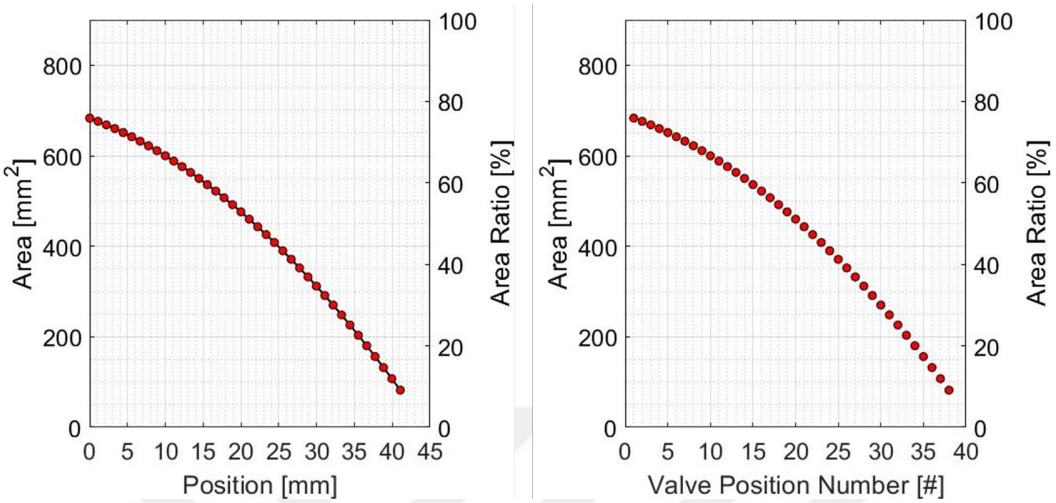


Figure 2-9. Change of the throttling area and the area ratio with the valve position (left) and the VPN (right).

2.5 Test Conditions

Experiments were conducted in a supersonic wind tunnel, where various Mach numbers were tested using different test items, as summarized in Table 2-3. Repeatability tests were performed for selected test cases, labeled with the addition of "Rep" at the end of their respective numbers in Table 2-3. Pressure measurements were taken at the test section and plenum chamber of the wind tunnel using pressure scanners with measurement ranges of 4 and 10 bar, respectively. The measurement inaccuracies for the 4 and 10 bar scanners are 200 Pa and 500 Pa, respectively. The corresponding measurement uncertainties for the test conditions, Mach number, and total pressure were 0.5% and 0.1%, respectively. The Mach number was calculated using isentropic relations based on the measured pressures. Variation of the Mach number and total pressure with time are given in Figure 2-10.

Table 2-3. Test conditions.

Test No	Bleed	Mach	Total Pressure [bar]	Total Temperature [K]
4331	With	2.99	6.06	292
4331-Rep		2.99	6.10	295
4340		2.63	4.98	292
4339		2.63	6.01	290
4339-Rep		2.63	6.15	291
4372	Without	3.00	6.10	287
4372-Rep		3.00	6.17	286
4373		2.64	4.97	288

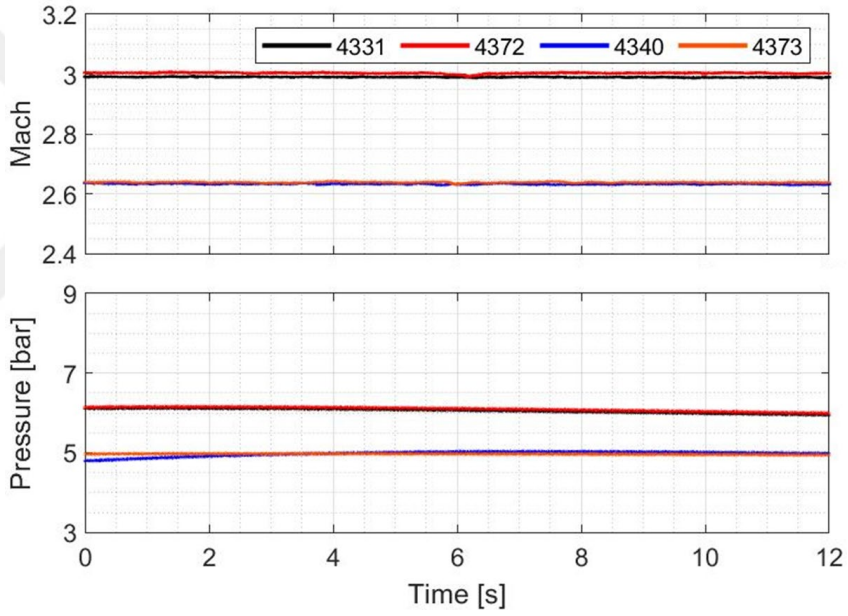


Figure 2-10. Variation of test section Mach number and total pressure with time.

2.6 Pressure Measurement

Pressure measurements were conducted at various points along the intake test item as described in section 2.3, using two different pressure scanners with a measurement range of 4 bar and 10 bar. The higher range scanner was used at locations with expected higher pressures. The pressure measurement taps connected to the

respective pressure scanners are outlined in Table 2-4. The measurement inaccuracies for the 4 and 10 bar scanners are 200 Pa and 500 Pa, respectively.

Table 2-4. Pressure measurement taps connected to the respective pressure scanners.

Scanner	Pressure Measurement Taps
4 bar	R1, R2, R3, R8, D1, D2, D3
10 bar	R4, R5, R6, R7, D4, D5, D6, D7, D8, D9, D10, V1, V12, V13, V14

The pressure distribution inside the intake undergoes changes when the position of the back pressure valve is altered. In other words, a new pressure level is achieved after each valve stop. This can be observed from the sample pressure data obtained from Test 4331, as shown in Figure 2-11. The pressure data at the exit of the intake, specifically at V1 tap, is presented in the figure. It is important to note that all pressure data presented are non-dimensional and divided by the measured real-time wind tunnel test section static pressure, which corresponds to the free stream static pressure of the flow. In the close-up view plots in Figure 2-11, the pressure data is also plotted with a moving averaged filter applied, using a window size of 16. Upon examining the close-up view plots, it can be observed that once the valve starts to move, the pressure begins to increase. As the valve comes to a stop, the pressure gradually settles and then starts oscillating around a mean value. To ensure that the settled pressure data is used for calculating the measured mean pressure, the last 30 data points of the dwell time for each VPN are taken into consideration for the calculation.

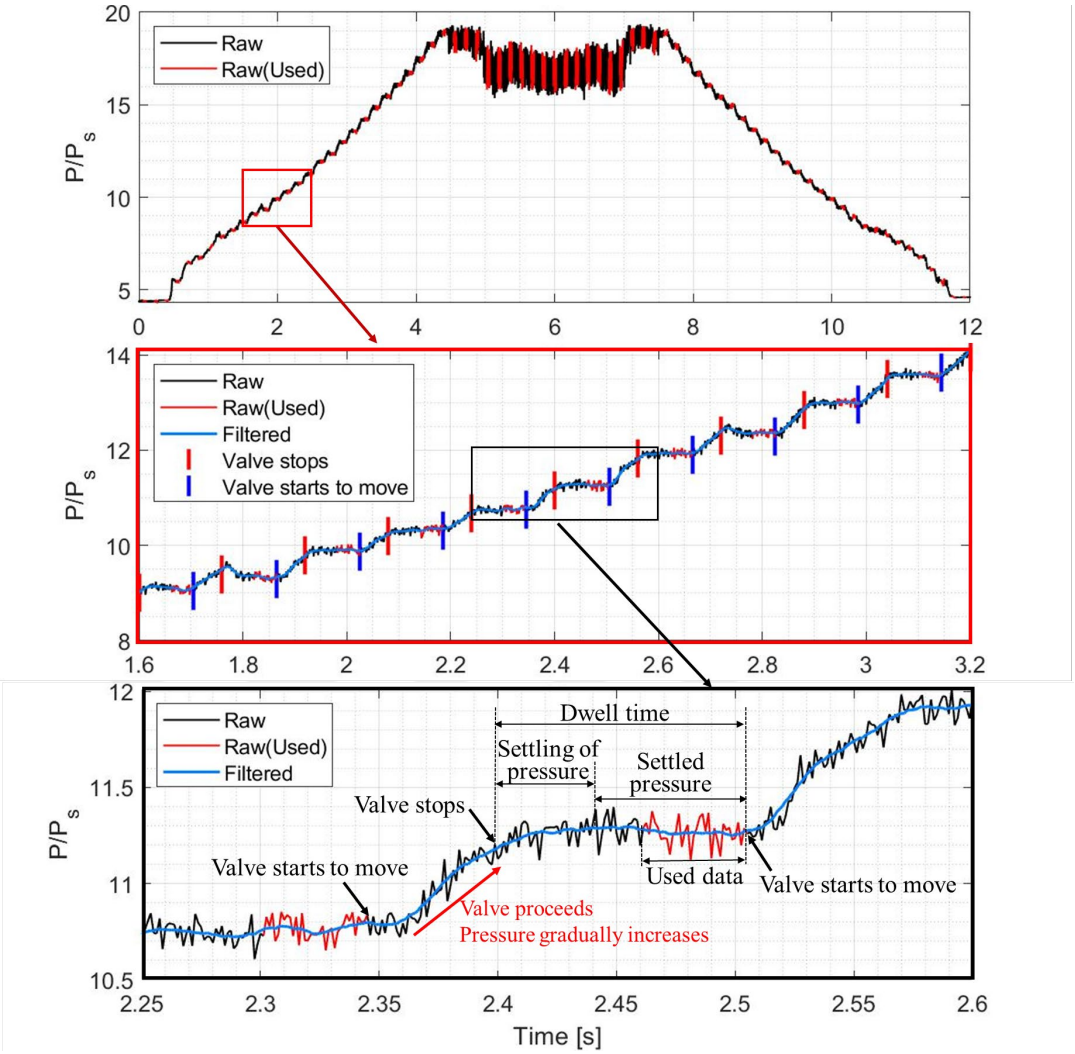


Figure 2-11. Change of the pressure with time at V1 for Test 4331 (Top: complete data, middle: close-up view-1, bottom: close-up view-2).

In the upcoming sections, the pressure data will be analyzed at the valve dwell points, and the average of the "used data" will be presented. Despite the pressure settling, the pressure data for all measurement points continue to oscillate due to flow characteristics. To account for these oscillations, error bars are included within the plots. Additionally, the error bars consider the measurement inaccuracies of the pressure scanners.

2.7 Calculation of Pressure Recovery and Mass Flow Ratio

The method presented here was used by Herrmann et al. [10]–[12], [75]. To determine the pressure recovery and the mass flow ratio, the static pressure p_{s3} and the critical valve cross-sectional area A_4 are used in combination. The pressure measurement taps V1, V12, V13, and V14 are located at section 3, which is the exit of the intake. The section 4 corresponds to the point where the valve restricts the flow, representing the smallest area along the valve.

The position of the valve is measured with the help of the encoder of the DC motor. Change of A_4 area with respect to valve position is calculated using geometric relations and measured from the solid model. The continuity equation is then employed for further calculations, with specific boundary conditions. These include the assumption of isentropic flow of a Mach number of 1 at throttle cross section at station 4, and negligible total pressure loss.

The Mach number at station 3 is determined through iterative calculations using Equation (2-1), followed by the computation of mass flow ratio with Equation (2-2), and the calculation of total pressure at station 3 using Equation (2-3). It is worth mentioning that the average of the measured pressures at V1, V12, V13, and V14 is used to calculate p_{s3}. The theoretical undisturbed mass flow, m_0, is then calculated using the measured static pressure of the test section and the Mach number of the free stream flow calculated by using Equation (2-4). A_0 is the projected area of the effective flow area perpendicular to the flow for 0 angle of attack at the front tip of the intake, which is 900 mm^2. Equation (2-5) can be utilized to calculate pressure recovery, where P_{t0} refers to the measured total pressure of the free stream flow in the test section.

$$\frac{A_3}{A_4} = \frac{1}{M_3}\left(\frac{1+\frac{\gamma+1}{2}M_3^2}{\frac{\gamma+1}{2}}\right)^{\frac{\gamma+1}{2(\gamma-1)}} \tag{2-1}$$

$$\frac{\dot{m}_3}{\dot{m}_0} = \frac{\frac{1}{\dot{m}_0} p_{t3}}{\sqrt{RT_{t0}}} A_3 M_3 \sqrt{\gamma} \left(1 + \frac{\gamma+1}{2} M_3^2\right)^{-\left(\frac{\gamma+1}{2(\gamma-1)}\right)} \tag{2-2}$$

$$p_{t3} = p_{s3} \left(1 + \frac{\gamma-1}{2} M_3^2\right)^{\frac{\gamma}{\gamma-1}} \tag{2-3}$$

$$\dot{m}_0 = A_0 \frac{p_{s0}}{\sqrt{T_s}} \sqrt{\frac{\gamma}{R}} M_0 \tag{2-4}$$

$$\frac{p_{t3}}{P_{t0}} = \frac{p_{s3}}{p_{t0}} \left(1 + \frac{\gamma-1}{2} M_3^2\right)^{\frac{\gamma}{\gamma-1}} \tag{2-5}$$

Change of throttling area, A_4, with respect to valve position has already been given in Section 2.4 with Figure 2-9. Area ratio is defined as A_4/A_0.

2.8 Response Analysis for the Pressure Measurement Tubing

The pressure tubing system and its response is modeled using a second-order differential equation, which was previously introduced by [81] and [82]. The equation is given as:

$$\frac{d^2 p_0}{d^2 t} + 2\omega_0 \zeta \frac{dp_0}{dt} + \omega_0^2 p_0 = \omega_0^2 p \tag{2-6}$$

In the Equation (2-6), p_0 represents pressure output of the sensor, which is the pressure at the dead end of the tubing, p represents the pressure at the open end of the measurement tap, $\omega_0 = 2\pi f_0$ and f_0 is the natural frequency of the system. f_0 is calculated using Equation (2-7).

$$f_0 = \frac{1}{2\pi} c \sqrt{\frac{A}{L\left(V + \frac{AL}{2}\right)}} \tag{2-7}$$

In Equation (2-7), c is the speed of sound, A is the cross sectional area of the tube and L is the length of the tube, V is the internal volume of the sensor which is assumed to be negligible. The damping ratio, ζ, in Equation (2-6) is calculated as follows.

$$\zeta = \frac{2\mu}{f_0 \rho A} \tag{2-8}$$

In Equation (2-8), μ is the dynamic viscosity of the fluid, ρ is the density of the fluid.

Differential equation is solved for the tubing used in the experiments which had a length up to 1.5 meters. Internal diameters of the tubes are 1 mm. The speed of sound, density, and dynamic viscosity of air at 1 bar and 290 K are calculated to be $c = 340\ m/s$, $\rho = 1.202\ kg/m^3$ and $\mu = 1.797\ x\ 10^{-6}\ Ns/m^2$, respectively.

The differential equation is solved numerically using the Runge-Kutta method. Time step used was 10^{-5} seconds. The initial conditions were taken to be 100000 Pa for the pressure response and 0 for the derivative of the pressure response. Four different response analysis were performed for the step input, linear rise input, oscillatory sine wave inputs at 14 Hz and at 200 Hz. The obtained pressure response for the step and linear rise inputs are both shown in Figure 2-12. The figure also includes a comparison of the response with the input pressure. If the difference between the response and input is less than 100 Pa, it is considered that the pressure response has reached the input. For the step input, the pressure response reaches the input value of 1.1 bar in 27 ms. For the linear rise input, after the rising phase of the input pressure is complete, the pressure response reaches the input in 15 ms. This response time is considered sufficiently high, given the valve dwell time of 0.1 s.

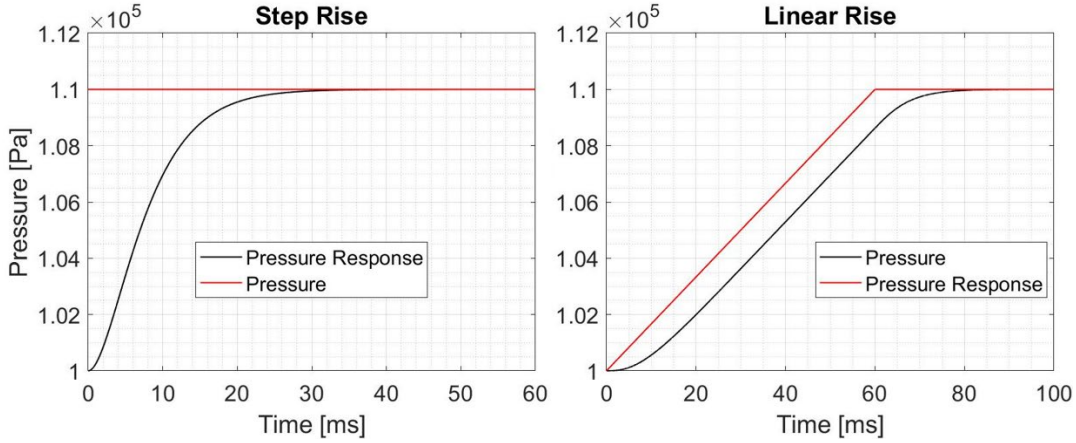


Figure 2-12. Pressure response of the tubing for the step rise input and linear rise input.

The pressure response to the oscillatory sine wave inputs is presented in Figure 2-13, which also includes a comparison with the input pressure. It is observed that the pressure response can accurately track the input pressure with a maximum error of 100 Pa and a noticeable time lag for a sine wave of 14 Hz. However, for a sine wave of 200 Hz, the pressure response is unable to follow the rapid oscillations and instead measures the mean of the oscillation.

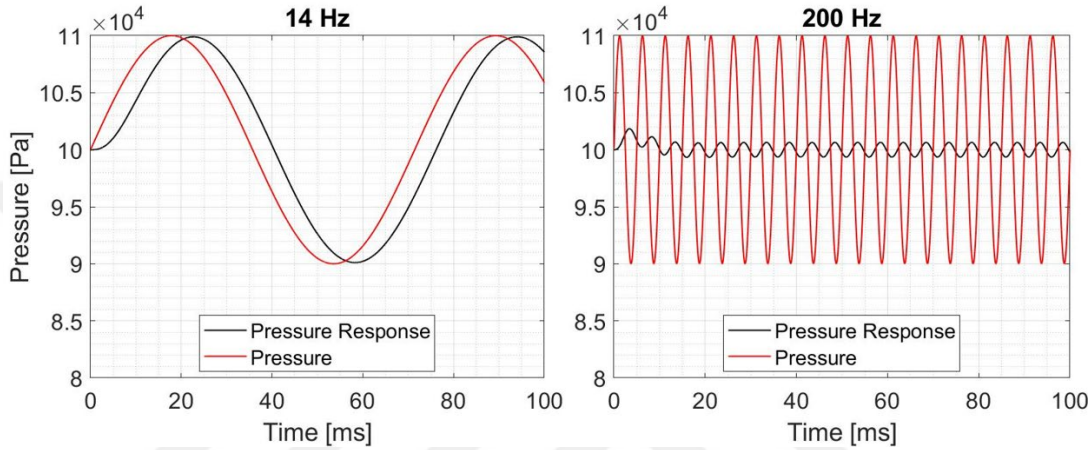


Figure 2-13. Pressure response of the tubing for the oscillatory input.

2.9 Shadowgraph Images and Edge Detection

Using the high-speed camera, shadowgraph images were captured during the experiments. Although the system is equipped with the capability to apply the Schlieren technique, preliminary trial tests were conducted with both Schlieren and Shadowgraph techniques. It was observed that the Shadowgraph technique yielded better visualization of the distinct shock structures under investigation. In the present study, the primary focus is on examining the locations and shapes of the shock structures, and the gradient magnitudes that can be obtained with Schlieren images are not the main objective. Therefore, the Shadowgraph technique was deemed more suitable and valuable for the purposes of the study. The 8000 fps shots allowed for the visualization of small-scale oscillations of shock structures inside the intake. Moreover, changes in the shock structures as the back pressure valve moved could

be observed. Additional, images provide insight into the intake operation conditions such as supercritical, subcritical, and critical flow regimes, as well as the occurrence of buzzing phenomena.

In addition to visual examination of the raw shadowgraph images, The Canny Edge Detector [83] was utilized to identify oblique shocks, pseudo-shock structures, and shock-related boundary layer separations. The lower and upper thresholds and the standard deviation for the Gaussian filter were determined through a trial-and-error process, with the following values chosen: 0.03 for the lower threshold, 0.15 for the upper threshold, and 2.1 for the standard deviation. For Test 4331, a comparison of the raw image and the image after edge detection at VPN 1 is shown in Figure 2-14. Undesirable artifacts in the raw image are indicated with white circles. As seen, the applied thresholds and filters are successful in terms of removing artifacts without losing important flow structures.

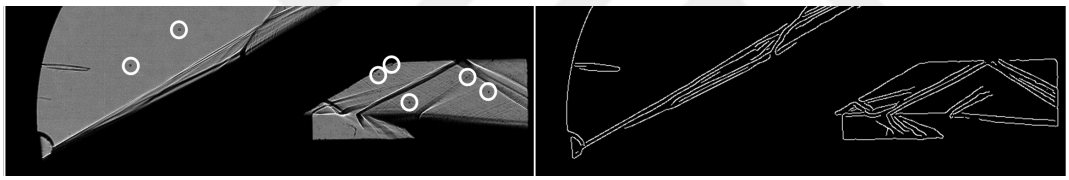


Figure 2-14. Comparison of the raw image and the edge detection map.

To illustrate the mapping of different flow features with edge detection, Figure 2-15 shows comparisons between the raw images and the edge detection maps for experiments 4331 and 4372, respectively. In Figure 2-15, at VPN 1, the tail of the cowl shock and bleed wedge shock can be seen. Additionally, expansion waves can be observed at the point where the diffuser angle increases from 1 to 7 degrees. As the back pressure valve moves to position number 12, the effect of the back pressure results in the formation of pseudo-shock structures related separation with the sonic line, and the separation shock. At VPN 18, the first shock of the pseudo-shock becomes more like a λ-type or similar to Type II according to Edney's classification, and the formation of triple points and slip lines can be observed. Thus, the edge detection method can be considered successful in capturing important flow structures related to shock waves.

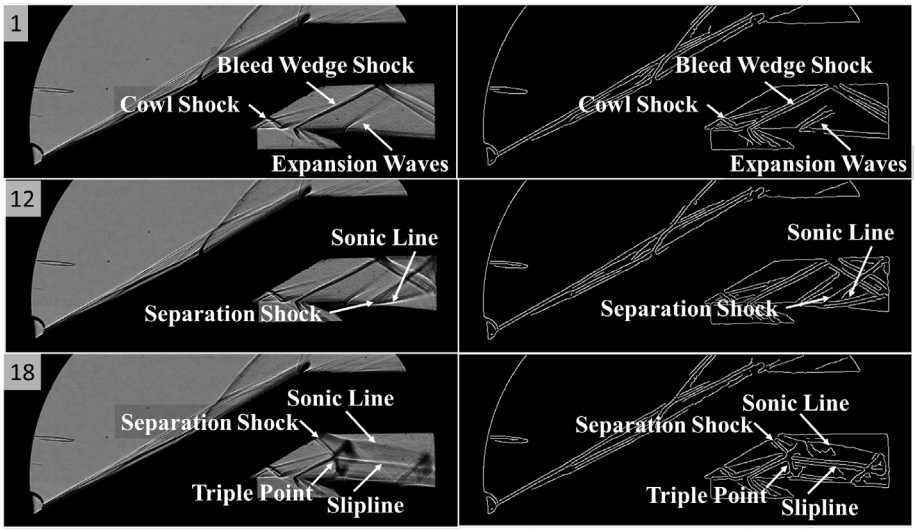


Figure 2-15. Comparison of the raw image and the edge detection map for Test 4331 at different VPNs.

To obtain the measurements in millimeters from the pixel lengths, calibration images presented in Figure 2-2 were utilized. The left image was used to calibrate the selected four lengths on the test item, while the right image was calibrated using a transparent ruler. Based on the calibration, it was determined that 55 pixels correspond to a length of 10 millimeters.

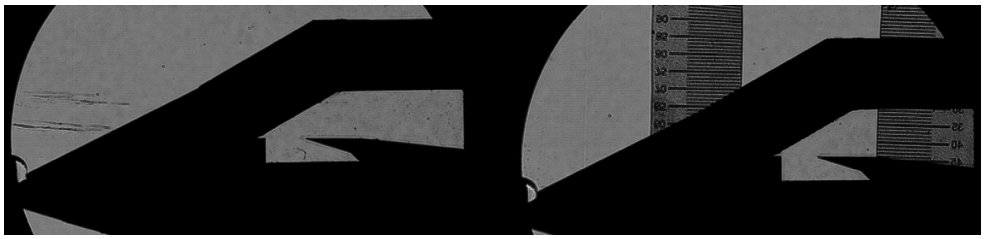


Figure 2-16. Calibration images.

The assumed error related to human eye while selecting pixels for calibration is 2 pixels, and the manufacturing tolerances of the test item are considered as 0.1 mm. To address the potential errors associated with the selection of pixels in examining shadowgraph images, an additional 2-pixel error is included in all measurements presented in the following section. As a result, all measurements are subject to a 4-pixel and 0.1 mm error, resulting in a total error of ±0.83 mm.

In the Experimental Results section, visual and quantitative examinations of shock structures using shadowgraph images from experiments 4331, 4340, 4372, and 4373 are presented. Firstly, the average of images for different VPNs at the dwell time was obtained. To find the dwell time, the camera capture signal and valve driver motor's encoder data were synchronized to identify the frames corresponding to the dwell times. To ensure that unsteadiness due to valve motion was removed, the first 250 images of each dwell time were excluded. The total number of the average images for each VPN are 500. Next, the average images were visually examined to observe the changes in flow structures as the valve position changes. If a significant change in structure was observed, other than the starting location of the pseudo-shock, the transition between those VPNs was examined in detail.

For each VPN, the oscillation of pseudo-shock structures was examined quantitatively using the edge detection method. To obtain quantitative information regarding the specific changes of interest, imaginary horizontal lines (named as Tracer Lines) were generated on the figure, and an algorithm was used to search for the intersection of the line and the shock of interest. Figure 2-17 displays a sample image illustrating the tracer line and its intersection point with the first edge. The image on the top (a) shows the raw image with the tracer line is placed on the image as a white line. The image on the top (a) displays the original(raw) image, with a white tracer line overlaid on it. After the edge detection algorithm is applied, the point of intersection between the tracer line and the first edge along the tracer line is found. This intersection point is depicted in the middle image (b), with a white horizontal line representing the y-coordinate of the tracer line, and a white vertical line indicating the intersection point in the x-direction. To highlight the detected point, it is marked in red and overlaid on the original image, resulting in the bottom image (c). In Figure 2-18, the locations of the tracer lines used for different tests are illustrated. However, due to the complex and intricate nature of the shock structures in Tests 4331 and 4340, a single tracer line was not sufficient.

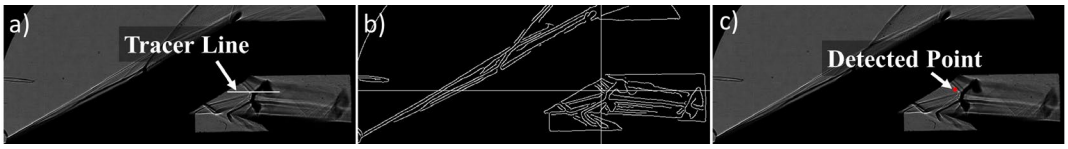


Figure 2-17. The tracer line (a), edge detection map (b), intersection point (c).

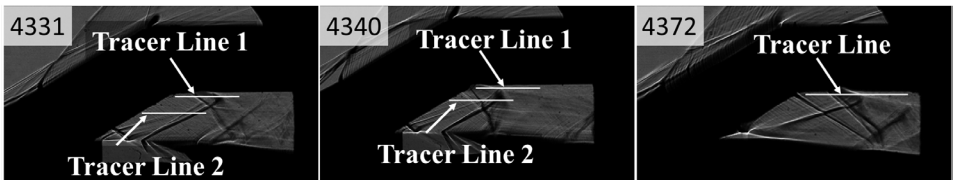


Figure 2-18. Tracer Lines.

The change in the intersection point was then used to determine the relative position with respect to the chosen starting point on the imaginary horizontal line. However, due to the complex and fast-moving nature of the shock waves, the edge detector may fail to detect the target shock and intersection search algorithm might produce inaccurate results. To ensure accuracy, the processed results obtained from the edge maps were visually verified against the raw images. Moreover, the amount of change in the shock point was recalculated using the raw images.

CHAPTER 3

EXPERIMENTAL RESULTS

In this section, the results obtained from the wind tunnel experiments are presented, focusing on the analysis of shock structures and the examination of pressure data along the intake.

The chapter begins by discussing the analysis of shock structures using shadowgraph images. The obtained shadowgraph images are examined to identify and characterize the shock structures present within the intake. The observations and findings regarding the change of shock structures with respect to back pressure throttling and oscillatory behavior of pseudo-shock are presented.

After the visual analysis of shock structures, the measured pressure data along and at the exit of the intake are presented. The pressure data collected at different locations along the intake are analyzed and discussed. Hysteresis behavior is examined through the pressure measurement data. Furthermore, characteristic diagrams are also presented to provide an overall understanding of the intake's performance.

3.1 Shock Structures

3.1.1 Mach = 3 with Bleed (Test 4331)

3.1.1.1 Average Images

The average images for different VPNs are shown in Figure 3-1 and Figure 3-2. Until VPN 11, no significant changes in the shock structures are observed through the shadowgraph window. The onset of the pseudo-shock is not sufficiently upstream to

be visible through the shadowgraph window, resulting in very similar images until VPN 11. At VPN 11 and preceding VPNs, the image captures the presence of the cowl shock hitting the bleed gap, the formation of the bleed wedge shock, its reflection, and the occurrence of expansion waves across the surface where the diffuser angle changes from 1 to 7 degrees. However, the effect of the back pressure is not yet apparent through the shadowgraph window in the test item. As the valve continues to move, the oscillatory motion of the pseudo-shock structure leads to blurriness in certain areas of the average image, indicating changes in the corresponding regions as the pseudo-shock moves upstream.

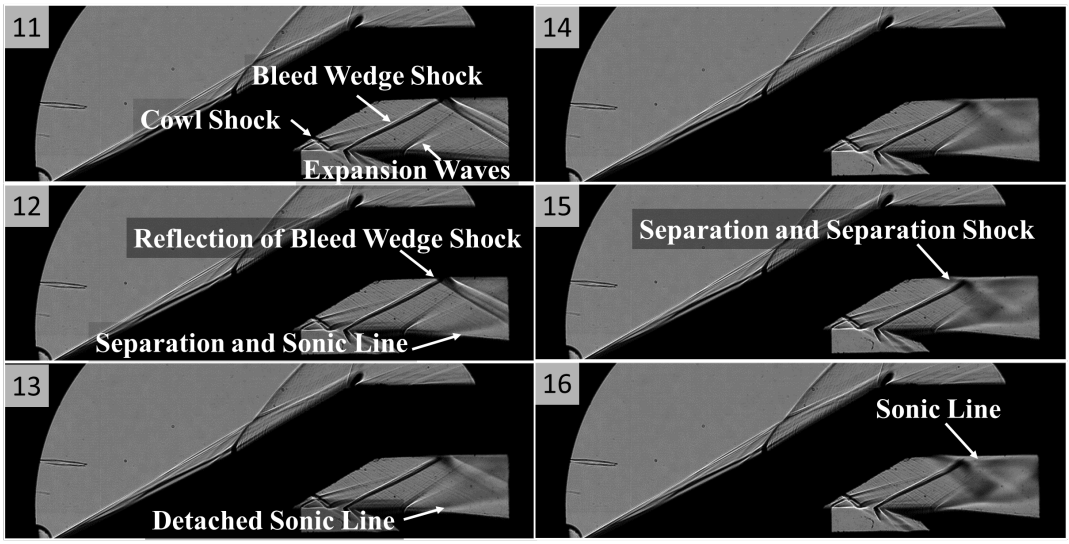


Figure 3-1. Average images for Mach = 3 with bleed (Test 4331) at VPNs 11 to 16.

Between VPNs 11 and 12, the effects of the pseudo-shock become visible, characterized by a blurry sonic line due to separation and a very faded darker region due to separation shock. There are no significant changes between VPNs 12 and 13, but the starting point of the pseudo-shock moves upstream, and the reflection of the bleed shock wave becomes blurry, indicating the presence of the pseudo-shock.

At VPN 14, vicinity of the point on the cowl side, where the bleed wedge shock hits, is distracted by the pseudo-shock, and indications of separation shock of the pseudo-shock is observed. This characteristic is even more evident at VPN 15, where a small and probably reattached separation bubble is characterized by the sonic line. The

mentioned separation bubble becomes thicker, and the sonic line is more clearly visible at VPN 16.

From VPN 16 to 17 major change of the flow field is observed. First observation is that, the detached sonic line on the bottom side (ramp side) of the intake becomes attached. Moreover, diamond shape structures faded at the downstream of separation points.

From VPN 17 to 18, the orientation of the pseudo-shock structures completely changes and becomes oriented toward the bottom side. Additionally, the formation of detached sonic line on the cowl side is observed. Another observation is the formation of the slip lines, which might be an indicator of the formation of λ-type shock structure. Moreover, nearly half of the bleed wedge shock is affected by the pseudo-shock.

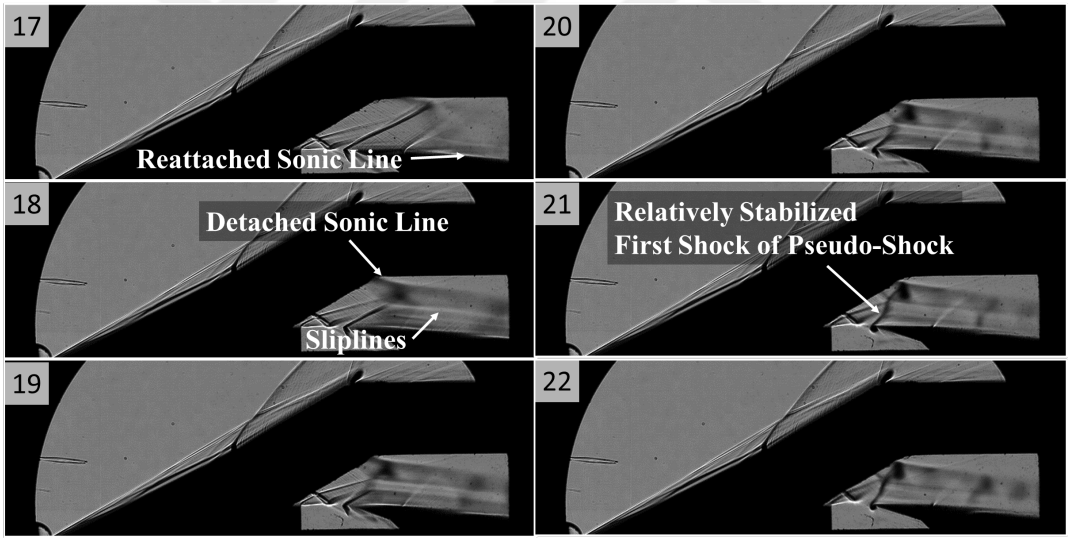


Figure 3-2. Average images for Mach = 3 with bleed (Test 4331) at VPNs 17 to 22.

Figure 3-3 shows a closer view of the shadowgraph images for VPN 18 to 21. As the valve progresses to position number 19, the pseudo-shock dominates the bleed wedge shock. Additionally, slip lines of the Mach stem become more spaced apart and the λ-type shock structure become clearer. Moreover, the flow structure in the bleed channel changes as the valve progresses from VPN 18 to 21, indicating a shift

from supercritical to subcritical intake operation mode and the effect of the back pressure on the bleed flow. Moreover, the first shock of the pseudo-shock becomes significantly more prominent, indicating a relatively low level of oscillation in the shock structure. The angle of the bleed wedge shock also changes as the valve proceeds. From VPN 20 to 21, the visible structures inside the bleed channel fade, which may indicate subsonic flow inside the bleed channel. However, examining instantaneous images instead of the averaged ones may provide better observations, as detailed in the following paragraphs.

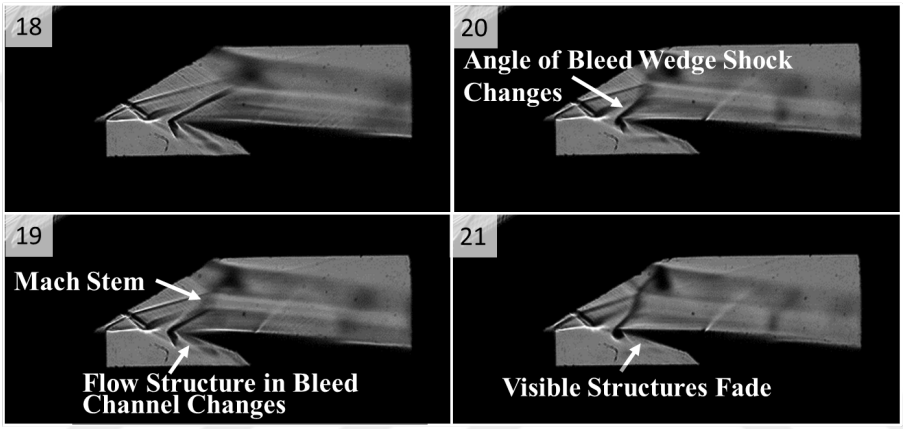


Figure 3-3. Closer view of the average images for Mach = 3 with bleed (Test 4331) at VPNs 18 to 21.

From the examination of the average images, it can be observed that there are significant changes in the shock structures between VPNs 11 and 12, 16 and 17, and 17 and 18.

3.1.1.2 Transitions and Change in The Shock Structures

Figure 3-4 shows the variation of the valve position over time and the changes in the shock structures with instantaneous images between VPNs 11 and 12. As seen, until point c, slight changes in the images are observed and the separation point is just observable at point c. From point c to d, a rapid change in 0.875 ms occurs and the separation point abruptly moves towards the upstream direction. It is worth noting

that the rapid change occurs immediately after the valve settles into its new position. The change in shock structures from point c to d is depicted in Figure 3-5. As seen, the separation point on the ramp side moves upstream consistently.

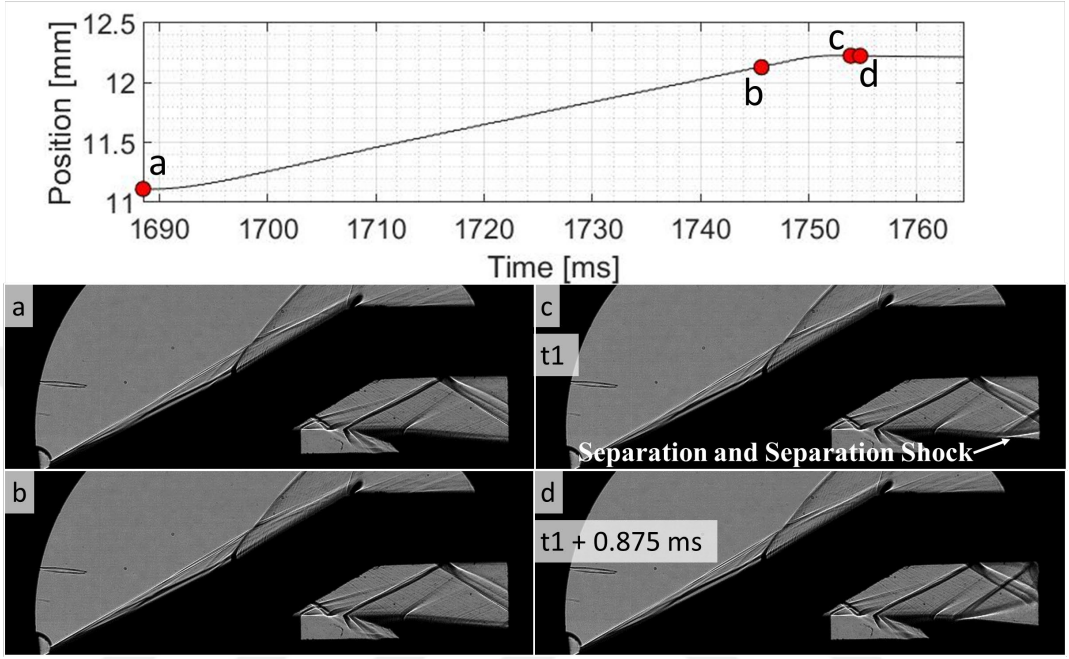


Figure 3-4. Variation of the position of the valve and change of shock structures between VPNs 11 and 12 for Mach = 3 with bleed (Test 4331).

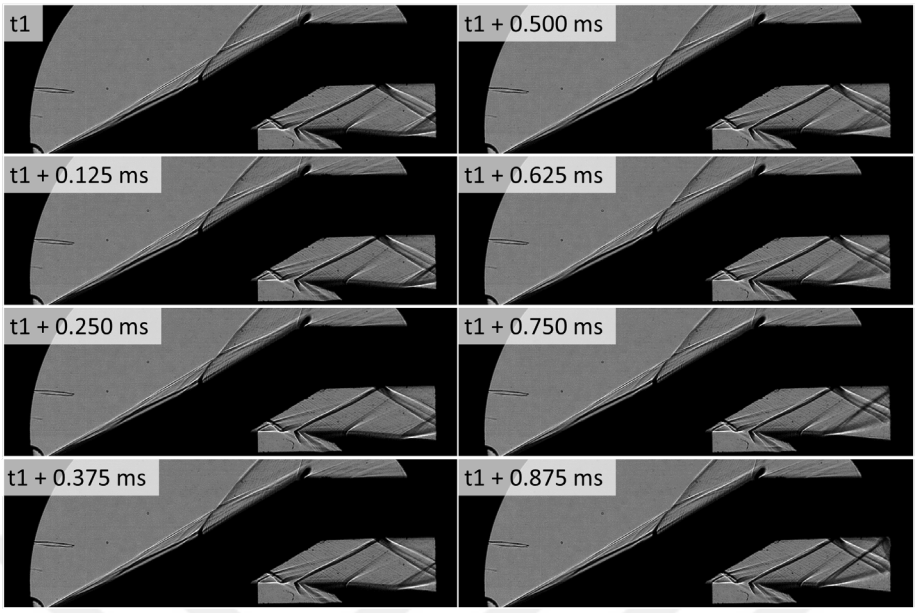


Figure 3-5. Change of the shock structures between VPNs 11 and 12 for Mach = 3 with bleed (Test 4331).

Figure 3-6 presents the changes in shock structures and the corresponding valve positions over time with instantaneous images between VPNs 16 and 17. From point a to b, the pseudo-shock structure moves downstream. From point b to c, the separation point on the ramp side begins to reattach, and at point d, a new shape of the pseudo-shock is observed, with reattached separation bubbles on both the cowl and the ramp sides. Additionally, two triple points are observed, which are characterized by the formation of the slip lines. Contrary to the Figure 3-4, it is important to note that the rapid change takes place while the valve is still in motion. The sequence of shock structure changes occurring rapidly from point c to d is given in Figure 3-7. As seen, as the separation shocks on both cowl and ramp side moves downstream, the sonic line on the ramp side attaches. Moreover, at t1 + 0.5 ms, slip lines are seen barely and they are clearly visible at t1 + 0.75 ms. Additionally, the separation bubble on the cowl side grows from t1 to t1 + 0.875 ms. It is worth noting that from t1 + 250 to t1 + 750 ms, the images are not sharp in the regions of the pseudo-shock, indicating a relatively fast movement of shock during these time intervals.

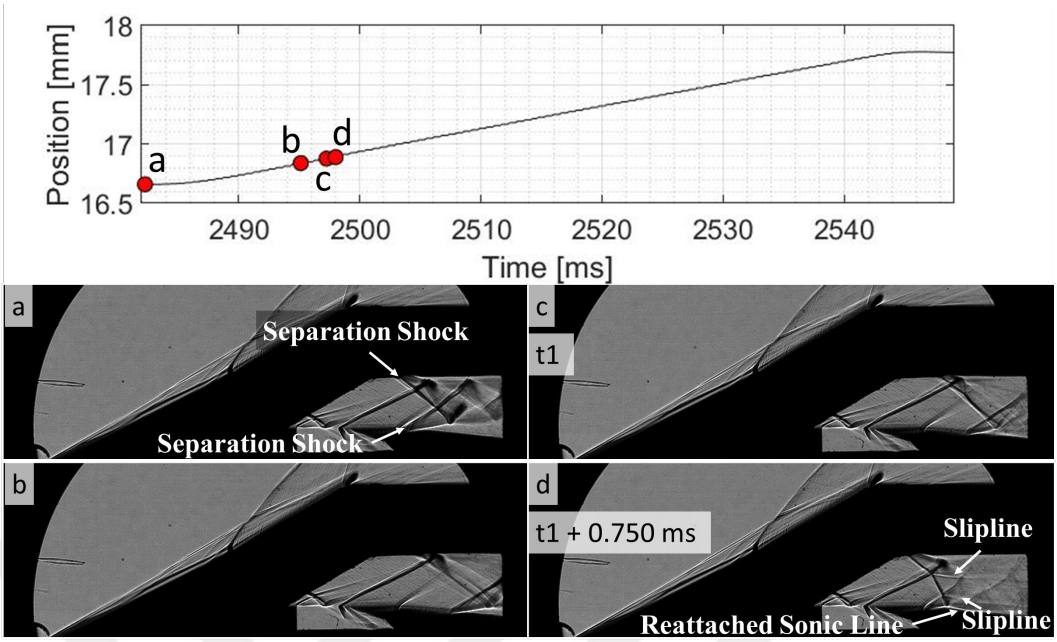


Figure 3-6. Variation of the position of the valve and change of the shock structures between VPNs 16 and 17 for Mach = 3 with bleed (Test 4331).

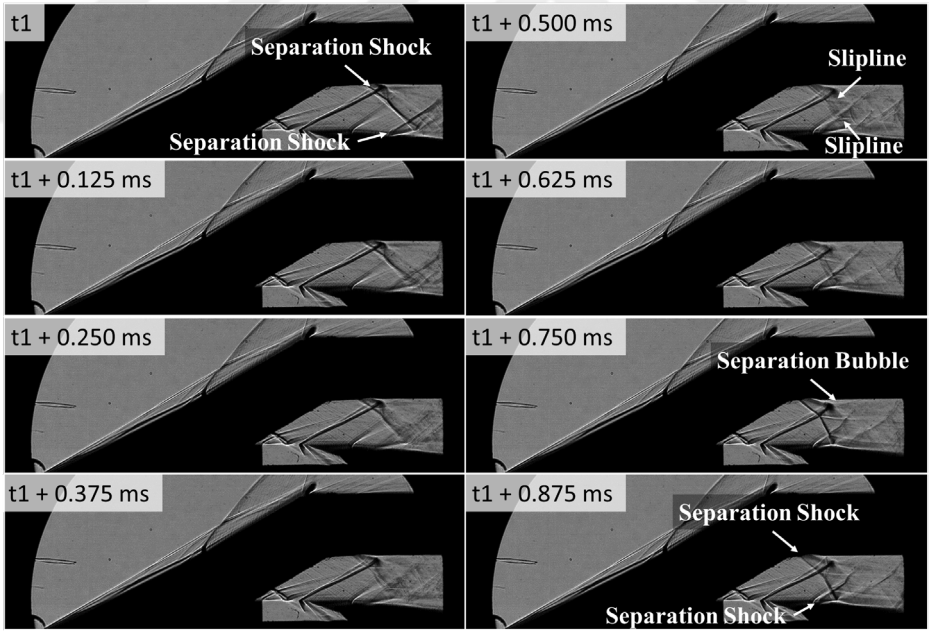


Figure 3-7. Change of the shock structures between VPNs 16 and 17 for Mach = 3 with bleed (Test 4331).

Figure 3-8 showcases the changes in the shock structures and the position of the valve over time, as depicted in the instantaneous images captured between VPNs 17

and 18. Significant alterations in the shock structures occur once the valve is settled in its new position. During the interval from point a to b, the separation bubble on the cowl side expands in thickness, and the separation shocks on both cowl and ramp side shift upstream. Within 1.5 ms from point b to c, the sonic line detaches on the cowl side, and at point d, the formation of a λ-type shock is evident. Additionally, with the emergence of a λ-type shock, more distinct slip lines become visible.

The series of the rapid shock structure changes from point b to d is given in Figure 3-9. It can be observed that the sonic line on the cowl side separates after 1.125 ms. Subsequently, the Mach stem component of the λ-type shock enlarges, and the distance between slip lines increases. Furthermore, as the shock structure moves upstream, the separation bubble on the ramp side contracts and almost vanishes.

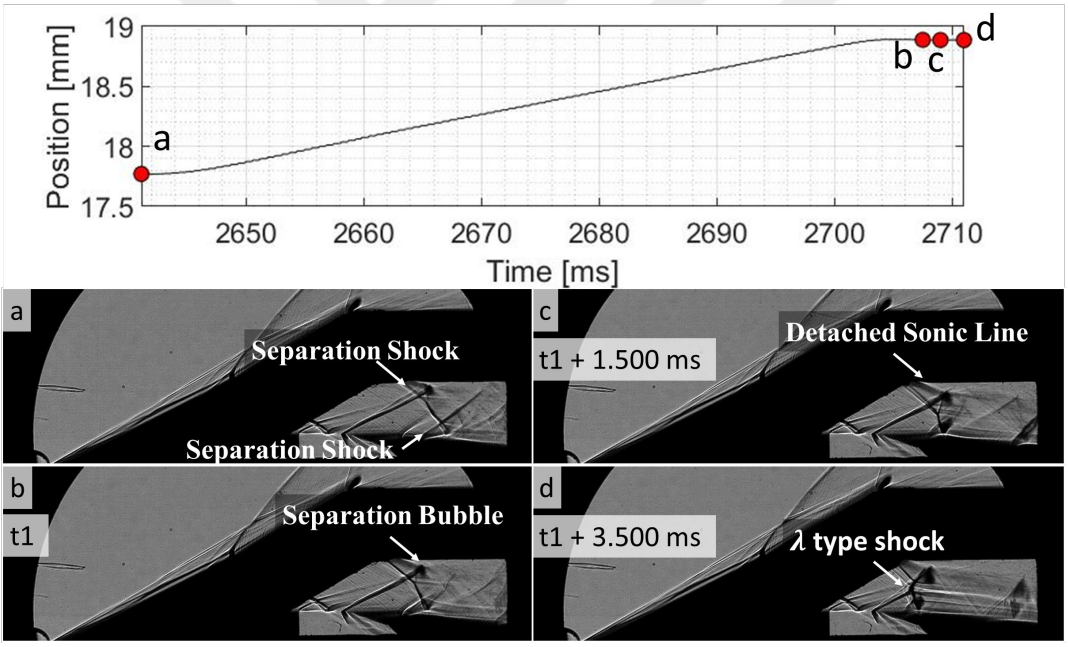


Figure 3-8. Variation of position of valve and change of shock structures between VPNs 17 and 18 for Mach = 3 with bleed (Test 4331).

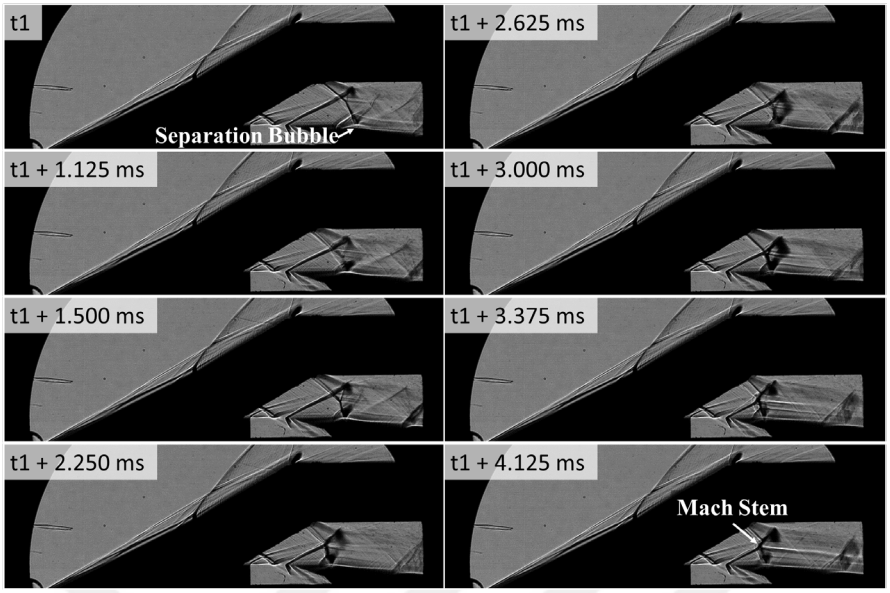


Figure 3-9. Change of shock structures between VPNs 17 and 18 for Mach = 3 with bleed (Test 4331).

3.1.1.3 Shock Oscillations

During the valve dwell time, it is observed that shock oscillations occur. These oscillations are first detected using edge detection maps, and then visually examined at the points where a relatively large change in distance is observed. Details of the method and definition of the tracer line are given in section 2.9. Line 1 is used to track the shock structures for VPNs 13 to 17, while Tracer Line 2 is used for positions 17 to 22.

The distance between the beginning of the tracer lines and the first intersected edge for VPNs 13 to 17 and 17 to 22 are shown in Figure 3-10 and Figure 3-12, respectively. In the plots on the left, to have an idea about the main trend of the change of relative distance to the intersection point, moving averaged filter is applied to raw calculated data. Window size is chosen to be 100. As seen in the plots on left, as the valve proceeds, intersection point moves toward upstream. Moreover, after the valve stops, during the dwell time of the valve, settling of the filtered data and oscillations are observed around a so-called a mean value. Plots on the right highlight

the intervals for the different valve positions numbers. The calculated distances between the starting point of the tracer lines and the detected shock point for each VPN, separately, are given in Appendix A. Additionally, the selected time intervals for the oscillations pattern which the shadowgraph images were visually examined in detail are marked in red on the figures. The aim is to select a cycle of positional change that exhibits the greatest degree of detected movement.

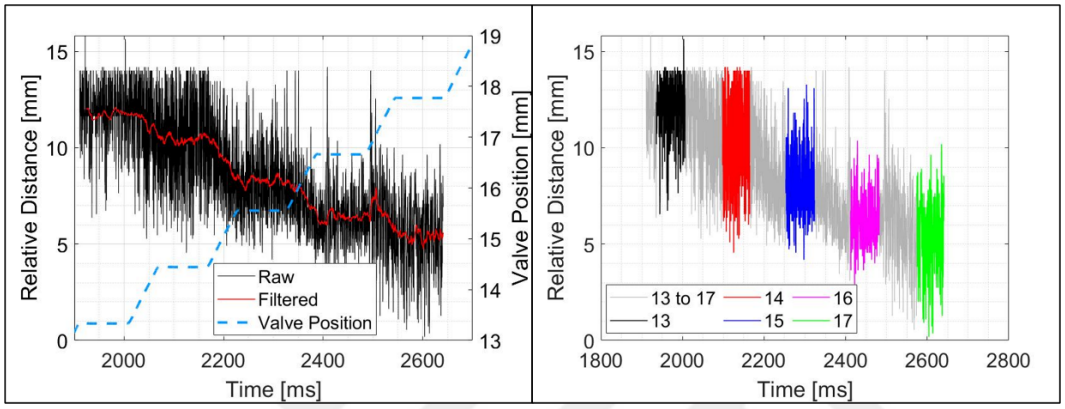


Figure 3-10. Calculated distances using tracer line 1 and corresponding valve positions for Mach = 3 with bleed (Test 4331).

It is observed from Figure 3-10 that the magnitude of oscillations decreases between VPNs 15 and 16, and then increases again between VPNs 16 and 17. To analyze the distribution of the detected positions, histogram plots based on the data presented in Figure 3-10 for VPNs 15 to 17 are shown in Figure 3-11. The plot on the left represents the detected position relative to the left end point of the tracer line, while the plot on the right shows the displacement around the calculated mean position for each VPN. The bin width is chosen to be 0.72 mm, which corresponds to 4 pixels.

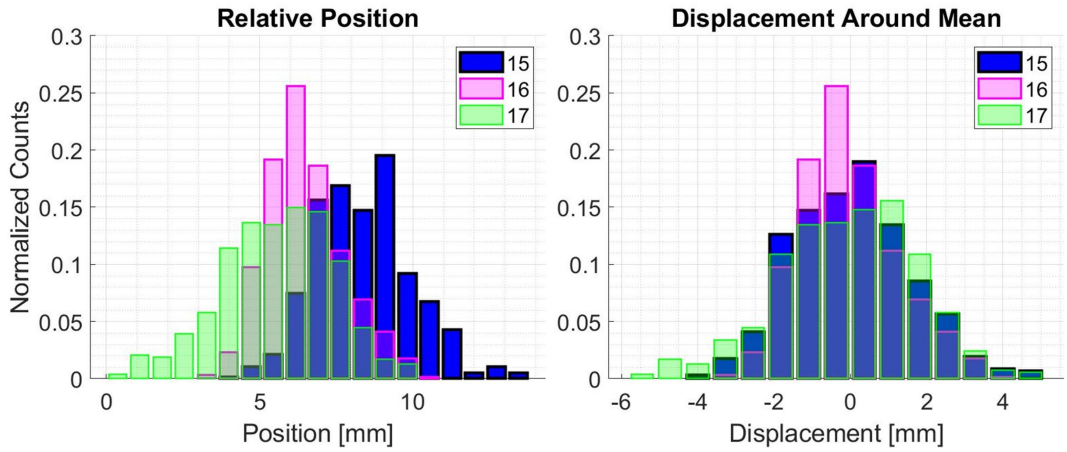


Figure 3-11. Histogram plots for VPNs 15 to 17 (Mach = 3, with bleed, Test 4331).

Analysis of the plot on the left, presented in Figure 3-11, reveals that as the valve position advances, the distribution of positions shifts towards the left or upstream. The plot on the right demonstrates that as the VPN changes from 15 to 16, the values become more concentrated around a value closer to the mean of data for each VPN. This indicates that the traced shock is more stable at position number 16. However, transitioning from position 16 to 17 leads to a more scattered distribution of values.

In Figure 3-12, it is observed that there is a relatively high change in the position of the intersection point between the valve positions 17 and 18, as seen by the sudden decrease in the filtered data in the graph. This observation is consistent with the discussions given in the preceding sections (section 3.1.1.1 and 3.1.1.2) where the shape of the shock structure changes significantly during the transition. Additionally, for the valve position 22, the minimum value of the data is restricted to around 1, which suggests that at certain points, the intersection point tends to move upstream beyond the beginning of the tracer line. In other words, the point of interest on the shock moves towards the upstream region of the tracer line's starting point.

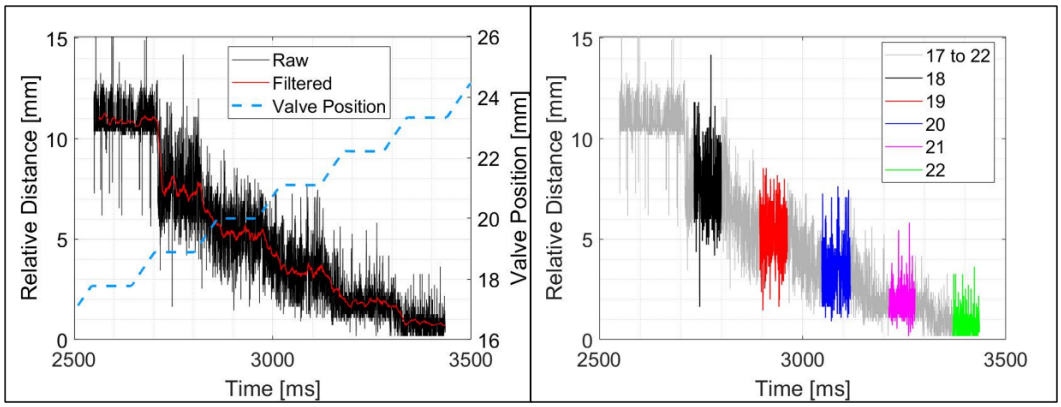


Figure 3-12. Calculated distances using tracer line 2 and corresponding valve positions for Mach = 3 with bleed (Test 4331).

Figure 3-12 indicates a decrease in the amount of oscillations when transitioning from valve position 19 to 21. In order to analyze the distribution of the detected positions, histogram plots were generated using the data presented in Figure 3-12 for VPNs 19 to 21. These histogram plots are presented in Figure 3-13.

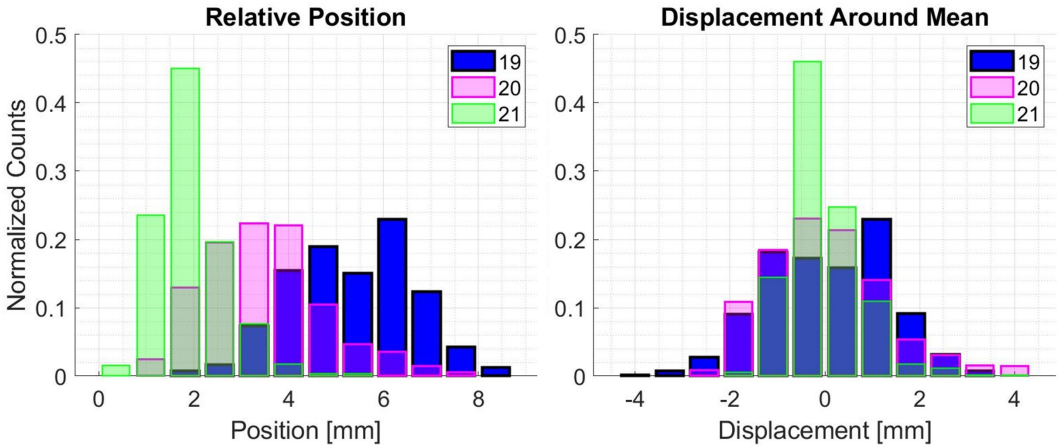


Figure 3-13. Histogram plots for VPNs 19 to 21 (Mach = 3, with bleed, Test 4331).

Upon examining the plot on the left side of Figure 3-13, it can be observed that the distribution of positions shifts towards the left or upstream as the valve proceeds. The plot on the right shows that as the valve position increases, the values become more concentrated around a value closer to the mean value of the each VPN, particularly at VPN 21. This indicates that the traced shock exhibits greater stability at position number 21.

For VPN 13, the oscillation pattern is shown in Figure 3-14. As seen, it takes 1.75 ms to complete the cycle and return to its initial position at t0. The oscillation of the pseudo-shock affects the reflection of the bleed wedge shock, resulting in a small separation bubble on the cowl side and an additional separation shock. At t0 + 750 ms, the pseudo-shock reaches its most upstream position, and after this point, the related shock structures move downstream as the separation bubble on the cowl side shrinks.

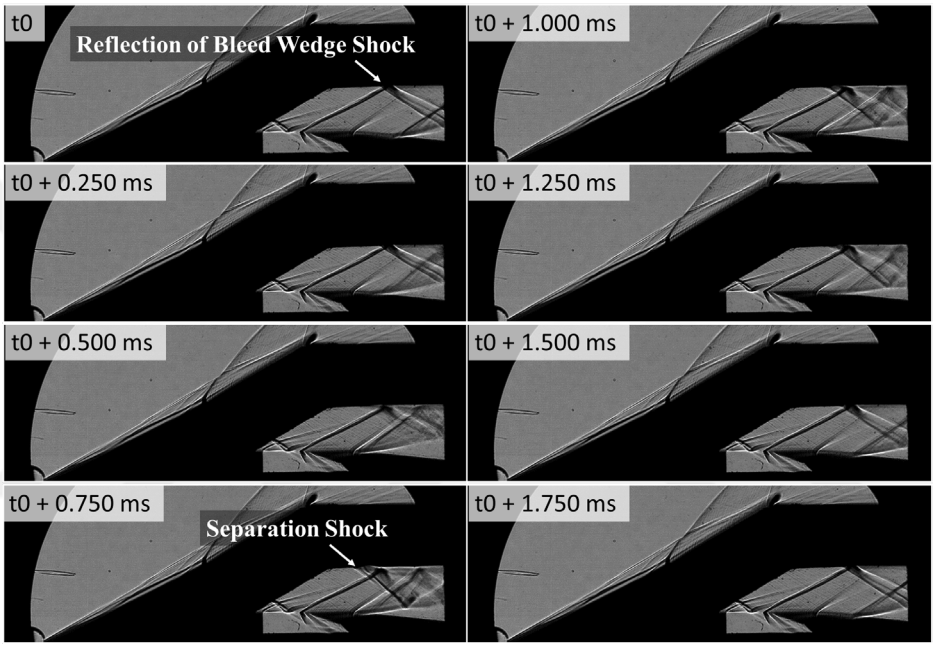


Figure 3-14. Oscillation of shock patterns at VPN 13 for Mach = 3 with bleed (Test 4331).

Figure 3-15 presents a comparison of the most upstream and downstream positions of the pseudo-shock for VPN 13. The left image shows the frame at the moment when the first shock of the pseudo-shock is at its most downstream position, while the right image shows the frame at the moment when the shock is at its most upstream position. In the figure, the blue vertical line on the left represents the x-coordinate of the interested shock point when the shock is at its most upstream position, and the green vertical line on the right represents the x-coordinate of the interested shock point when the shock is at its most downstream position. The calculated distance between these points is represented by the length of the horizontal red line. The

difference in the position of the shock has been measured along an imaginary line that shares the same y-coordinate as the horizontal red line. The intersected shock positions have been manually marked through visual examination along the horizontal line. The length of the horizontal red line has been calculated to be 12.9 mm.

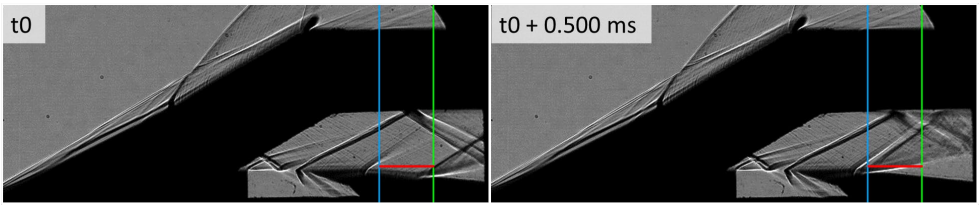


Figure 3-15. Comparison of shock positions at VPN 13 for Mach = 3 with bleed (Test 4331).

For VPN 14, a similar oscillation pattern as VPN 13 is observed (See Appendix B). However, there are some differences observed. Firstly, when the pseudo-shock is at its most upstream position, a thicker separation bubble on the cowl side is observed compared to VPN 13. Secondly, the oscillation occurs at a more upstream position relative to VPN 13. Comparison of the most upstream and downstream positions of the pseudo-shock for VPN 14 is presented in Figure 3-16. The length of the horizontal red line has been calculated to be 10.9 mm.

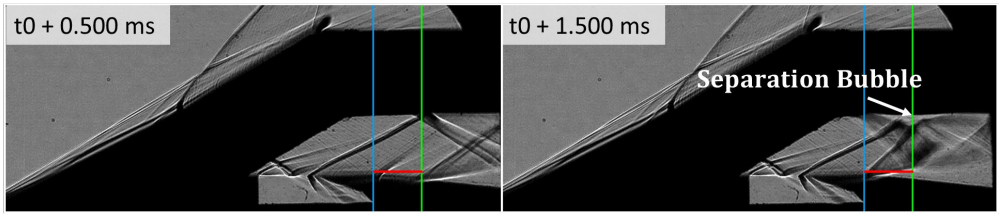


Figure 3-16. Comparison of shock positions at VPN 14 for Mach = 3 with bleed (Test 4331).

Images for VPN 15 exhibit a similar oscillation pattern (See Appendix B) to VPN 13 and 14. However, there are several notable differences. Firstly, a thicker separation bubble on the cowl side is observed when the pseudo-shock is at its most upstream position compared to the valve positions 13 and 14. The second difference observed is that the oscillation occurs at a location closer to the upstream region.

Third, the presence of a separation shock on the cowl side is observed when the pseudo-shock is at its most downstream position, rather than a similar structure to the shock reflection of the bleed wedge shock. Figure 3-17 illustrates the comparison of the most upstream and downstream positions of the pseudo-shock for VPN 15. The distance between these two positions is represented by the length of the horizontal red line, which is determined to be 8.2 mm.

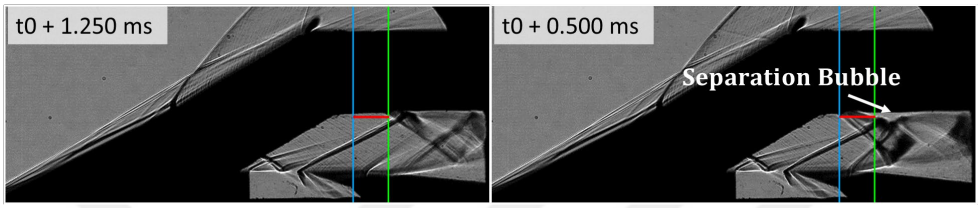


Figure 3-17. Comparison of shock positions at VPN 15 for Mach = 3 with bleed (Test 4331).

The oscillation pattern observed at VPN 16 is very similar to that seen at VPN 15 and it is given in Appendix B. The calculated distance between two shock points located along the line of interest is displayed in Figure 3-18, which is measured to be 6.5 mm.

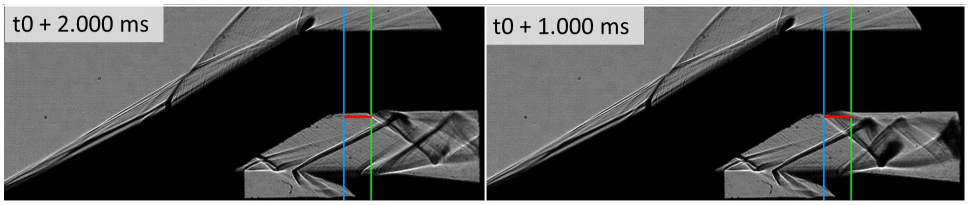


Figure 3-18. Comparison of shock positions at VPN 16 for Mach = 3 with bleed (Test 4331).

The oscillation pattern observed at VPN 17 is given in Figure 3-19. Similar to the figures for the former VPNs, separation shock oscillates back and forth. The time to complete one cycle and return to the initial position at t0 is found to be 3 ms. The shock structures shown in Figure 3-19 appear to display Edney's Type I interference. Four shocks label C1 to C4 can be observed observed in the figure. As the pseudo-shock moves upstream, the point at which these four shocks intersect moves downstream. Additionally, the angle of shock C3 appears to change, becoming more

perpendicular to the flow direction. The location of C2, C3, and C4 shocks changes during the oscillation, while the angle and starting position of the C1 shock remain constant. This is because shocks C2, C3, and C4 are related to shock boundary layer interaction of the pseudo-shock, while C1 shock is formed due to the bleed wedge. The separation shock on the cowl side starts at its most downstream position at t0 and moves upstream until it reaches its most upstream position at t0 + 1.375 ms. Then, by t0 + 3.00 ms, it returns to a position similar to its initial location at t0. The calculated distance between two shock points located along the line of interest is displayed in Figure 3-20, which is measured to be 7.5 mm.

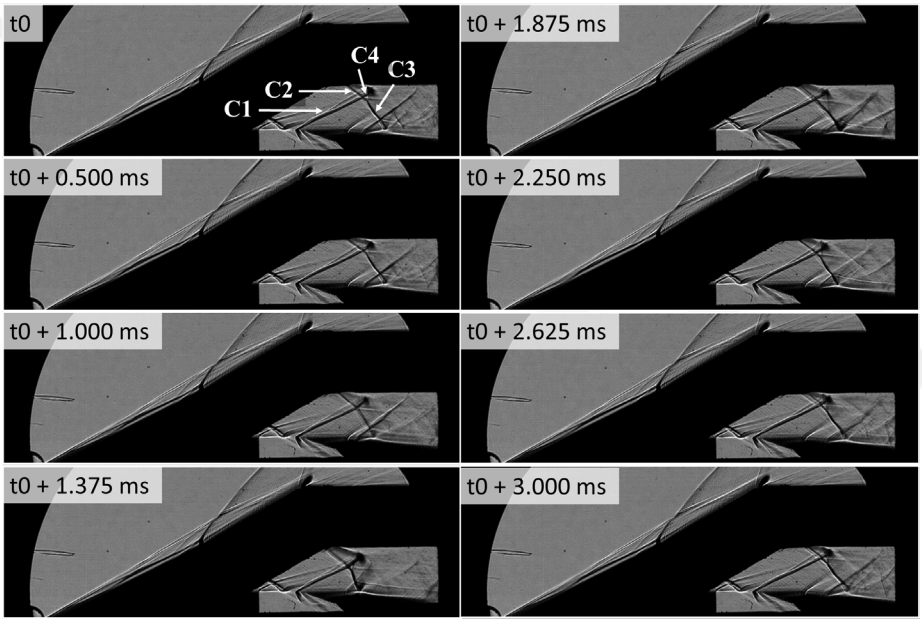


Figure 3-19. Oscillation of shock patterns at VPN 17 for Mach = 3 with bleed (Test 4331).

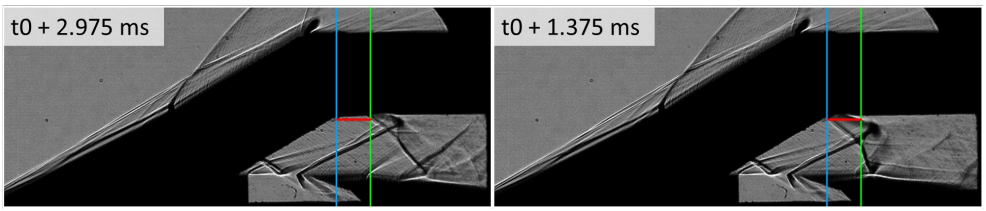


Figure 3-20. Comparison of shock positions at VPN 17 for Mach = 3 with bleed (Test 4331).

Figure 3-21 illustrates the oscillation pattern observed at VPN 18. This time, a structure similar to Edney's Type II interference is observed. The location of C2, C3, and C4 shocks changes during the oscillation, while the angle and starting position of the C1 shock remain constant. Additionally, when the pseudo-shock is at its most upstream position, a wider Mach stem is formed, and for the downstream position, the Mach stem narrows down, resulting in a similar structure to an X-type shock or Edney's Type I interference. The formation of slip lines downstream of the Mach stem is evident, with the vertical distance between them appears decreasing as the pseudo-shock moves downstream, and vice versa.

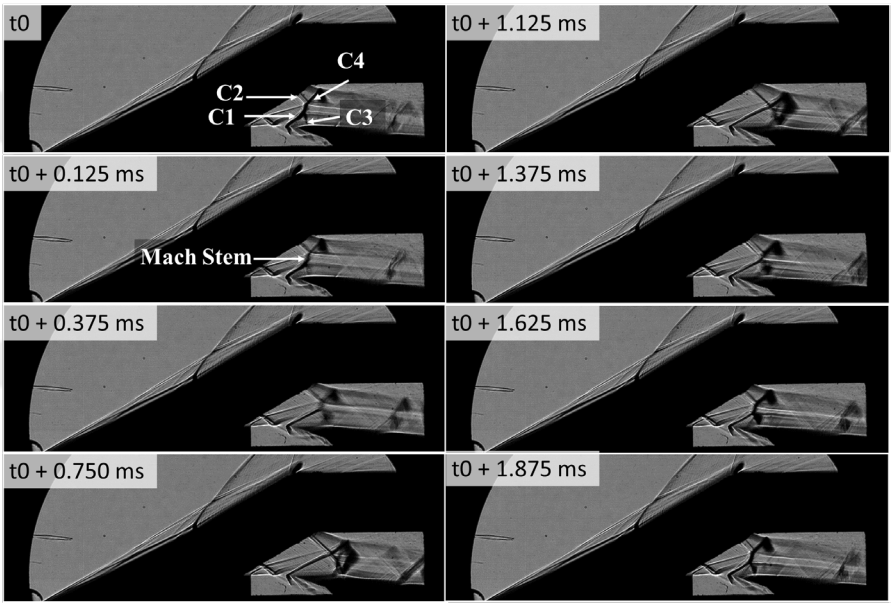


Figure 3-21. Oscillation of shock patterns at VPN 18 for Mach = 3 with bleed (Test 4331).

Figure 3-22 presents the distance between two shock points measured along the line of interest, which is calculated to be 6.5 mm. This distance is smaller than the distances observed for the previous valve positions. However, it should be noted that the y-coordinate of the horizontal red line is different from the previous positions, as the intersection point with the shock extends beyond the upstream boundary of the intake's shadowgraph window.

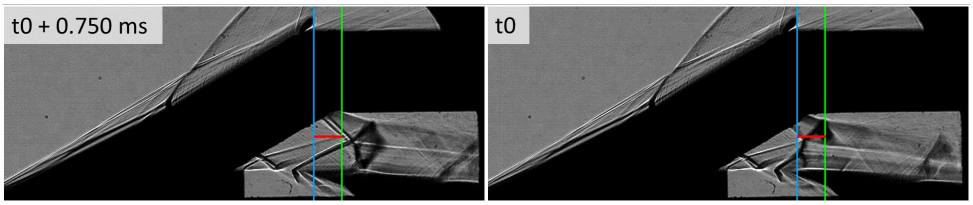


Figure 3-22. Comparison of shock positions at VPN 18 for Mach = 3 with bleed (Test 4331).

Figure 3-23 shows the oscillation pattern observed at VPN 19, which exhibits Edney's Type II interference similar to VPN 18. However, there is no formation of an X-type shock structure during the oscillation of the shock at position number 19. At t0 + 0.500 ms, a small change in the bleed channel is observed. This indicates that back pressure is starting to affect the bleed flow at VPN 19, and the intake is operating in a mode very close to critical, oscillating between subcritical and supercritical conditions. It is important to note that in Figure 3-2 in which the average images are presented, the flow field in the bleed channel was observed to change the at VPN 19 and continues to change for subsequent positions. Figure 3-24 displays the calculated distance between two shock points along the line of interest, which is found to be 4.9 mm. This value is less than the value obtained for VPN 18.

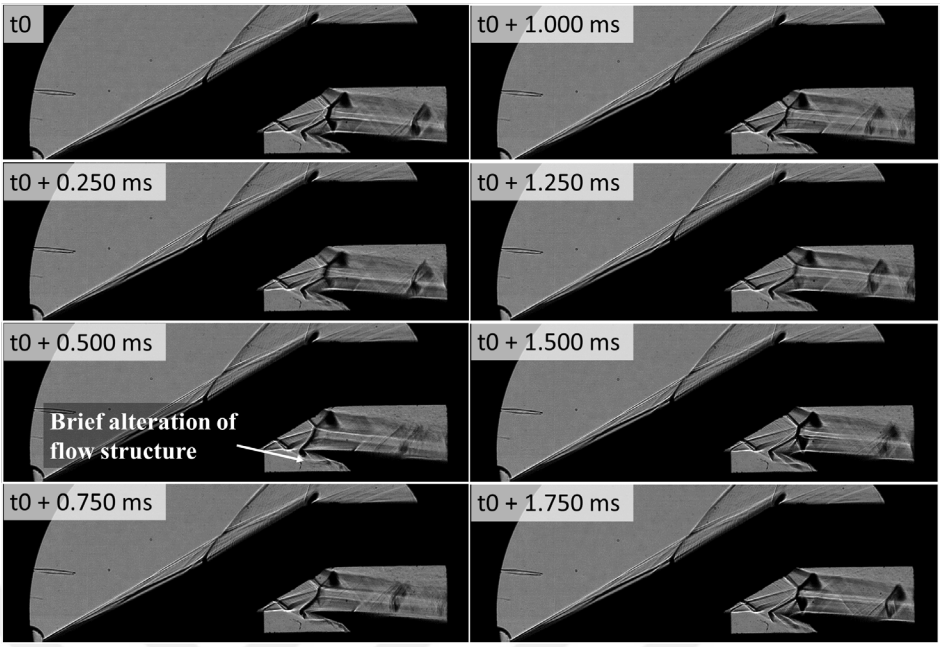


Figure 3-23. Oscillation of shock patterns at VPN 19 for Mach = 3 with bleed (Test 4331).

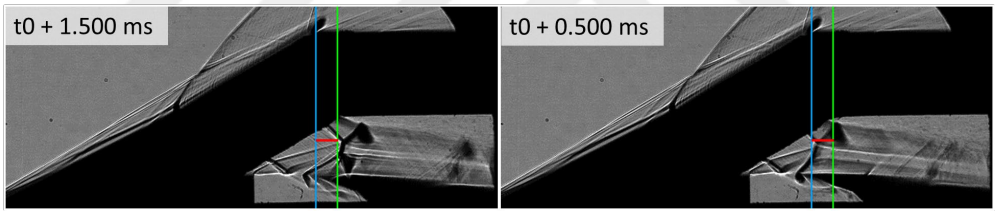


Figure 3-24. Comparison of shock positions at VPN 19 for Mach = 3 with bleed (Test 4331).

The oscillation pattern observed at VPN 20 is depicted in Figure 3-25, and it displays similar features to the previous position. The oscillation in the diffuser influences the bleed channel. Therefore, it can be inferred that VPN 20 corresponds to subcritical operation mode. At t0, an additional second shock is observed on the cowl side, but the reason for its formation is unknown. Additionally, the C3 shock of the λ-type partially disappears and reappears, although the corresponding slip line remains present.

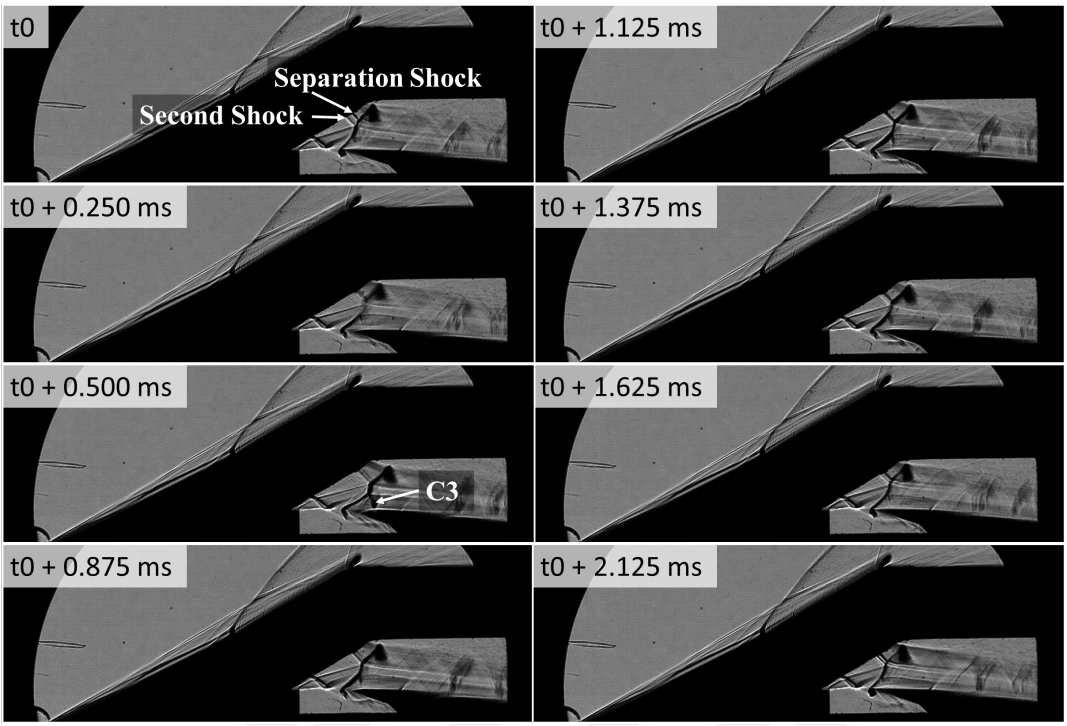


Figure 3-25. Oscillation of shock patterns at VPN 20 for Mach = 3 with bleed (Test 4331).

The distance between two shock points along the line of interest is shown in Figure 3-26, and it is calculated to be 4.7 mm. This value is the smallest among all the previously presented VPNs for Test 4331.

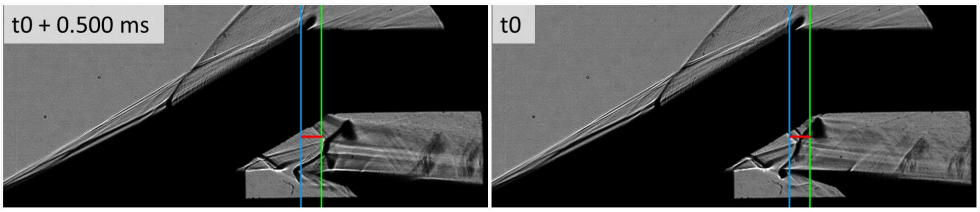


Figure 3-26. Comparison of shock positions at VPN 20 for Mach = 3 with bleed (Test 4331).

Oscillation pattern for VPN 21 is similar to one observed for 20. One noticeable difference is that reappearance of C3 shock is less distinct. Comparison of the most upstream and downstream positions of the first shock of the pseudo-shock is given in Figure 3-27. On the left, displacement of the separation shock on the cowl side is marked and on the right, displacement of the Mach stem part is marked. Calculated

displacements are 3.5 and 2.2 mm, respectively. Oscillation of Mach stem part is lower than the separation shock. Calculated displacement of the separation shock is similar with the one for VPN 20.

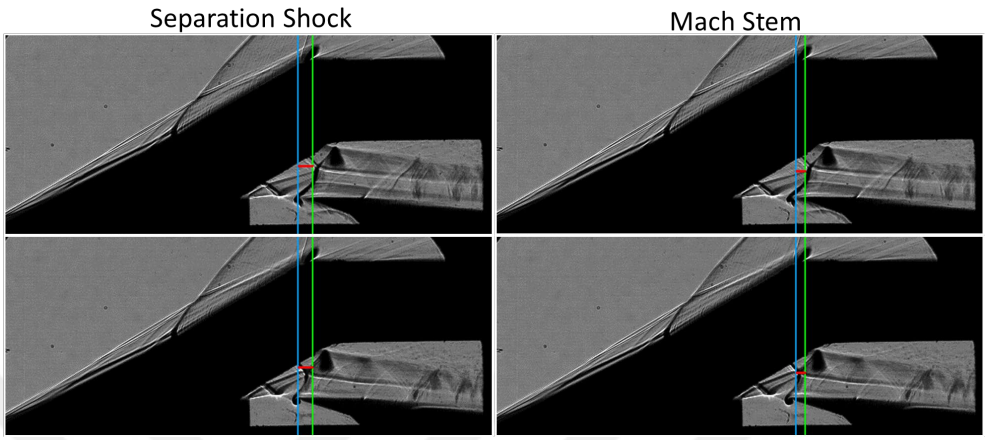


Figure 3-27. Comparison of shock positions at VPN 21 for Mach = 3 with bleed (Test 4331).

Comparison of the most upstream and downstream positions of the first shock of the pseudo-shock for VPN 22 is given in Figure 3-28. Calculated displacements for the separation shock and the Mach stem part are 2.5 and 1.6 mm, respectively. Oscillation of Mach stem part is lower than the separation shock. Calculated displacement of both separation shock and the Mach stem part are less than the ones for VPN 21.

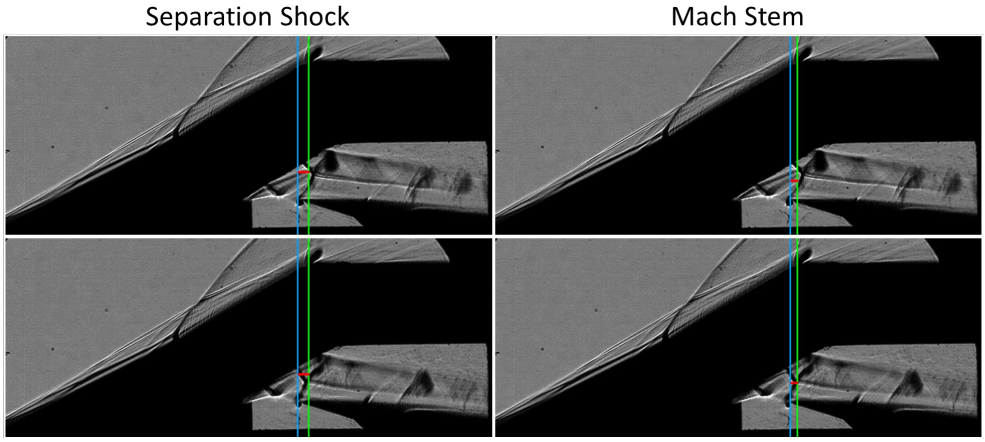


Figure 3-28. Comparison of shock positions at VPN 22 for Mach = 3 with bleed (Test 4331).

Table 3-1 provides a summary of the distances measured for the change in position of the shock point along the related y-coordinate or horizontal red lines. The non-dimensional amplitude of the displacement, relative to throat height of the intake, is determined by dividing the calculated difference by 2 and then by the throat height.

The results indicate that the calculated displacement decreases from VPN 13 to 16. However, a subsequent increase in displacement is observed when moving from valve position 16 to 17. This change in displacement may be associated with the abrupt change in the shock structures, as discussed in section 3.1.1.2, where the separated sonic line on the ramp side attaches. Upon examining the difference values for VPNs 18-22, it can be observed that the amount of displacement drops after the interaction of the pseudo-shock with the bleed region.

Table 3-1. Summary of changes in shock positions for Mach = 3 with bleed (Test 4331).

VPN	Pixel 1	Pixel 2	Difference [Pixels]	Difference [mm]	Amplitude [%]	Shock Type
13	661	590	71	12.9	45	X
14	631	571	60	10.9	38	X
15	607	562	45	8.2	28	X
16	592	556	36	6.5	23	X
17	583	542	41	7.5	26	X
18	555	519	36	6.5	23	X and λ
19	534	507	27	4.9	17	λ
20	526	500	26	4.7	16	λ
21	511	492	19	3.5	12	λ
22	502	488	14	2.5	9	λ

Figure 3-29, Figure 3-30 and Figure 3-31 provide a comparison of instantaneous shock positions for various VPNs. On the left side of each figure, the position of the first shock of the pseudo-shock related shock structures is at the most downstream, and on the right side, it is at the most upstream during the oscillation cycle of interest. In the figure, the red vertical lines represent the x-coordinate of the interested shock

point along the horizontal red line. The calculated distance between these points is represented by the length of the horizontal red line. The figures show that as the valve proceeds, both the most upstream and most downstream position of the first shock of the pseudo-shock (the separation shock) move upstream.

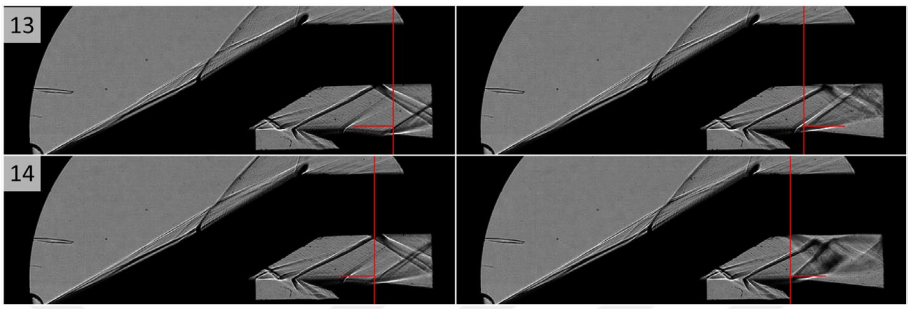


Figure 3-29. Comparison of shock positions at VPNs 13 and 14 for Mach = 3 with bleed (Test 4331).

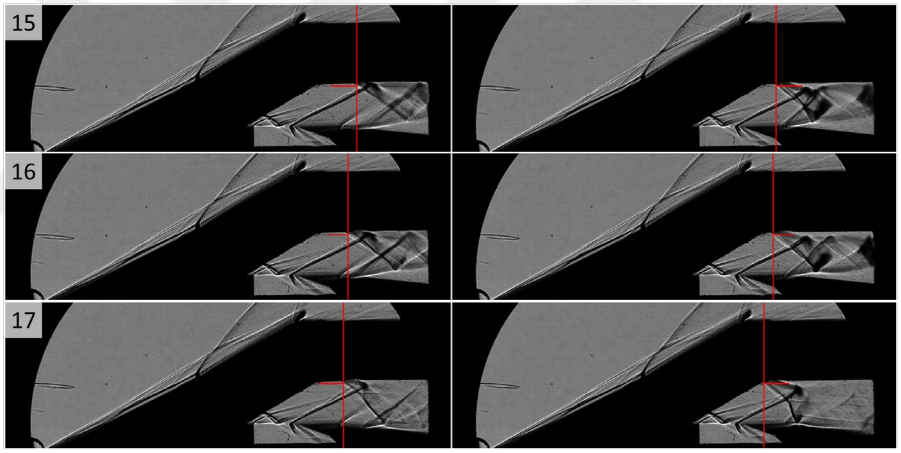


Figure 3-30. Comparison of shock positions at VPNs 15, 16 and 17 for Mach = 3 with bleed (Test 4331).

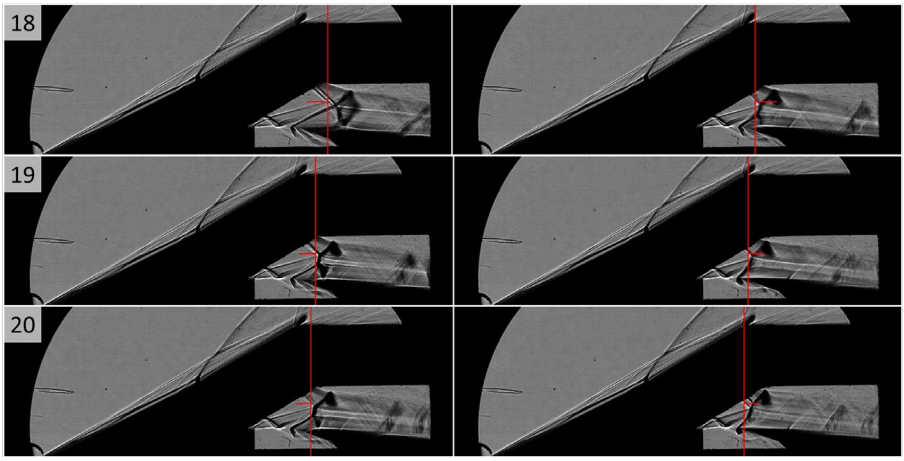


Figure 3-31. Comparison of shock positions at VPNs 18, 19 and 20 for Mach = 3 with bleed (Test 4331).

3.1.2 Mach = 2.63 with Bleed (Test 4340)

3.1.2.1 Average Images

Figure 3-32 and Figure 3-33 present the average images for different VPNs in Test 4340. Similar to Test 4331, the effects of back pressure are not visible through the test item's window until VPN 11.

As the valve moved, the oscillatory motion of the pseudo-shock structure results in certain regions of the average image becoming blurred, and changes are observed in the corresponding areas as the pseudo-shock moved upstream. Similar changes are observed between VPNs 11 and 16 when compared to Test 4331. In summary, as the valve approaches position 16, the separation shock on the ramp side moves upstream and a separation shock on the cowl side is formed with a thicker separation bubble.

The average images reveal that after the valve shifts from position number 16 to 17, there is separation of the sonic line on the cowl side and attachment of the sonic line on the ramp side. As the valve moves towards position 18, there is a brief appearance of the slip lines in the images, and at position 19, they become visible again with more clarity. Changes in the bleed channel are observed between valve positions 19

and 20, suggesting a shift from supercritical to critical or subcritical intake operation. Furthermore, at position 20, the view of the first shock of the pseudo-shock starts to become sharper, and at 21, a relatively stable shock can be observed.

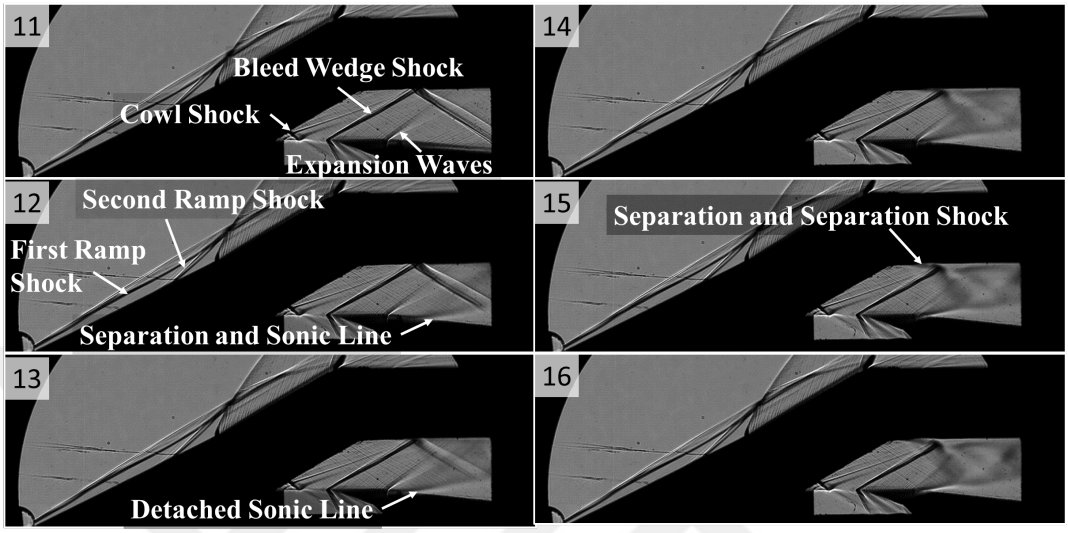


Figure 3-32. Average images for Mach = 2.63 with bleed (Test 4340) at VPNs 11 to 16.

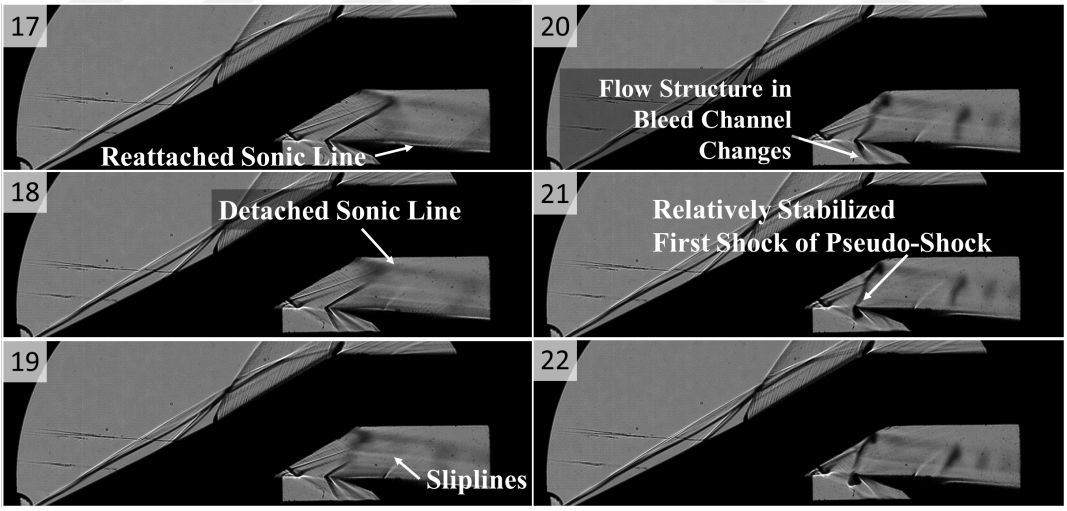


Figure 3-33. Average images for Mach = 2.63 with bleed (Test 4340) at VPNs 17 to 22.

Examination of the average images reveals that there are significant alterations in the shock structures between VPNs 11 and 12, as well as 16 and 17.

Before the effect of the pseudo-shock is seen, some differences in the shock structures compared to Test 4331 are observed. Due to the fact that Test 4340 is conducted at a lower Mach number, the angle of shock waves is expected to change independent from the back pressure effects. First, it is seen that the first and second ramp shocks are visible because of the fact that the intake operates at a Mach number lower than its design Mach number, which is 3. Moreover, the point where the cowl shock hits the bleed channel and the point where the bleed wedge shock hits the cowl are downstream compared to Test 4331. A visual comparison is given in Figure 3-34. In the figure, the vertical orange lines represent the position of the mentioned locations for the tests at Mach number of 3 (Test 4331).

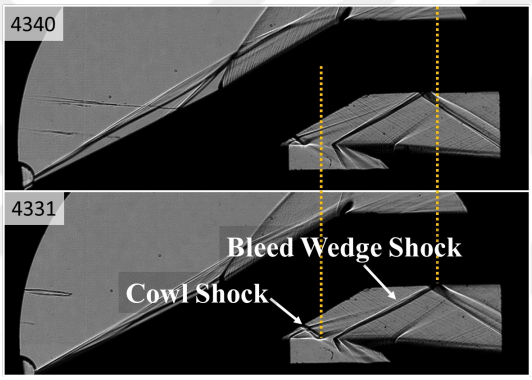


Figure 3-34. Comparison of shock structures between the Mach = 2.63 (Test 4340) and Mach = 3 (Test 4331) with bleed for VPN 11.

3.1.2.2 Transitions and Change in the Shock Structures

Figure 3-35 displays the valve position changes over time along with the changes in the shock structures using instantaneous images captured between VPNs 11 and 12. It is notable that while slight changes in the images are observed until point c, the separation shock becomes just visible at this point. Between points c and d, a sudden shift occurs where the separation shock moves upstream over the course of 2 ms. It is noteworthy that the shift happens during the motion of the valve, which is different from the transition between position numbers 11 and 12 in Test 4331. Similar to the Test 4331, the separation shock on the ramp side continuously shift upstream.

Change of the shock structures with instantaneous images between point c and d is given in Appendix C

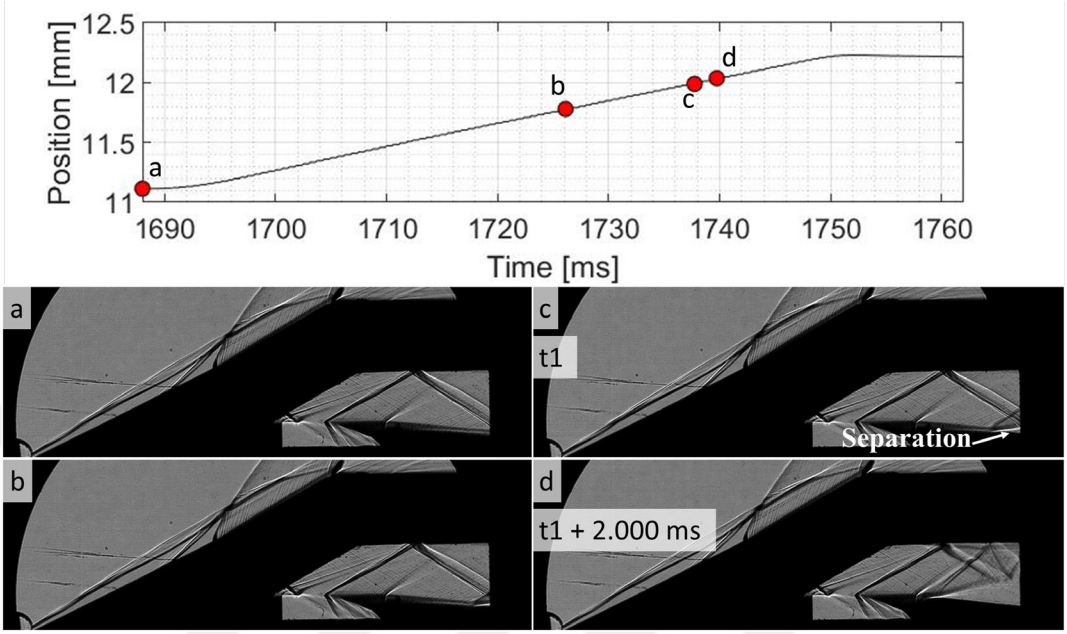


Figure 3-35. Variation of the position of the valve and change of shock structures between VPNs 11 and 12 for Mach = 2.63 with bleed (Test 4340).

The changes in shock structures and corresponding valve positions over time are depicted in Figure 3-36 with instantaneous images between VPNs 16 and 17. From point a to c, no significant changes are observed. From point c to d, a new shape of the pseudo-shock is observed. A detachment on the cowl side and attachment of the sonic line on the ramp side are observed, and the orientation of the pseudo-shock changes its direction from parallel to the cowl side to the ramp side.

Figure 3-37 shows the rapid sequence of changes in the shock structure occurring between point c to d. The image sequence shows that the separation bubble on the cowl side thickens at t1 + 0.5 ms. At t1 + 1 ms, the sonic line on the cowl side completely detaches and the sonic line on the ramp side partially attaches and then detaches again downstream. By t1 + 1.5 ms, the sonic line on the ramp side attaches. At t1 + 2 ms, the sonic line on the cowl side completely detaches. Finally, at t1 + 2.5 ms, formation of a λ-type shock is observed. Although the exact structure of the λ

shape is not clearly visible, the presence of the slip lines with sufficient vertical distance between them suggests the formation of a Mach stem.

After the sudden shift in shocks, it is notable that the separation point on the cowl side moves closer to the point where the bleed wedge shock hits to the cowl surface. This indicates that the adverse pressure gradient of the bleed wedge shock has already established a location that is susceptible to separation, and the back pressure effect contributes to the thickening of the separation bubble on the cowl side. The combination of these two effects ultimately leads to complete separation of the sonic line from the cowl side. Similar observations have been made by Wang et al. [84]. Their test configuration is symmetrical and motion of first shock of pseudo-shock with respect to back pressure has been investigated. They have commented that the pseudo-shock moves upstream suddenly when the leading edge of the pseudo-shock encounters the separation bubble near the shock reflection point or a region with adverse pressure gradient. On the other hand, the pseudo-shock moves relatively slow when the leading shock of the shock-train is in the favorable pressure gradient region.

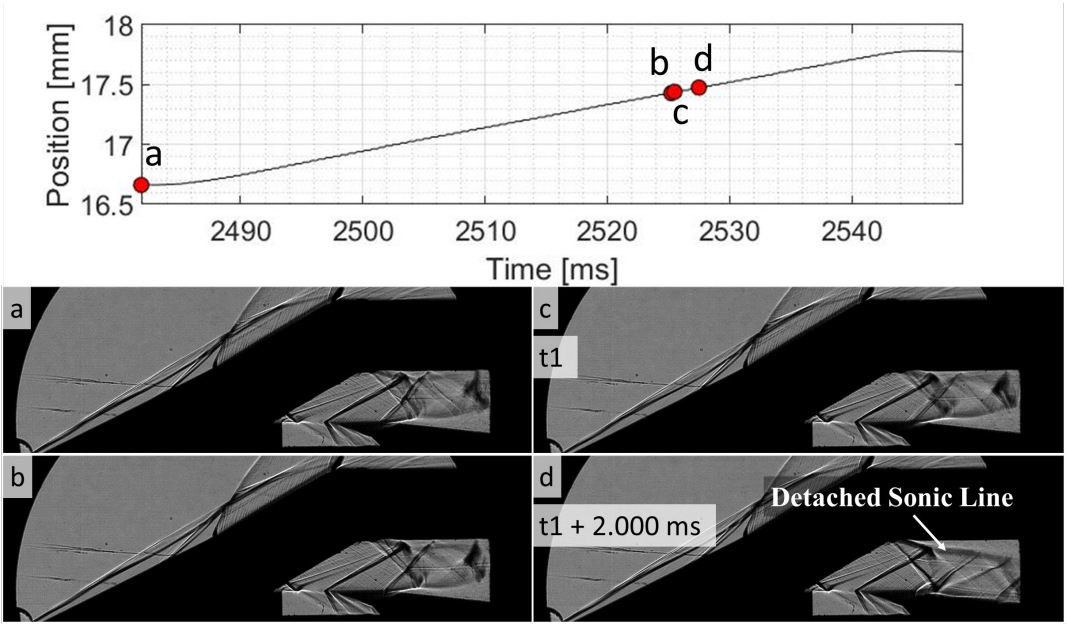


Figure 3-36. Variation of the position of the valve and change of shock structures between VPNs 16 and 17 for Mach = 2.63 with bleed (Test 4340).

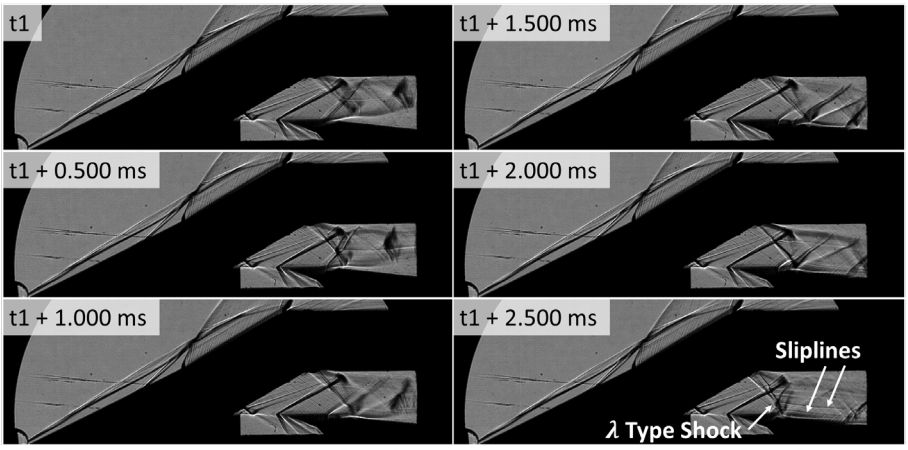


Figure 3-37. Change of the shock structures between VPNs 16 and 17 for Mach = 2.63 with bleed (Test 4340).

3.1.2.3 Shock Oscillations

Tracer Line 1 is utilized to monitor the shock structures between valve positions 13 to 16, while Tracer Line 2 is used to track positions 17 to 19. Figure 3-38 and Figure 3-40 display the calculated relative distances using tracer lines, the interval of considered images for dwell times, and the change in valve position. Both the raw and moving averaged data indicate oscillation around a mean value during the dwell time. Furthermore, is Figure 3-38, the duration between approximately 2500 ms to 2550 ms corresponds to the transition from VPN 16 to 17 and it is evident that a relatively rapid change in trend is observed in both raw and filtered data, which is consistent with the observations made regarding the average images.

The calculated distances between the starting point of the tracer lines and the detected shock point for each VPN, separately, are given in Appendix A.

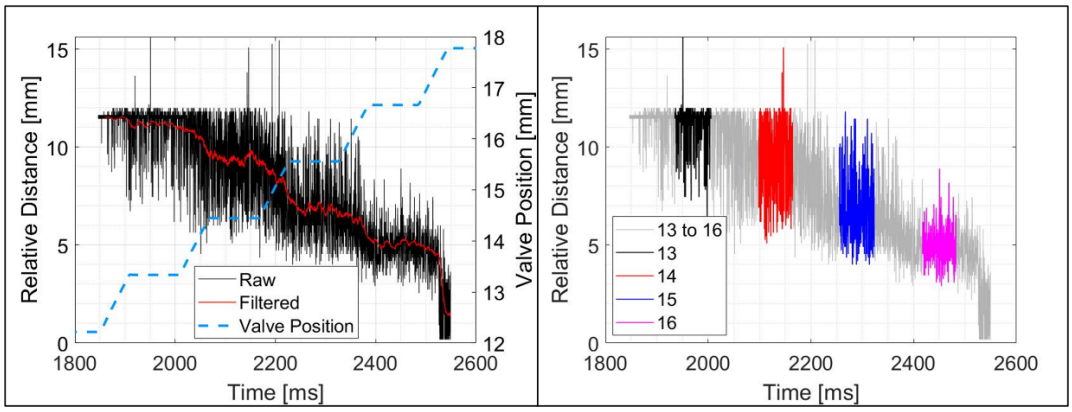


Figure 3-38. Calculated distances using tracer line 1 and corresponding valve positions for Mach = 2.63 with bleed (Test 4340).

It is observed from Figure 3-38 that the magnitude of oscillations decreases between VPNs 15 and 16. Histogram plots based on the data presented in Figure 3-38 for VPNs 15 and 16 are shown in Figure 3-39.

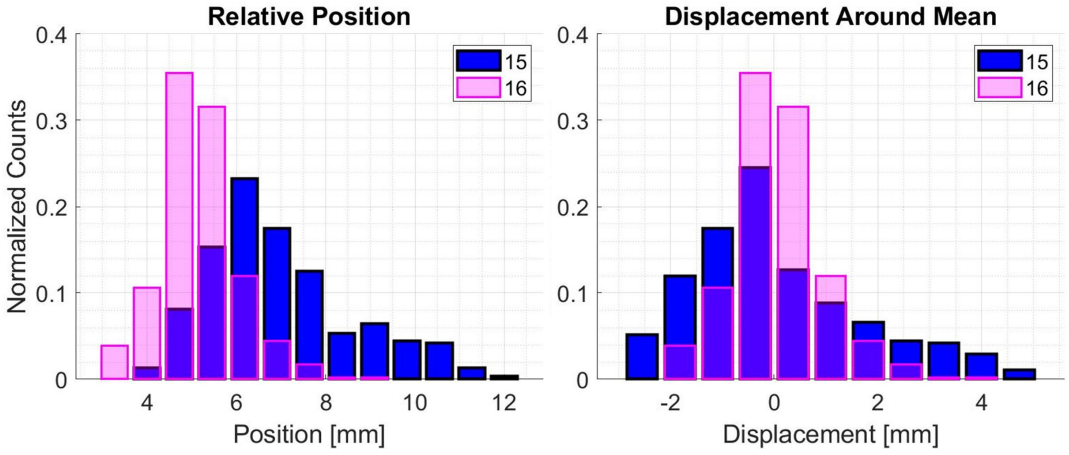


Figure 3-39. Histogram plots for VPNs 15 and 16 (Mach = 2.63, with bleed, Test 4340).

Analysis of the plot on the left, presented in Figure 3-39, reveals that as the valve position advances, the distribution of positions shifts towards the left or upstream. The plot on the right demonstrates that as the VPN changes from 15 to 16, the values become more concentrated around a value closer to the mean of data for each VPN. This indicates that the traced shock is more stable at position number 16.

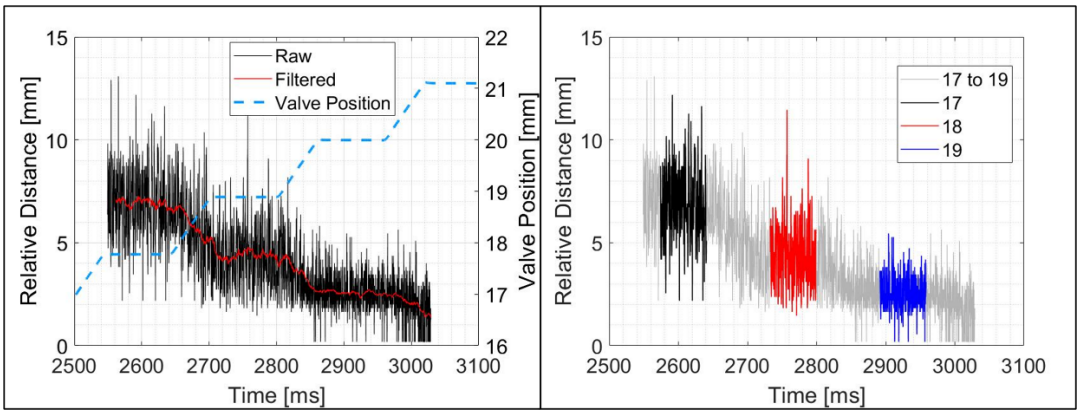


Figure 3-40. Calculated distances using tracer line 2 and corresponding valve positions for Mach = 2.63 with bleed (Test 4340).

Figure 3-40 indicates a decrease in the amplitude of oscillations from VPN 17 to 19. Generated histogram plots using the data presented in Figure 3-40 for VPNs 17 to 19 are given in Figure 3-41.

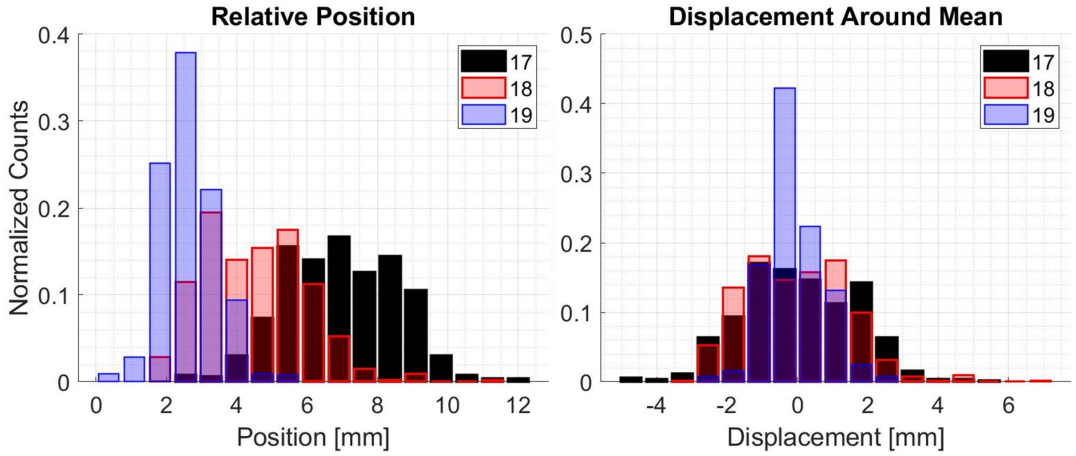


Figure 3-41. Histogram plots for VPNs 17 to 19 (Mach = 2.63, with bleed, Test 4340).

Upon analyzing the plot on the left side of Figure 3-41, it is observed that as the valve position increases, the distribution of positions shifts upstream. Additionally, for VPN 19, the values are more tightly clustered around a mean value. This indicates that the traced shock is more stable at position number 19. It is noteworthy that the distribution around the mean values for VPNs 17 and 18 are similar.

During the oscillations, conceptually similar changes of the shock structures are to the ones obtained with Test 4331 are observed at VPNs 13, 14, 15,17 and 18 and they are given in the Appendix B. However, maximum amount of displacement during the oscillations are different. Figure 3-42, Figure 3-43 and Figure 3-44 illustrates the comparison between the positions of the pseudo-shock at its most upstream and downstream points for VPN 13, 14 and 15 respectively. The distance between these two points, which is represented by the horizontal line, is measured to be 8.5, 8.1 and 7 mm, respectively.

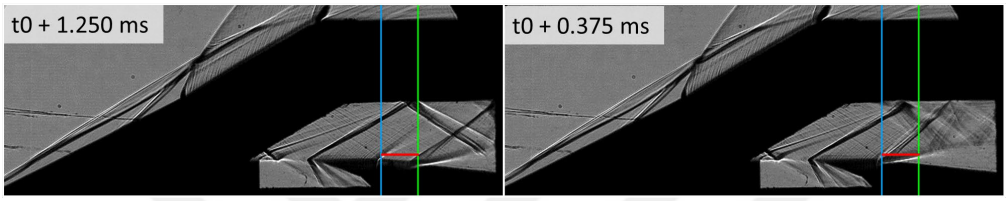


Figure 3-42. Comparison of shock positions at VPN 13 for Mach = 2.63 with bleed (Test 4340).

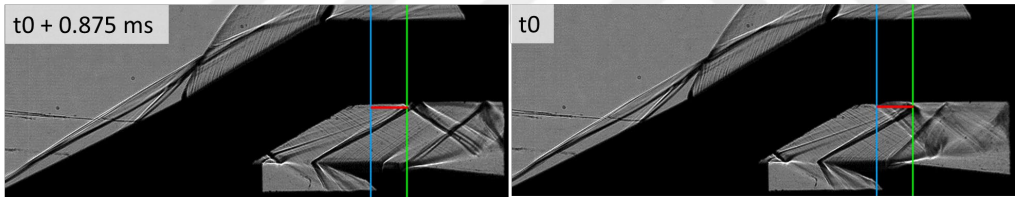


Figure 3-43. Comparison of shock positions at VPN 14 for Mach = 2.63 with bleed (Test 4340).

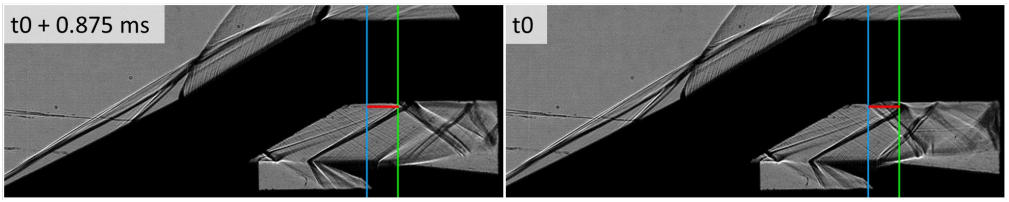


Figure 3-44. Comparison of shock positions at VPN 15 for Mach = 2.63 with bleed (Test 4340).

The oscillation pattern for VPN 16 is given Figure 3-45. The main noticeable feature of the pattern is that between t0 and t0 + 0.75 ms, as the pseudo-shock structure moves upstream and the separation bubble on the cowl side thickens, the sonic line

on the cowl side tends to detach while the one on the ramp side tends to attach. Then, after t0 + 0.75 ms, as the pseudo-shock moves downstream, these tendencies disappear and the flow structure returns to a similar state as at t0. It is worth to highlight that a significant and abrupt change in the shock structures occurs when transitioning from VPN 16 to VPN 17. At this point, the shock-train part undergoes a sudden and pronounced shift in its orientation, transitioning from the cowl side to the ramp side.

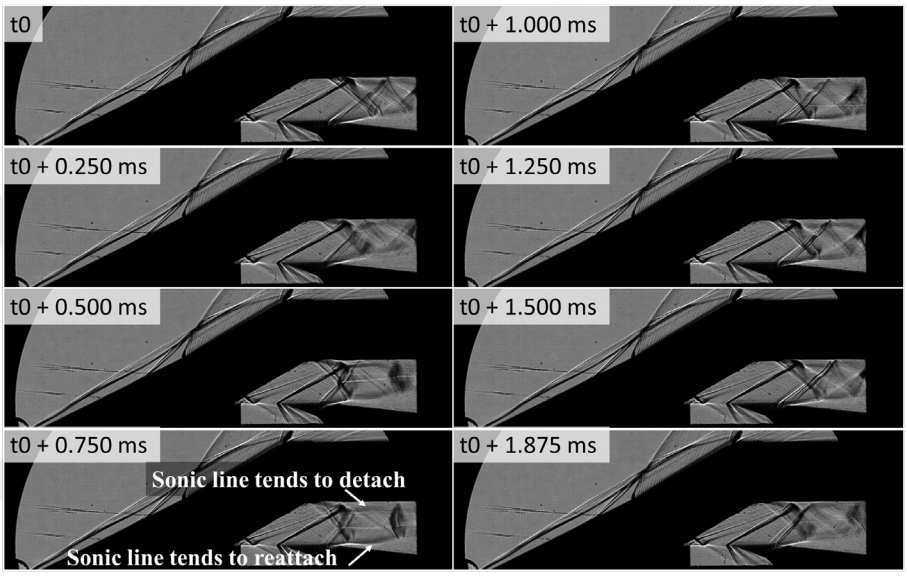


Figure 3-45. Oscillation of shock patterns at VPN 16 for Mach = 2.63 with bleed (Test 4340).

The comparison of the most upstream and downstream positions of the pseudo-shock for position number 16 is presented in Figure 3-46. The measured distance between these two points is 4.4 mm, which is smaller than the values obtained for VPNs 14 and 15.

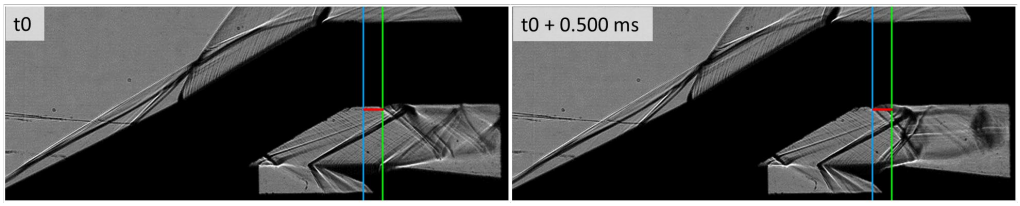


Figure 3-46. Comparison of shock positions at VPN 16 for Mach = 2.63 with bleed (Test 4340).

At VPN 17, leading shock of the pseudo-shock changes its structure from X-type to λ-type and then returns to X-type. As the shock structures move upstream the formation of a Mach stem and λ-type shock structure is observed. When the tail of the C3 shock intersects with the high angle (7 degrees) part of the diffuser, the formation of an X-type shock is observed, while its intersection with the lower angle (1 degrees) part leads to a λ-type structure. Similar observations are made for VPN 18 in Test 4331 (see Figure 3-21). The most upstream and downstream positions of the pseudo-shock are compared in Figure 3-47 for position number 17. The distance between these two points is found to be 6.7 mm.

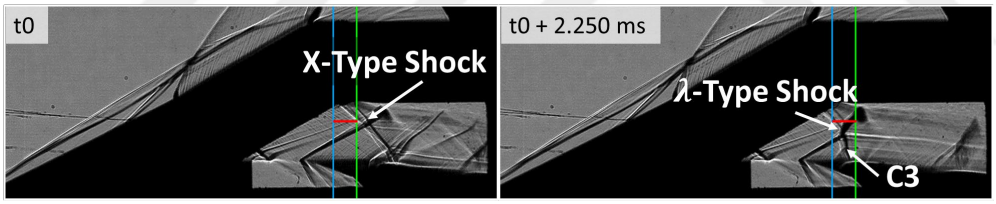


Figure 3-47. Comparison of shock positions at VPN 17 for Mach = 2.63 with bleed (Test 4340).

Oscillation pattern at VPN 18, to the one observed at VPN 17. However, the Mach stem observed for VPN 18 is wider than the one observed for VPN 17, as can be visually compared in Figure 3-48. The comparison of the most upstream and downstream positions of the pseudo-shock for position number 18 is presented in Figure 3-49. The measured distance between these two points is 8.4 mm, which is higher than the calculated values for the position number 17.

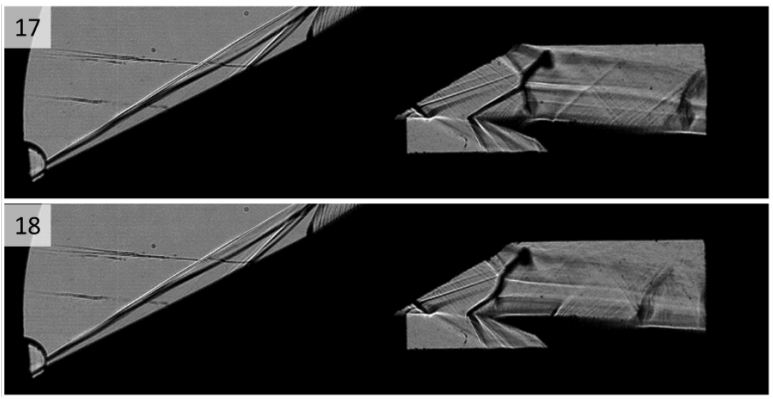


Figure 3-48. Comparison of Mach stems at VPNs 17 and 18 for Mach = 2.63 with bleed (Test 4340).

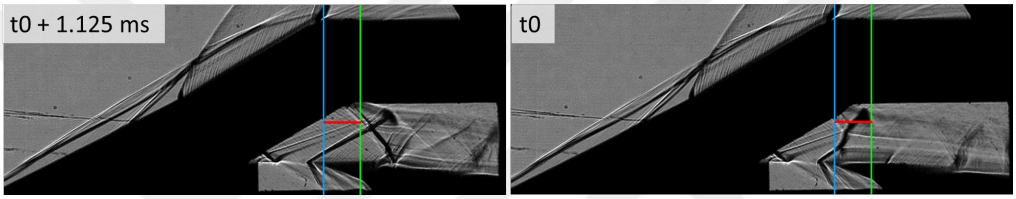


Figure 3-49. Comparison of shock positions at VPN 18 for Mach = 2.63 with bleed (Test 4340).

The shock oscillation pattern for VPN 19 is presented in Figure 3-50. The pseudo-shock at its relatively upstream position at t0 and then moves downstream until t0 + 1.125 ms. It then moves upstream again and reaches its most upstream position at t0 + 2.25 ms. During this motion, Slip Line 2 (shown in the figure) disappears and the C3, C5 shocks and the bleed wedge shock merge. The tail of the resulting shock hits the front edge of the bleed wedge, forming a new shock structure. As a result, the C3 shock no longer hits the ramp side surface, and there is no thickening or separation of the boundary layer, as evidenced by the disappearance of the sonic line.

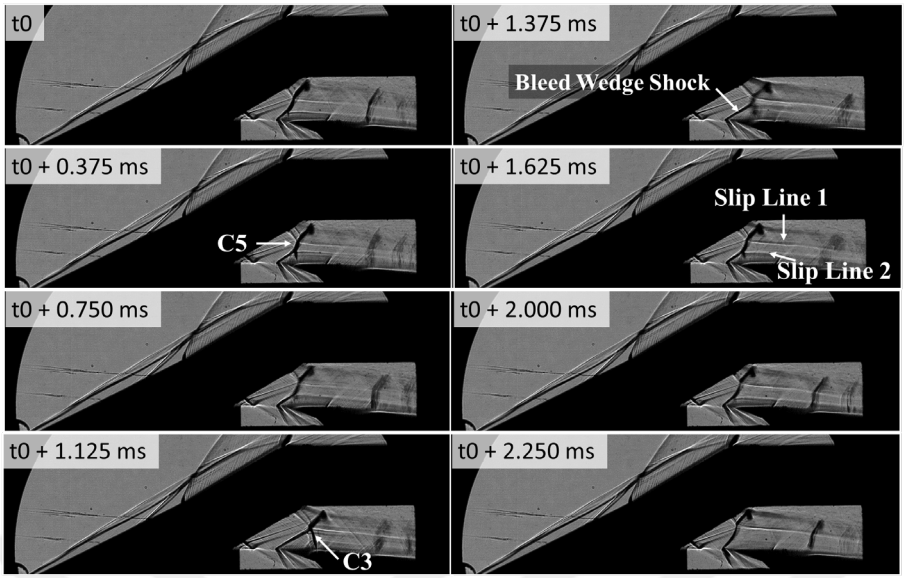


Figure 3-50. Oscillation of shock patterns at VPN 19 for Mach = 2.63 with bleed (Test 4340).

Figure 3-51 displays the comparison of the most upstream and downstream positions of the pseudo-shock for position number 19. The measured distance between these two points is 5.6 mm, which is less than the calculated values for the position number 18. In addition, at t0 + 2.25 ms, a very short-lived alteration in the flow structure within the bleed channel is observed, indicating a possible shift in the intake's mode of operation from supercritical to critical or subcritical.

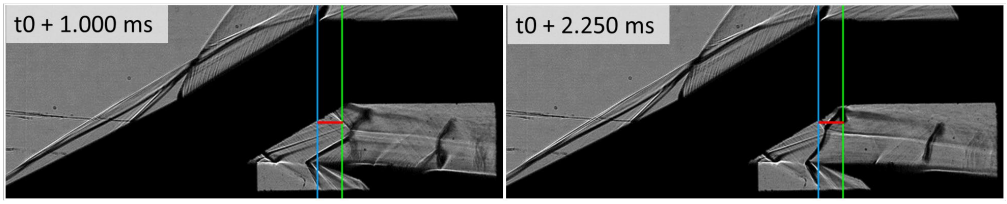


Figure 3-51. Comparison of shock positions at VPN 19 for Mach = 2.63 with bleed (Test 4340).

Valve position 20 did not produce a suitable point for any oscillating shock structure using the algorithm. Therefore, the images are examined visually, and a relatively small change in position is observed, as suggested by the average images. Figure 3-52 shows the images at the instant when the positions of the separation shock of

the pseudo-shock are at their most upstream and downstream points. On the left, displacement of the separation shock on the cowl side is marked and, on the right, displacement of the Mach stem portion is marked. The displacement of the Mach stem is measured along a line that intersects with the Mach stem portion of the first shock of the pseudo-shock. Calculated displacements for the separation shock and the Mach stem are 4.2 and 3.1 mm, respectively. Displacement of the Mach stem part is lower than the separation shock. Calculated displacement of the separation shock is less than the one for VPN 20. Although the shock structures are conceptually similar to the ones with VPN 19, the Mach stem is wider, and the most downstream position is relatively more upstream. The observed change in the flow structure in the bleed channel indicates a transition from supercritical to subcritical operation during the oscillations.

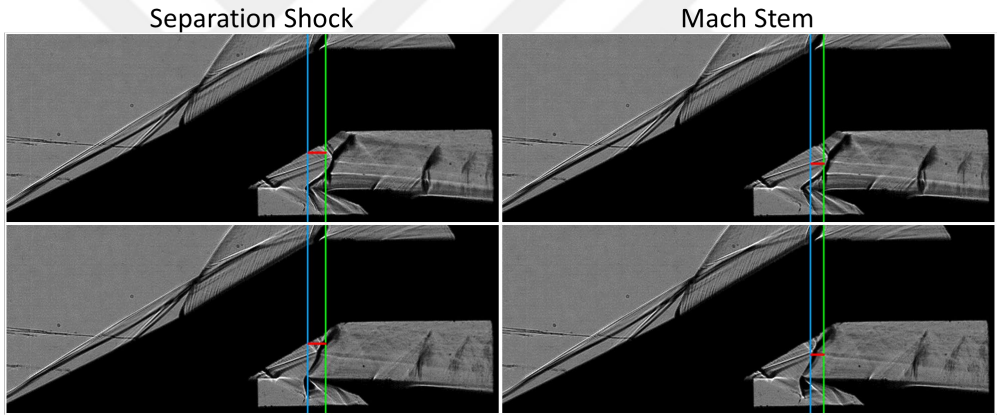


Figure 3-52. Comparison of shock positions at VPN 20 for Mach = 2.63 with bleed (Test 4340).

Figure 3-53 shows the positions of the separation shock of the pseudo-shock at its most upstream and downstream points for VPN 21. Calculated displacements for the separation shock and Mach stem part are 3.8 and 2.4 mm, respectively. The values are less than the ones obtained for VPN 20.

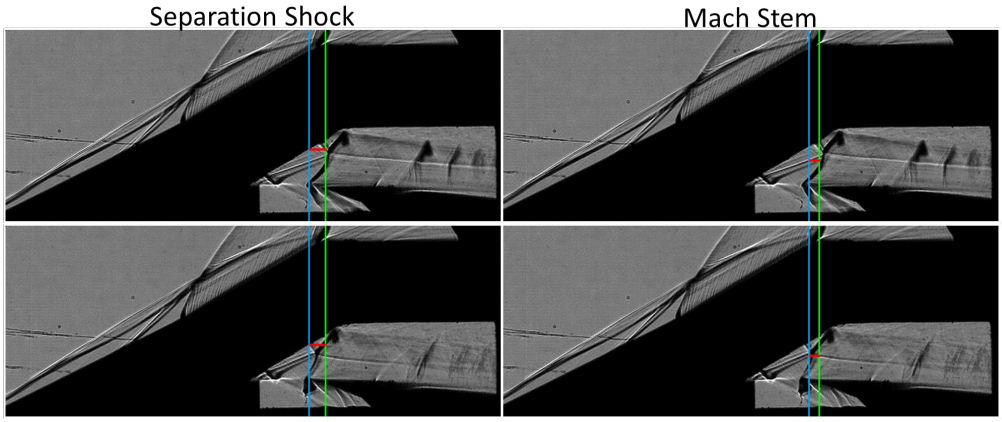


Figure 3-53. Comparison of shock positions at VPN 21 for Mach = 2.63 with bleed (Test 4340).

Table 3-2 summarizes the distances measured for the change in position of the shock point along the horizontal red lines. The results indicate that the calculated displacement decreases from VPN 13 to 16. However, there is a subsequent increase in displacement when moving from valve position 16 to 17. This change in displacement might be associated with the abrupt change in the shock structures, where the sonic line on the cowl side separates and attaches to the ramp side. After VPN 18, as the pseudo-shock structures begin to interact with the bleed region, the magnitude of the measured difference consistently decreases.

Table 3-2. Summary of changes in shock positions for Mach = 2.63 with bleed (Test 4340).

VPN	Pixel 1	Pixel 2	Difference [Pixels]	Difference [mm]	Amplitude [%]	Shock Type
13	607	560	47	8.5	29	X
14	585	540	45	8.1	28	X
15	580	541	39	7.1	24	X
16	559	535	24	4.4	15	X
17	541	504	37	6.7	23	X
18	533	487	46	8.4	29	X and λ
19	512	481	31	5.6	19	λ
20	492	469	23	4.2	14	λ
21	489	468	21	3.8	13	λ

Comparison of instantaneous images for the shock positions of various VPNs are presented in Figure 3-54 and Figure 3-55. On the left side of each figure, the position of the first shock of the pseudo-shock related shock structures is at the most downstream, and on the right side, it is at the most upstream during the oscillation cycle of interest. The figures indicate that as the VPN increases, both the most upstream and most downstream shock structures shift upstream.

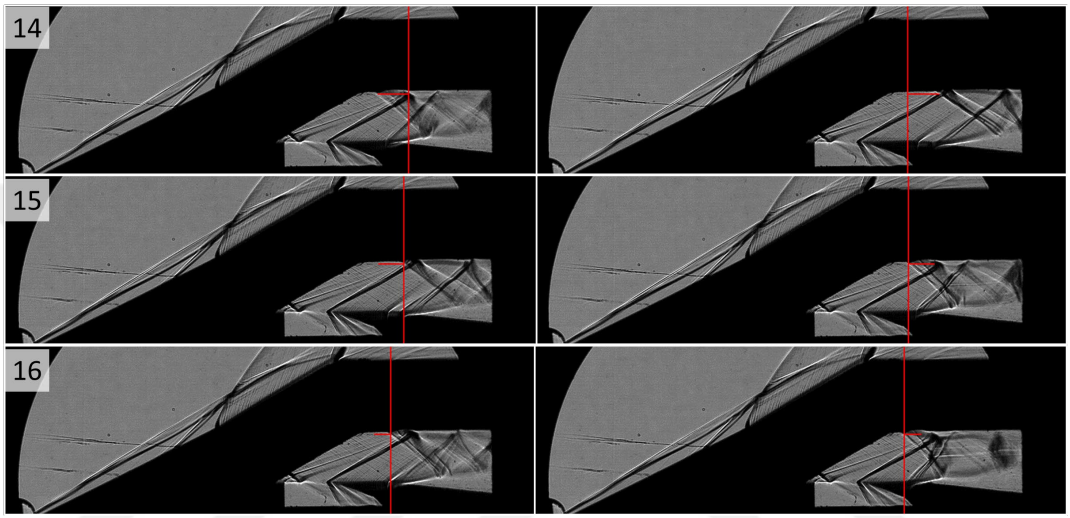


Figure 3-54. Comparison of shock positions at VPNs 14, 15 and 16 for Mach = 2.63 with bleed (Test 4340).

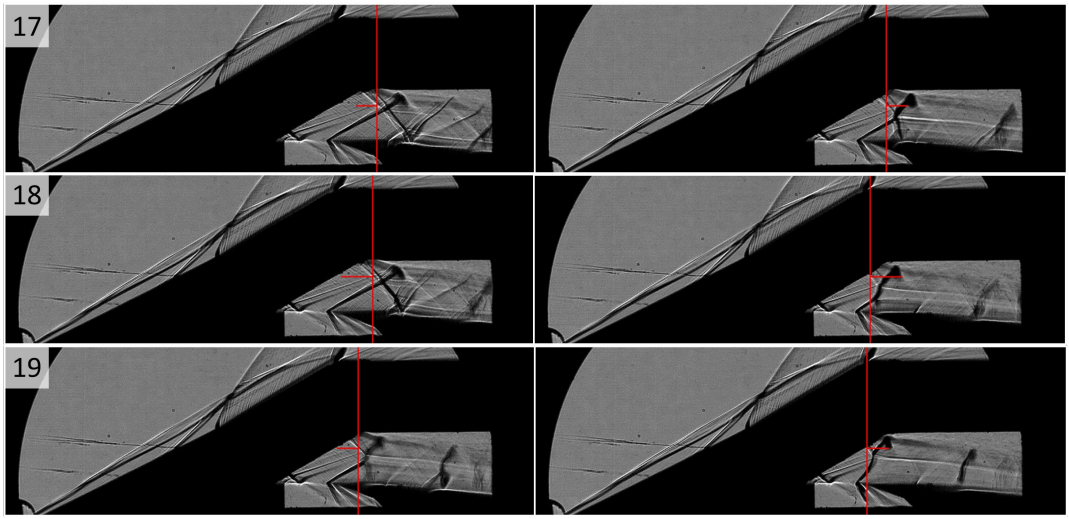


Figure 3-55. Comparison of shock positions at VPNs 17, 18 and 19 for Mach = 2.63 with bleed (Test 4340).

3.1.3 Mach = 3 without Bleed (Test 4372)

3.1.3.1 Average Images

The average images for Test 4372 at various valve positions are given in Figure 3-56 and Figure 3-57. Until valve position 11, no significant changes are observed at between the preceding VPNs. At valve position 11, the effects of back pressure become visible through the shadowgraph window of the test item. Test 4372 differs from tests 4331 and 4340 in that the air intake test item does not involve a bleed. Consequently, even before the effects of the pseudo-shock are observed, distinct shock structures are noticeable in Test 4372 as compared to those observed in tests with a bleed.

In contrast to the tests with bleed, in Test 4372, the cowl shock directly hits the surface on the ramp side leading to the formation of a separation bubble, which causes two additional shock structures to appear. The first one is the reattachment shock, observed due to the reattachment of the separation shock, and the second one is the formation of an additional separation shock at the beginning of the separation bubble. However, this additional shock is not visible due to the fact that the shadowgraph window does not cover that area, but the reflection of the separation shock can be seen through the window.

As the valve proceeds, the back pressure causes separation and separation shock on the cowl side, which is first observed at VPN 11. As the VPN increases, the separation shock on the cowl side moves monotonically upstream, and the blurry region also travels upstream. When the VPN changes from 15 to 16, the sharpness of the reflection of the separation shock fades a little, indicating that the shock starts to oscillate. Additionally, as the position number changes from 16 to 17, the shock completely disappears. Furthermore, the reattachment shock starts to fade.

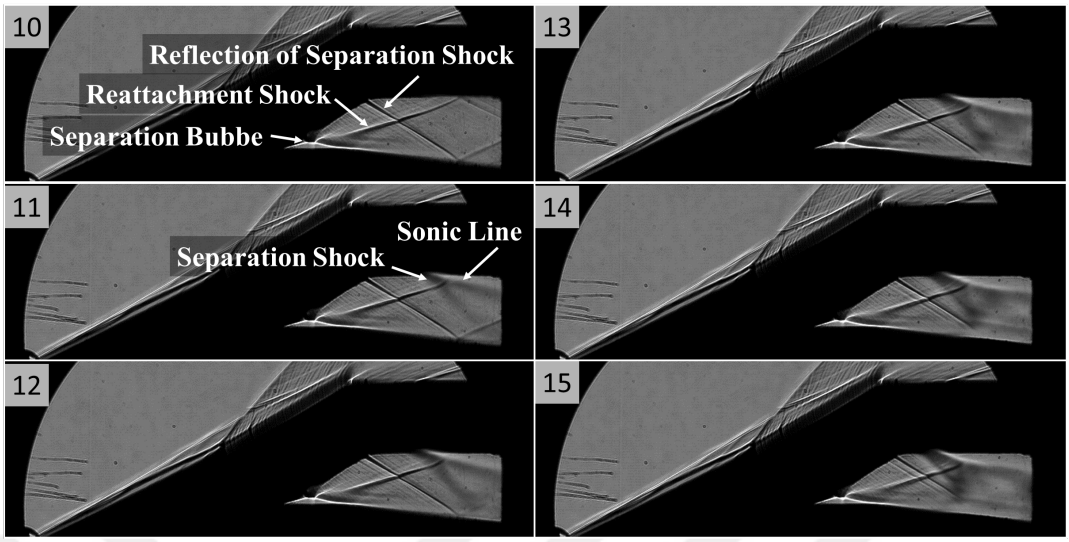


Figure 3-56. Average images for Mach = 3 without bleed (Test 4372) at VPNs 11 to 15.

At VPN 18, both the reattachment shock and the reflection of the separation shock disappear, and a detached sonic line on the ramp side is visible. At VPN 18, a flow structure similar to position 17 is observed, but with a separation shock of the pseudo-shock on the cowl side slightly upstream. All of the observations discussed above suggest that as the valve position changes from 15 to 18, the back pressure begins to affect the separation bubble formed by the cowl shock. As a result, the separation bubble begins to oscillate due to the oscillatory nature of the pseudo-shock. Additionally, as the valve position increases, the starting point of the separation bubble moves upstream due to the influence of the back pressure. Consequently, the separation point moves upstream along with its associated separation shock, and it is no longer visible within the edges of the shadowgraph window. Upon reaching VPN 20, there is a significant change in the orientation of the shock-train, and a fully detached sonic line is observed on the ramp side.

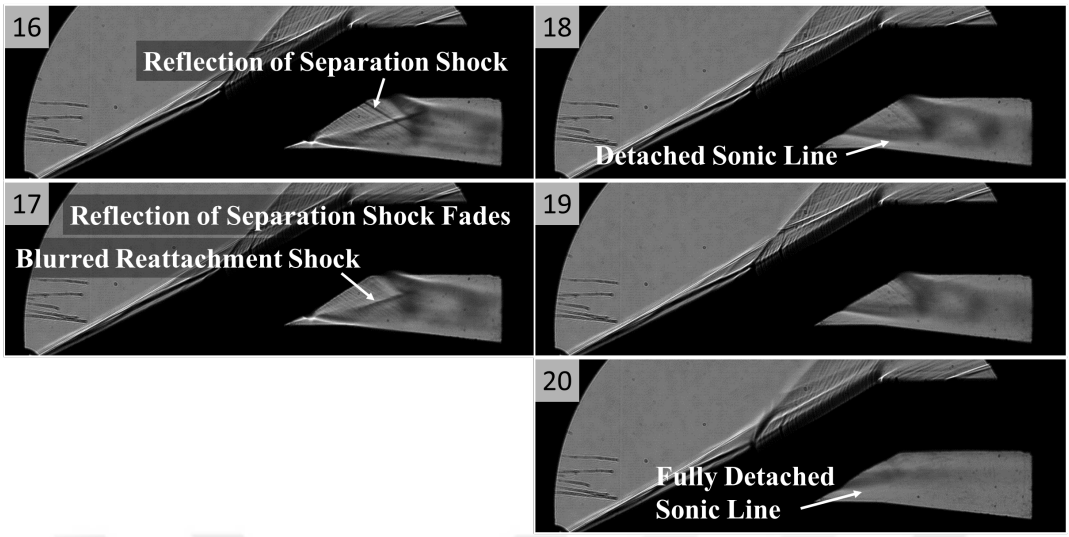


Figure 3-57. Average images for Mach = 3 without bleed (Test 4372) at VPNs 16 to 19.

Examination of the average images reveals that there are significant changes in between VPNs 11 and 12, as well as 19 and 20.

3.1.3.2 Transitions and the Change in the Shock Structure

Figure 3-58 illustrates the changes in the valve position and shock structures over time using instantaneous images captured between VPNs 10 and 11. The images show that there are only slight changes until point c, where the separation point becomes visible. Between points c and d, there is a sudden shift in the shock structures as the separation point moves upstream over the course of 1 millisecond. It is important to note that this shift happens while the valve is in motion.

Notably, after the abrupt shift in shocks, the separation point on the cowl side approaches the point where the reattachment shock from the separation bubble caused by the cowl shock impacts. This suggests that the adverse pressure gradient of the reattachment shock has already created a location that is prone to separation, and the back pressure effect causes the separation point to suddenly move closer to that location.

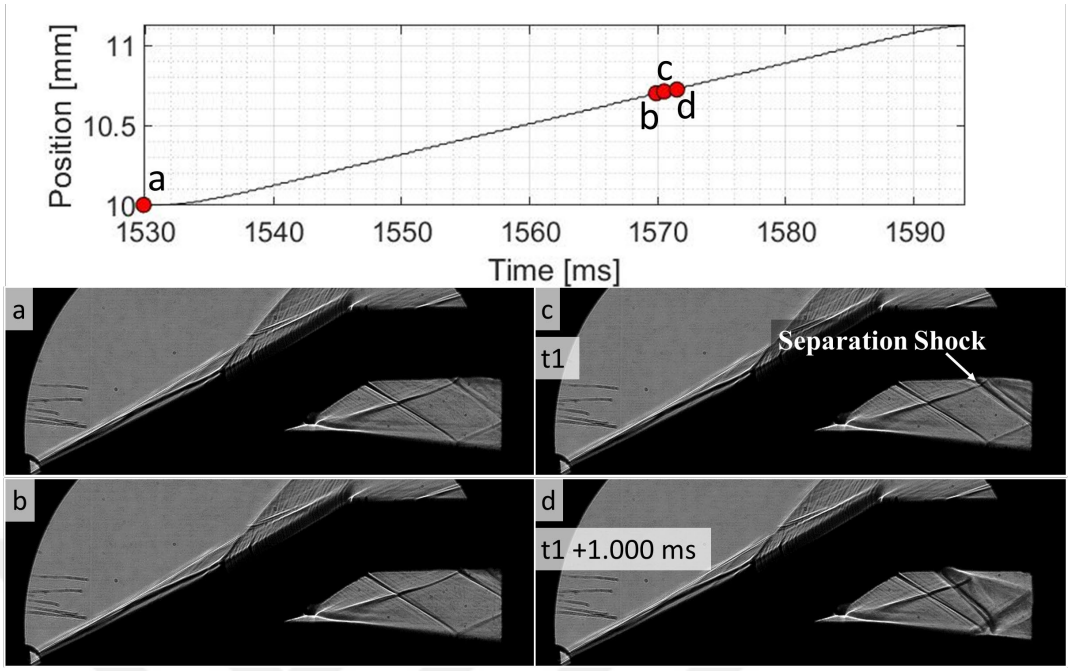


Figure 3-58. Variation of the position of the valve and change of shock structures between VPNs 10 and 11 for Mach = 3 without bleed (Test 4372).

3.1.3.3 Shock Oscillations

Figure 3-59 shows the results of the calculated relative distances using tracer lines, the interval of considered images for the dwell times, and the change in the valve position. The detected position moves upstream during the valve motion, as indicated by both the raw and moving averaged data. During the dwell time, there is oscillation around a mean value. However, for the interval corresponding to the dwell time of VPN 11, the moving averaged data shows relatively higher changes in oscillation compared to the other VPNs. Reason for this variation could not be understood.

The calculated distances between the starting point of the tracer lines and the detected shock point for each VPN, separately, are given in Appendix A.

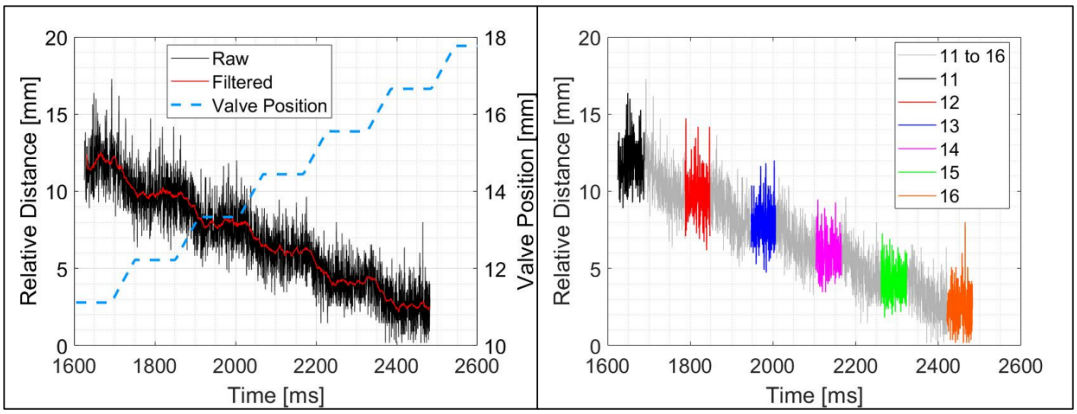


Figure 3-59. Calculated distances using tracer line and corresponding valve positions for Mach = 3 without bleed (Test 4372).

Generated histogram plots using the data presented in Figure 3-59 for VPNs 13 to 15 are given in Figure 3-60. Examination of the plot on the left side shows that as the valve position increases, the distribution of positions shifts upstream. Additionally, for VPN 15, the values are slightly more tightly clustered around a mean value.

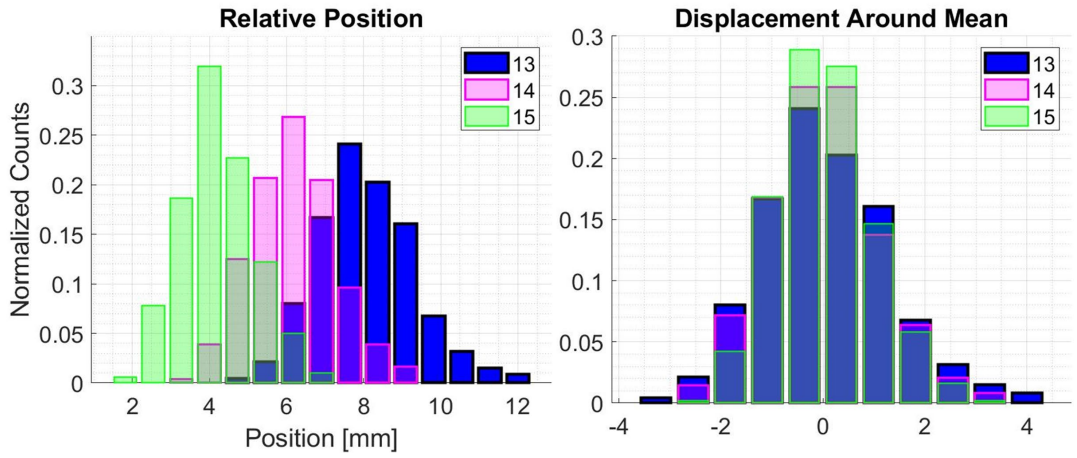


Figure 3-60. Histogram plots for VPNs 13 and 15 (Mach = 3, without bleed, Test 4372).

The oscillation pattern at VPNs 11 is presented in Figure 3-61, where the shock moves back and forth. When the shock is at its most downstream position, detached sonic line nearly attaches at t0 + 0.750 ms for position number 11. However, for position number 12, an additional separation shock on the ramp side is observed

(Figure 3-63). As the separation shock on the cowl side moves upstream, it interacts with the ramp side and forms a separation and separation shock on the ramp side. The interaction point of the shock with the ramp side corresponds to the interaction point with the reflection of the separation shock of the cowl shock, as marked on the figure. It can be inferred that the summation of the adverse pressure gradient effects of the shocks on the boundary layer leads to the observed separation and separation shock on the ramp side.

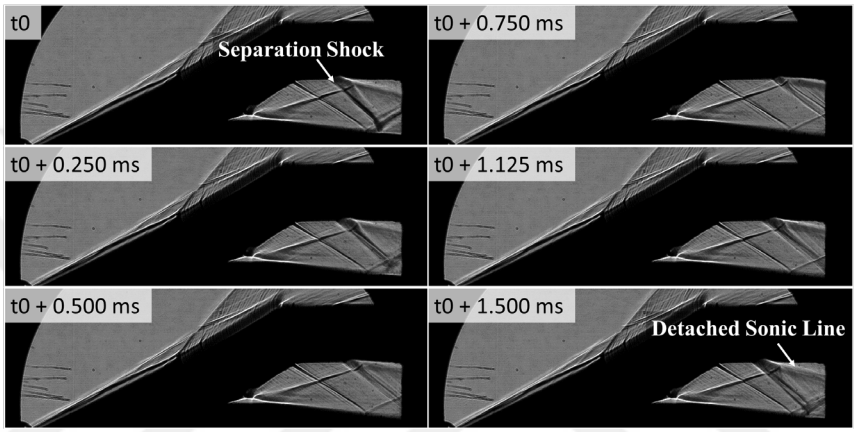


Figure 3-61. Oscillation of shock patterns at VPN 11 for Mach = 3 without bleed (Test 4372).

The comparison between the positions of the pseudo-shock at its most upstream and downstream points for VPNs 11 and 12 are depicted in Figure 3-62 and Figure 3-63, respectively. The length of the horizontal red line calculated for the position number 11 and 12 are 6.7 and 7.6 mm, respectively.

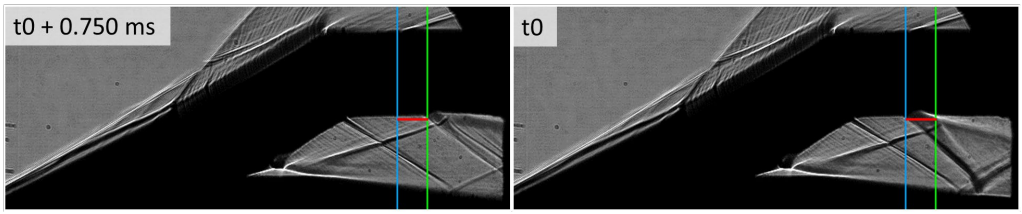


Figure 3-62. Comparison of shock positions at VPN 11 for Mach = 3 without bleed (Test 4372).

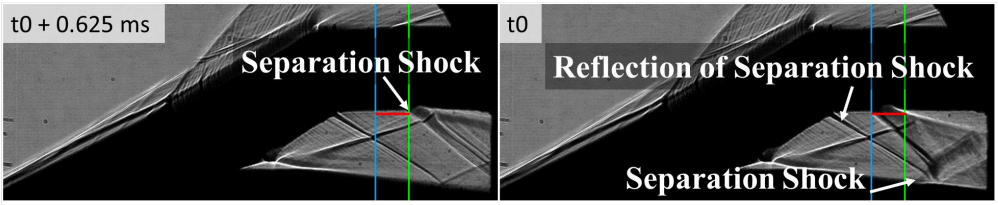


Figure 3-63. Comparison of shock positions at VPN 12 for Mach = 3 without bleed (Test 4372).

The oscillation pattern at VPN 13 is similar to VPN 12 in terms of the oscillation of the separation shock on the cowl side. However, there are some differences observed at the most upstream position of the pseudo-shock (Figure 3-64). Specifically, the formation of slip lines and a narrow Mach stem are observed for VPN 13. Additionally, the separation shock on the ramp side is located more upstream at the most upstream position of the pseudo-shock compared to VPN 12. The comparison between the positions of the pseudo-shock at its most upstream and downstream points for VPN 13 is presented in Figure 3-64. The length of the horizontal red line calculated for the position number 13 is 6.7 mm which is a similar value compared to the ones for position numbers 11 and 12.

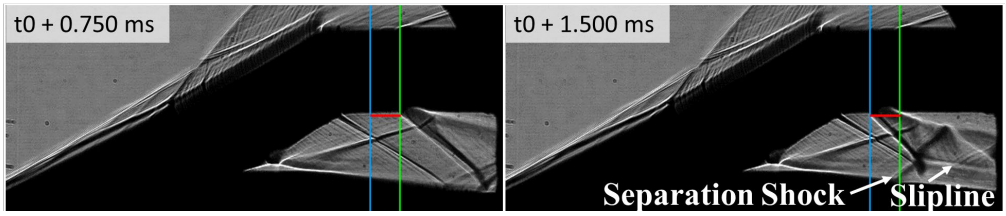


Figure 3-64. Comparison of shock positions at VPN 13 for Mach = 3 without bleed (Test 4372).

Oscillation pattern at VPN 14 shares similarities with VPNs 12 and 13 regarding the oscillation of the separation shock on the cowl side. Nevertheless, some distinctions are noticeable at the most upstream position of the pseudo-shock. The comparison between the positions of the pseudo-shock at its most upstream and downstream points for VPN 14 is presented in Figure 3-65. VPN 14 exhibits the formation of slip lines and a wider Mach stem, indicating a more pronounced formation of λ-shock structure. Additionally, the separation shock on the ramp side is situated farther

upstream at the most upstream position of the pseudo-shock compared to VPN 13. The separation shock on the cowl side starts at the initial time (t0) for VPN 13 and exhibits a structure similar to λ-shock structure. However, as the shock moves downstream and reaches its maximum point, X-type shock structures become apparent. The calculated length of the change of position of the interested point is 5.1 mm which is slightly less then the values compared to the ones for position numbers 12 and 13.

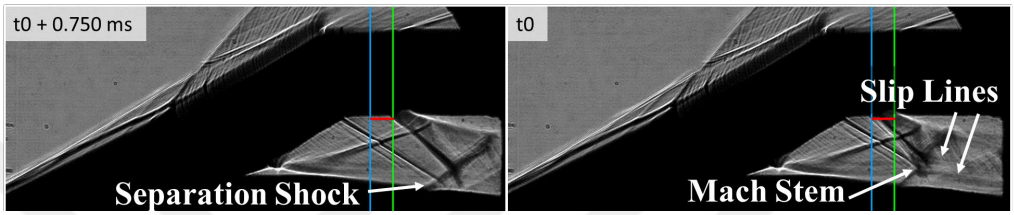


Figure 3-65. Comparison of shock positions at VPN 14 for Mach = 3 without bleed (Test 4372).

Oscillation patterns observed for VPNs 15 and 16 are very similar to each other. Figure 3-66 depicts the oscillation pattern at VPNs 15, which is different from the previous position as it does not show any transitions between X and λ-type structures. Instead, the formation of a consistent Mach stem and slip lines is observed. At t0, the shock structures are at the most upstream position. The separation shocks move downstream and reach their maximum point at t0 + 1.125 ms and then return to starting position by t0 + 1.875 ms. Figure 3-67 and Figure 3-68 compare the positions of the pseudo-shock at its most upstream and downstream points for VPNs 15 and 16. The calculated length of the horizontal red lines are 4.7 and 3.5 mm, respectively.

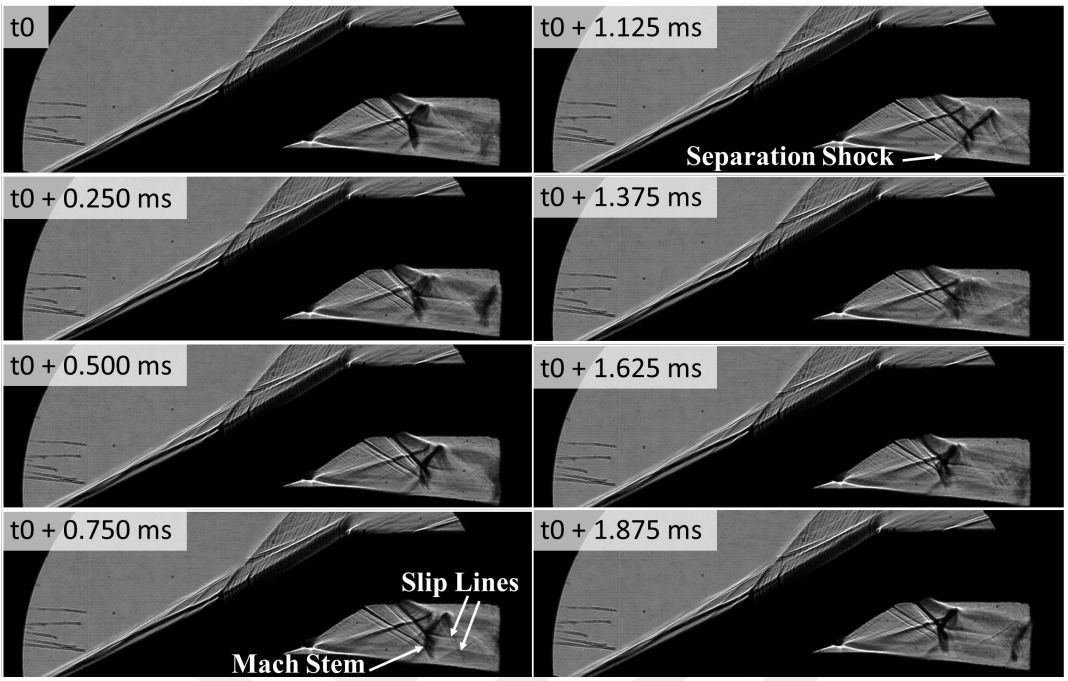


Figure 3-66. Oscillation of shock patterns at VPN 15 for Mach = 3 without bleed (Test 4372).

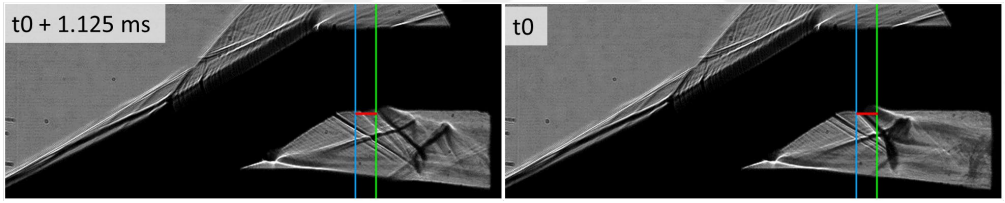


Figure 3-67. Comparison of shock positions at VPN 15 for Mach = 3 without bleed (Test 4372).

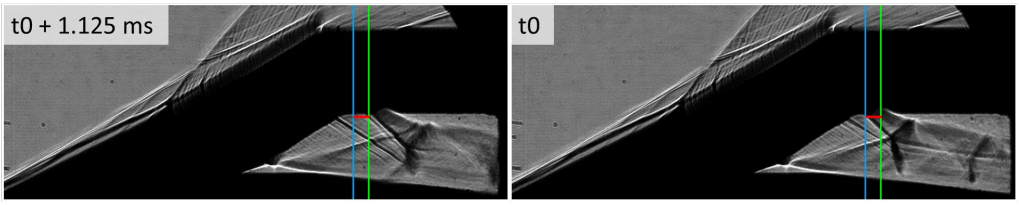


Figure 3-68. Comparison of shock positions at VPN 16 for Mach = 3 without bleed (Test 4372).

The distances measured for the change in the shock position along the horizontal red lines are summarized in Table 3-3. The data shows that the measured distances are similar for VPNs between 11 to 13. As for VPNs beyond 13, where the pseudo-shock

structures start to exhibit λ-type shock characteristics, there is a consistent decrease in the amount of oscillation.

Table 3-3. Summary of change in shock positions for Mach = 3 without bleed (Test 4372).

VPN	Pixel 1	Pixel 2	Difference [Pixels]	Difference [mm]	Amplitude [%]	Shock Type
11	627	590	37	6.7	23	X
12	617	575	42	7.6	26	X
13	600	563	37	6.7	23	X
14	587	559	28	5.1	18	X and λ
15	576	550	26	4.7	16	λ
16	564	539	25	4.5	16	λ

Figure 3-69 and Figure 3-70. Compare the measured shock positions at different valve positions. The left side of each figure shows the first shock of the pseudo-shock at the most downstream, while the right side shows it at the most upstream. Both figures demonstrate a consistent upstream shift of shock structures as the VPN increases.

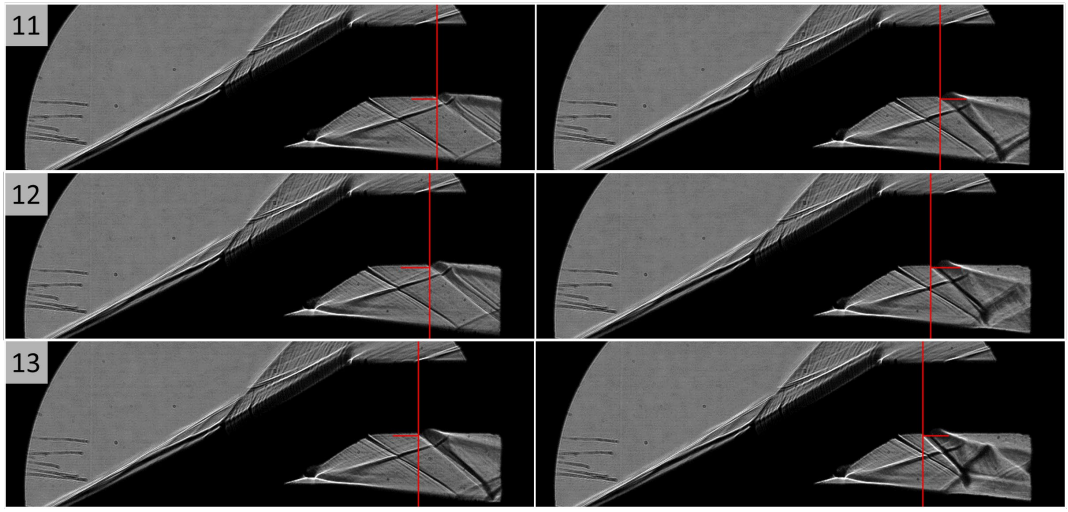


Figure 3-69. Comparison of shock positions at VPNs 11, 12 and 13 for Mach = 3 without bleed (Test 4372).

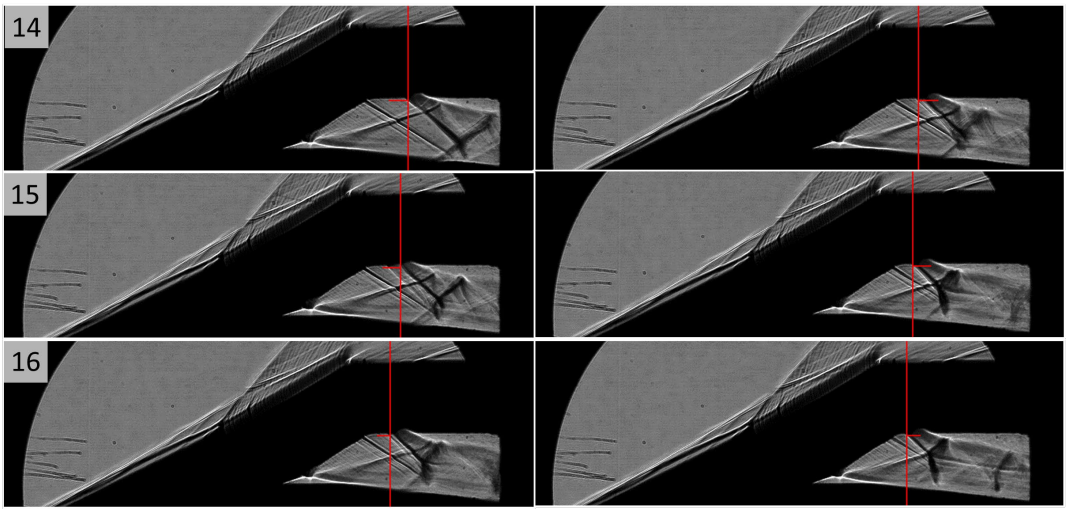


Figure 3-70. Comparison of shock positions at VPNs 14, 15 and 16 for Mach = 3 without bleed (Test 4372).

While a suitable position to trace a shock point quantitively could not be found for VPN 17, the oscillation of a separation bubble formed with the effect of cowl shock was observed visually. An oscillation pattern for this valve position is given in Figure 3-71, which shows the pseudo-shock structures at their downstream position at t0. As time proceeds to t0 + 1.5 ms, the sonic line of the separation bubble, which forms due to the cowl shock, detaches, and the detachment is clearly visible at t0 + 2 ms. Additionally, the reflection of the separation shock of the mentioned separation bubble changes its location. This suggests that back pressure affects the shape of the separation bubble and the location or angle of separation shock. Moreover, as the sonic line of the separation bubble detaches, disappearance of the slip lines is observed, and shock structures resembling X-type are seen. Finally, at t0 + 4 ms, shock structures return to downstream, sonic line attaches, and slip lines are visible again.

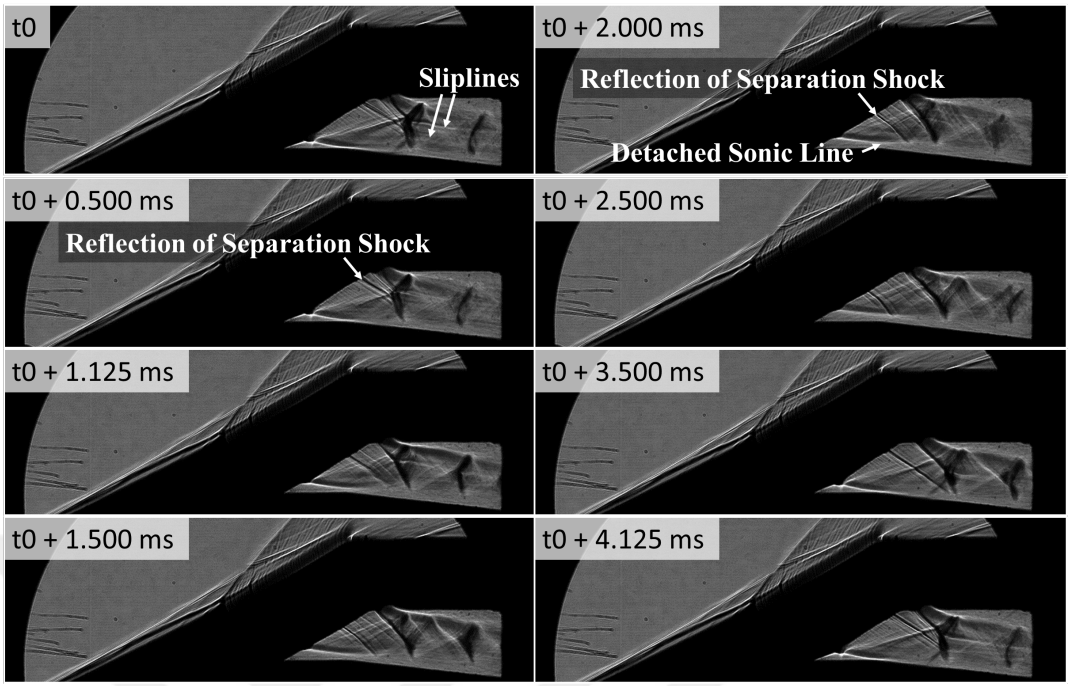


Figure 3-71. Oscillation of shock patterns at VPN 17 for Mach = 3 without bleed (Test 4372).

3.1.4 Mach = 2.63 without Bleed (Test 4373)

3.1.4.1 Average Images

The average images acquired at different VPNs for Test 4373 are displayed in Figure 3-72 and Figure 3-73. Similar structures to those seen in Test 4372, which also utilized the air intake without bleed, are observed. However, Test 4373 was conducted with a freestream flow with a lower Mach number. As a result, the location of the shocks before the pseudo-shock effects, the location of the separation bubble, and the location of the separation and reattachment shocks are different. Specifically, the reflection of the separation shock and the reattachment shock impacts the ramp surface at a more upstream position.

Until VPN 10, there are no observable changes, but at position 11, the effects of back pressure become visible through the shadowgraph window of the test item. From

positions 11 to 13, a blurry region near the right edge of the window widens upstream. At position 13 to 14, a significant change occurs where the separated sonic line on the cowl side becomes visible. Moving from positions 14 to 17, the separation point of the sonic line on the cowl side consistently moves upstream. However, at position 18, there is separation of the sonic line on the ramp side, and the sonic line on the cowl side disappears, indicating that the shock train may be attached on the cowl side. The instantaneous images will be examined in the following section to confirm this.

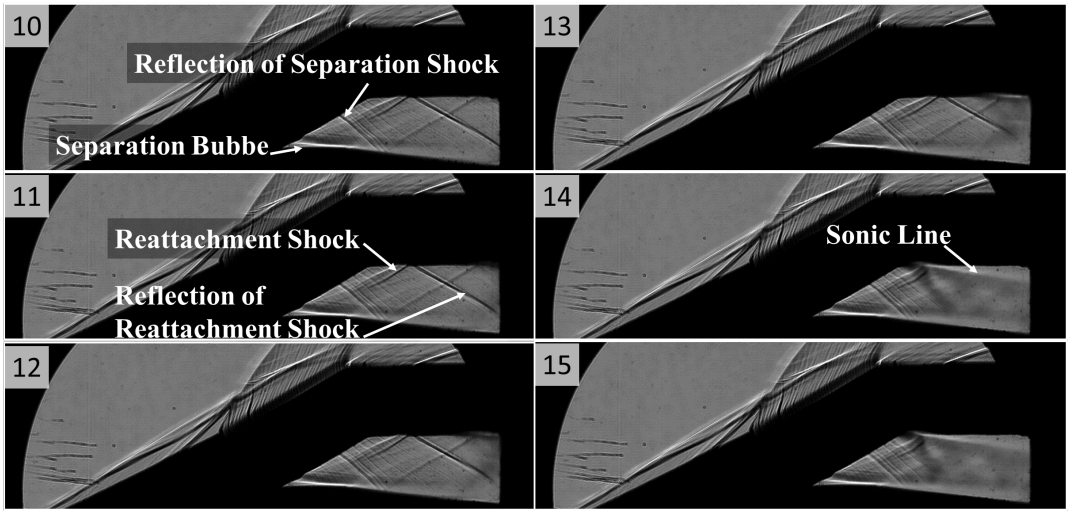


Figure 3-72. Average images for Mach = 2.63 without bleed (Test 4373) at VPNs 10 to 15.

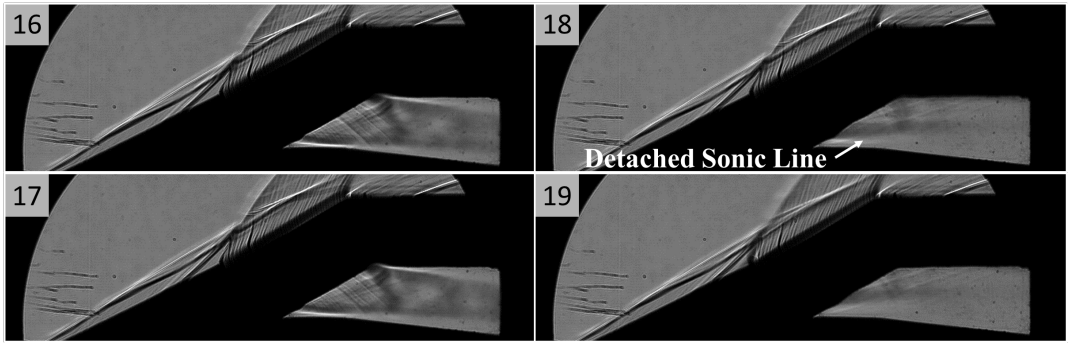


Figure 3-73. Average images for Mach = 2.63 without bleed (Test 4373) at VPNs 16 to 19.

Upon analyzing the average images, notable variations can be observed particularly between VPNs 13 and 14, as well as 17 and 18.

3.1.4.2 Transitions and the Change in the Shock Structures

Figure 3-74 illustrates the changes in valve position and shock structures over time, as captured by instantaneous images between VPNs 13 and 14. The images show that until point c, there are only slight changes in the shock structures and the separation shock on the cowl side moves upstream only slightly. However, a sudden shift occurs between points c and d, with the separation point rapidly moving upstream over a period of 2.5 ms. It is worth noting that, following the sudden shift in the shocks, the separation point on the cowl side moves close to the point of impact of the reattachment shock from the separation bubble caused by cowl shock. This suggests that the adverse pressure gradient of the reattachment shock has already established a location prone to separation, and the back pressure effect causes the separation point to move suddenly towards a point closer to that location.

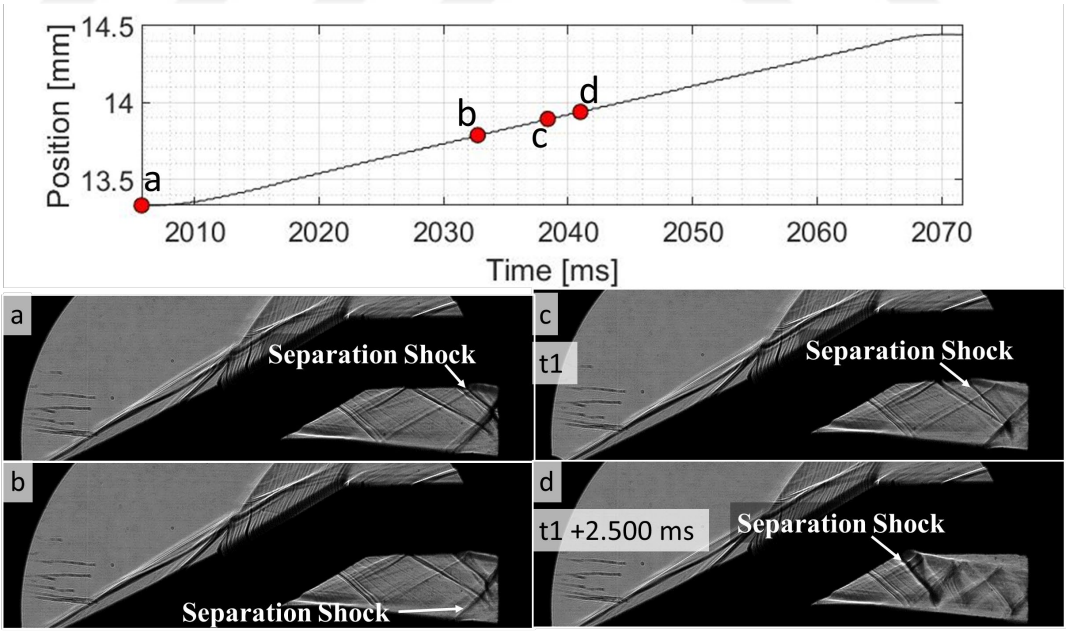


Figure 3-74. Variation of the position of the valve and change of shock structures between VPNs 13 and 14 for Mach = 2.63 without bleed (Test 4373).

Change of the shock structures with instantaneous images between point c and d is given in Appendix C.

Changes in the shock structures and the corresponding valve positions over time using the instantaneous images captured between VPNs 17 and 18 are displayed in Figure 3-75. Minor changes are observed from point a to c, where the orientation of the pseudo-shock moves slightly towards parallel to the cowl side. Additionally, the reflection of the separation shock disappears, indicating that the separation bubble formed due to the effect of the cowl shock is beginning to be affected. Nonetheless, from point c to d, a new shape and orientation of the pseudo-shock is observed. A complete detachment on the ramp side and attachment of a sonic line on the cowl side are observed, and the orientation of the pseudo-shock changes from being parallel to the ramp side to being parallel to the cowl side. Interestingly, the sudden change occurs after a quiet period following the settling of the valve position, around 18 ms, which is contrary to observations in the other tests. Change of the shock structures with instantaneous images between point c and d is given in Appendix C.

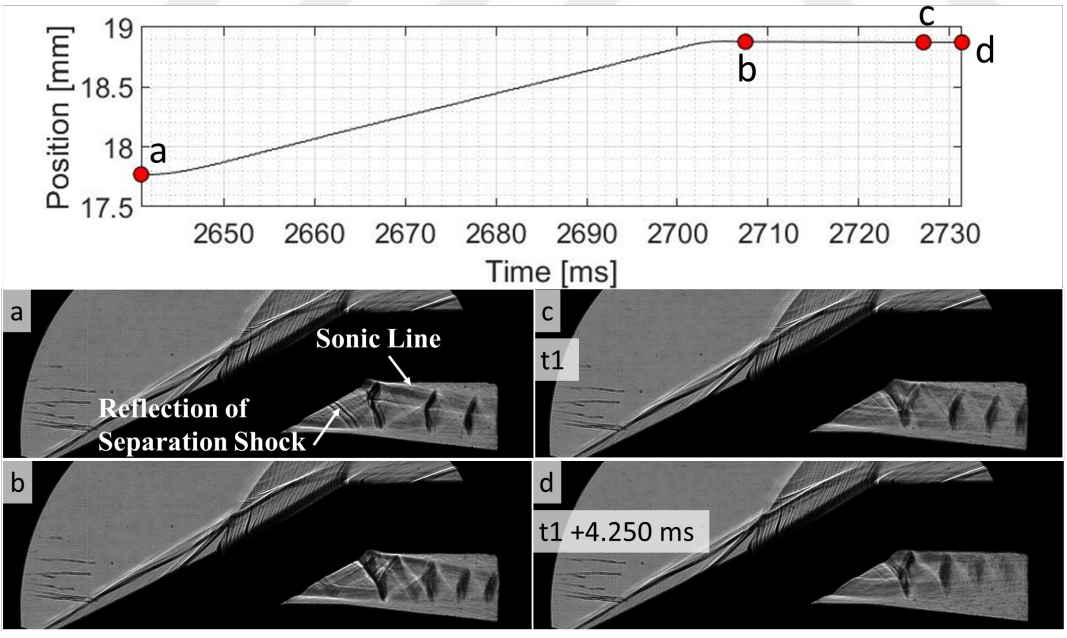


Figure 3-75. Variation of the position of the valve and change of shock structures between VPNs 17 and 18 for Mach = 2.63 without bleed (Test 4373).

3.2 Pressure Measurements

3.2.1 Overall Behavior and Repeatability Tests

Figure 3-76 and Figure 3-77 display the overall behavior of the intake during the tests by showing the change of V1 pressure, which corresponds to the static pressure at the exit of the intake. The blue vertical lines in the figures indicate the time at which the pseudo-shock structures were observed through the shadowgraph window. As shown in the figures, a monotonic increase in the exit pressure is observed as the back pressure valve closes after the formation of the pseudo-shock structures. However, high amplitude oscillations with buzzing characteristics are seen after some point. In Figure 3-76, the test item with a bleed first shows relatively small-scale oscillations after the buzzing characteristics are observed. The shadowgraph images reveal the movement of a separation shock in front of the intake during this duration, referred to as the "small buzz". As the back pressure valve proceeds, higher amplitude oscillations are seen, and the shadowgraph images show that the separation shock in front of the intake oscillates in a way that it reaches the tip of the first ramp at its most upstream position, which is referred to as the "big buzz". Sample shadowgraph images during the buzz cycles for Test 4331 are given in Appendix D.

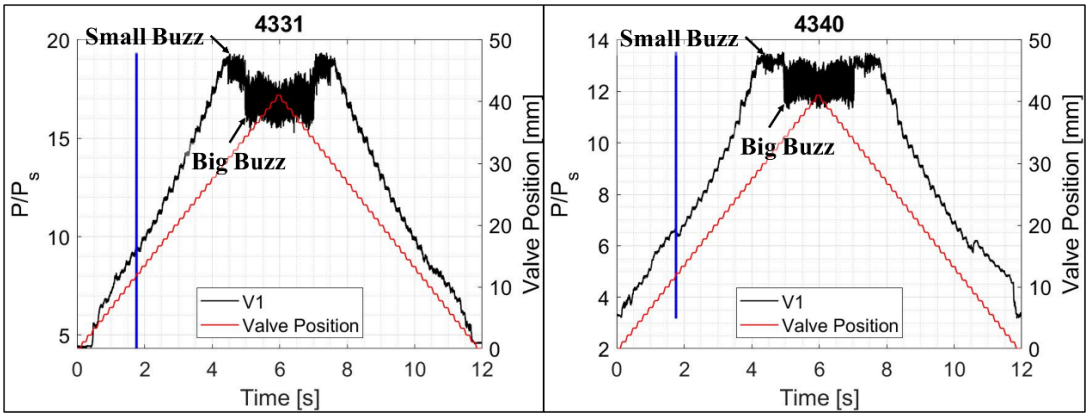


Figure 3-76. Variation of V1 pressure and valve position with respect to time for Mach = 3 (Test 4331) and for Mach = 2.63 (Test 4340) with bleed.

Figure 3-77 shows a similar pattern of behavior to Figure 3-76 between the blue line and buzz region. However, it is important to highlight that, in Test 4372, there is a sudden increase in pressure very close to the time when the pseudo-shock is first observed. This suggests that the effect of back pressure was not noticeable until that point, and the formation of the pseudo-shock was not yet observed. Only after a further throttling, did the pseudo-shock form abruptly. Upon examination of Figure 3-77 it is noted that there is abnormal behavior in the pressure data around the 6 second. This can be attributed to the formation of a separation shock at the front of the intake, which is caused by the buzzing effect. As a result, the static pressure measurement tap in the wind tunnel section is affected, leading to a short period where the calculation of the non-dimensional pressure is also affected.

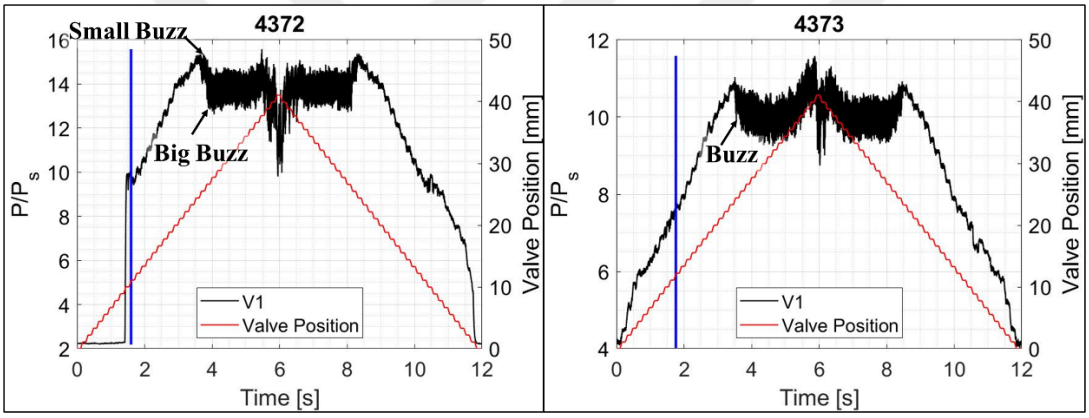


Figure 3-77. Variation of V1 pressure and valve position with respect to time for Mach = 3 (Test 4372) and for Mach = 2.63 (Test 4373) without bleed.

The repeatability tests were conducted to ensure that the test data is consistent and repeatable. Figure 3-78 presents the pressure changes at different pressure taps for Test 4331 and its corresponding repeatability test. It should be noted that the valve motion profile for the repeatability test was different from the original test, with smaller steps. Therefore, the figure is given in terms of valve position instead of time. This test also provides information about the effect of using a valve profile with smaller steps for pressure mapping. The data between the observation of the pseudo-shock and the buzzing region shows only one noticeable difference, which is marked in the figure. This difference occurs because the repeatability test had an additional

valve position due to the smaller valve steps, allowing for measurements at intermediate valve positions. Examining the results in terms of VPN provides insights into this reasoning, as the comparison is done for the same valve positions, and it is given in Figure 3-79. The data indicates that there is only one noticeable difference between the two tests, occurring at position number 32 during the transition between small buzz and big buzz. It can be inferred that differences in the valve position profile intervals may affect the buzzing phenomena and result in slight variations. However, since the focus of the study is on the operational points before the buzzing, the tests are considered repeatable.

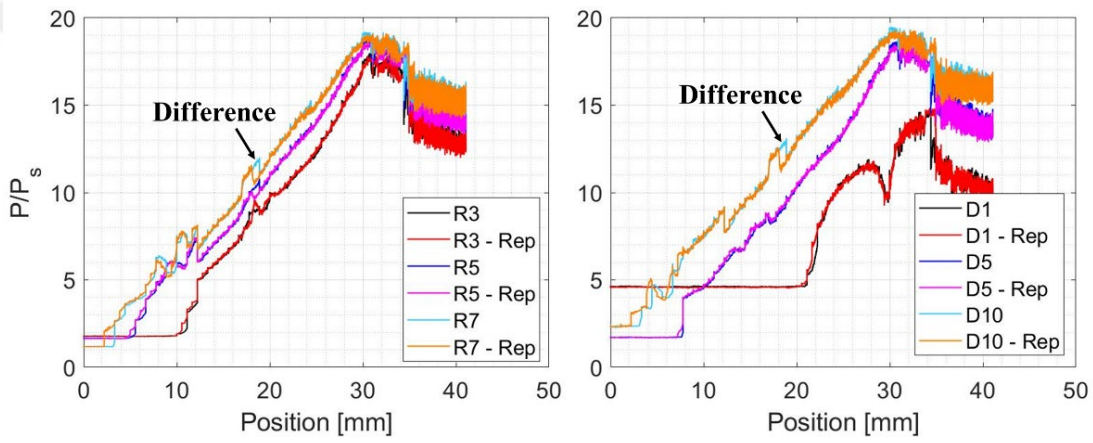


Figure 3-78. Variation of pressures with respect to valve position for Mach = 3, with bleed (Test 4331 and 4331-rep).

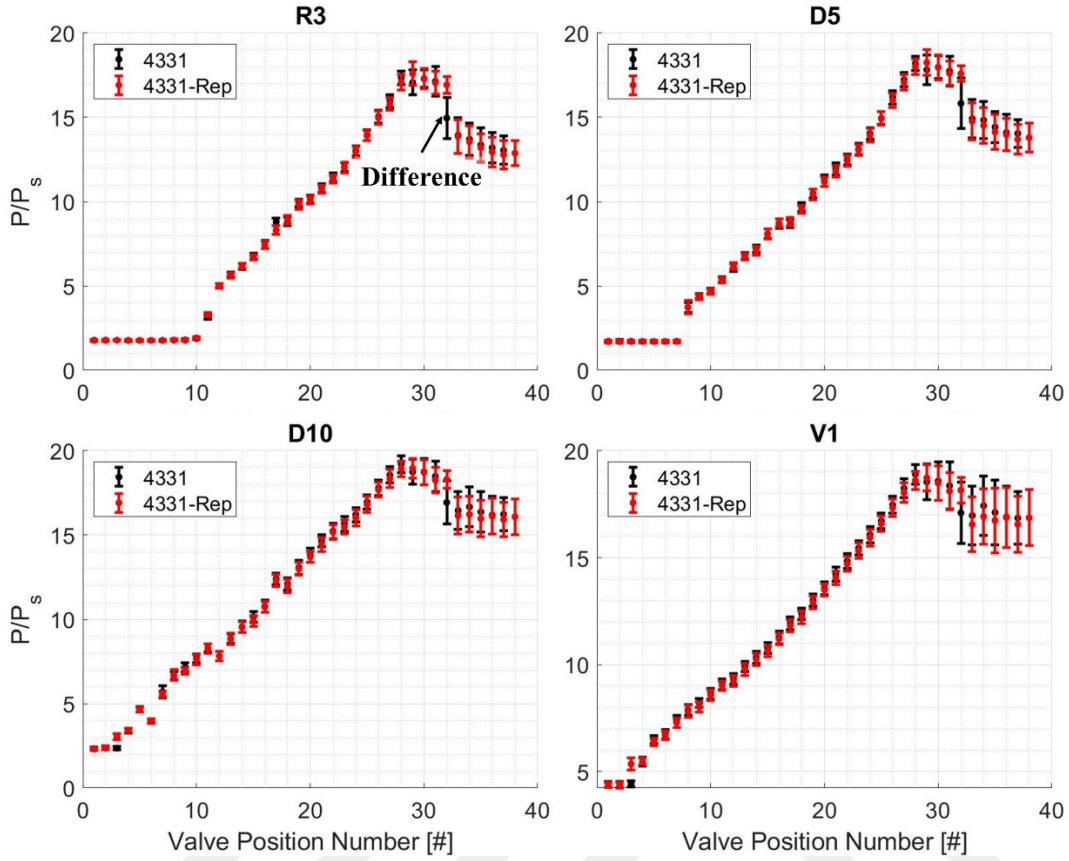


Figure 3-79. Variation of pressure with respect to VPN for Mach = 3, with bleed (Test 4331 and 4331-rep).

Appendix E contains a comparison of the other tests with their respective repeatability tests. It is concluded that the tests are repeatable, especially after the interval at which the pseudo-shock is observed in the shadowgraph images.

3.2.2 Change of Pressure Along the Intake and Hysteresis

3.2.2.1 Mach = 3 with Bleed (Test 4331)

3.2.2.1.1 Change of Pressure Along the Intake

The variation of pressure along the intake for Test 4331, at VPNs between 1 and 9 are given in Appendix F. Figure 3-80 shows the pressure variation along the intake

at the VPNs 9-13. The names of the measurement taps are indicated on the plots, with V1 and V13 being the measurements taken at the exit of the intake on the measurement pipe section. The position of pressure taps is measured with respect to the tip of the ramp in the longitudinal axis of the intake. The starting point of the pressure rise due to the pseudo-shock moves upstream as the valve progresses, with V1 and V13 also showing consistent increases. It should be noted that pressure at R2 is not expected to change until buzzing due to its location on the second ramp. At VPN 12, there is a significant change in the pressure profile on both the cowl and ramp side. The zig-zag pattern on the ramp side transforms into a monotonically increasing profile, while the monotonically increasing profile on the cowl side starts to show a zig-zag pattern. This transition is also associated with the appearance of the pseudo-shock, as shown in Figure 3-4. The separation of the sonic line occurs on the ramp side, and the attachment of it occurs on the cowl side. When the pseudo-shock structures are attached to a wall, shock-train part of it might lead a fluctuating pattern in the pressure variation on the wall(See Section 1.3.2). Gradual changes in pressure are seen on the side at which sonic line is separated. While the pseudo-shock structures at VPN 11 were not visible through the shadowgraph window, images for VPN 12 show that there is separation of the sonic line on the ramp side. Although the transition from position 11 to 12 results in decreasing pressure at the most downstream points on the diffuser section (R7 and D10), the pressure at the exit of the air intake increases. This suggests that the compression achieved through the diffuser with the newly formed shock structure at VPN 12 is less than the shock structure that occurred at VPN 11.

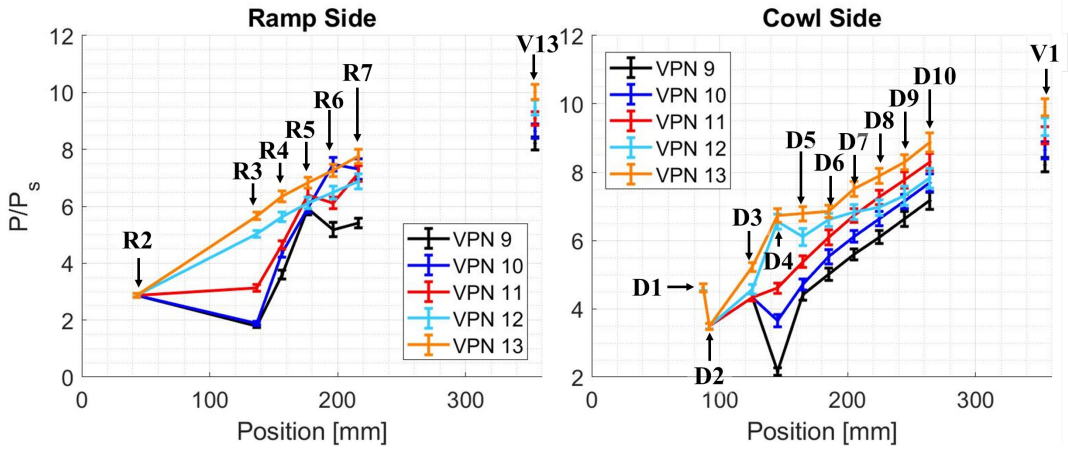


Figure 3-80. Change of pressure along the intake at VPNs between 9 and 13 for Mach = 3 with bleed (Test 4331).

Figure 3-81 shows the pressure changes along the intake at VPNs 14-18. Gradual pressure increase is seen until VPN 16 across all the taps, except for R2, D1, and D2. The pseudo-shock related separation occurs downstream of D2. When the VPN changes from 16 to 17, there is a sudden change in the pressure profile on both the ramp and cowl sides. This change is characterized by the appearance of zig-zag patterns on both sides. Additionally, there is a relatively higher increase in pressure at the downstream pressure taps, R5-R7 and D6-D10, compared to the previous transitions. Another change of profile is observed when moving from position 17 to 18. According to the shadowgraph images in Figure 3-6 and Figure 3-8, the shock train part of the pseudo-shock structure is attached to both the ramp and cowl sides at position 17, but detaches from the cowl side at position 18. Furthermore, at position 17, contrary to the position number 18, the pressure measured at D10 is higher than at the exit of the intake, suggesting that a shorter pseudo-shock structure is formed at lower throttle conditions, which is capable of compressing the flow over a shorter length. Additionally, even though back throttling increases from position 17 to 18, there is a drop in pressure at D10 and a slight reduction in pressure at R7. This indicates that although back throttling increases, the pseudo-shock still compresses the flow over a longer distance. Thus, observations imply that pseudo-shock structure attached or reattached on both ramp and cowl side is capable of compressing the flow in a shorter distance.

Upon transitioning from VPN 17 to 18, while the flow is separated on the cowl side and the pseudo-shock is attached on the ramp side, the zig-zag pattern on the ramp side is absent. This observation can be attributed to two possible reasons. Firstly, the shadowgraph images at position 18 reveal that the first shocks of the pseudo-shock exhibit λ-type shock characteristics, might have a shorter shock-train region. Secondly, the pressure measurement at D2 tap at position 18 also starts to increase, suggesting the starting point of the pseudo-shock moves upstream. As a result, the shock-train region may have already completed its existence until the first pressure measurement point on the ramp side of the diffuser, which is R3.

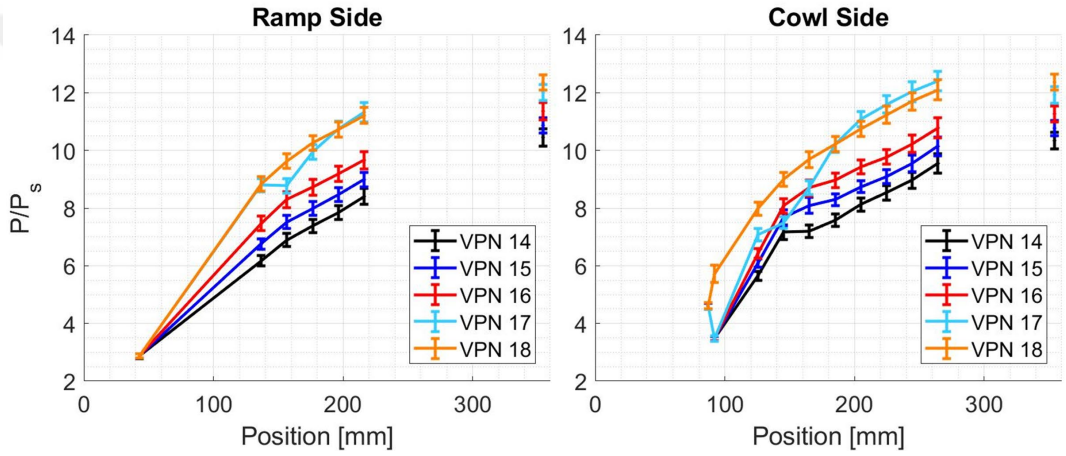


Figure 3-81. Change of pressure along the intake at VPNs between 14 and 18 for Mach = 3 with bleed (Test 4331).

The variation of the pressure along the intake at VPNs 18 to 22 is given in Figure 3-82. At position 20, the pseudo-shock also affects the D1 tap, and all pressure data within the intake monotonically increase.

Figure 3-83 shows the pressure variation along the intake for VPNs 23 to 30. Monotonic increase continues until position 27, followed by a relatively small rise from 27 to 29 and a very small rise from 29 to 30. Moreover, from position 29 onwards, the length of the error bars increases, indicating an increase in the magnitude of oscillations and indicating buzzing characteristics. As previously shown in Figure 3-76 and Figure 3-79, a small buzz occurs at position 29.

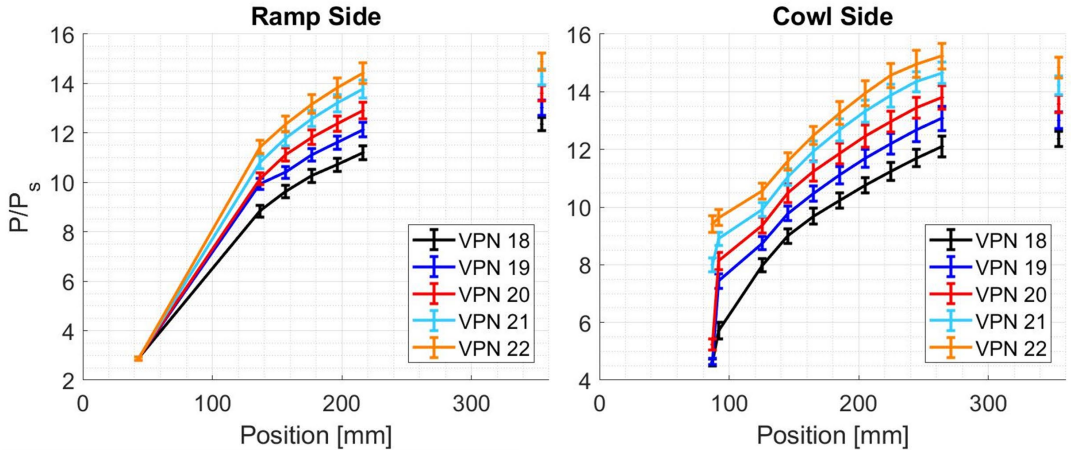


Figure 3-82. Change of pressure along the intake at VPNs between 18 and 22 for Mach = 3 with bleed (Test 4331).

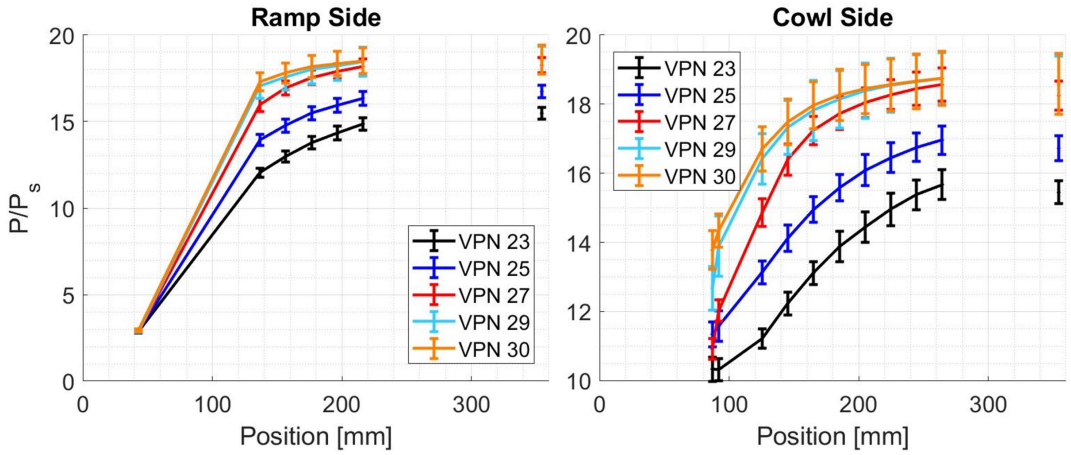


Figure 3-83. Change of pressure along the intake at VPNs between 23 and 30 for Mach = 3 with bleed (Test 4331).

3.2.2.1.2 Investigation of Hysteresis Phenomenon

An investigation into the hysteresis effect of the back pressure throttling direction involved analyzing pressure changes at different measurement points for a given VPNs during both the opening and closing phases and is given in Figure 3-84. Prior to reaching VPN 12 at which the formation of the pseudo-shock is detected in the shadowgraph images, there are several pressure measurement points where the measured pressure varies between the closing and opening phases. It is worth noting

that the effect of hysteresis on the V1 pressure tap, exit pressure, is minimal before position number 12, and it is not observed after that point. Thus, the intake experiences hysteresis effects in terms of back pressure throttling prior to the consistent formation of the terminal shock or the pseudo-shock. As discussed in section 1.3.2, the amount of back throttling required for the formation or disappearance of a terminal shock exhibits hysteresis characteristics. However, according to Figure 3-84, sudden formation of a terminal or a pseudo-shock is not observed, and instead, there is a gradual increase in the pressure. Furthermore, hysteresis is clearly evident prior to the visually observable formation of the pseudo-shock.

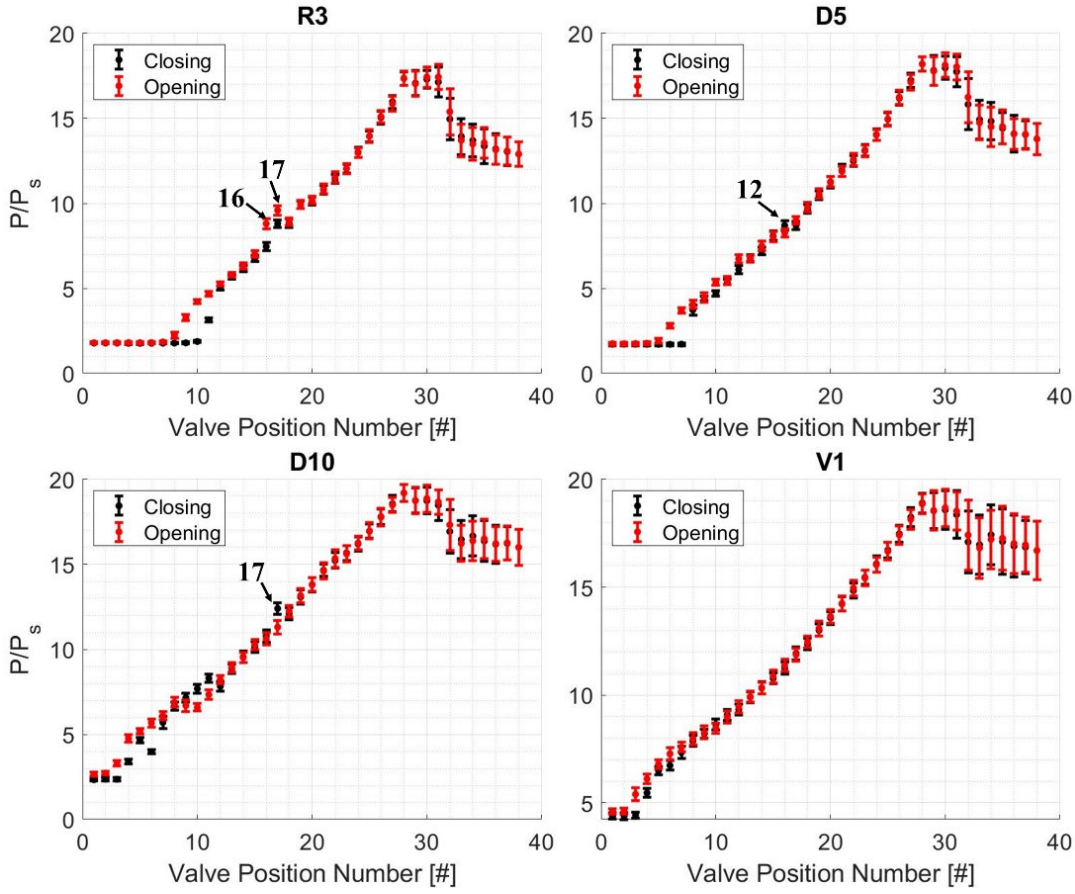


Figure 3-84. Variation of pressure with respect to VPN and comparison of throttling direction for Mach = 3 with bleed (Test 4331).

In Figure 3-84, VPNs 16 and 17 are marked as positions where the hysteresis behaviour is observed, after position 12. Consequently, the change of the pressure along the intake at VPNs 16 and 17, as well as their adjacent position numbers (15 and 18), are analyzed in the plots that display the pressure variations at these VPNs along the intake in Figure 3-85.

IN Figure 3-85, it can be observed that the measured pressure at position number 15 is nearly identical for both the closing and opening phases. However, at position number 16, some minor changes are visible, especially at the R3 tap. Figure 3-86 shows more pronounced hysteresis effects. At position number 18, the profiles for both opening and closing throttling directions are very similar, while at position number 17, the profiles are quite different. Furthermore, at both the cowl and ramp sides, the pressure measurements at the most downstream point of the diffuser are noticeably higher during opening, even though the exit pressures are almost identical. Additionally, the difference in pressure profiles between opening and closing at position number 17 exhibits similar characteristics to the change of profile observed going from position number 16 to 17, as demonstrated in Figure 3-81. Therefore, it can be inferred that the shock-train portion of the pseudo-shock is attached to both the ramp and cowl sides during the closing phase, and during the opening phase, it is separated from the cowl side and attached to the ramp side.

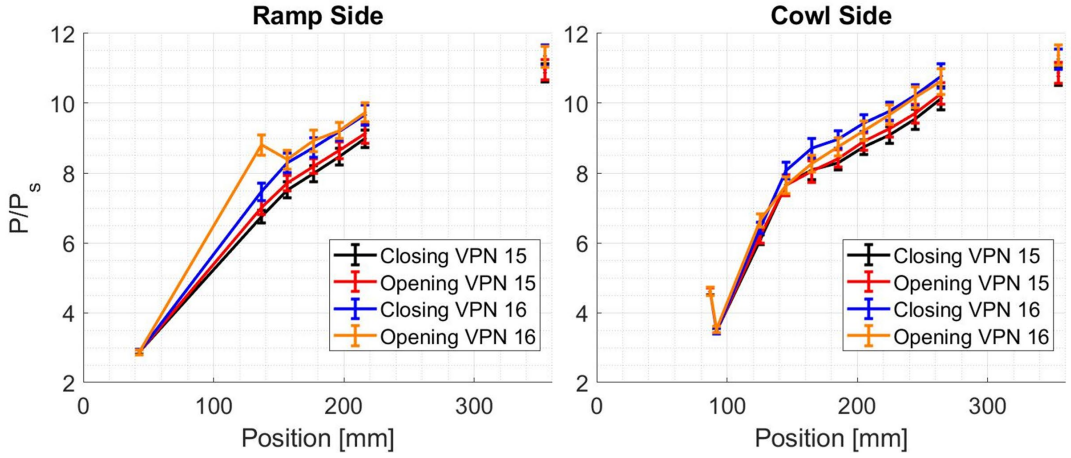


Figure 3-85. Change of pressure along the intake and comparison of throttling direction at VPNs 15 and 16 for Mach = 3 with bleed (Test 4331).

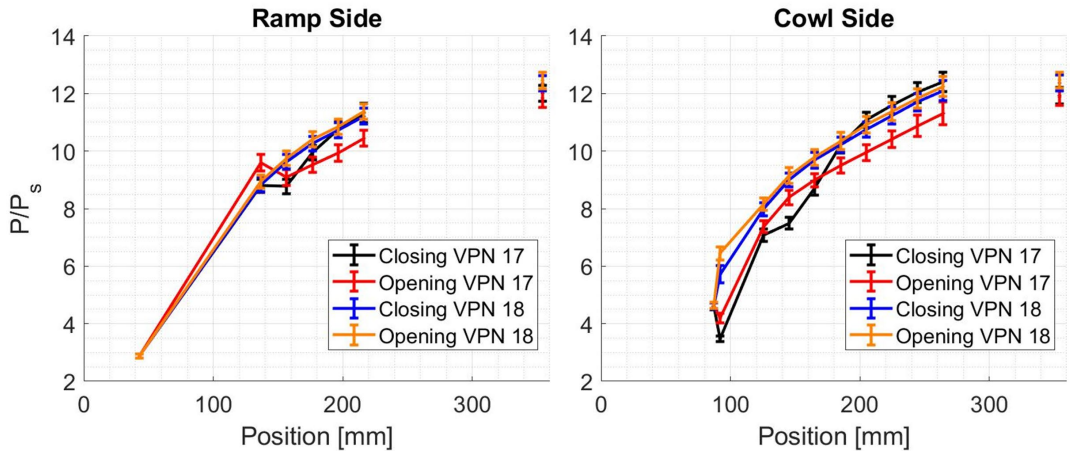


Figure 3-86. Change of pressure along the intake and comparison of throttling direction at VPNs 17 and 18 for Mach = 3 with bleed (Test 4331).

3.2.2.2 Mach = 2.63 with Bleed (Test 4340)

3.2.2.2.1 Change of Pressure Along the Intake

The variation of pressure along the intake for Test 4340, at VPNs between 1 and 9 are given in Appendix F. Figure 3-87 displays the alterations in pressure along the intake at VPNs 9 to 13. The graph shows a gradual increase in the pressure from position number 9 to 11, downstream of the starting point of the pseudo-shock. Additionally, pressure at R3 also begins to rise, indicating that the impact of the pseudo-shock is reaching that point on the ramp side as well. A sudden change in the pressure profile is observed when moving from position number 11 to 12. It is important to note that this transition results in a sudden movement of the separation points of the pseudo-shock, as shown in Figure 3-35. Furthermore, the pressure data along the cowl side suggests that the shock-train is attached to the cowl side after the transition between 11 to 12, as evidenced by the change in pressure profile from monotonically increasing to zig-zag pattern. In addition, it should be noted that this transition also causes a significant pressure drop at the most downstream pressure taps in the diffuser. The pressure at the exit of the air intake drops slightly. This

suggests that the pseudo-shock structure that occurs at position 11 achieves higher compression of the flow a shorter distance.

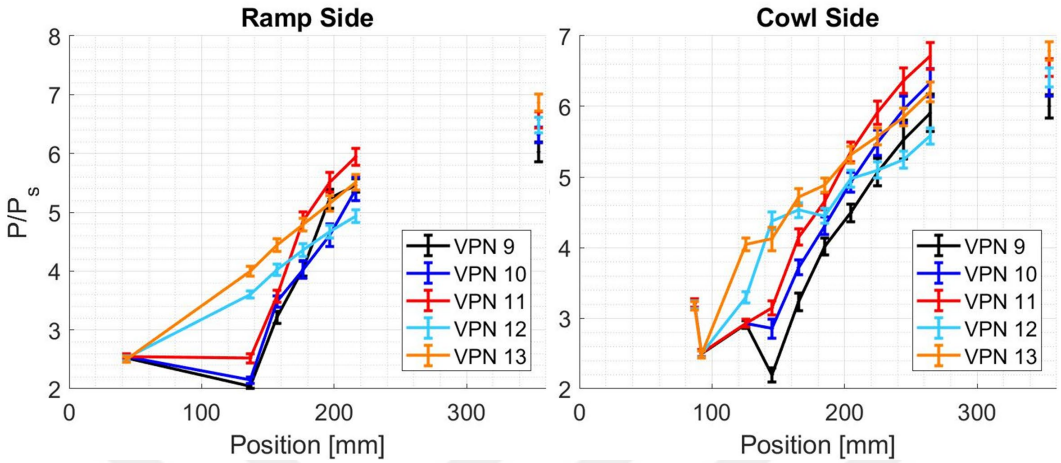


Figure 3-87. Change of pressure along the intake at VPNs between 9 and 13 for Mach = 2.63 with bleed (Test 4340).

Figure 3-88, pressure changes along the intake at VPNs 14 to 18 are shown. Up to position 16, there is a gradual increase in pressure at all measurement points downstream of D2. However, a small change in the pressure profile is observed when the valve reaches position 17. This is also the point where the separation of the shock-train from the cowl side and its attachment to the ramp side are observed in the shadowgraph images, as shown in Figure 3-36. Pressure profiles also indicate this change, with the formation of a zig-zag pattern on the ramp side. Additionally, on the cowl side, D3 and D4 remain unchanged when going from position 16 to 17, which suggests that there is no significant change in the position of the starting point of the pseudo-shock on the cowl side, or it is relatively small. Moving from position 17 to 18, the pseudo-shock shifts upstream and affects the pressure at D2. The disappearance of zig-zag patterns on both the cowl and ramp sides suggests that the shock-train part may have finished before reaching the first downstream measurement tap on the ramp side, or its effect is relatively small.

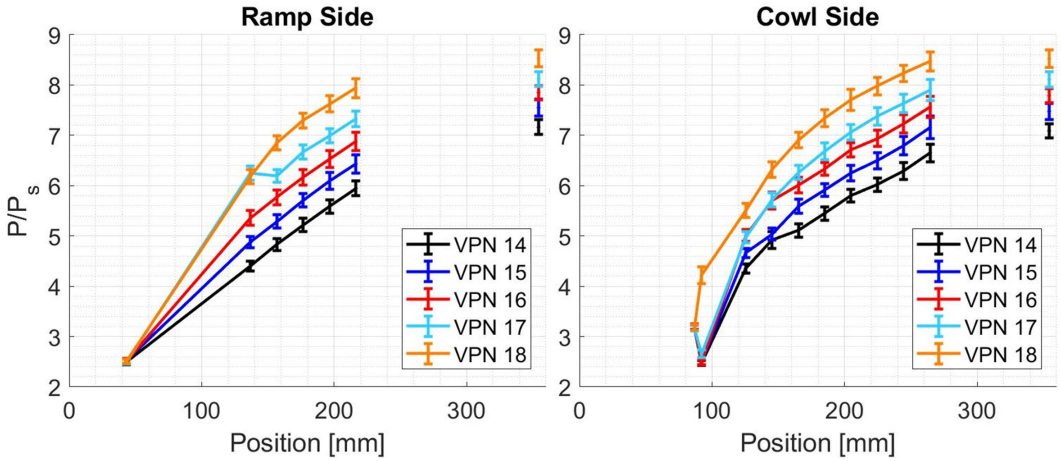


Figure 3-88. Change of pressure along the intake at VPNs between 14 and 18 for Mach = 2.63 with bleed (Test 4340).

Change of pressure along the intake for VPNs 18 to 30 are given in the Appendix F. The monotonic increase continues until the buzz, similar to Test 4331.

3.2.2.2.2 Investigation of Hysteresis Phenomenon

Figure 3-89 presents an analysis of pressure changes at various measurement points during the opening and closing phases of the back pressure throttling direction, investigating the hysteresis effect. Prior to reaching VPN 12, where the pseudo-shock is detected in shadowgraph images, pressure measurements at several points exhibit variations between the opening and closing phases. Notably, unlike Test 4331, the impact of hysteresis on the exit pressure (V1 pressure tap) is relatively significant before position number 12. However as in Test 4331, the effect of the hysteresis behaviour is not observed after this VPN at V1 but seen at R3. Thus, the intake experiences hysteresis effects due to back pressure throttling before the consistent formation of the terminal or the pseudo-shock, and the sudden formation of a terminal or pseudo-shock is not observed. Rather, the pressure gradually increases.

Figure 3-89 highlights VPN 16 as the point where the hysteresis is detected, occurring after position number 12. As a result, the pressure alterations along the

intake are examined in Figure 3-90 for VPNs 14, 16, and 18. These plots depict the variations in the pressure at these VPNs throughout the intake for different throttling directions.

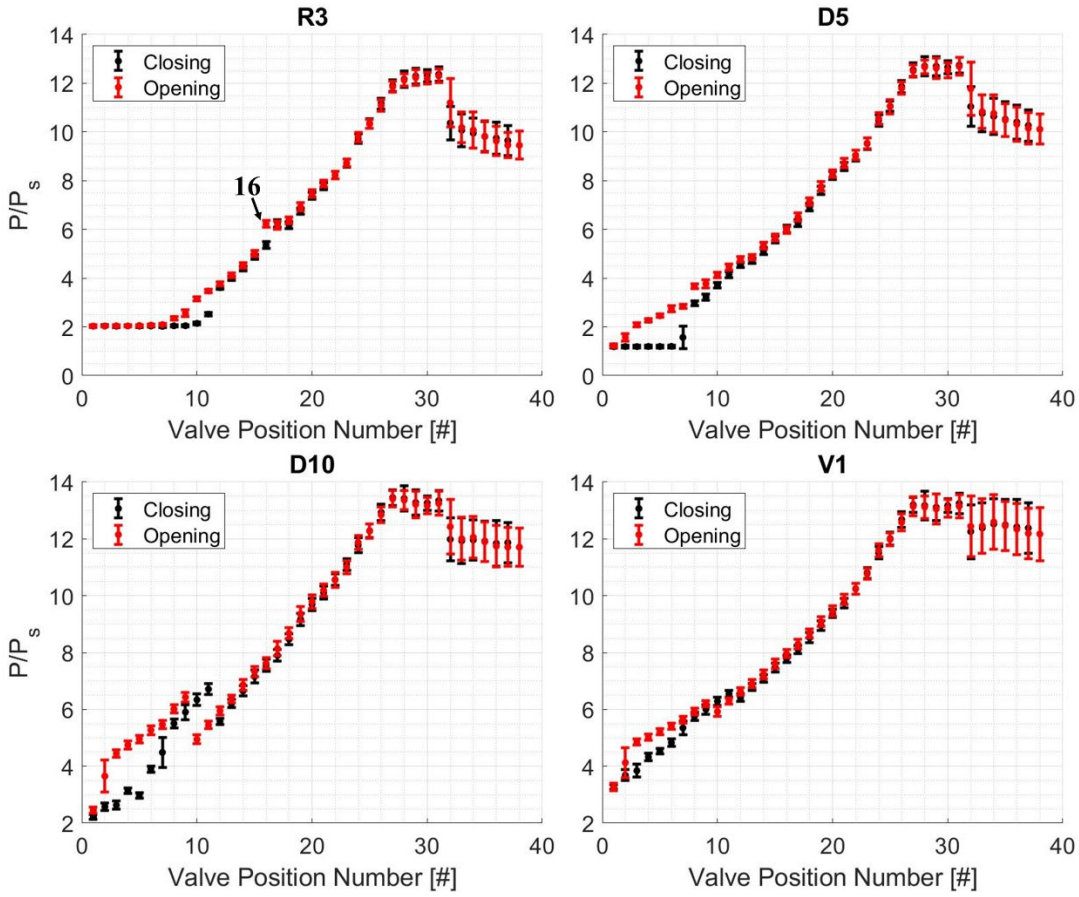


Figure 3-89. Variation of pressure with respect to VPN and comparison of throttling direction for Mach = 2.63 with bleed (Test 4340).

Upon examining Figure 3-90, it becomes apparent that the pressure measurements at VPNs 14 and 18 remain largely consistent between the closing and opening phases. Conversely, at position 16, significant changes are present, particularly at the R3 and R4 taps. The difference in pressure profiles between the opening and closing phases at position 16 bears a resemblance to the change in profile observed between positions 16 and 17 in Figure 3-88. This suggests that, at position number 16, during the closing phase, the shock-train section of the pseudo-shock is separated from the ramp side, while during the opening phase, it is attached to the ramp side.

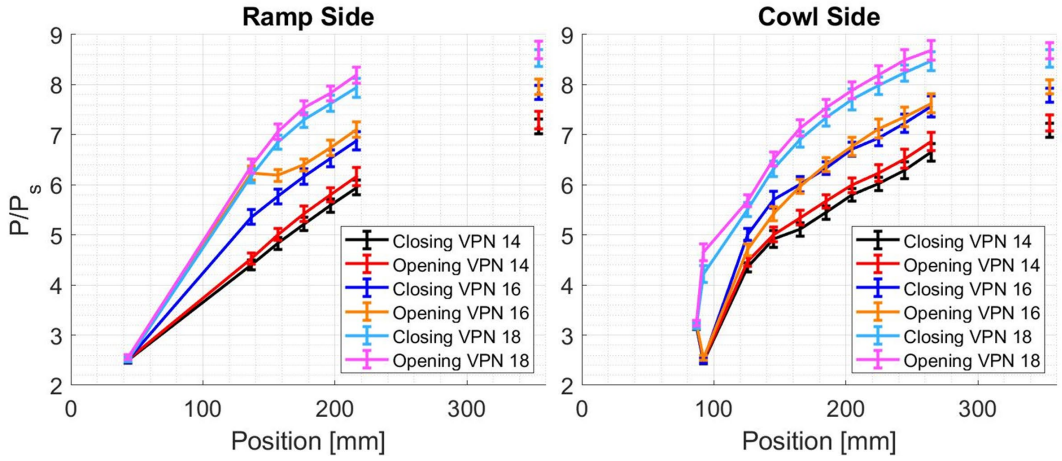


Figure 3-90. Change of pressure along the intake and comparison of throttling direction at VPNs 14, 16 and 18 for Mach = 2.63 with bleed (Test 4340).

3.2.2.3 Mach = 3 without Bleed (Test 4372).

3.2.2.3.1 Change of Pressure Along the Intake

The variation of pressure along the intake for Test 4372, at VPNs between 1 and 9 are given in Appendix F. Figure 3-91 depicts the changes in pressure along the intake at VPNs 9 to 13. A sudden increase in pressures is noticeable when moving from position 9 to 10, indicating that the formation of the pseudo-shock or terminal shock has occurred. At position 10, a zig-zag pattern can be seen on both the ramp and cowl side. As the valve moves to position 11, the zig-zag pattern on the cowl side disappears, and a significant decrease in pressure is observed downstream of the diffuser on the cowl side (D9 and D10). As discussed earlier, the characteristics at position 10 suggest that the shock-train of the pseudo-shock is attached to both the cowl and ramp side and separates from the cowl side, attaching to the ramp side at position 11. Furthermore, corresponding shadowgraph images (Figure 3-56) show that at position 11, the shock-train of the pseudo-shock is detached from the cowl side.

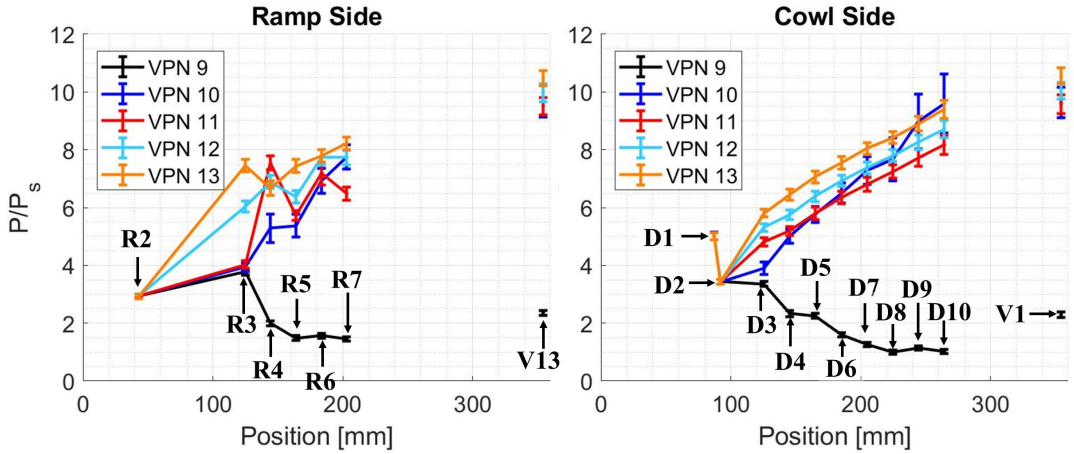


Figure 3-91. Change of pressure along the intake at VPNs between 9 and 13 for Mach = 3 without bleed (Test 4372).

Figure 3-92 displays the pressure variations along the intake at VPNs 14 to 18. From position 14 to 16, there is a gradual increase in pressure downstream of D2. Interestingly, a change in pressure profiles on the ramp side is observed from position 14 to 15, where pressure at R3 and R4 decreases and R5-R7 increases. The reason for this phenomenon remains unknown. Up to 17, no significant pressure changes are detected at D1, and only a small change is observed at D2, indicating that the onset of the pseudo-shock has not yet reached D1. However, a sudden increase in pressure at D1 is observed when the VPN changes from 17 to 18. The shadowgraph images presented in Figure 3-57 show that a detached sonic line is observed on the ramp side after transitioning from position 17 to 18, but there is no full detachment of the shock-train from the ramp side, and attachment on the cowl side is not observed. The location of the separation shock of the separation bubble formed by the cowl shock also changes its location. Therefore, it is believed that the sudden increase in the D1 pressure is related to the disturbed separation bubble of the cowl shock and the movement of the pseudo-shock related separation point on the cowl side upstream. The pressure variations along the intake at VPN 18 to 20 are depicted in Figure 3-93. The pressure downstream of D2 increases steadily, at both ramp and cowl surfaces, from VPN 18 to 19. However, a significant drop in pressure at D1 is observed when the VPN changes from 19 to 20. In addition, there is a slight increase

in pressure at downstream of diffuser R7, while R10 experiences a decrease in pressure. It is worth noting that the shadowgraph images for VPN 20 (Figure 3-57) demonstrate the complete separation of the sonic line from the ramp side and the attachment of the shock-train to the cowl side. Thus, the drop in D1 pressure can be explained by the attachment of the shock-train on the cowl side.

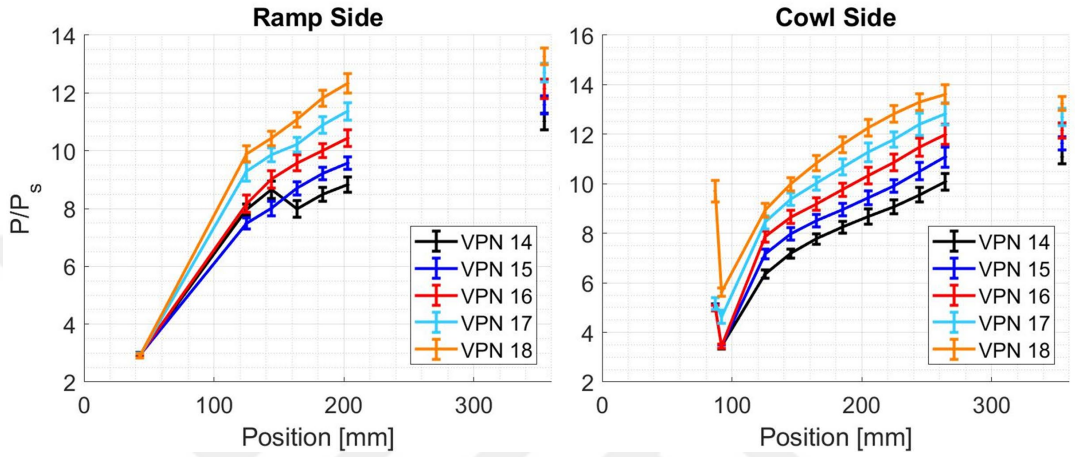


Figure 3-92. Change of pressure along the intake at VPNs between 14 and 18 for Mach = 3 without bleed (Test 4372).

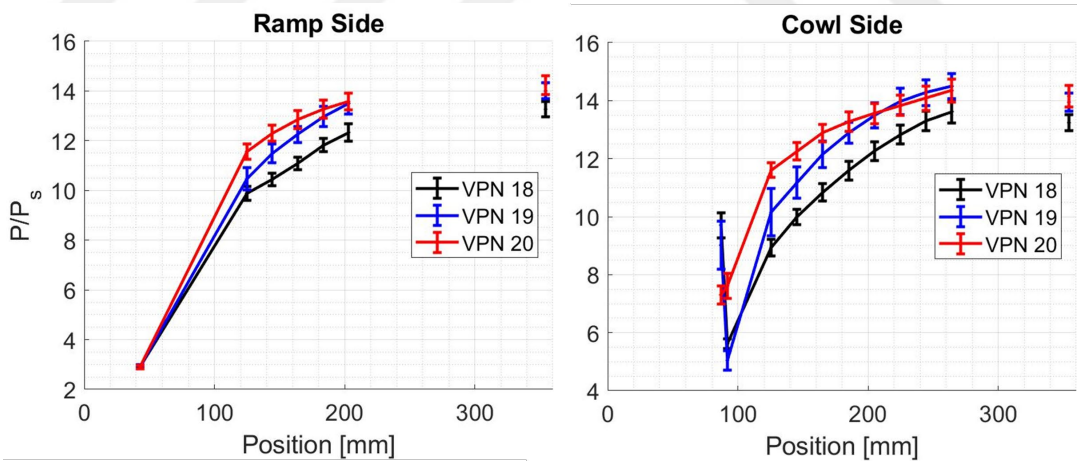


Figure 3-93. Change of pressure along the intake at VPNs between 18 and 20 for Mach = 3 without bleed (Test 4372).

The pressure changes along the intake for VPNs 20 to 24 are given in Appendix F, revealing a monotonic increase until the buzz, similar to the preceding discussions.

3.2.2.3.2 Investigation of Hysteresis Phenomenon

Figure 3-94 compares pressure changes at various measurement points during back pressure throttling in different directions to investigate the hysteresis effect. Before reaching VPN 11, where the shadowgraph images revealed the pseudo-shock, the pressure measurements at almost all points exhibit significant variations between the opening and closing phases. Interestingly, the impact of hysteresis on the exit pressure (V1 pressure tap) is relatively significant before position number 11, but as in Test 4331 and 4340, it is not observed after this valve position. Effect of the hysteresis behaviour is seen at R3 and D5 taps. This indicates that the intake experiences hysteresis effects before the consistent formation of the terminal or the pseudo-shock.

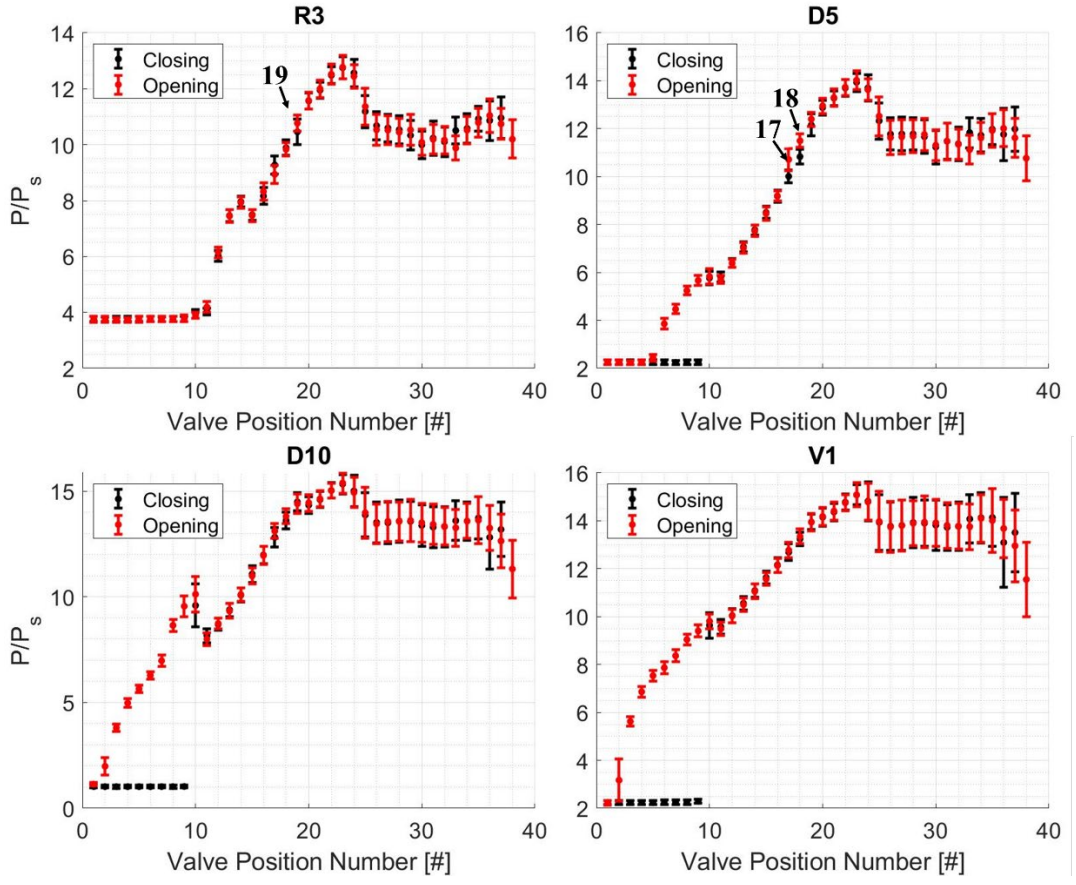


Figure 3-94. Variation of pressure with respect to VPN and comparison of throttling direction for Mach = 3 without bleed (Test 4372).

Additionally, unlike Test 4331 and 4340, a sudden formation of the terminal or the pseudo-shock is observed and the disappearance of the pseudo-shock or the terminal shock does not occur suddenly as the back pressure valve opens. As it is highlighted in Figure 3-94 at VPNs 17, 18 and 19, hysteresis behaviour is detected, occurring after position 12. Figure 3-95 illustrates the investigation of the hysteresis in the pressure changes along the intake for VPNs 16 and 17. The results show that at position number 16, the measured pressure values are almost identical. However, for position number 17, although the exit pressure of the intake remains the same, there are noticeable differences, especially on the cowl side. A similar observation can be made for Figure 3-96, in which a comparison is made between VPNs 19 and 20. At VPN 20, the hysteresis behaviour is clearly visible.

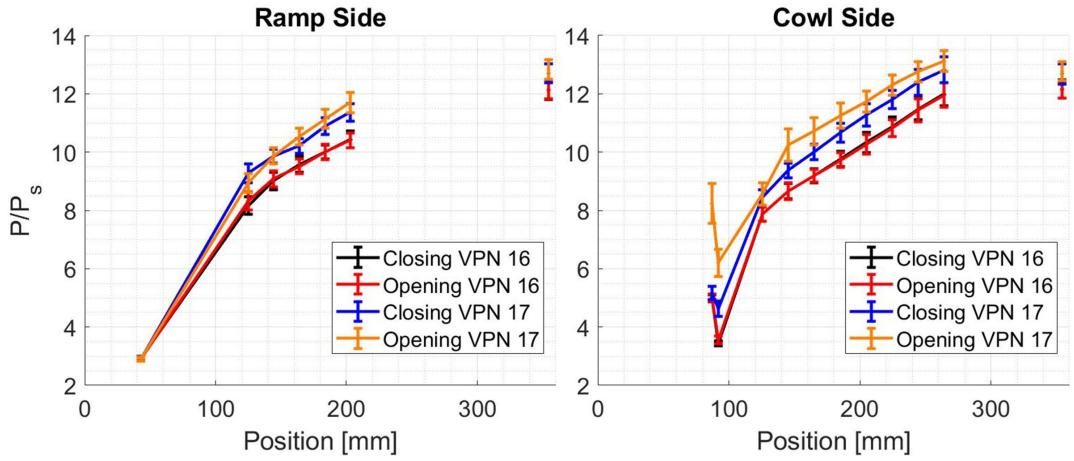


Figure 3-95. Change of pressure along the intake and comparison of throttling direction at VPNs 16 and 17 for Mach = 3 without bleed (Test 4372).

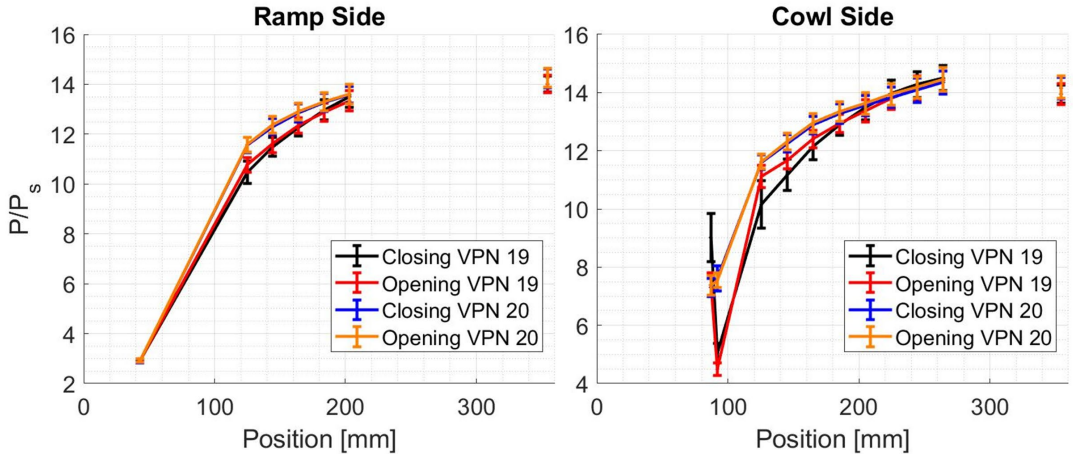


Figure 3-96. Change of pressure along the intake and comparison of throttling direction at VPNs 19 and 20 for Mach = 3 without bleed (Test 4372).

3.2.2.4 Mach = 2.63 without Bleed (Test 4373).

3.2.2.4.1 Change of Pressure Along the Intake

The variation of pressure along the intake for Test 4373, at VPNs between 1 and 9 are given in Appendix F. Figure 3-97 shows the changes in pressure along the intake for VPN 9 to 13, where a gradual increase in pressure occurs and the pseudo-shock moves upstream. However, as shown in Figure 3-98, a different pressure profile is observed when going from position number 13 to 14. While the pressure at the exit of the intake and at D10 are higher, the pressure at D4 and D5 is lower. Additionally, the shadowgraph images in Figure 3-72 indicate a complete separation of the shock-train from the ramp side at VPN 14. The separation shocks on both ramp and cowl sides in Figure 3-74 suggest that the shock-train is not entirely separated from any surface at position number 13. Therefore, it can be inferred that the change from position 13 to 14 leads to a complete separation of the shock-train from the cowl side while the shock train stays attached to the ramp side.

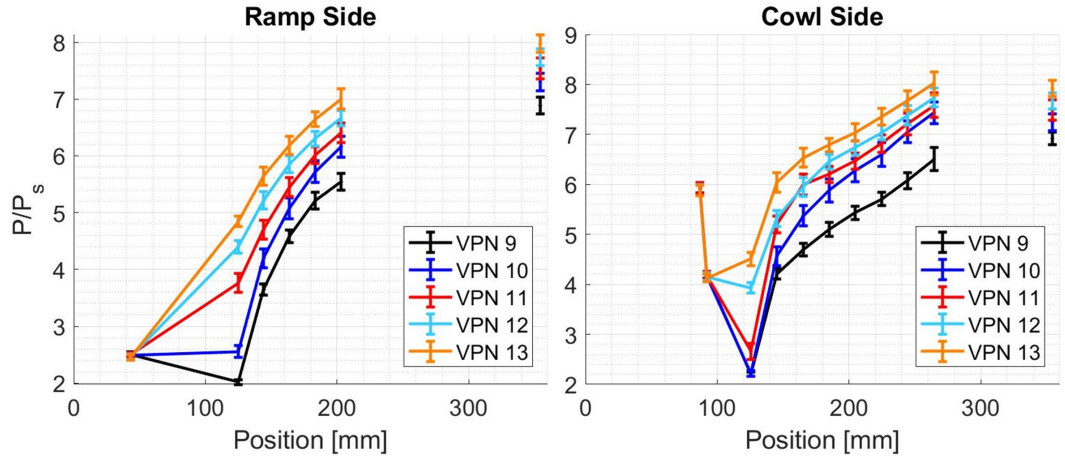


Figure 3-97. Change of pressure along the intake at VPNs between 9 and 13 for Mach = 2.63 without bleed (Test 4373).

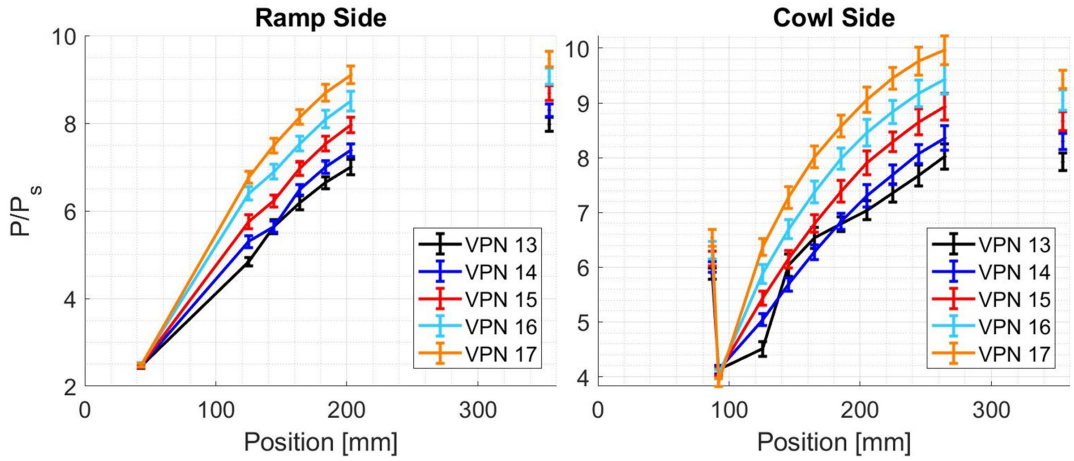


Figure 3-98. Change of pressure along the intake at VPNs between 13 and 17 for Mach = 2.63 without bleed (Test 4373).

A decrease in pressure at location D1 in the intake when the VPN changes from 17 to 18 is observed in Figure 3-99. This change is similar with Test 4372, where a similar pressure drop was observed during the VPN change from 19 to 20. In both cases, shadowgraph images showed that the shock-train fully separated from the ramp side and attached to the cowl side. Furthermore, it is worth noting that during these valve position changes, the pressure at all the other measurement points on both the ramp and cowl sides within the intake increased, except for location D1.

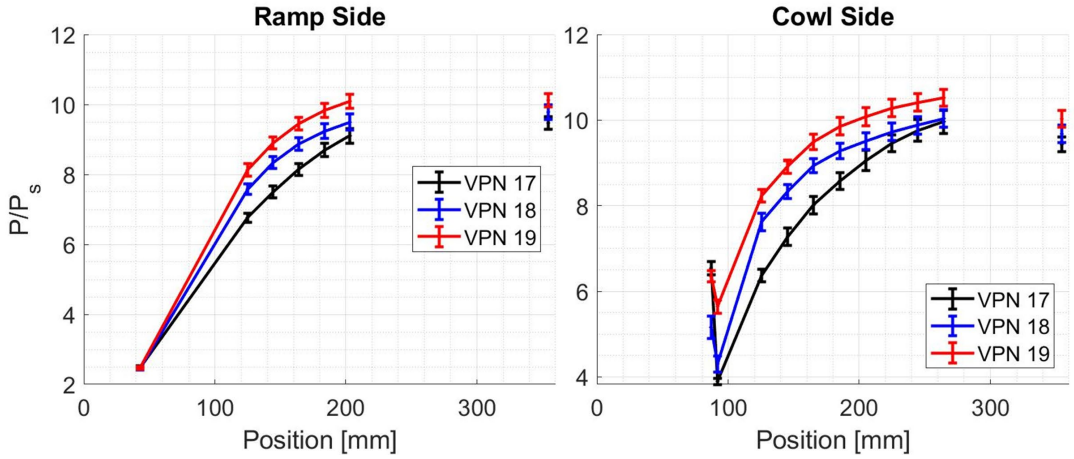


Figure 3-99. Change of pressure along the intake at VPNs between 17 and 19 for Mach = 2.63 without bleed (Test 4373).

The pressure changes along the intake for VPNs 19 to 23 are given in Appendix F, revealing a monotonic increase until the buzz, similar to the preceding discussions.

3.2.2.4.2 Investigation of Hysteresis Phenomenon

According to Figure 3-100, hysteresis is detected at VPN 17 after VPN 13. However, it should be noted that the effect of hysteresis is observed at several points before the VPN 13. Furthermore, measurements taken at the V1 pressure tap indicate that the effect of hysteresis at the exit of the intake is minimal compared to the other pressure measurement locations within the intake.

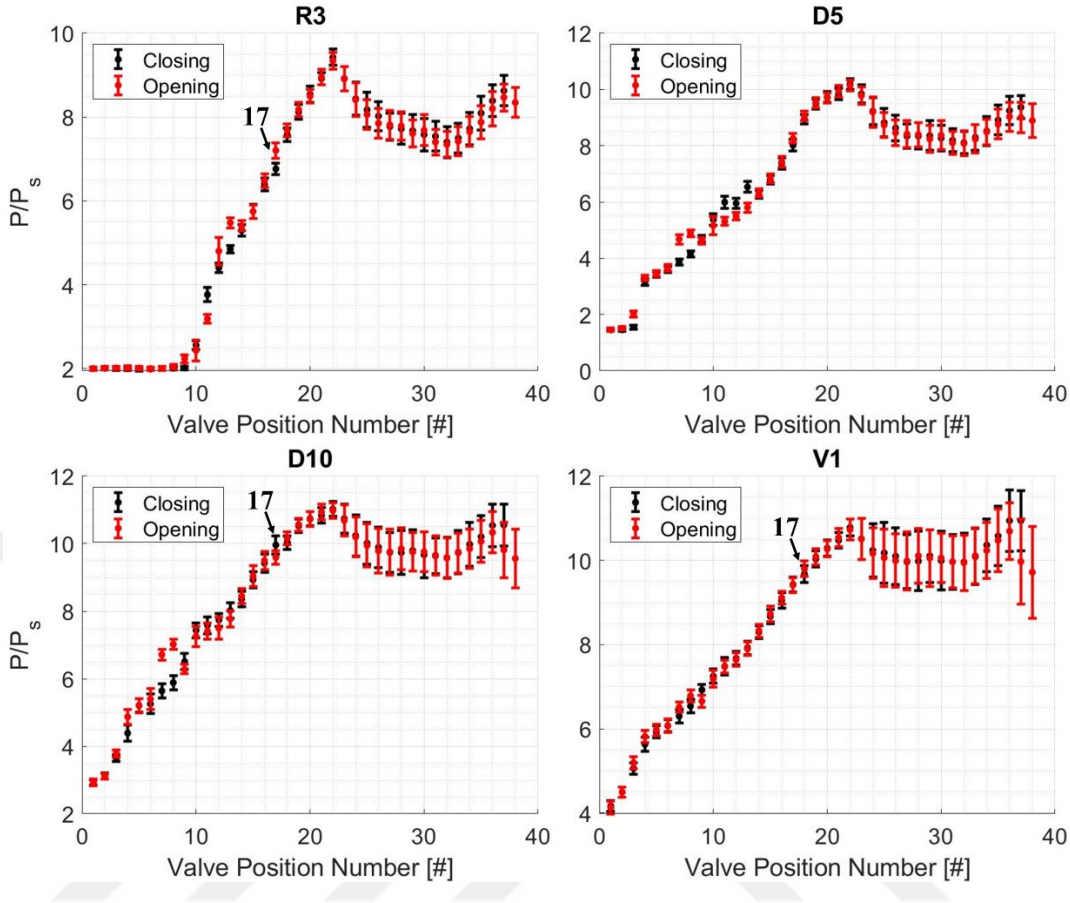


Figure 3-100. Variation of pressure with respect to VPN and comparison of throttling direction for Mach = 2.63 without bleed (Test 4373).

Figure 3-101 is presented to examine the impact of hysteresis at VPNs 16 and 17. The plot indicates that there is no significant difference between closing and opening directions at the VPN 16. However, at 17, hysteresis behavior is observed. As the valve is opened from VPN 17 to 18, the pressure at the D1 location drops (as shown in Figure 3-99), and the difference between the pressure profiles of opening and closing throttling directions at VPN 17 is similar to this change. This indicates that during the opening of the valve, the shock-train part of the pseudo-shock is still detached from the ramp side at the VPN 17, unlike during closing. Additionally, as shown in Figure 3-102, at VPN 18, the pressure profiles are similar, and the effect of hysteresis disappears. It should be mentioned that the hysteresis mentioned above also has a slight effect on the pressure at V1.

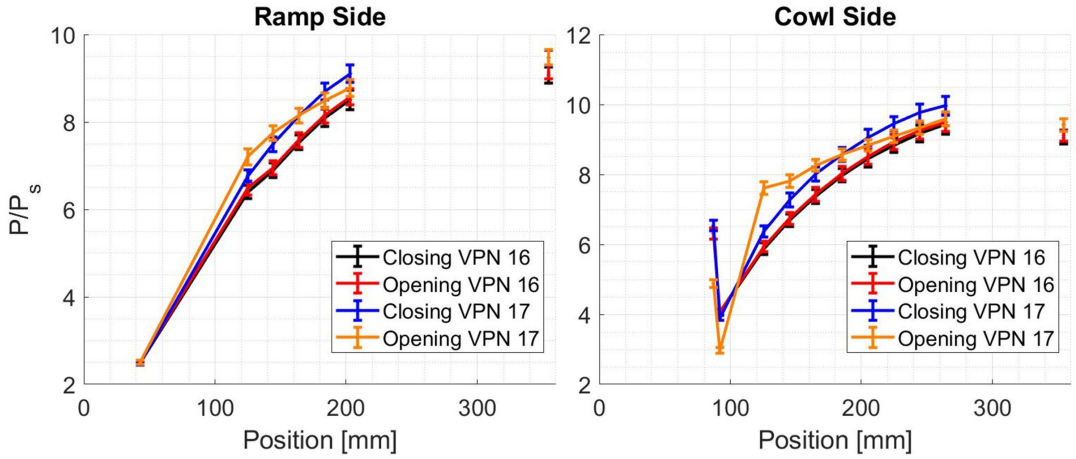


Figure 3-101. Change of pressure along the intake and comparison of throttling direction at VPNs 16 and 17 for Mach = 2.63 without bleed (Test 4373).

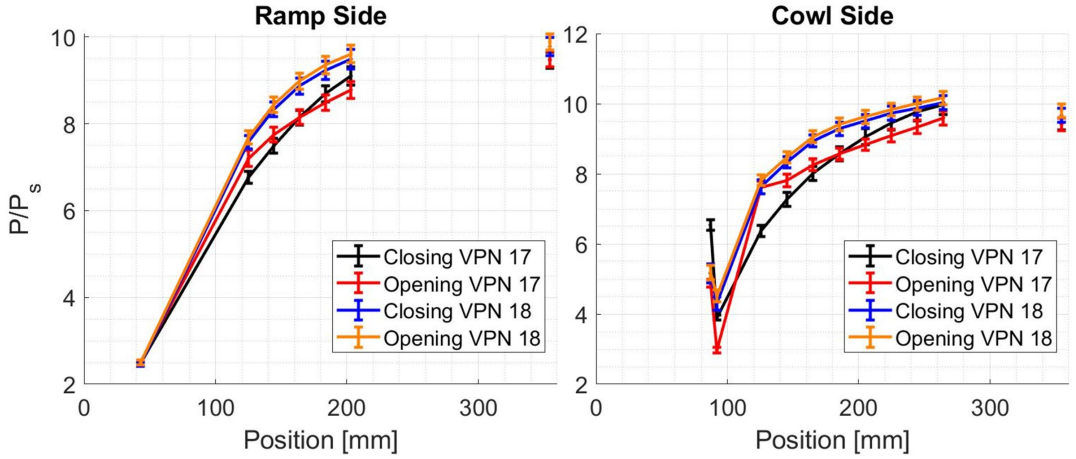


Figure 3-102. Change of pressure along the intake and comparison of throttling direction at VPNs 17 and 18 for Mach = 2.63 without bleed (Test 4373).

3.2.3 Characteristics Diagrams

Figure 3-103 provides the obtained characteristic diagrams of the intake to evaluate the overall performance of the intake. These diagrams start from VPN 13, after which shadowgraph images reveal a pseudo-shock for all tests. The points at which the intake experiences buzzing, which can be either small or big, based on the shadowgraph images and oscillation of the pressure are indicated on the diagrams. The figures show that the air intake test item with bleed have a higher pressure

recovery at the points where buzz starts. Specifically, the maximum achievable pressure recovery without bleed is %56 at Mach = 2.63 and %45 at Mach = 3. However, with bleed, the maximum obtained pressure recovery is %67 at Mach = 2.63 and %56 at Mach = 3. To investigate the effect of bleed on the mass flow ratio, Figure 3-104 is presented. The figure shows that the supercritical mass flow ratio is lower with bleed. The maximum measured supercritical mass flow ratios for the tests at Mach = 3 are 0.98 without bleed and 0.93 with bleed. For the tests at Mach = 2.63, the maximum measured supercritical mass flow ratios are 0.87 without bleed and 0.77 with bleed.

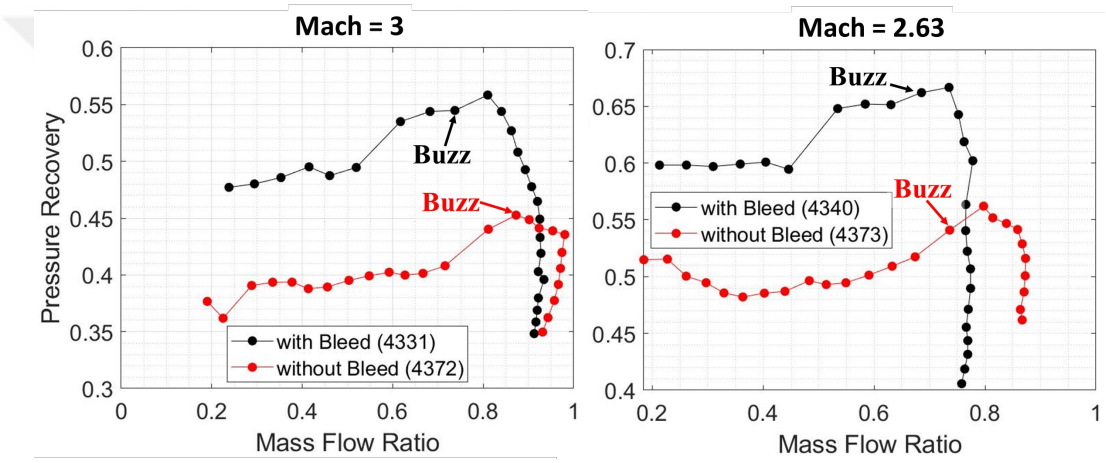


Figure 3-103. Characteristic diagrams for the tests.

In Figure 3-104 the points where changes in the flow structures inside the bleed are detected from the averaged shadowgraph images, denoted as "bleed is affected". Although there may be some minor changes in the mass flow rate at those points, they are relatively insignificant. Therefore, from an operational perspective, the mass flow ratio (MFR) begins to decrease at higher throttled conditions, and the operational mode of the intake transitions to a subcritical mode. An interesting profile is observed in Test 4340 on the right plot. After the bleed is affected according to the shadowgraph images, a small but noticeable drop is observed in the MFR. However, after a certain point, the MFR increases and then begins to decrease again. The region between the first and second drop points of the MFR is referred to as the "quasi-subcritical" region by the author of the present study.

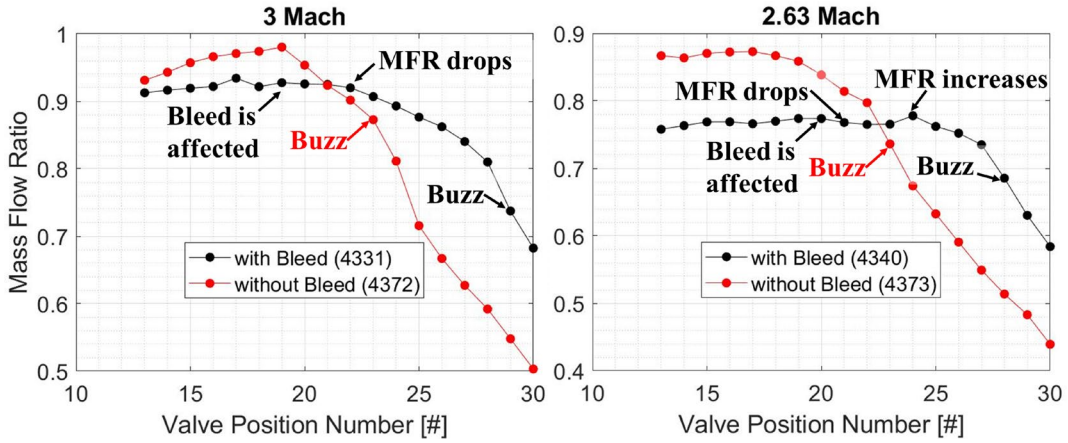


Figure 3-104. Variation of mass flow ratio with respect to the VPN.

Figure 3-105 shows the variation of pressure inside the bleed channel as a function of the VPN. The graph provides insight into the changes in the pressure before and after the pseudo-shock begins to impact the bleed. It can be observed that there is a brief increase in the bleed pressure at VPNs 19 and 20 for the tests conducted at Mach numbers of 3 and 2.63, respectively. These valve positions coincide with the point where the pseudo-shock starts to affect the bleed, as indicated by the averaged shadowgraph images. Subsequently, after VPN 21, a more significant increase in the pressure is observed. Notably, these specific valve positions also align with the points where the MFR starts to decrease.

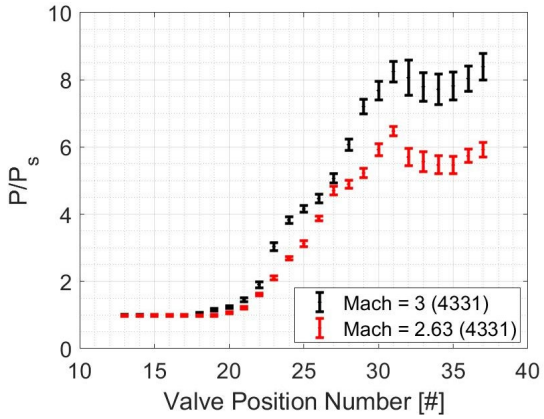


Figure 3-105. Variation of the bleed pressure with the VPN.

CHAPTER 4

NUMERICAL SIMULATIONS AND COMPARISONS WITH THE EXPERIMENTS

In this chapter, the details of the 3-dimensional Computational Fluid Dynamics (CFD) simulations for the Wind Tunnel Test Item conducted using a commercial software Fluent 2021 R1 are provided. The chapter begins by describing the setup and configuration of the CFD simulations, including the geometry of the wind tunnel test item and the boundary conditions applied. The numerical methodology, such as the governing equations and the turbulence modeling approach, is also presented.

Following the simulation setup, the computed results from the CFD simulations are presented. The results include various flow parameters, such as Mach number profiles, pressure distributions, and shock structures, which are obtained through post-processing of the simulation data. The results are visually represented through contour plots and vector plots. Moreover, comparisons are made between the numerical results and the corresponding experimental data.

4.1 Geometry, Grid, Boundary Conditions and Method

The geometry of the Wind Tunnel Test Item model has been generated, including all essential components. However, small details such as bolts, screws and holes of the pressure measurement taps have been omitted for simplicity and to reduce computational complexity. Grid sizing has been done according to grid sensitivity study. Simulations are conducted for the test items with and without bleed at different back pressure valve positions. A new geometry and grid have been generated for each of the back pressure valve position. Although the position of the back pressure valve affects the computational domain slightly, the mesh resolution was maintained. In other words, the total number of grids vary slightly between different valve

positions, but the overall mesh quality and resolution were maintained throughout the simulations.

For the test item with bleed, the generated geometry and the types of the boundary conditions for the surfaces are presented in Figure 4-1. It should be noted that the CFD simulations were performed on the geometry, where a section of the intake was removed at the symmetry plane and half of the geometry was modeled to decrease the computational cost. As seen in Figure 4-1, pressure far-field type boundary condition is applied to the outer surfaces of the solution domain. On the downstream boundary surfaces of the solution domain, a pressure outlet boundary condition is applied. Since only half of the geometry is modeled, a symmetry boundary condition is applied on the cut surface that divides the intake into half. The types of boundary conditions applied to this geometry are the same as those used for the geometry without bleed.

The maximum edge length within the region of interest for the grid was set to 1 mm, while the cells near the walls were sized such a way that the maximum y+ value along the geometry did not exceed unity. It should be emphasized that the cell sizes were increased in the vicinity of the far-field boundary condition surfaces. Since the focus of the study is primarily on the interior flow structures within the intake, a coarser grid resolution in the far-field regions helps reduce the computational time while still capturing the relevant flow features and phenomena of interest.

The first layer thickness of the cells near the walls is approximately one micron. Following each simulation, y+ values were checked to ensure that the mesh resolution was sufficient. Isometric view of the generated grid for the test item with bleed is given in Figure 4-2.

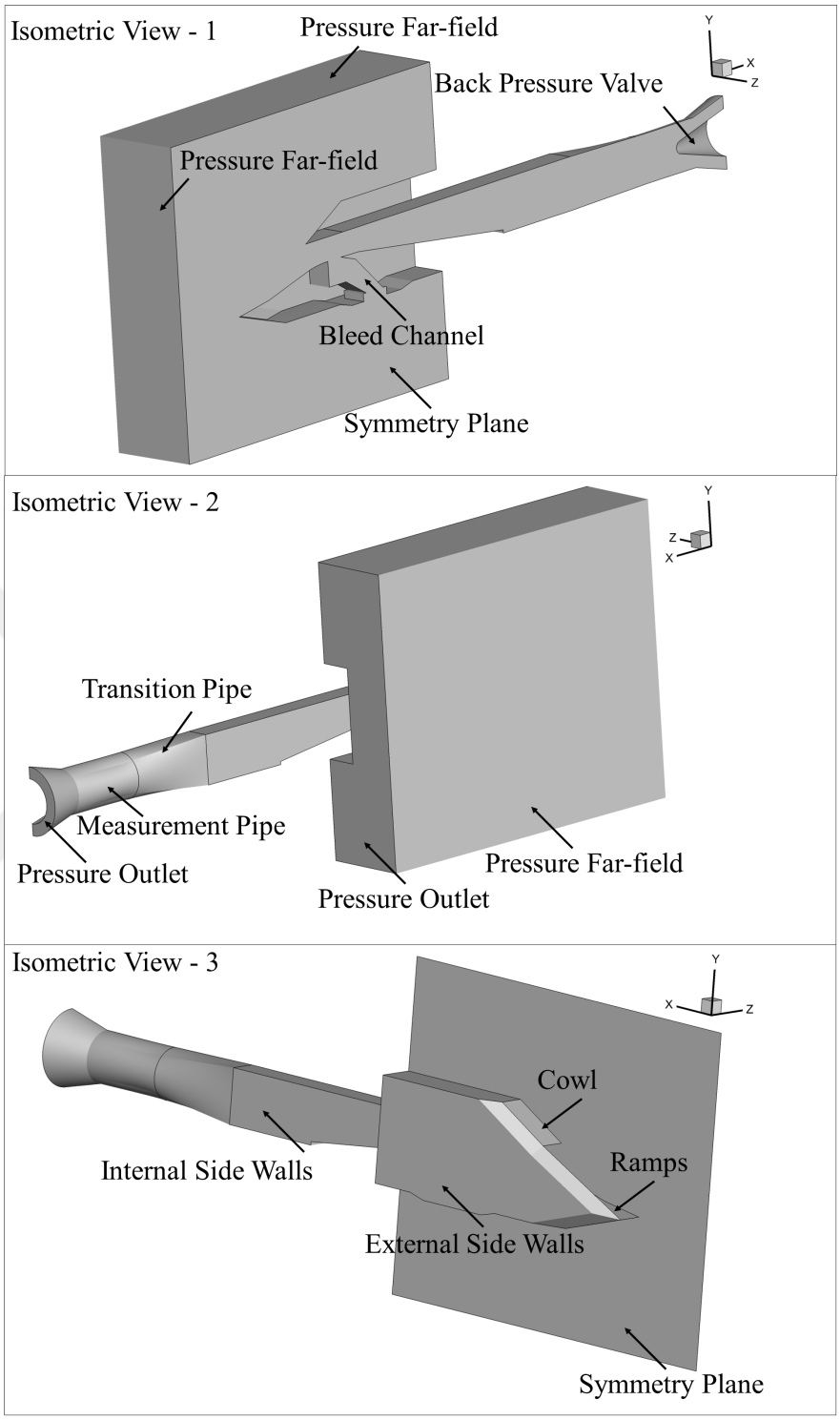


Figure 4-1. CFD geometry and definition of boundary conditions for the test item with bleed.

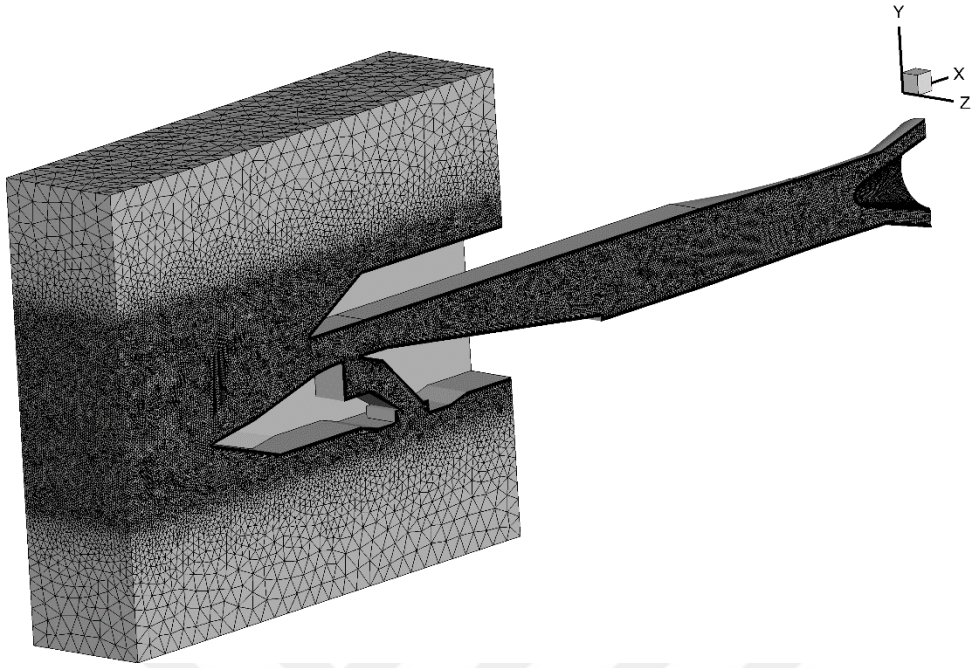


Figure 4-2. Isometric view of the generated grid for the test item with bleed.

The simulations were performed using the Reynolds Averaged Navier-Stokes (RANS) formulation. For flux splitting, the Advection Upstream Splitting Method (AUSM) [85] was selected due to its accuracy in capturing shock structures and numerical stability. The turbulence models used in the simulations are discussed in section 4.2. The air was modeled as an ideal gas, and the viscosity of air was calculated using Sutherland's law. The boundary conditions for Mach, pressure, and temperature were chosen to match the test conditions and are presented in Table 4-1. Total temperature of the flow was specified as 290 K. The turbulence intensity at the far-field boundary was set to a typical value of 1% [86] for blowdown wind tunnels. For the length scale of turbulence, an approximation suggested by references [87], [88] was employed such that the turbulent length scale is defined as 7% of the width of the test section, which is equal to 10.5 mm.

Table 4-1. Pressure far-field boundary conditions.

Mach	Static Temperature [K]	Static Pressure [Pa]	Total Pressure [kPa]
3.00	103.6	16334	600
2.63	121.7	23922	500

4.2 Turbulence Models

Menter's [89] $k-\omega$ Shear Stress Transport (SST) and Baseline (BSL) $k-\omega$ two-equation eddy-viscosity models are recommended for most industrial applications due to their high accuracy for flows with adverse pressure gradients and separation [90]. However, as discussed in the literature review section, Carroll et al. [57], [59], [60] have proposed that the shock-train segment of the pseudo-shock amplifies the turbulence kinetic energy. Furthermore, the first shock of the pseudo-shock produces anisotropic turbulence, making it challenging to model the flow using isotropic turbulence models. In their study, Boychev et al. [91] conducted a numerical analysis of pseudo-shock structures in a constant area channel using the RANS approach with isotropic turbulence models. They compared the results obtained with the SST and BSL models and found significant differences between them. Specifically, they observed that the SST model tends to predict longer pseudo-shock structures compared to the BSL model. Based on these findings, the present study includes simulations using BSL and SST model to further investigate the characteristics of pseudo-shock structures.

Equations for the turbulence kinetic energy, k, and specific dissipation rate, ω, for the SST and BSL models are same. However, the constants used in these equations and the definition of the eddy viscosity differ between the two models.

Definition for the k and ω are as follows:

$$\frac{D\rho k}{Dt} = \tau_{ij}\frac{\partial u_i}{\partial x_j} - \beta^*\rho\omega k + \frac{\partial}{\partial x_j}\left[(\mu + \sigma_k\mu_t)\frac{\partial k}{\partial x_j}\right] \tag{4-1}$$

$$\frac{D\rho\omega}{Dt} = \frac{\gamma}{\nu_t}\tau_{ij}\frac{\partial u_i}{\partial x_j} - \beta\rho\omega^2 + \frac{\partial}{\partial x_j}\left[(\mu + \sigma_\omega\mu_t)\frac{\partial \omega}{\partial x_j}\right] + 2(1-F_1)\rho\sigma_{\omega 2}\frac{1}{\omega}\frac{\partial k}{\partial x_j}\frac{\partial \omega}{\partial x_j} \tag{4-2}$$

Let ϕ represent any constant $(\sigma_k, \sigma_\omega, \beta, \beta^*, \gamma)$ used in the k and ω equations. To calculate the ϕ, two sets of constants are used, set 1, ϕ_1 $(\sigma_{k1}, \sigma_{\omega 1}, \beta_1, \beta^*, \gamma_1)$ and set

2, ϕ_2 $(\sigma_{k2}, \sigma_{\omega 2}, \beta_2, \beta^*, \gamma_2)$. Any constant, ϕ, is calculated using the blending function as follows:

$$\phi = F_1\phi_1 + (1 - F_1)\phi_2 \tag{4-3}$$

For the BSL model, the set of constants for ϕ_1 are as follows:

$$\sigma_{k1} = 0.5, \quad \sigma_{\omega 1} = 0.5, \quad \beta_1 = 0.0750, \quad \beta^* = 0.09,$$
$$\gamma_1 = \frac{\beta_1}{\beta^*} - \frac{\sigma_{\omega 1}\kappa^2}{\sqrt{\beta^*}}, \quad \kappa = 0.41 \tag{4-4}$$

and the set of constants for ϕ_2 are as follows:

$$\sigma_{k2} = 1.0, \quad \sigma_{\omega 2} = 0.856, \quad \beta_2 = 0.0828, \quad \beta^* = 0.09,$$
$$\gamma_2 = \frac{\beta_2}{\beta^*} - \frac{\sigma_{\omega 2}\kappa^2}{\sqrt{\beta^*}}, \quad \kappa = 0.41 \tag{4-5}$$

The definition for the turbulent viscosity is as follows:

$$\nu_t = \frac{k}{\omega} \tag{4-6}$$

The definition for F_1 is as follows:

$$F_1 = \tanh\left(arg_1^4\right) \tag{4-7}$$

$$\arg_1 = \min\left[\max\left(\frac{\sqrt{k}}{0.09wy}; \frac{500\nu}{y^2\omega}\right); \frac{4\rho\sigma_{w2}k}{CD_{k\omega}y^2}\right] \tag{4-8}$$

where y is the distance to the next surface and $CD_{k\omega}$ is the positive portion of the cross-diffusion term and defined as follows:

$$CD_{k\omega} = \max\left(2\rho\sigma_{\omega 2}\frac{1}{\omega}\frac{\partial k}{\partial x_j}\frac{\partial \omega}{\partial x_j}, 10^{-20}\right) \tag{4-9}$$

For the SST model, the constants are as follows:

$$\sigma_{k1} = 0.85, \quad \sigma_{\omega 1} = 0.5, \quad \beta_1 = 0.0750, \quad \beta^* = 0.09,$$
$$\gamma_1 = \frac{\beta_1}{\beta^*} - \frac{\sigma_{\omega 1}\kappa^2}{\sqrt{\beta^*}}, \quad \kappa = 0.41 \tag{4-10}$$

The turbulent viscosity is defined as follows:

$$\nu_t = \frac{a_1 k}{\max\left(a_1\omega; \Omega F_2\right)} \tag{4-11}$$

where a_1 is the shear stress limiter parameter which has a default value of 0.31. F_2 is calculated as follows:

$$F_2 = \tanh\left(arg_2^2\right) \tag{4-12}$$

$$\arg_2 = \max\left(\frac{2\sqrt{k}}{0.09\omega y}; \frac{500\nu}{y^2\omega}\right) \tag{4-13}$$

In a best practice report prepared by Menter [90], it is mentioned that the SST model's ability to accurately predict separation in complex flow scenarios is highly dependent on the SST-limiter (Shear Stress Limiter Parameter) which reduces the eddy-viscosity in such regions. However, in certain cases, larger separation zones may be encountered, which could result from complex 3D geometry-flow interactions and may lead undesirable results. In these situations, it is suggested that the a_1 coefficient can be increased within the range of a_1 = 0.31 to 1.0 to minimize separation. The stress limiter parameter has been found to be effective in SWBLI [92]–[94]. Moreover, Zeng et al. [95] found that, for a constant area duct, a_1 is the most sensitive turbulence model parameter in terms of predicting pseudo-shock structures. Another paper [96] investigated the range of 0.31-0.40 for the a_1 coefficient in shock-separated flows, finding that increasing the coefficient beyond 0.40 resulted in results similar to the BSL model. Additionally, Schaefer et al. [93] examined turbulence model closure coefficients for transonic wall-bounded flows and adjusted the a_1 coefficient within the same range of 0.31 to 0.40. The researchers claimed that, in the content of a_1 coefficient range, Menter agreed with their assessment in a private communication. In light of these findings, simulations using the SST model with various a_1 parameters according to the matrix of simulations (see Section 4.4) were conducted.

4.3 Grid Sensitivity Study

To assess the grid sensitivity, a series of simulations were performed for the intake geometry without bleed at Mach = 3 condition. Three different grids were generated with maximum element edge sizes of 0.7 mm, 1 mm, and 1.5 mm, called coarse, nominal, and fine grids, respectively. The coarse, nominal (mid), and fine grids consisted of approximately 2.5, 7.1, and 15.9 million cells, respectively.

The computed pressure along the intake is compared in Figure 4-3. The results show that the pressure is very similar among the three grids upstream of about 180 mm on the cowl side and around 160 mm on the ramp side. Downstream of those points, the effect of the pseudo-shock is observed. The pressure rise characteristics at 180 mm on the cowl side show slight differences between the coarse and nominal (mid) grids, but they are similar between the nominal and fine grids. The same can be said for the ramp side at around 160 mm. There are noticeable differences at around 260 mm on the cowl side, especially between the coarse and the nominal grids. However, the difference between the mid and fine grids is lower. Therefore, it is concluded that the nominal grid is sufficiently dense to obtain grid independence, and all the simulations can be conducted using the settings of the nominal (mid) grid.

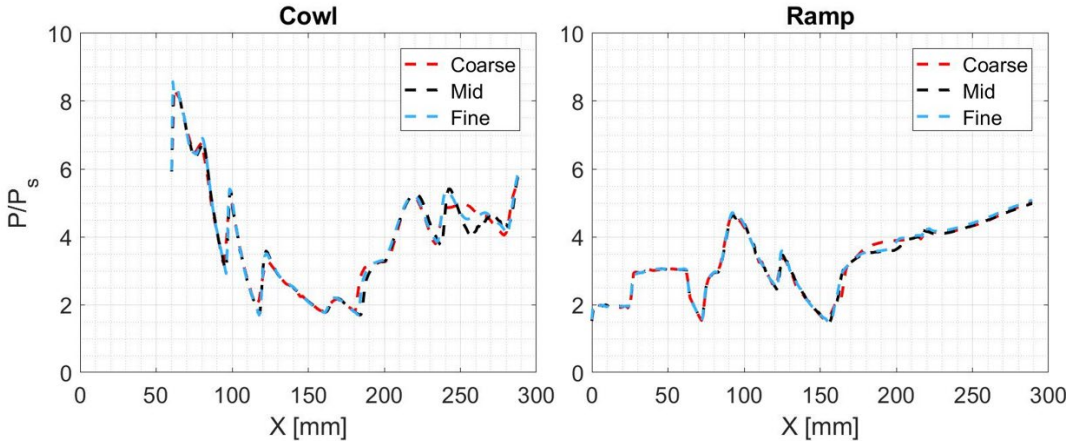


Figure 4-3. Change of pressure along the intake for different grid sizes.

4.4 Matrix of Simulations

The simulations were performed for test items with and without bleed at Mach numbers of 2.63 and 3, as well as at different back pressure valve positions. In addition, the effect of turbulence model on the results of the simulations was investigated by conducting the simulations with both Menter's SST and BSL models. The effect of a coefficient, a_1, related to the shear stress limiter of the SST model, was also investigated by conducting the simulations for different values of the a_1. The matrix of simulations is presented in Table 4-2. A total of 52 simulations were performed.

Table 4-2. Matrix of simulations.

Test	Mach	Bleed	Valve Position No	Turbulence Model [Eqn. (4-1) to (4-13)]
4331	3.00	with	1	$SST, a_1 = 0.34, BSL$
			15	$SST, a_1 = 0.34, a_1 = 0.38, BSL$
			18	$SST, a_1 = 0.34, BSL$
			19	$SST, a_1 = 0.34, BSL$
			20	$SST, a_1 = 0.34, BSL$
4340	2.63		1	$SST, a_1 = 0.34, BSL$
			15	$SST, a_1 = 0.34, BSL$
			18	$SST, a_1 = 0.34, BSL$
			19	$SST, a_1 = 0.34, BSL$
			20	$SST, a_1 = 0.34, BSL$
4372	3.00	without	1	$SST, a_1 = 0.34, BSL$
			15	$SST, a_1 = 0.34, a_1 = 0.38, BSL$
			18	$SST, a_1 = 0.34, a_1 = 0.38, BSL$
4373	2.63		1	$SST, a_1 = 0.34, BSL$
			15	$SST, a_1 = 0.34, a_1 = 0.38, BSL$
			18	$SST, a_1 = 0.34, BSL$

4.5 Results and Comparison with The Experimental Data

In the first part of this section the results of the simulations conducted at VPN 1 (fully open) are presented and are compared with the experimental data to evaluate the predictive capability of the computational method and turbulence models, especially upstream of the pseudo-shock. Subsequently, in section 4.5.2, the results for different back throttling conditions are presented and analyzed, including an examination of the predictive capability along and beyond the pseudo-shock region.

Through the section, Mach number contour plots are presented with a black Mach equal to 1 line to facilitate differentiation between supersonic and subsonic areas.

4.5.1 Simulations at VPN 1

4.5.1.1 Simulations at Mach = 3

Mach number contour plot for the corresponding condition to Mach = 3 with bleed test (Test 4331) at VPN 1 obtained using the SST turbulence model with original coefficients is given in Figure 4-4. There are no noticeable differences in the Mach number contour plots of the computations with the BSL and $a_1 = 0.34$. As seen, formation of the pseudo-shock nearly does not exist and chocking at the back pressure valve is not achieved. Diffusive appearance observed in the shock structure forming on the top of the cowl can be attributed to the grid sizes used in that portion of the geometry. As mentioned in section 4.1, larger grid sizes were employed in the vicinity of the top and bottom far-field boundary surfaces. This coarser resolution in those regions can lead to a less accurate representation of the shock structure, resulting in a diffusive appearance.

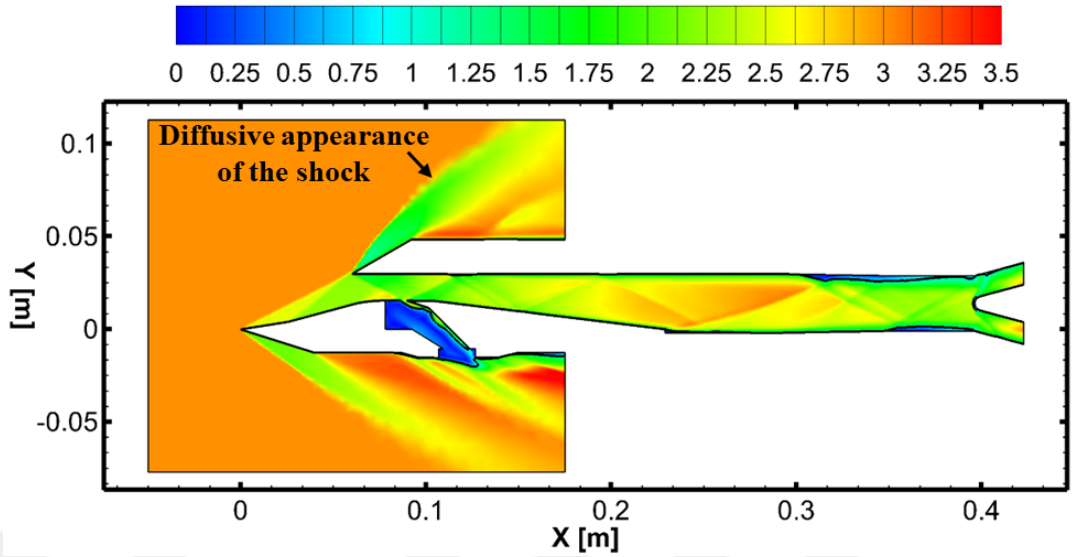


Figure 4-4. Mach number contour for the numerical simulation corresponding to Mach = 3 with bleed (Test 4331) at VPN 1.

The plots presented in Figure 4-5 compare the variation of pressure along the intake between the computation and experimental data for the fully open valve position in Test 4331. The measured pressure values show good agreement with the numerical data until the point of pressure rise due to the formation of the pseudo-shock observed in the experiment. The experiment shows the presence of back pressure effect on measured pressure values at taps D9, D10, and the exit of the intake, which is not captured in the simulations. As a result, all of the turbulence modeling approaches used in the computations are capable of predicting pressure upstream of the pseudo-shock. However, all the numerical simulations fail to predict the formation of the pseudo-shock at the fully open valve condition for Test 4331.

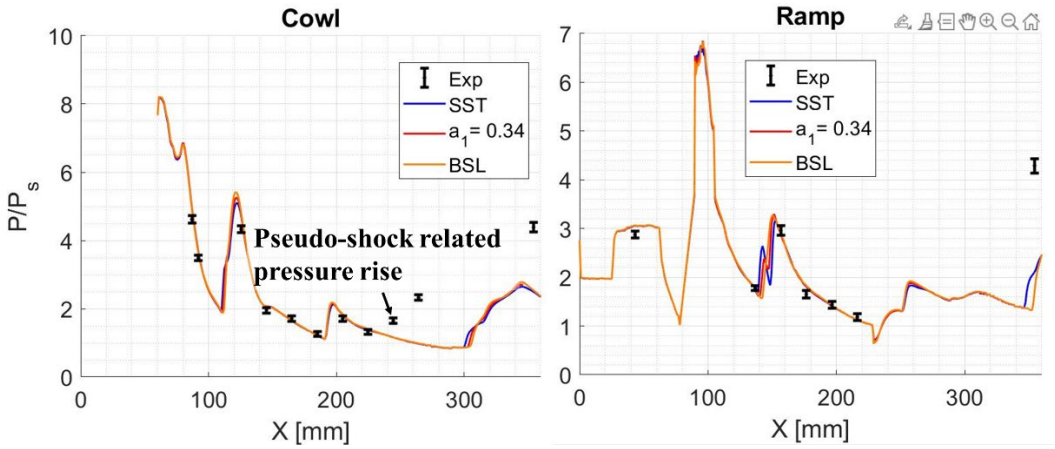


Figure 4-5. Comparison of pressure distribution along the intake between numerical and experimental data for Mach = 3 with bleed (Test 4331) at VPN 1.

Figure 4-6 shows a comparison between the density gradient magnitude contour plot of the computation with SST and the shadowgraph image from the experiment. In the figure, the bleed wedge shock, which causes thickening of the boundary layer or separation, is named as the incident shock. A very small separation bubble is visible on the simulation result at a particular point, and it is likely that this is also the case for the experiment, based on the similarity between the experimental and the numerical pressure distributions. Furthermore, the formation of the reattachment shock might also indicate the existence of a small separation bubble. Velocity vectors colored with Mach number contour plot and zero velocity line are presented in Figure 4-7 to examine the separation bubble. As shown, the zero velocity line covers a very small region, and very brief backflow is observed inside the boundary layer vicinity of the interaction point between the incident shock and cowl surface. Therefore, although the shadowgraph images might appear as a shock reflection of that point, a detailed examination with the results of the CFD simulation reveals that the formation of a very small separation bubble exists.

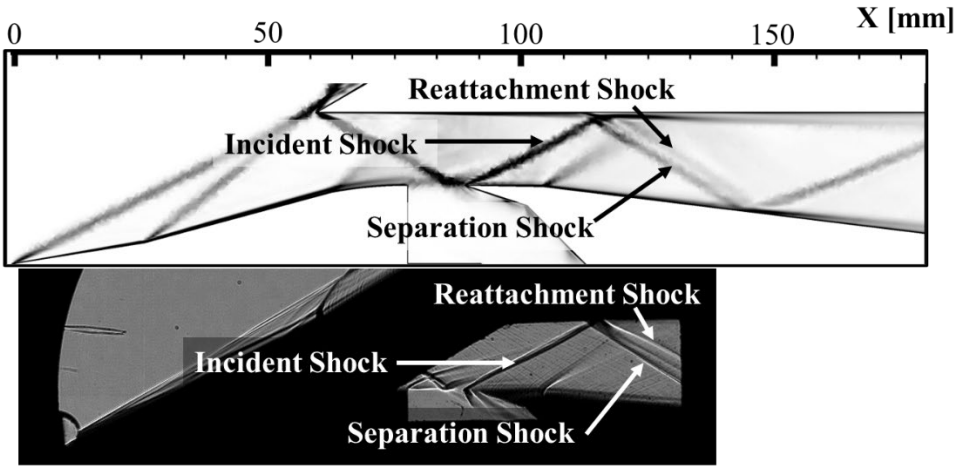


Figure 4-6. Comparison between the numerical density gradient magnitude contour and experimental shadowgraph image for Mach = 3 with bleed (Test 4331) at VPN 1.

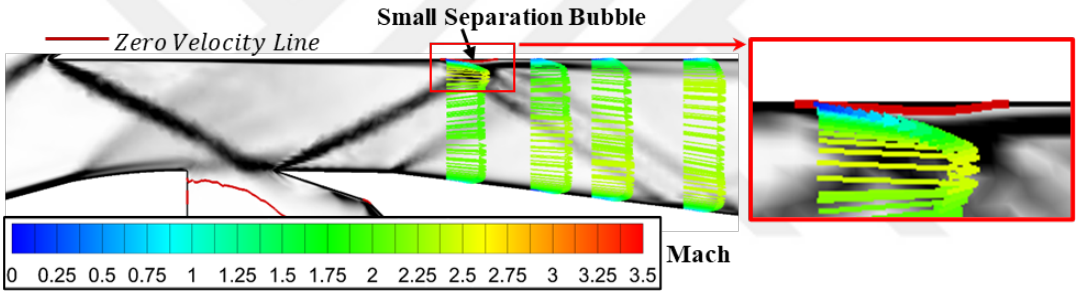


Figure 4-7. Density gradient magnitude contour with velocity vectors and zero velocity line for the numerical simulation corresponding to Mach = 3 with bleed (Test 4331) at VPN 1.

Figure 4-8 presents the Mach number contour plot for the SST turbulence model with original coefficients at VPN 1, corresponding to Mach = 3 without bleed test (Test 4372). The Mach number contour plots for the BSL and $a_1 = 0.34$ computations are similar, with visible pseudo-shock structures. However, in the experiment, as shown in Figure 4-9, the effect of the pseudo-shock is not observed at measurement taps D9 and D10. Upstream of the pseudo-shock, the results of the CFD simulations and experiment are consistent except for points R3, R5 and D5 where the BSL model shows a discrepancy in estimating the separation bubble that forms due to the cowl shock. Moreover, in Figure 4-10, a comparison is made between the separation bubble obtained with the SST model and the BSL model. The

red dashed line indicates the starting point of the sonic line detachment due to separation bubble, while the blue dashed line represents the interaction point of the separation shock of the bubble with the cowl surface, obtained with the SST model using the original coefficients. The computation with $a_1 = 0.34$ predicts a separation bubble that is slightly downstream compared to the SST model with original coefficients. On the other hand, the BSL model shows a more noticeable downstream shift in the separation bubble and separation shock compared to the SST model.

Comparing the numerical pressure data in the vicinity of the separation bubble with the experimental data, it can be concluded that the SST model is better at predicting the cowl shock-related separation bubble. Figure 4-11 compares the density gradient magnitude contour obtained with the SST model and shadowgraph image of the experiment, revealing similar flow structures. The zero-velocity line shows the formation of a separation bubble, and velocity vectors reveal thickening of the boundary layer downstream of the bubble.

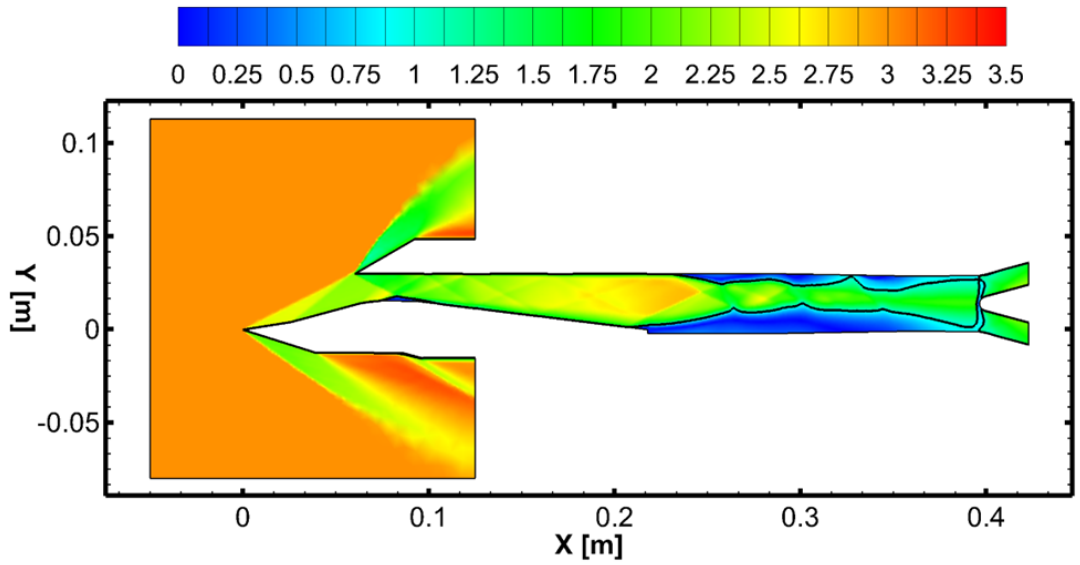


Figure 4-8. Mach number contour for the numerical simulation corresponding to Mach = 3 without bleed (Test 4372) at VPN 1.

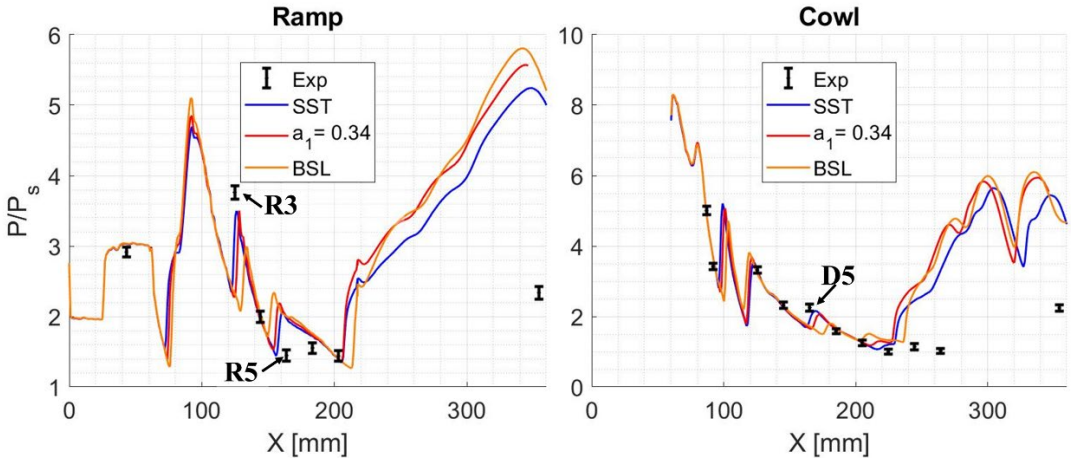


Figure 4-9. Comparison of pressure distribution along the intake between numerical and experimental data for Mach = 3 without bleed (Test 4372) with fully open valve.

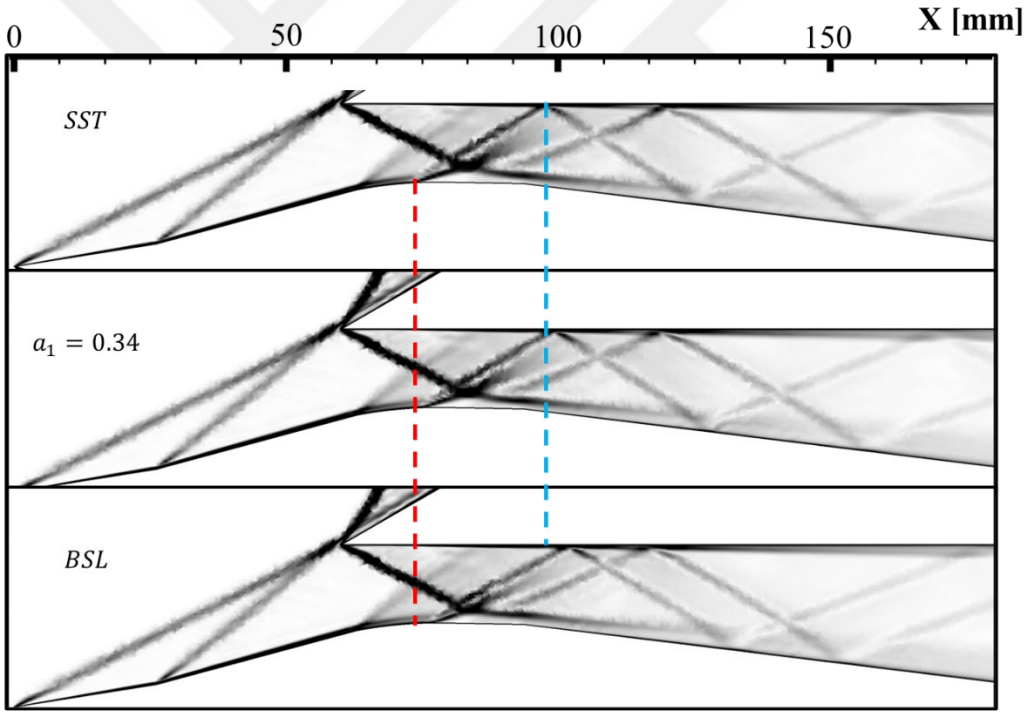


Figure 4-10. Comparison of the density gradient magnitude contours of numerical simulations for the corresponding condition to Mach = 3 without bleed (Test 4372) at VPN 1.

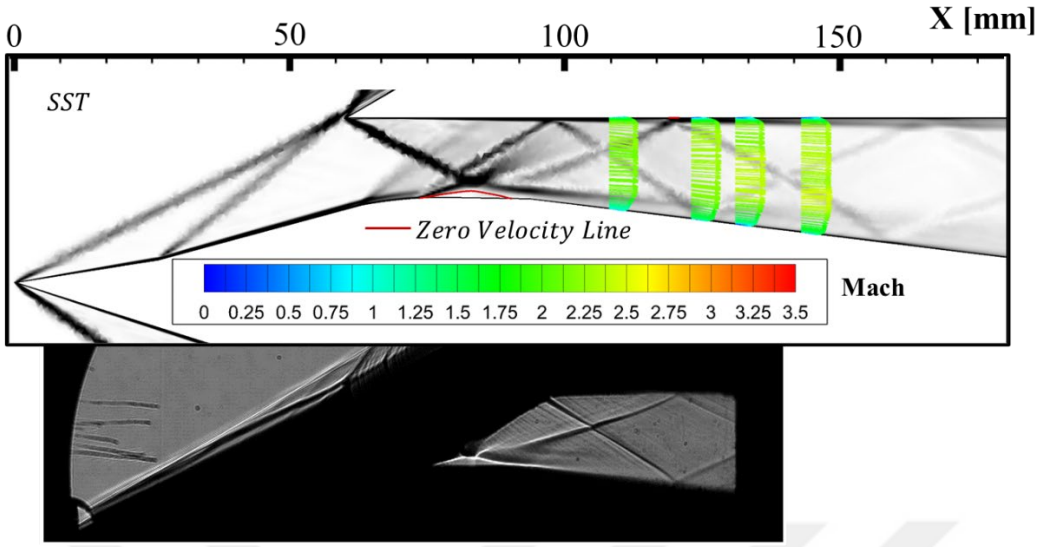


Figure 4-11. Comparison of the numerical density gradient magnitude contour (with velocity vectors) and experimental shadowgraph images for Mach = 3 without bleed (Test 4372) at VPN 1.

4.5.1.2 Simulations for Mach = 2.63

Figure 4-12 displays the Mach number contour plots for Mach = 2.63 with bleed case (Test 4340) at VPN 1, obtained with the SST turbulence model with original coefficients, SST turbulence model with $a_1 = 0.34$, and the BSL turbulence model. While there are minor variations in the bleed channel, the Mach number contour plots upstream of the pseudo-shock show no other significant differences. However, the orientation of the pseudo-shock differs between the SST models and the BSL model. The simulations with SST models indicate a reattached Mach=1 line on the ramp side, while the BSL model results in a detached Mach=1 line.

This difference is further reflected in the pressure data presented in Figure 4-13. Downstream of the starting point of the pseudo-shock, the pressure data for the computation with SST model exhibit a fluctuating pattern on the ramp side along the x-axis, unlike the one with the BSL model. However, there are no noticeable differences upstream of the pseudo-shock, and all the numerical simulations' pressure data agree with the experimental data. The pressure data for the numerical

computations with SST, for both original coefficients and with $a_1 = 0.34$, show better agreement with the experimental data at D9 and D10 measurement points, as well as the pressure at the exit on the cowl and ramp side. Compared to the cases at Mach = 3, the formation of the pseudo-shock and pressure rise characteristics are better simulated for Mach = 2.63. Regarding the effect of bleed wedge shock, similar observations can be made by examining shadowgraph images and numerical density gradient magnitude contours, as previously discussed with Figure 4-6.

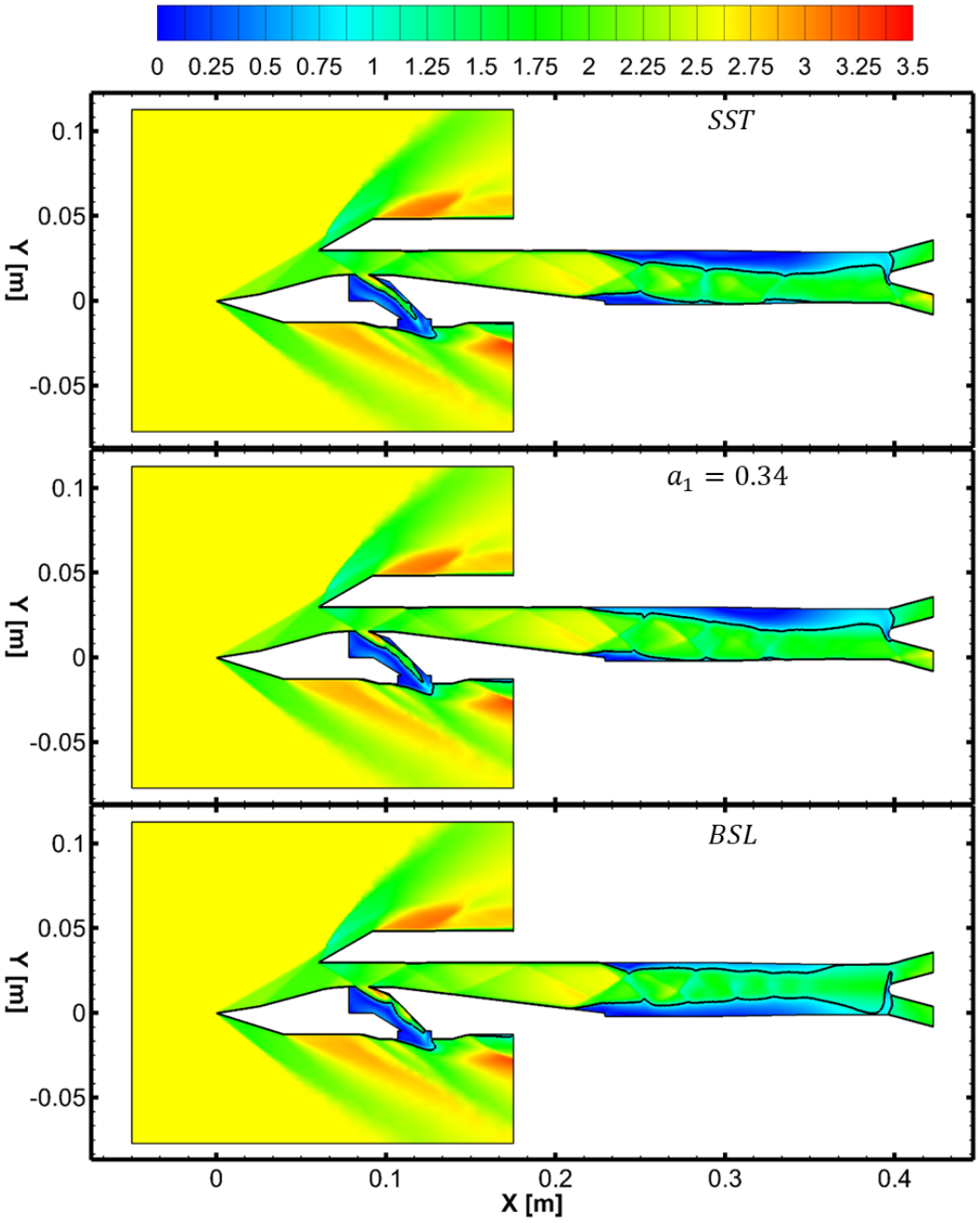


Figure 4-12. Mach number contours for the numerical simulations corresponding to Mach = 2.63 with bleed (Test 4340) at VPN 1.

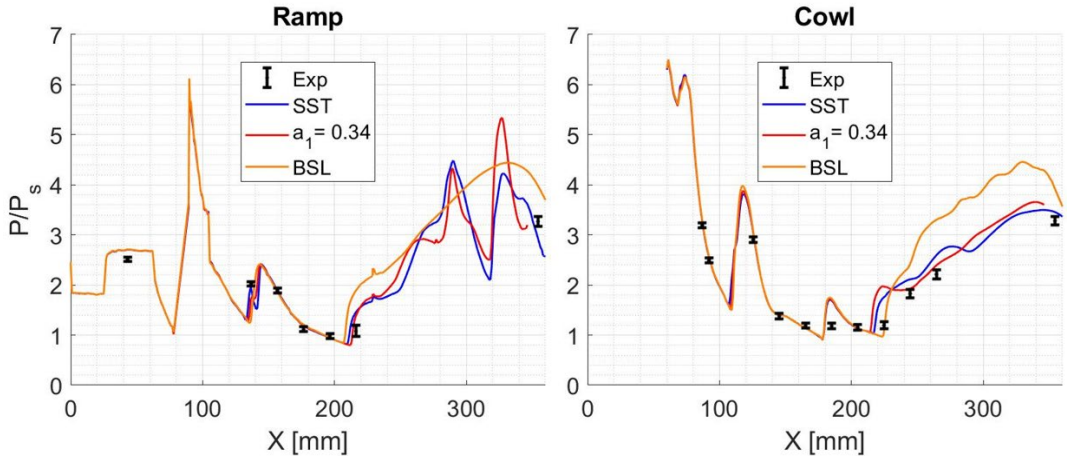


Figure 4-13. Comparison of pressure distribution along the intake between numerical and experimental data for Mach = 2.63 with bleed (Test 4340) at VPN 1.

Figure 4-14 illustrates the Mach number contour plot for Mach = 2.63 without bleed case (Test 4373) at VPN 1, obtained with the SST turbulence model using the original coefficients, and no significant differences are observed in the Mach number contour plots for the simulations with $a_1 = 0.34$ and BSL models. However, a closer examination of the pressure distribution along the intake in Figure 4-15 reveals some differences. As with Test 4372 without bleed at Mach = 3, there are discrepancies in the vicinity of the separation bubble formed due to the cowl shock in Test 4373 as well. These differences lead to disparities in the results on the cowl side, particularly closer to the D1 tap. Moreover, the R7 pressure is lower on the ramp side, indicating that the effect of the pseudo-shock is not seen on the R7 tap, and the related separation shock is downstream of the R7. However, on the cowl side, the pressure rise of the pseudo-shock is observed at the D7 tap, and it is also estimated in the numerical simulations.

The difference related to the separation bubble, which forms due to the cowl shock, can be examined closely in Figure 4-16. The red dashed line indicates the starting point of the sonic line detachment due to the separation bubble, while the blue dashed line represents the interaction point of the separation shock of the bubble with the cowl surface, obtained with the SST model using the original coefficients. The simulation with $a_1 = 0.34$ predicts a separation bubble that is slightly downstream

compared to the SST model with original coefficients. On the other hand, the BSL model shows a more noticeable downstream shift in the separation bubble and separation shock compared to the SST model, which is similar to the observations made for the Mach = 3 case without bleed (Test 4372).

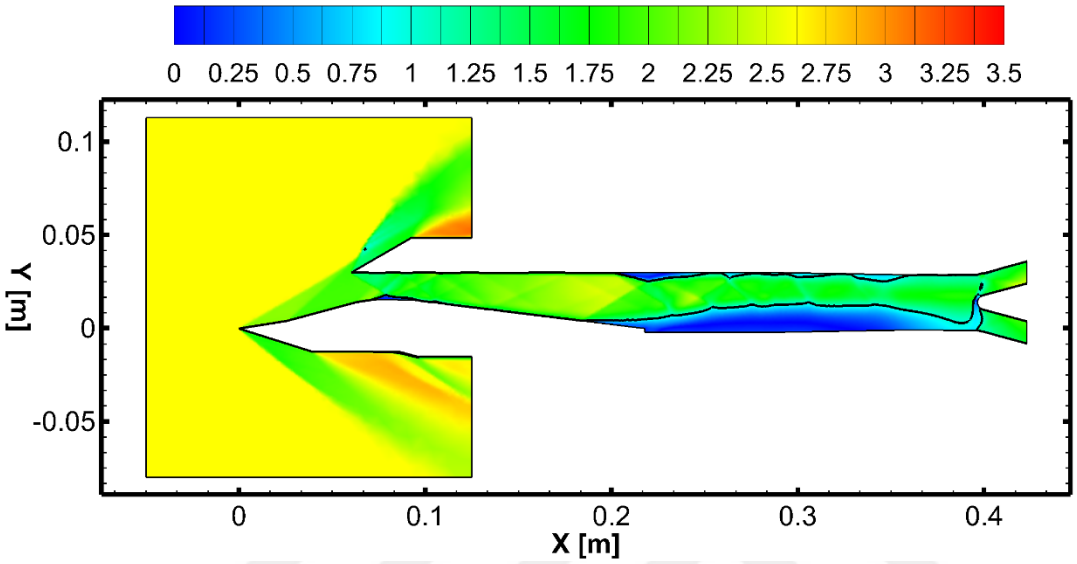


Figure 4-14. Mach number contours for the numerical simulations corresponding to Mach = 2.63 without bleed (Test 4373) at VPN 1.

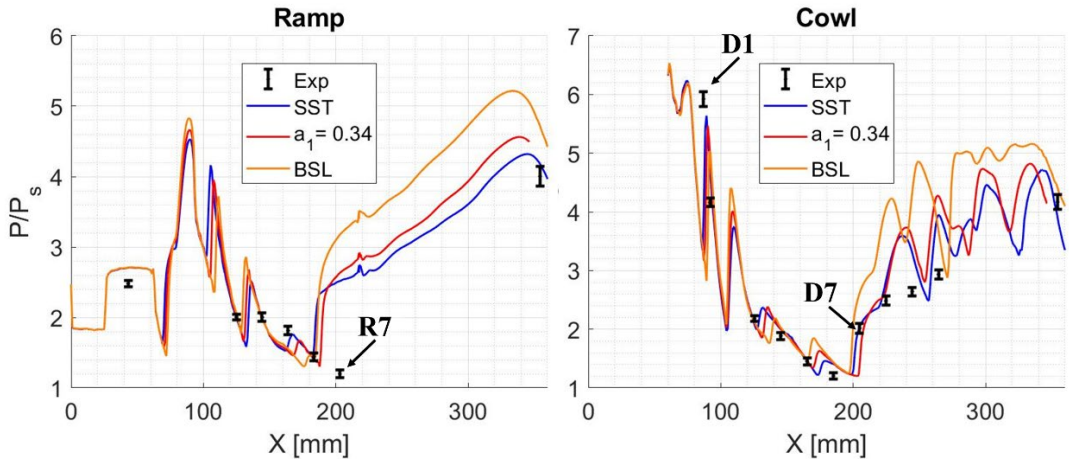


Figure 4-15. Comparison of pressure distribution along the intake between numerical and experimental data for Mach = 2.63 without bleed (Test 4373) at VPN 1.

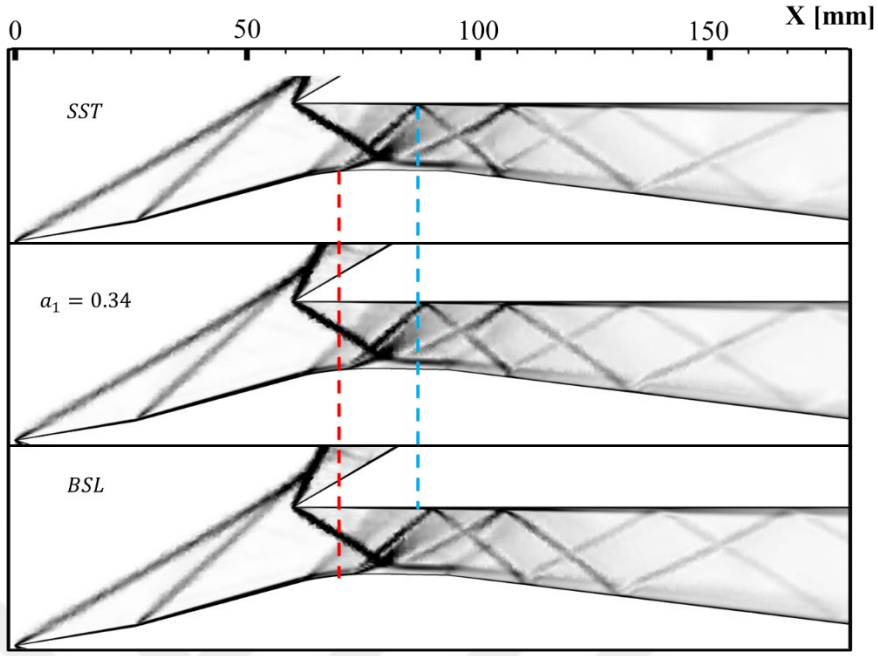


Figure 4-16. Comparison of the density gradient magnitude contours of numerical simulations for the corresponding condition to Mach = 2.63 without bleed (Test 4373) at VPN 1.

4.5.1.3 Examination of Pre-Shock Mach Number

In section 1.3, it was discussed that the pre-shock Mach number is an important parameter that influences the structure of the pseudo-shock. Studies investigating the effect of the pre-shock Mach number typically focus on isolated duct flows, where the flow conditions upstream of the pseudo-shock are relatively homogenous. However, in the case of a supersonic intake, the complex shape of the intake and the presence of oblique shocks and their reflections result in a heterogeneous distribution of flow parameters, including the Mach number.

As discussed in the preceding sections, the simulations conducted in this study are in good agreement with the experimental data in the upstream region of the pseudo-shock. Therefore, the results of the simulations can be valuable for examining the distribution of the pre-shock Mach number observed in the experiments. By combining the experimental data with the simulation results, a more comprehensive

understanding of the effect of pre-shock Mach distribution in the intake flow can be obtained.

Mach number distributions were analyzed along several lines positioned on the symmetry plane at various locations throughout the diffuser downstream of the bleed channel. These lines are shown in Figure 4-17. The L1 line is positioned 95 mm downstream from the ramp tip, and successive lines are placed at 2 mm intervals. It should be noted that line L6 is positioned at the corner on the ramp side where the diffuser angle transitions from 1 degree to 7 degrees.

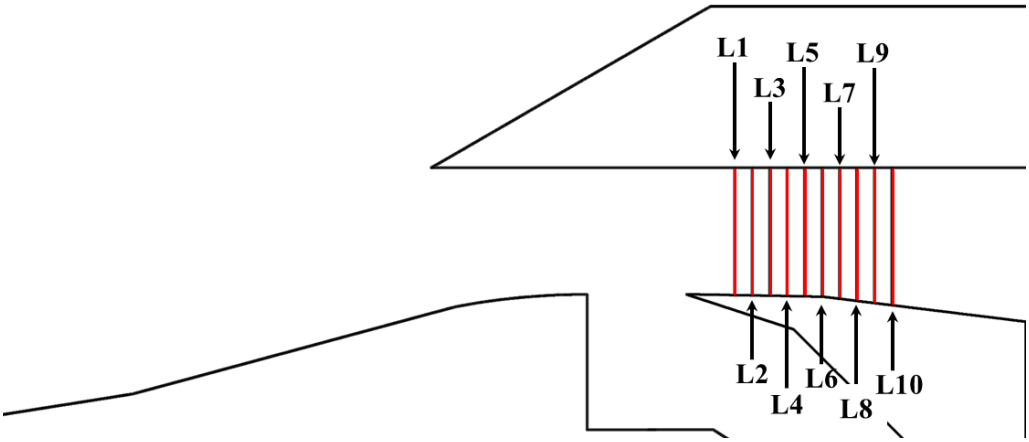


Figure 4-17. Placed lines.

Obtained Mach number distributions with the SST model using the original coefficients for freestream Mach numbers of 2.63 and 3 are given in Figure 4-18. As seen, going toward downstream, the Mach number closer to the ramp side increases and the Mach number closer to the cowl side decreases.

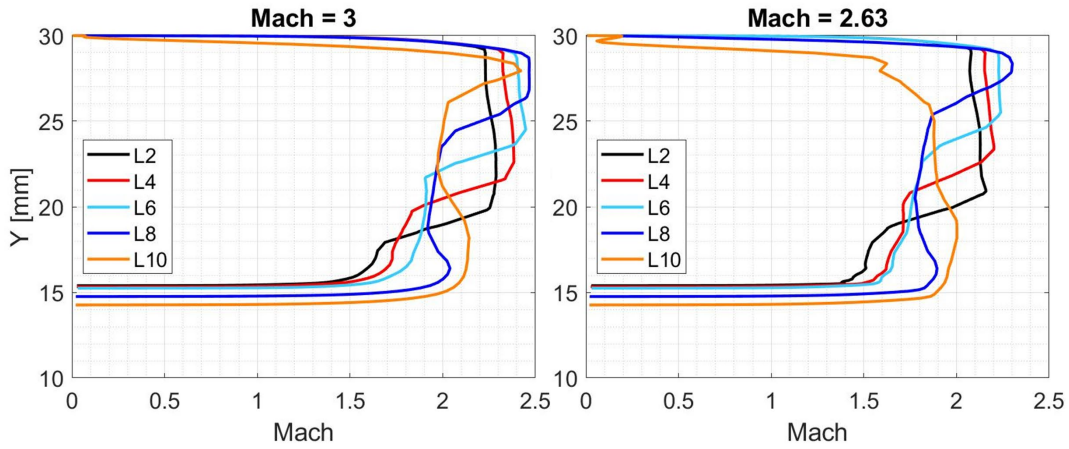


Figure 4-18. Variation of Mach number distribution along placed lines obtained from the numerical simulations corresponding to Mach = 2.63 and Mach = 3 with bleed at VPN 1.

The shadowgraph images, obtained with tests in which the intake with bleed is tested, presented in sections 3.1.1 and 3.1.2 provide a visual evidence that when the first shock of the pseudo-shock on the ramp side reaches the diffuser section with a lower angle, λ-type shock structures are observed instead of X-type structures. This behavior is observed in tests conducted at both Mach numbers of 3 and 2.63. To further understand the transition from X-type to λ-type shocks, a comparison of Mach number distributions inside the diffuser at different freestream Mach numbers are given in Figure 4-19 and Figure 4-20. The trend of the distributions is similar, but the values obtained at Mach number 3 are higher. This suggests that the angle of the diffuser is a significant factor in determining the change of shock type, and in this particular case, it may be more influential than the pre-shock Mach number.

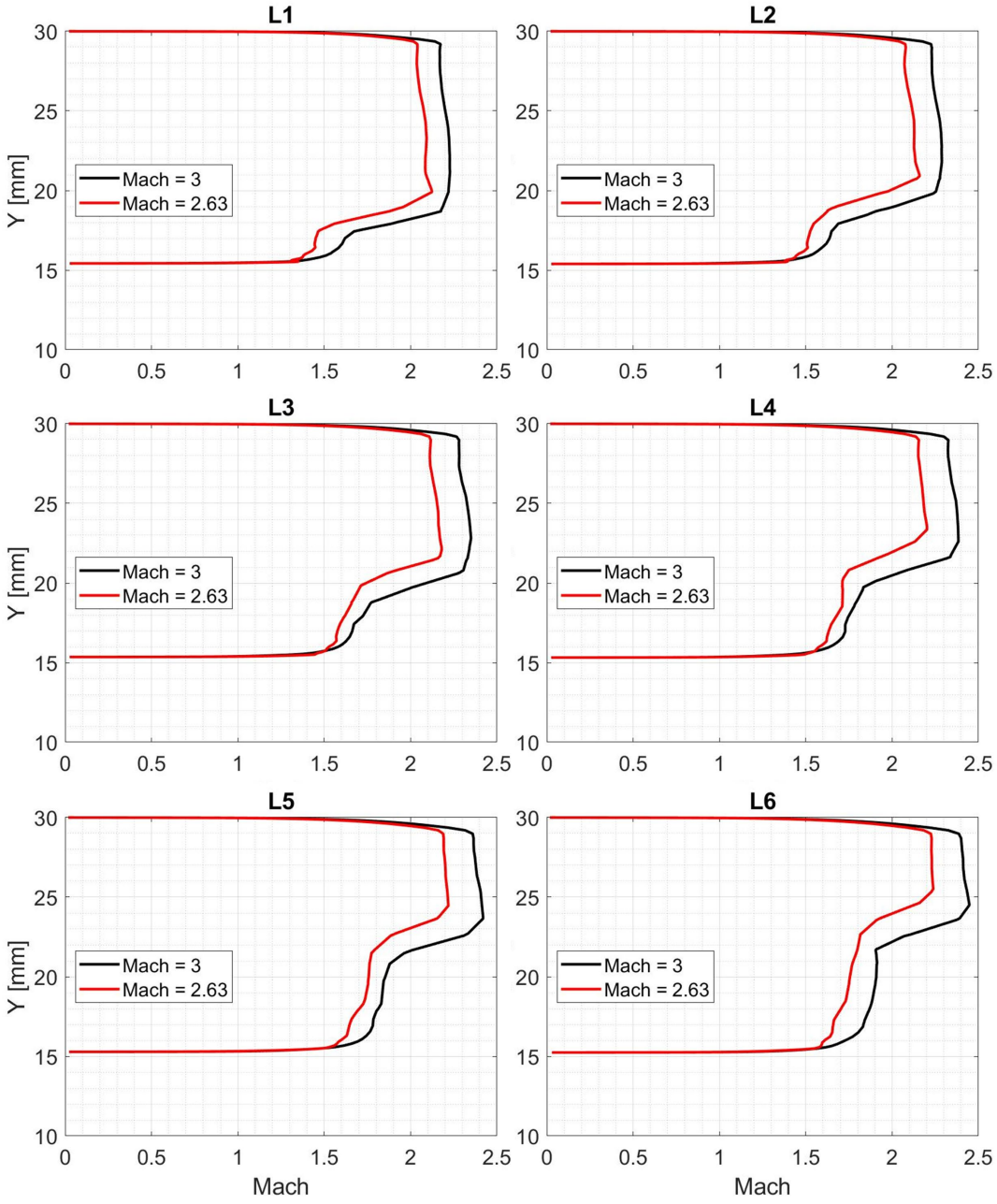


Figure 4-19. Comparison of Mach number distribution along L1-L6 obtained from the numerical simulations corresponding to Mach = 2.63 and Mach = 3 with bleed at VPN 1.

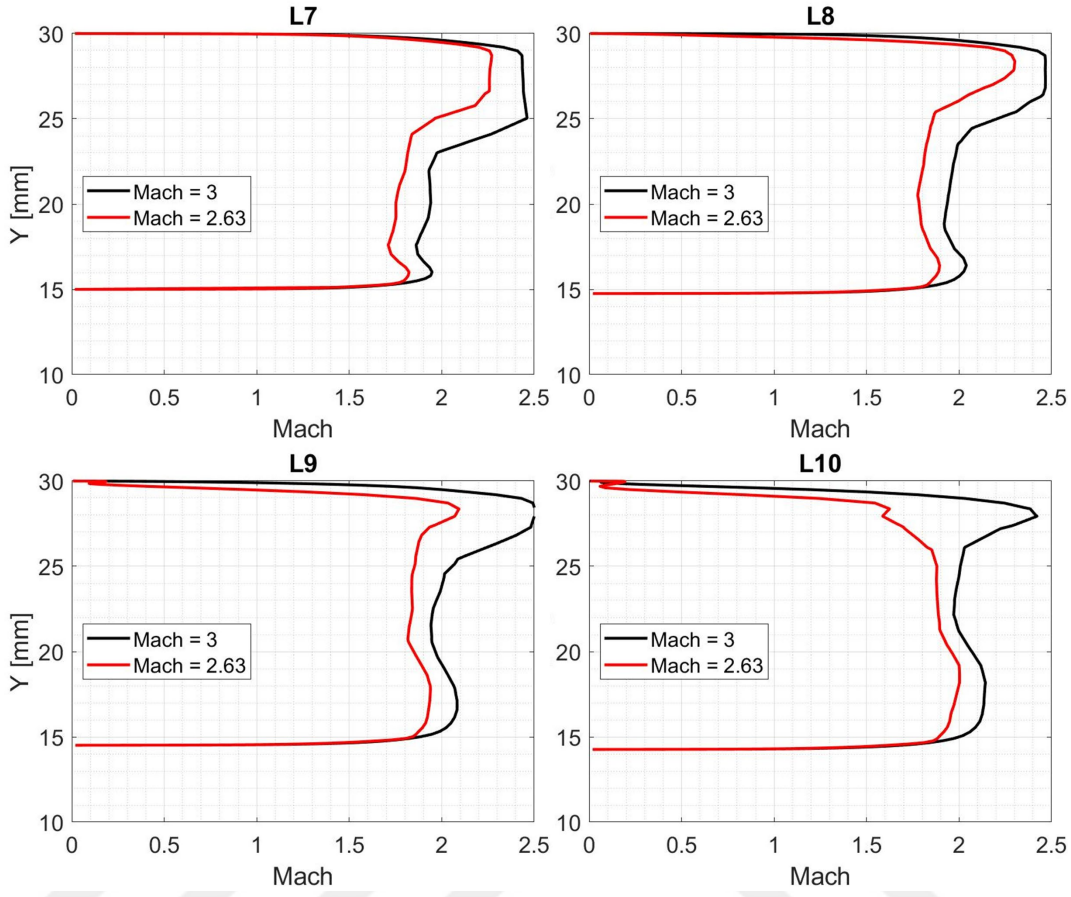


Figure 4-20. Comparison of Mach number distribution along L7-L10 obtained from the numerical simulations corresponding to Mach = 2.63 and Mach = 3 with bleed at VPN 1.

4.5.2 Simulations at Different Back Throttling

4.5.2.1 Mach = 3 with Bleed (Test 4331)

Numerical simulations were performed for Mach = 3 with bleed case (Test 4331) at VPNs 1, 15, 18, 19, and 20. The results for VPN 1 were already presented in the previous section, and this section covers the results for the other valve positions.

4.5.2.1.1 VPN 15

Figure 4-21 compares the Mach number contour plots for VPN 15, where the most significant difference observed is the reduction in the length of the pseudo-shock as a_1 increases for the SST model and the BSL model showing the shortest pseudo-shock. Figure 4-22 compares the pressure data obtained from numerical simulations and experiments. The SST model with original coefficients shows the largest deviation from the experimental data, while the SST model with $a_1 = 0.38$ and the BSL model demonstrate better agreement. It is worth noting that no significant differences are observed upstream of the pseudo-shock. Upon analyzing the pressure distribution obtained from the numerical simulations, it becomes evident that following the initiation of the pseudo-shock, the pressure on the ramp side consistently increases, while on the cowl side, it fluctuates along the x-axis. This behavior has also been observed by Lee et al. [16]. The researchers proposed that the asymmetric orientation of the pseudo-shock makes the surfaces where the pseudo-shock is oriented susceptible to the influence of shock waves and expansion waves from the shock-train, resulting in pressure fluctuations in the streamwise direction.

It is important to note that the difference in the behavior discussed in the preceding paragraph is not observed in the experimental data. On the ramp side, both experimental and numerical data show a monotonic increase after the onset of the pseudo-shock. However, on the cowl side, only the experimental data exhibit such variation, whereas the numerical data fluctuate along the x-axis. This deviation is attributed to the oscillatory behavior of the pseudo-shock, which moves back and forth. The pressure measurement tubing causes damping of high-frequency oscillations, resulting in the measured value being closer to the mean of the oscillations, as discussed in Section 2.8.

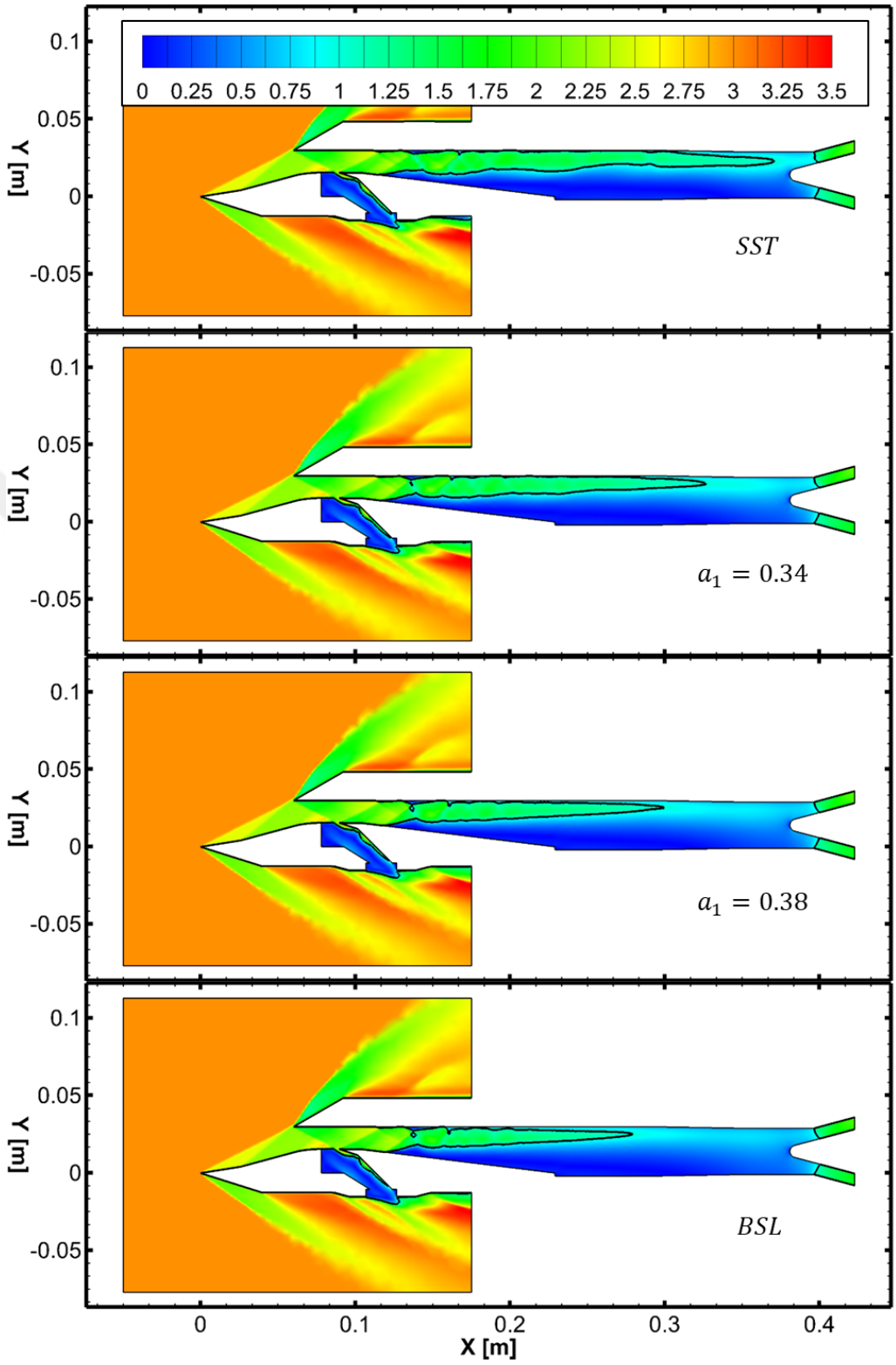


Figure 4-21. Mach number contours for the numerical simulations corresponding to Mach = 3 with bleed (Test 4331) at VPN 15.

The pressure distribution shows that the location of the starting point for the sonic line separation due to the pseudo-shock slightly differs among numerical simulations, with the SST model estimating 4 mm more upstream starting point than the BSL model on the ramp side. Visual comparison is presented in Figure 4-23, where the red dashed line represents the starting point of the sonic line separation on the ramp side calculated with the SST model which confirms that the starting point of the pseudo-shock is relatively downstream for the BSL model. The figure also includes the shadowgraph image from the experiment, showing that the orientation of the pseudo-shock is similar to that of the numerical simulations. Additionally, the shock structures, specifically the first separation shocks on the cowl and ramp side, are also similar between the experiment and numerical simulations.

The pressure variation along the intake reveals slight differences in the location where the pressure rise due to the pseudo-shock starts, particularly in the vicinity of D2 tap. The simulations with $a_1 = 0.34$ and $a_1 = 0.38$ estimate the starting point slightly better, while the BSL model predicts the pressure rise to occur slightly downstream.

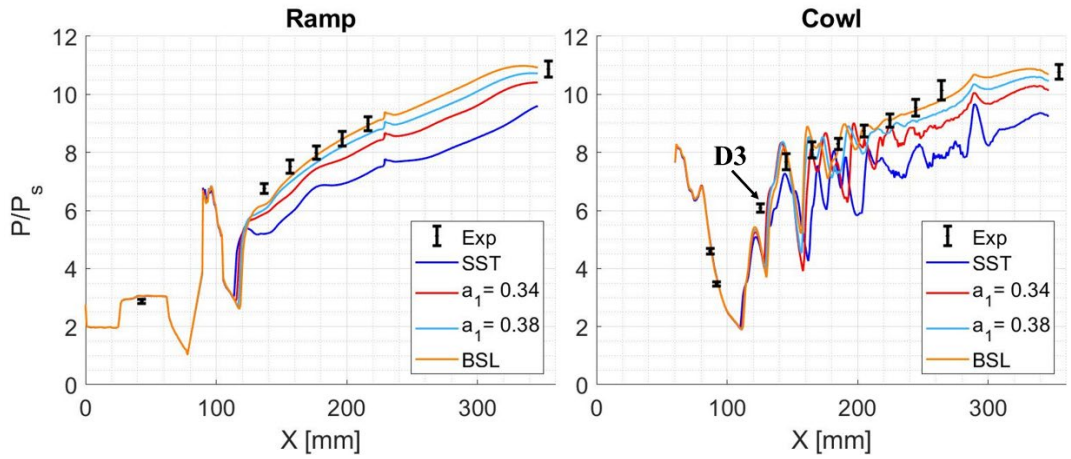


Figure 4-22. Comparison of pressure distribution along the intake between numerical and experimental data for Mach = 3 with bleed (Test 4331) at VPN 15.

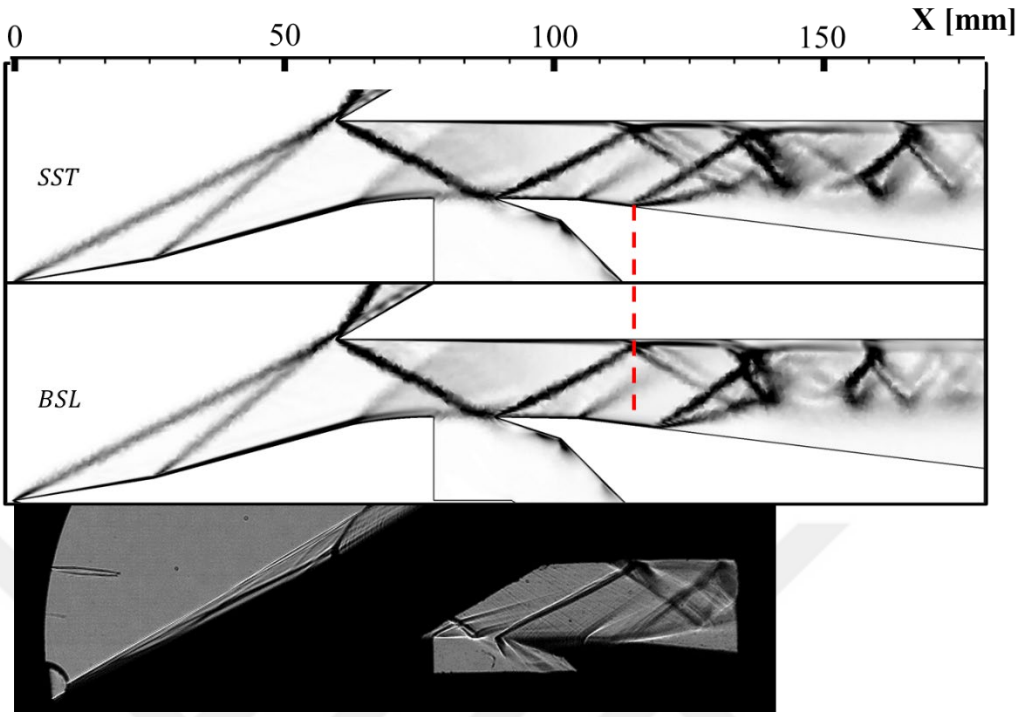


Figure 4-23. Numerical density gradient magnitude contours and experimental shadowgraph image for Mach = 3 with bleed (Test 4331) at VPN 15.

To gain insight into the separation characteristics, velocity vectors and zero velocity lines obtained with $a_1 = 0.38$ were examined, as shown in Figure 4-24. The results indicate a relatively small separation bubble on the cowl side, which leads to a separation shock. On the ramp side, although the sonic line and shock-train part of the pseudo-shock are completely detached from the ramp side, the flow tends to reattach at some point. Beyond the separation bubble, thickening of the boundary layer is observed, and the subsonic layer also thickens, generating a confinement effect for the pseudo-shock. As a result, the supersonic portion of the pseudo-shock narrows down at the downstream.

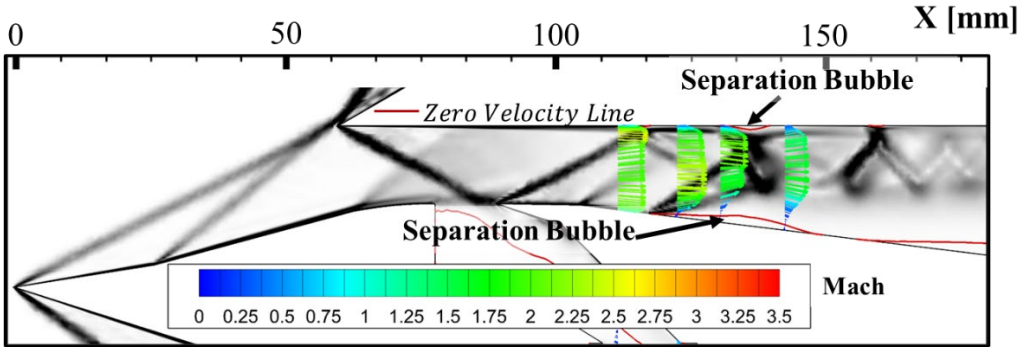


Figure 4-24. Density gradient magnitude contour with velocity vectors and zero velocity line for the numerical simulation corresponding to Mach = 3 with bleed (Test 4331) at VPN 15.

The pressure distribution at the exit of the intake is compared in Figure 4-25. It is observed that the simulations with the BSL and $a_1 = 0.38$ models give better agreement with the experimental data. The SST model with the original coefficients estimates a longer pseudo-shock, which results in insufficient pressure rise. The Mach number distribution is also provided in the figure, and it is seen that estimating a longer pseudo-shock with the SST model results in a more heterogeneous Mach distribution, with the maximum Mach number exceeding 1. However, a comparison of the pressure with the experiments reveals that the pressure rise characteristics of the pseudo-shock are better predicted with the $a_1 = 0.38$ and BSL models, and their distribution of Mach number does not exceed 1.

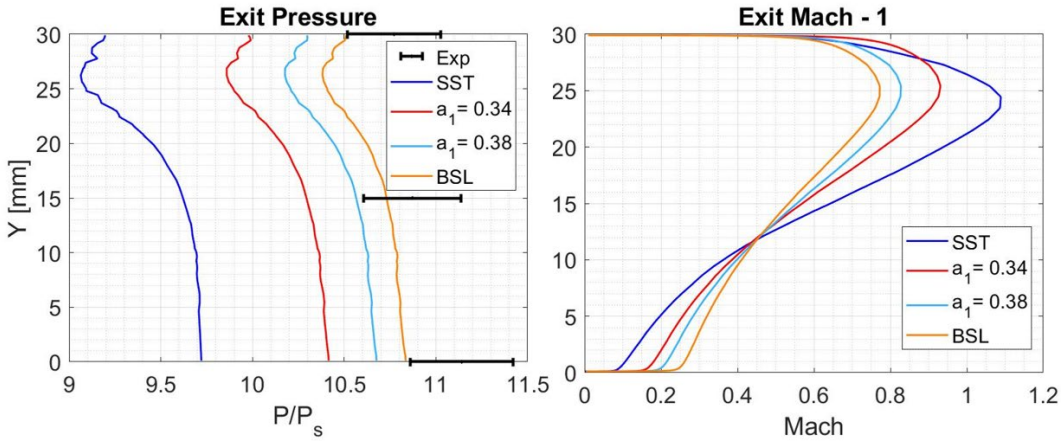


Figure 4-25. Comparison of pressure distribution and Mach number at the exit of the intake for Mach = 3 with bleed (Test 4331) at VPN 15.

4.5.2.1.2 VPN 18

Figure 4-26 presents a comparison of the Mach number contour plots for VPN 18, highlighting the shape differences of the pseudo-shock with increasing a_1 values for the SST model. A thicker and a shorter pseudo-shock obtained with the SST model using original coefficients. The orientation of the pseudo-shocks is similar, directed towards the ramp side, with the separation of the Mach=1 line observed on the cowl side.

In Figure 4-27, the pressure data obtained from numerical simulations and experiments are compared for VPN 18, showing a smaller deviation than that observed for VPN 15. The SST model with original coefficients underestimates the pressure along the pseudo-shock on both ramp and cowl sides, while the SST model with $a_1 = 0.34$ and the BSL model demonstrate better agreement. The starting point of the pressure rise due to the pseudo-shock, near D2 on the cowl side, is estimated to be more upstream with the SST and SST with $a_1 = 0.34$ models compared to BSL with a difference of 6 mm in the x-distance. However, all simulations estimate the location slightly downstream compared to the experiments, and the predictions with SST models are closer to the experimental data.

The pressure variation along the ramp side shows fluctuations along the x-axis for the numerical simulations due to the shock-train being attached to the ramp side. Fluctuating pattern is not observed in the experimental results. This deviation is attributed to the same reason discussed with previously Figure 4-22.

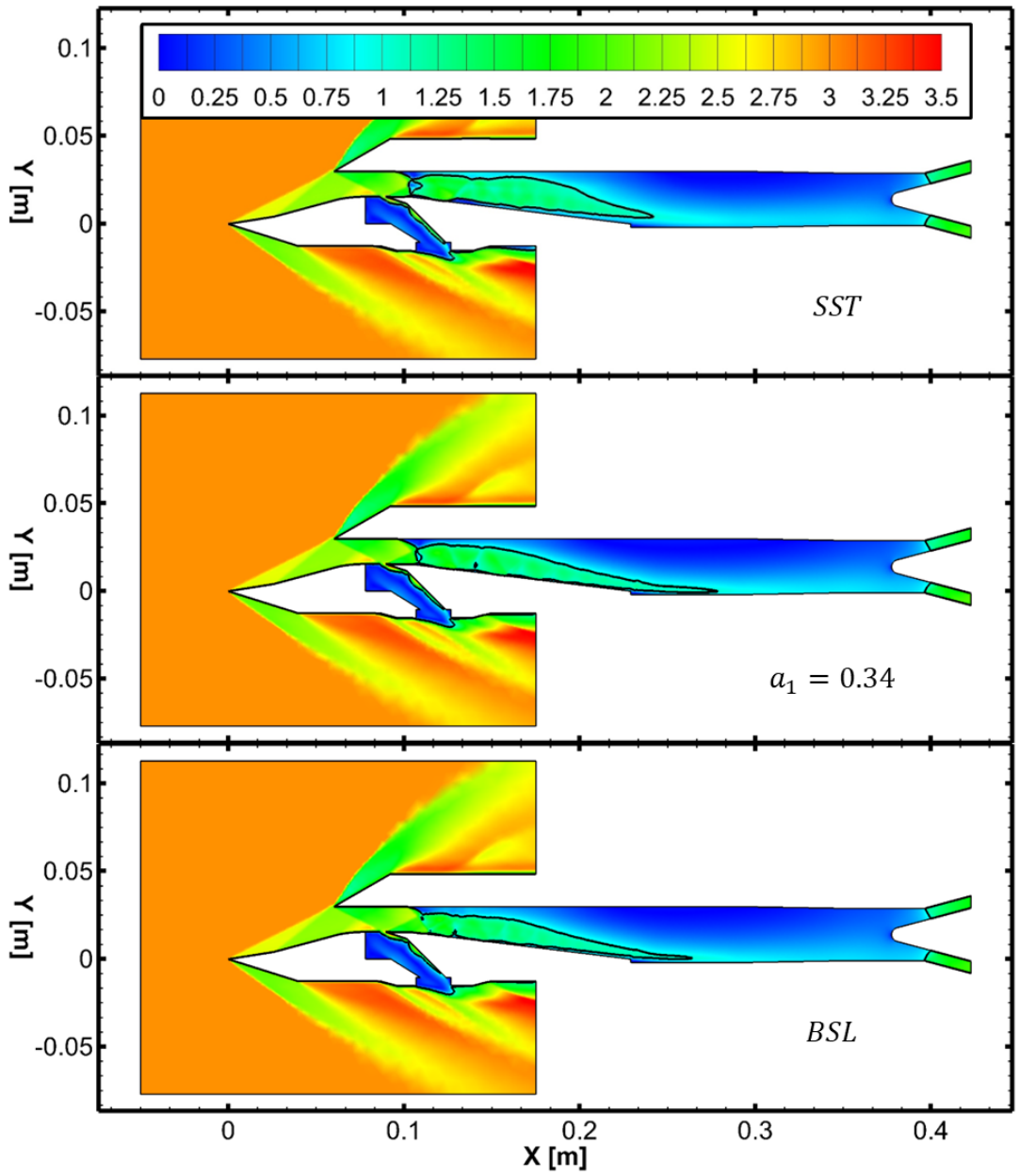


Figure 4-26. Mach number contours for the numerical simulations corresponding to Mach = 3 with bleed (Test 4331) at VPN 18.

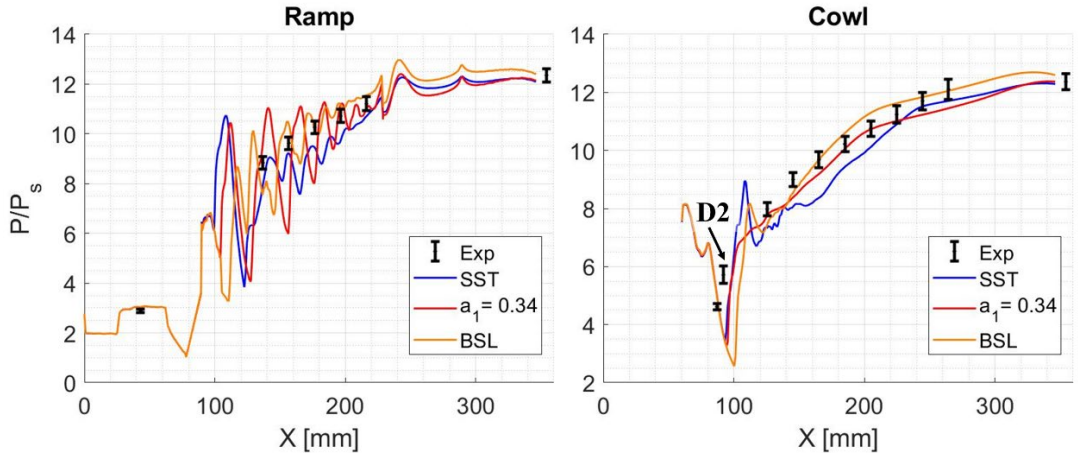


Figure 4-27. Comparison of pressure distribution along the intake between numerical and experimental data for Mach = 3 with bleed (Test 4331) at VPN 18.

Figure 4-28 provides a comparison of the shock structures, with the red dashed line indicating the starting point of the sonic line separation on the cowl side calculated using the SST model with $a_1 = 0.34$. The BSL model shows the starting point of the pseudo-shock to be relatively downstream compared to the other models. The figure also includes a shadowgraph image at the moment when the starting point of the pseudo-shock is in the downstream position during oscillation. The orientation of the pseudo-shock in the experiment is similar to that of the numerical simulations. Moreover, the types of the shock interactions and the locations of the separation bubbles on both the cowl and the ramp side are similar. On the contrary, while the detached sonic line on the cowl side observed in the experiment moves away from the cowl surface, in the numerical simulations it tends to reattach. In Figure 4-29, detailed observations can be made with velocity vectors and zero velocity lines obtained from simulations with $a_1 = 0.34$. The results reveal that the separation bubble on the cowl side is larger than that on the ramp side, leading to the orientation of the pseudo-shock towards the ramp side. However, the difference compared to experiment related to the sonic line on the cowl side suggests that the experiment shows a thicker or longer separation bubble on the cowl side, causing the separated sonic line to move away from the cowl surface.

The numerical simulations of valve 18 indicate that as the valve moves from position 15 to 18, the brief formation of the separation bubble at the point where the bleed wedge shock hits, merges with the separation bubble related to the pseudo-shock.

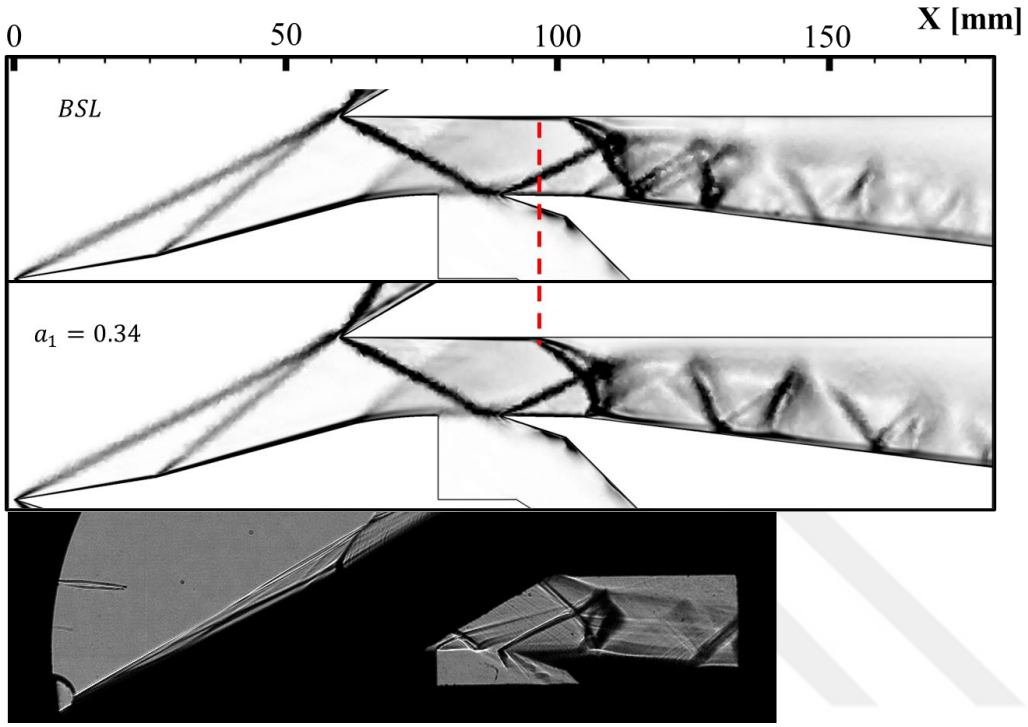


Figure 4-28. Numerical density gradient magnitude contours and experimental shadowgraph image for Mach = 3 with bleed (Test 4331) at VPN 18.

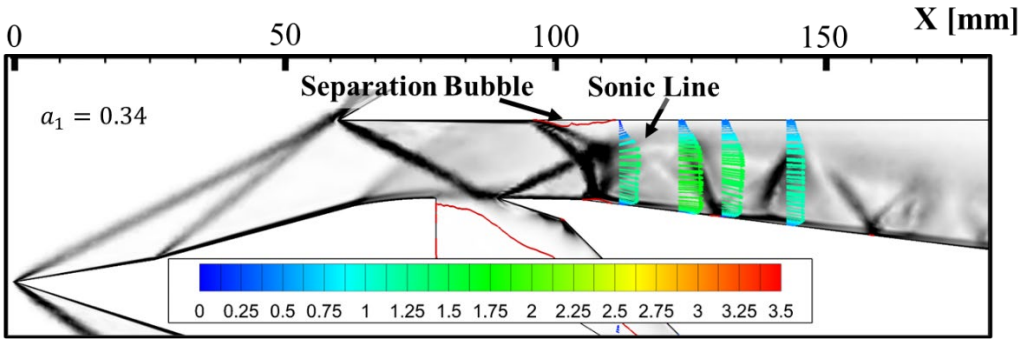


Figure 4-29. Density gradient magnitude contours with velocity vectors and zero velocity line for the numerical simulation corresponding to Mach = 3 with bleed (Test 4331) at VPN 18.

Figure 4-30 presents a comparison of the pressure distribution at the exit, showing that the numerical simulations exhibit relatively low differences. Additionally, all approaches provide compatible predictions for the exit pressure, with the BSL model performing better. Furthermore, the comparison of the Mach number distribution indicates that the estimations are similar. Notably, simulations with the BSL model provide a more homogeneous distribution, and the maximum observed Mach number is slightly lower.

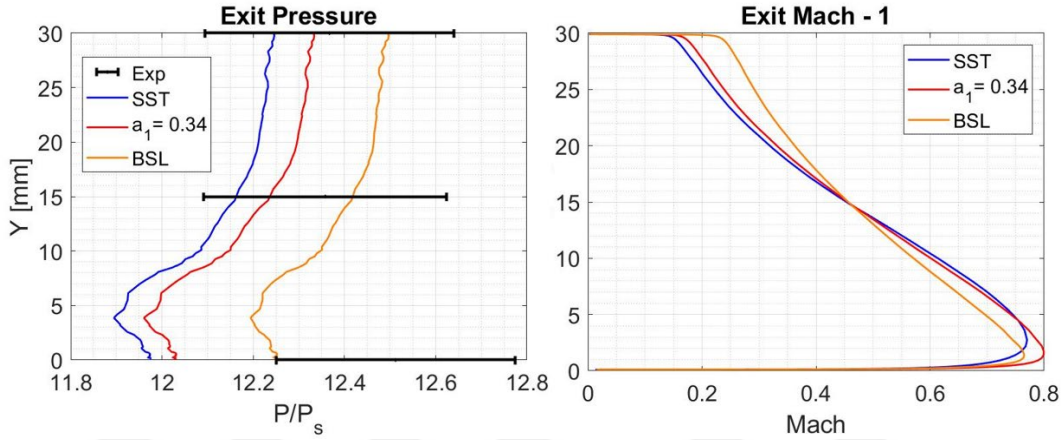


Figure 4-30. Comparison of pressure distribution and Mach number at the exit of the intake for Mach = 3 with bleed (Test 4331) at VPN 18.

4.5.2.1.3 VPN 19

Numerical simulations were performed for Test 4331 at valve position number 19 using both the SST and BSL models, as specified in the simulation matrix. However, convergence could not be achieved with the SST model using the original coefficients. Increasing the a_1 coefficient to 0.34 resulted in the elimination of pressure oscillations during the iterations. The results obtained using the SST model with $a_1 = 0.34$ and the BSL model are presented for valve position number 19 in Appendix G.

4.5.2.1.4 VPN 20

In Figure 4-31, the Mach number contour plots for VPN 20 are compared, revealing a decrease in the length of the pseudo-shock for the SST model as the a_1 coefficient increases from 0.31 to 0.34.

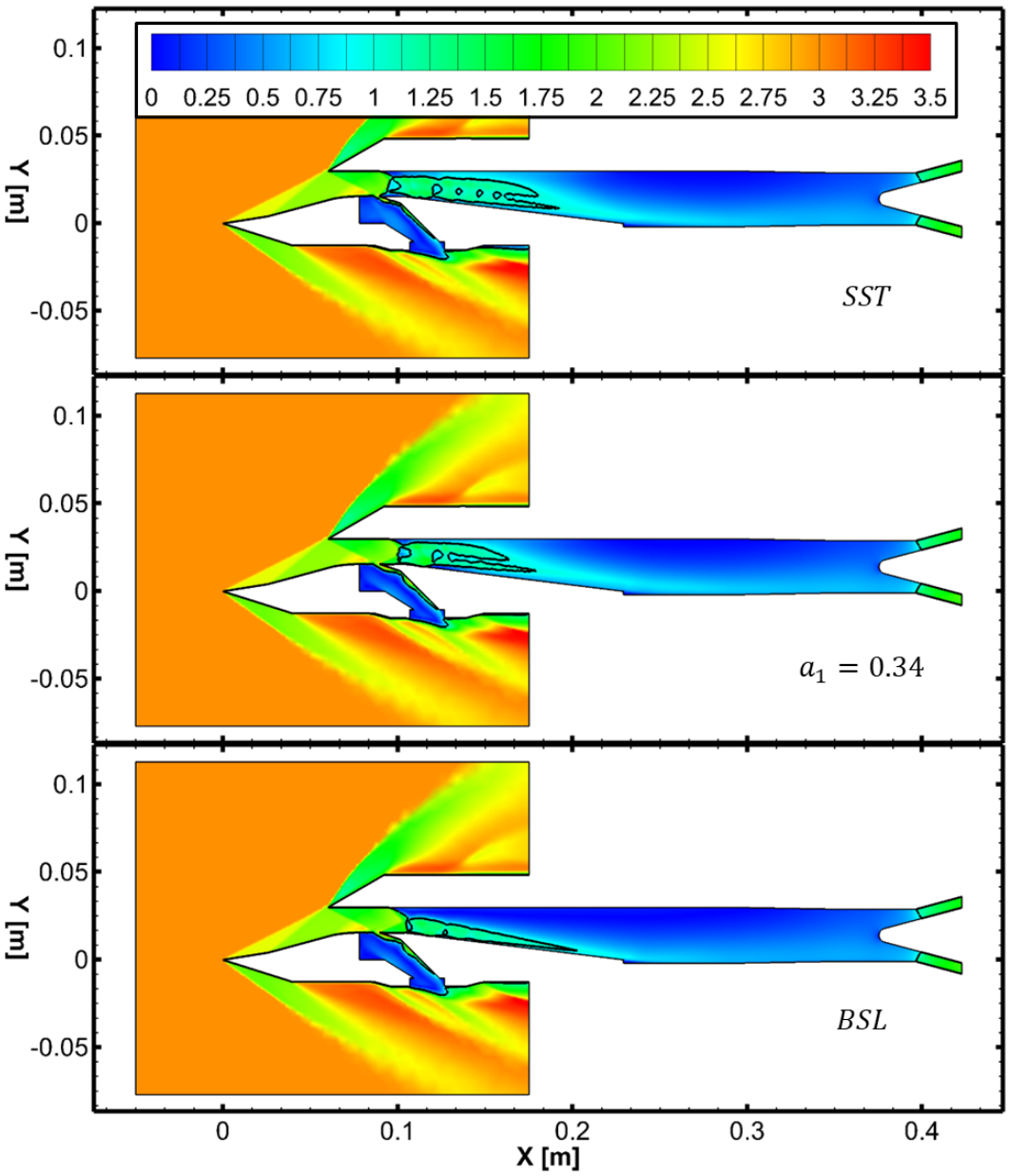


Figure 4-31. Mach number contours for the numerical simulations corresponding to Mach = 3 with bleed (Test 4331) at VPN 20.

The BSL model shows a different shock structure. However, the pseudo-shock oriented parallel to the ramp side in all results. In [91] it was observed that the formation of pseudo-shocks in a flow with back pressure leads to a structure known as the "supersonic tongue" in a constant area symmetric channel. The simulations with the SST model in this study also exhibit a similar structure.

Figure 4-32 compares the pressure distribution along the intake, with the SST model accurately predicting the starting point and amount of pressure rise for the pseudo-shock. Even though BSL model also predicts a compatible pressure distribution downstream of D2 tap, it fails to capture the pressure rise along D1 and D2. The difference between the predicted starting points for the pressure rise with SST and BSL is 5 mm. Figure 4-33 presents a visual comparison for the shock structures. The SST model exhibits a more similar structure to λ-type shock interaction, while the BSL model results in a fully separated sonic line on the cowl side and the pseudo-shock starting at a more downstream position on the ramp side.

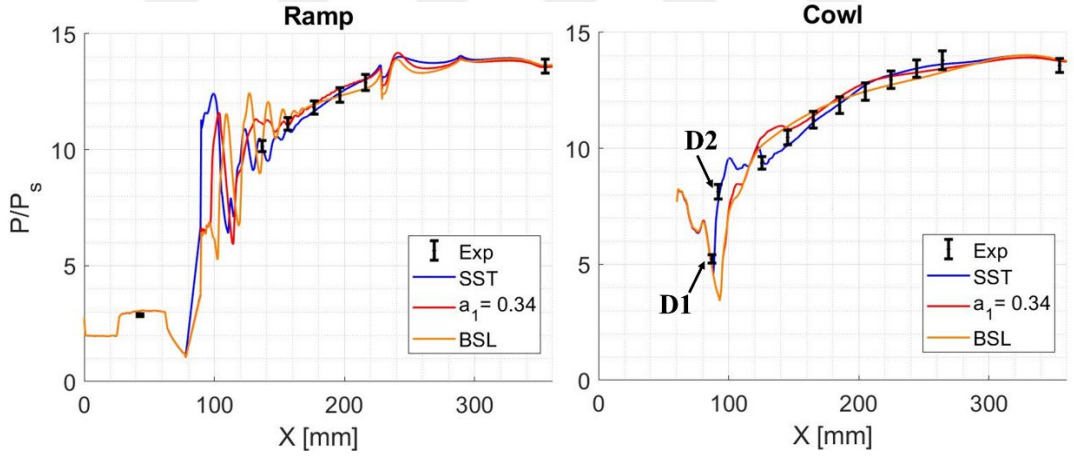


Figure 4-32. Comparison of pressure distribution along the intake between numerical and experimental data for Mach = 3 with bleed (Test 4331) at VPN 20.

Figure 4-33 presents a comparison of the shock structures with velocity vectors and zero-velocity lines, together with an experimental shadowgraph image taken at the instant when the pseudo-shock is at a relatively downstream position during oscillations at VPN 20. The density gradient magnitude contour plots obtained with the SST model shows conceptual similarities with the experimental image, including

the formation of a Mach stem, a brief detachment of the sonic line on the low angle diffuser part of the ramp side, and detachment of the sonic line on the cowl side. However, the separation bubble due to the pseudo-shock on the cowl side in the SST model is smaller than in the experiment, as the sonic line moves away from the cowl surface in the experiment, a behavior more similar to the results of the simulation with BSL. Nonetheless, the pressure distribution after the pseudo-shock starts is compatible with the experimental data for all models.

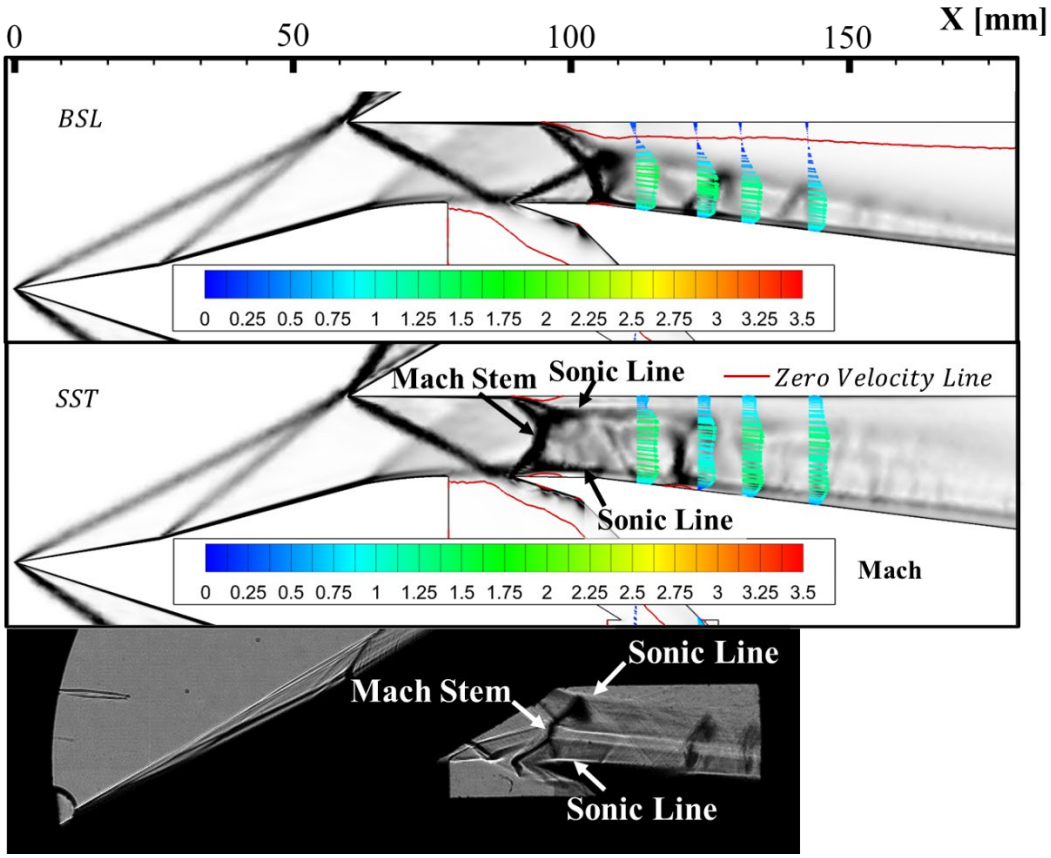


Figure 4-33. Density gradient magnitude contours with velocity vectors and zero velocity line for the numerical simulations corresponding to Mach = 3 with bleed (Test 4331) and shadowgraph image at VPN 20.

A further comparison can be made using the pressure distribution at the exit, shown in Figure 4-34. It can be observed that the numerical results obtained with different models are in close agreement with each other and with the experimental data. The

Mach number distribution is also quite similar among the different simulations, although the BSL model shows a slightly more uniform distribution.

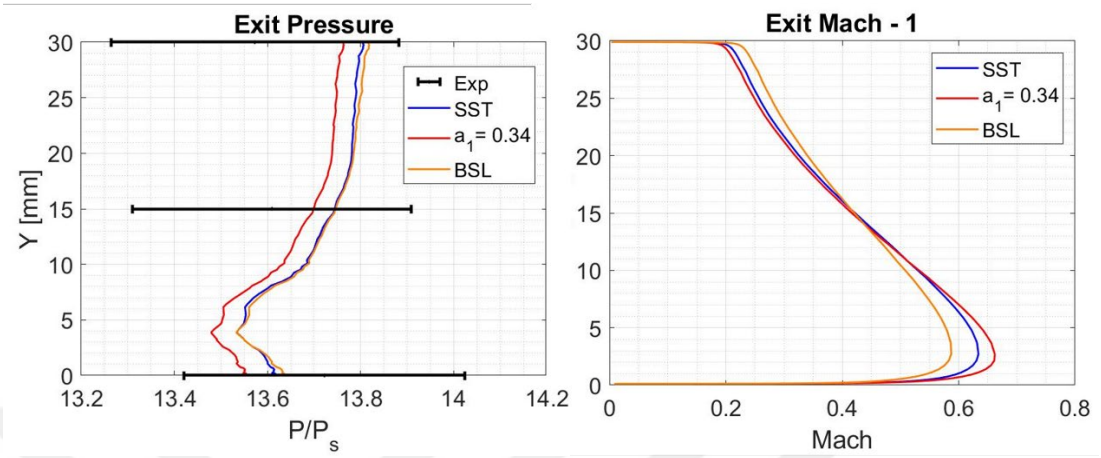


Figure 4-34. Comparison of pressure distribution and Mach number at the exit of the intake for Mach = 3 with bleed (Test 4331) at VPN 20.

4.5.2.2 Mach = 3 without Bleed (Test 4372)

Numerical simulations were performed for Mach = 3 without bleed case (Test 4372) at VPNs 1, 15 and 18. The results for VPN 1 were already presented in section 4.5.1, and this section covers the results for the other valve positions.

4.5.2.2.1 VPN 15

Figure 4-35 presents the comparison of Mach number contour plots for VPN 15, which highlights a reduction in the length of the pseudo-shock as a_1 increases for the SST model. This finding is consistent with that of Test 4331 in Figure 4-22, where the BSL model exhibits a shorter pseudo-shock than the SST simulations for $a_1 = 0.31$ and 0.34, and the shortest pseudo-shock is observed at $a_1 = 0.38$.

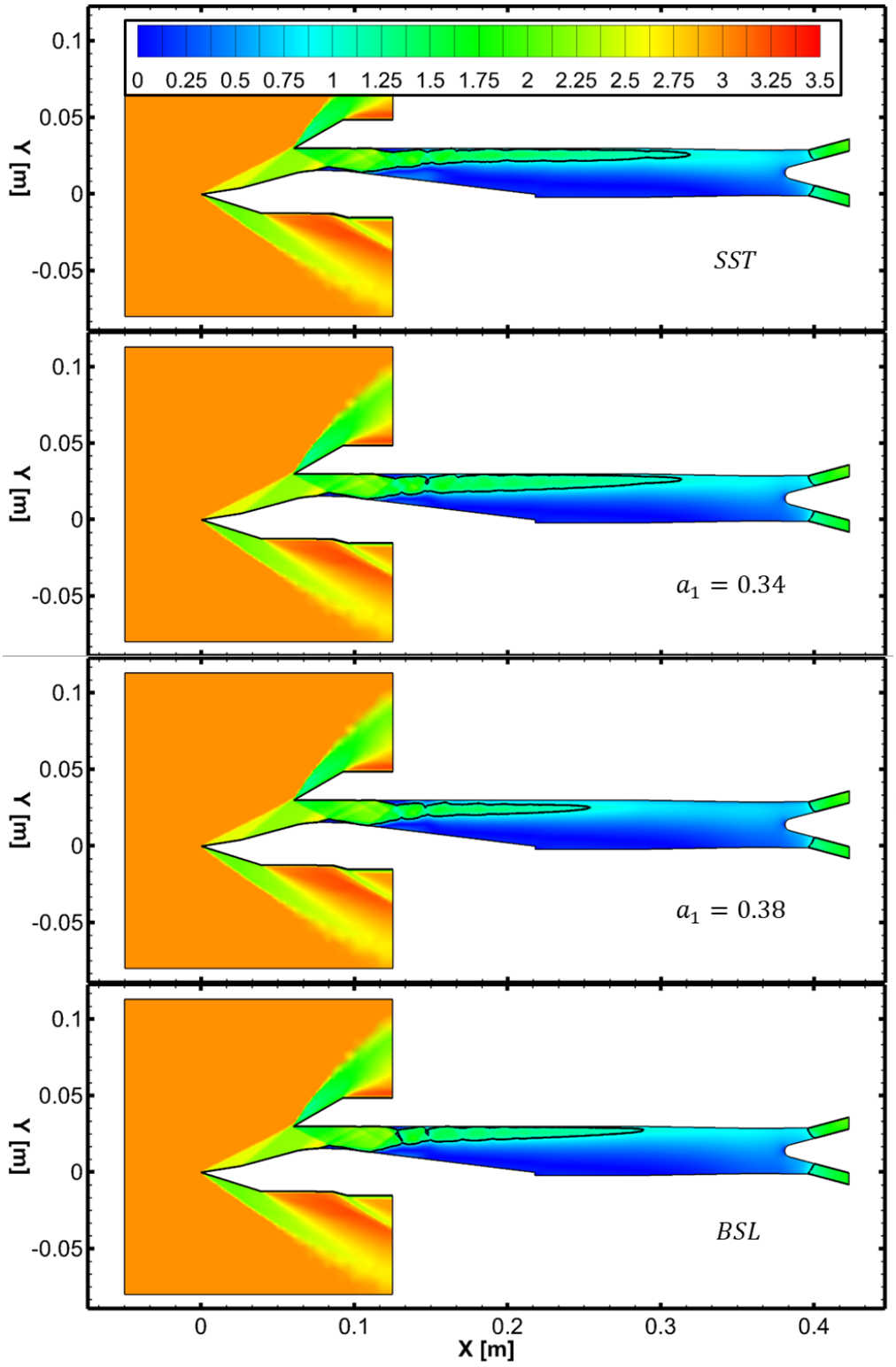


Figure 4-35. Mach number contours for the numerical simulations corresponding to Mach = 3 without bleed (Test 4372) at VPN 15.

Figure 4-36 shows the comparison of pressure data obtained from numerical simulations and experiments at VPN 15. As with Test 4331, the original coefficients SST model demonstrates the largest deviation from the experimental data, while the SST model with $a_1 = 0.38$ and the BSL model exhibit better agreement. The onset of pressure rise due to the pseudo-shock is observed at the D3 tap in the experiment, and both the SST model with $a_1 = 0.38$ and the BSL model capture this feature. However, starting point of the pressure rise on the cowl side are slightly different, 3 mm. Notably, no significant differences are observed upstream of the pseudo-shock.

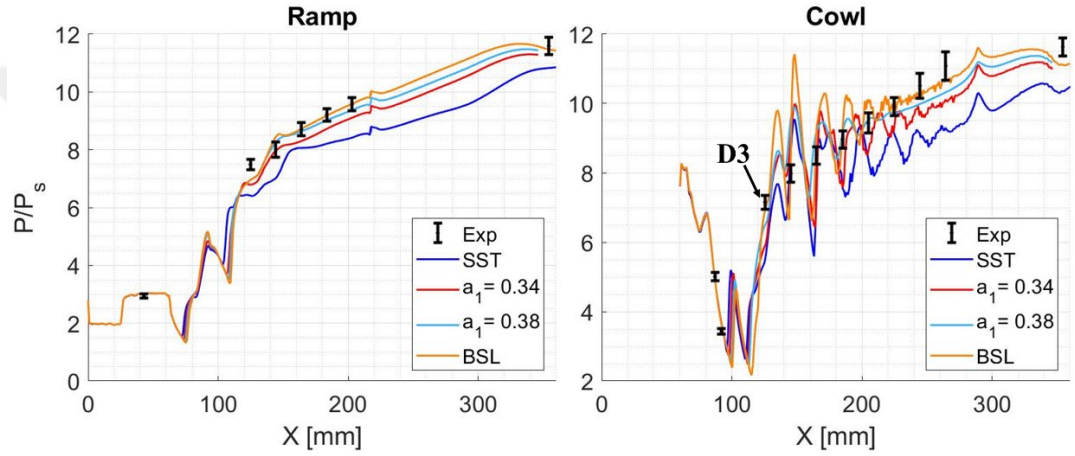


Figure 4-36. Comparison of pressure distribution along the intake between numerical and experimental data for Mach = 3 without bleed (Test 4372) at VPN 15.

Figure 4-37 illustrates the shock structures obtained from numerical simulations with the SST model and the BSL model, as well as the corresponding shadowgraph image at the moment when the pseudo-shock is relatively downstream during oscillation at VPN 15. The predicted orientation of the pseudo-shock is opposite to that observed in the experiment. Both the test and numerical results show separation shocks on the cowl and ramp side, but the numerical simulations predict a smaller separation bubble on the cowl side and a larger one on the ramp side, leading to a different orientation. When comparing the results of the numerical simulations, the SST model with $a_1 = 0.38$ estimates a larger separation bubble on the cowl side, which is more similar to the experiment than the results obtained with the BSL model.

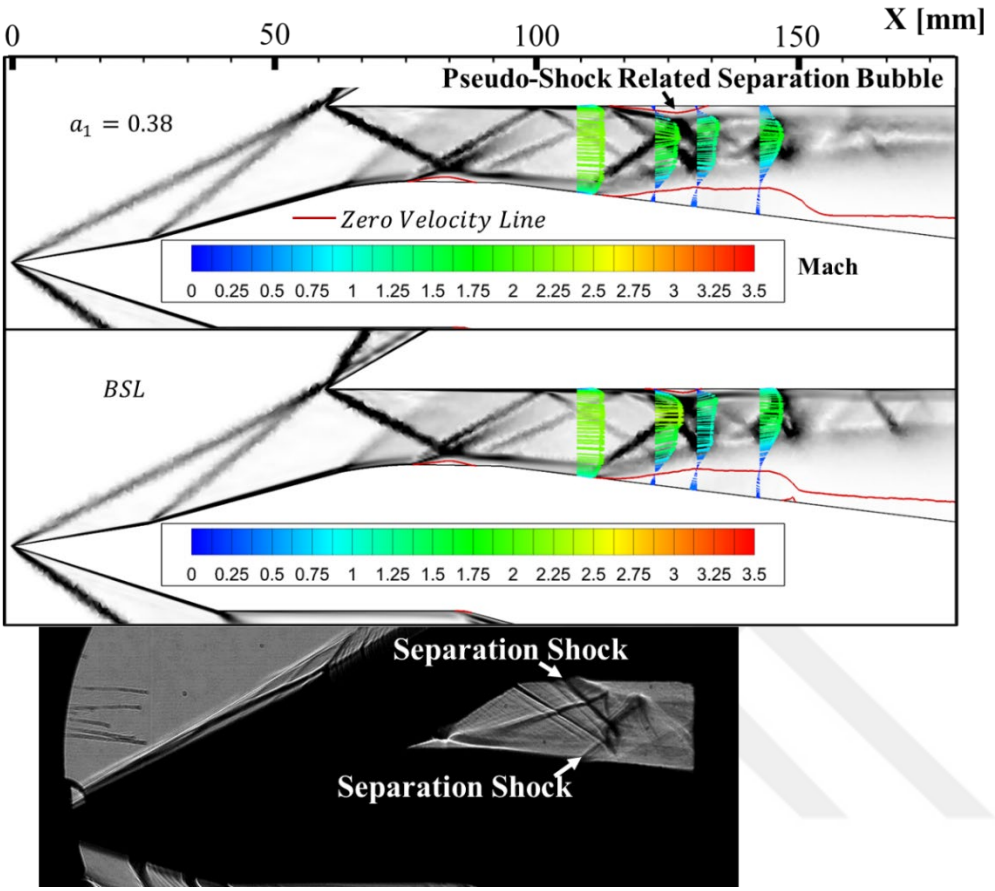


Figure 4-37. Density gradient magnitude contours with velocity vectors and zero velocity line for the numerical simulation and the shadowgraph image corresponding to Mach = 3 without bleed (Test 4372) at VPN 15.

Figure 4-38 compares the pressure distribution at the exit, showing that the original SST model underpredicts the exit pressure, while increasing the a_1 parameter improves the accuracy of the predictions. The best agreement with the experimental data is obtained with the BSL model, followed by the SST model with $a_1 = 0.38$. However, when examining the Mach number distribution at the exit, noticeable differences are observed between the BSL and SST with $a_1 = 0.38$ simulations. These differences are likely due to the variation in predicted lengths of the pseudo-shock. As illustrated in Figure 4-35, the BSL model predicts a longer pseudo-shock

than the SST with $a_1 = 0.38$, and resulting in a more heterogeneous Mach number distribution with a higher maximum Mach number.

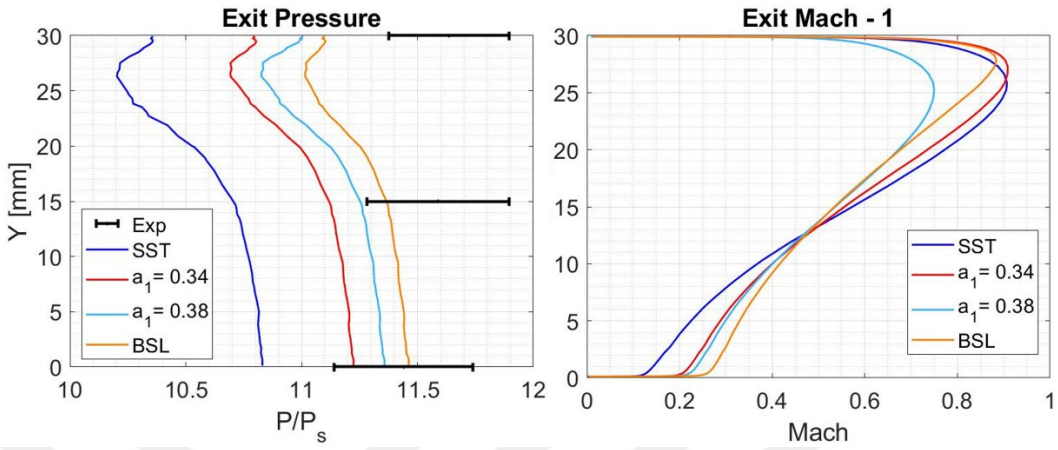


Figure 4-38. Comparison of pressure distribution and Mach number at the exit of the intake for Mach = 3 without bleed (Test 4372) at VPN 15.

4.5.2.2.2 VPN 18

Figure 4-39 compares the Mach number contour plots for VPN 18. The results show that increasing a_1 from 0.31 to 0.34 reduces the length of the pseudo-shock, but further increases in a_1 do not significantly affect the length of the pseudo-shock. The BSL model estimates a slightly longer pseudo-shock length than the SST model with original coefficients. Figure 4-40 presents a comparison of pressure data obtained from numerical simulations and experiments for VPN 18. The difference between the numerical results is relatively less compared to VPN 15. The results of the SST model with $a_1 = 0.34$ and $a_1 = 0.38$ are similar, indicating that increasing a_1 from 0.34 to 0.38 does not have a significant effect for this condition. The results of both SST models are also similar to those of the BSL model, but the BSL model exhibits slightly higher pressure upstream of D6. Despite the better agreement with the experiments of the SST model with higher a_1 and the BSL model, all approaches underpredict the pressure between D7 to D10 on the cowl side, and R6, R7 on the ramp side. However, at the exit, the numerical results get closer to the experimental ones.

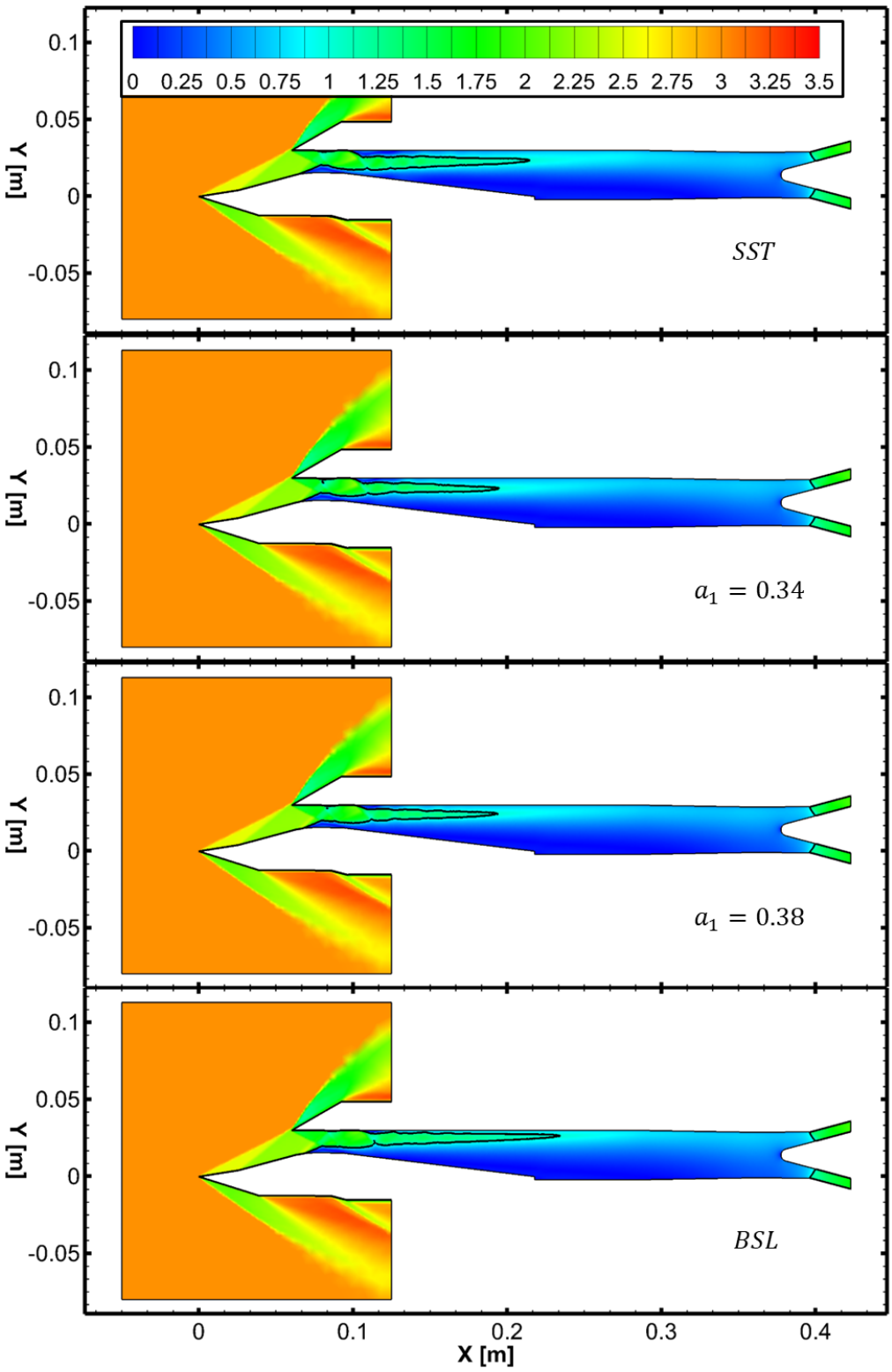


Figure 4-39. Mach number contours for the numerical simulations corresponding to Mach = 3 without bleed (Test 4372) at VPN 18.

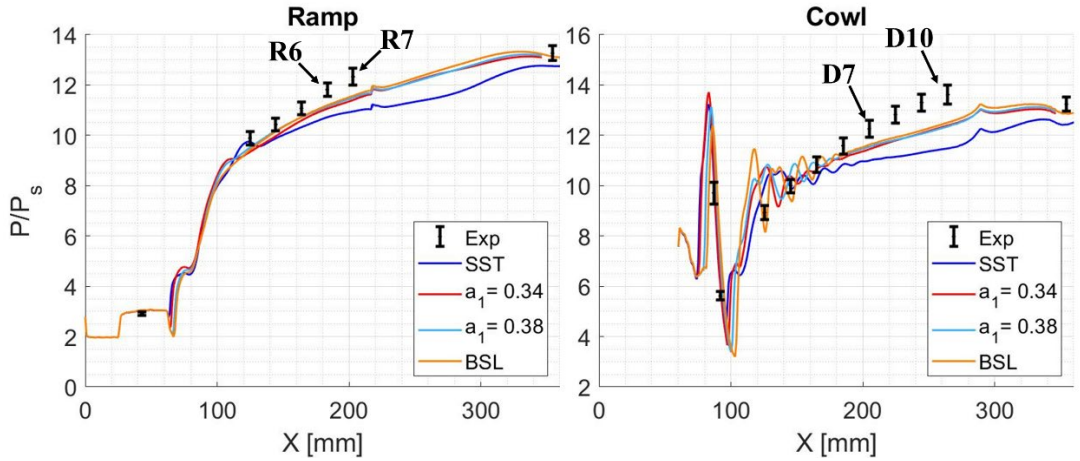


Figure 4-40. Comparison of pressure distribution along the intake between numerical and experimental data for Mach = 3 without bleed (Test 4372) at VPN 18.

Figure 4-41 provides a more detailed comparison of the numerical results and the experiments at the exit of the intake. The difference between the numerical results is relatively low, and increasing a_1 from 0.31 to 0.34 has a relatively high impact, but increasing it further to 0.38 has a relatively low impact. Among all the approaches, the BSL model shows better predictions in terms of estimating the pressure distribution along and exit of the intake.

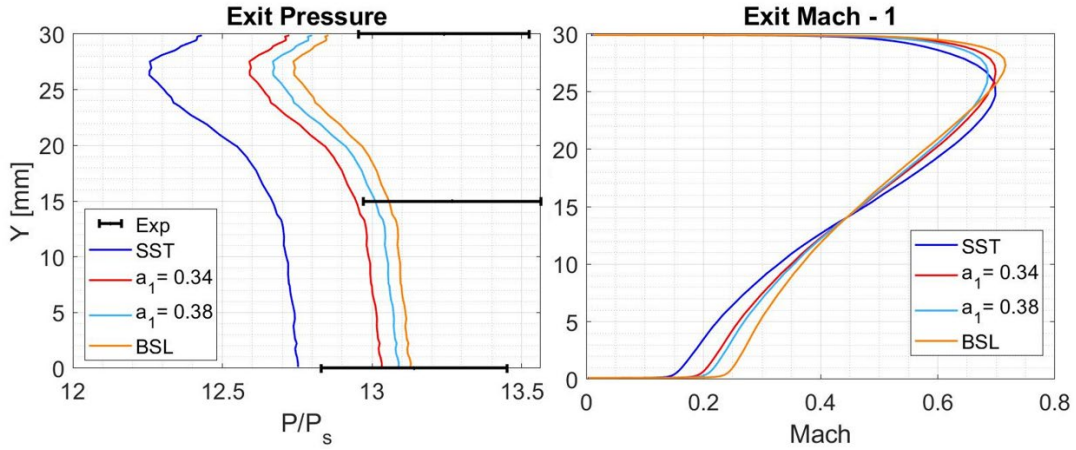


Figure 4-41. Comparison of pressure distribution and Mach number at the exit of the intake Mach = 3 without bleed (Test 4372) at VPN 18.

The shock structures obtained from the numerical simulations with the SST and BSL models, along with the corresponding shadowgraph image at a specific moment when the pseudo-shock is upstream during oscillation at position 18 are given in Figure 4-42. The predicted orientation of the pseudo-shock in the simulations differs from that observed in the experiment. Both the experimental and numerical results show separated sonic lines on the cowl and ramp side. The reason for the difference in orientation is likely due to a different separation bubble on the cowl side predicted by the numerical simulations. When comparing the results of the numerical simulations, the SST model with original coefficients estimates a larger separation bubble on the cowl side. This results in a clearer separation of the sonic line on the cowl side, which is close to the experimental results than the results obtained with the BSL model. It is also should be noted that, increasing a_1 leads to a shrinkage of the pseudo-shock-related separation bubble on the cowl side.

The experiments and numerical simulation showed that on the ramp side, the subsonic region inside the separation bubble formed by the cowl shock merges with the subsonic region caused by the pseudo-shock. Although the flow downstream of the separation bubble reattaches, the sonic line remains detached due to the thickening of the boundary layer, resulting in the thickening of the subsonic layer which further confines the pseudo-shock.

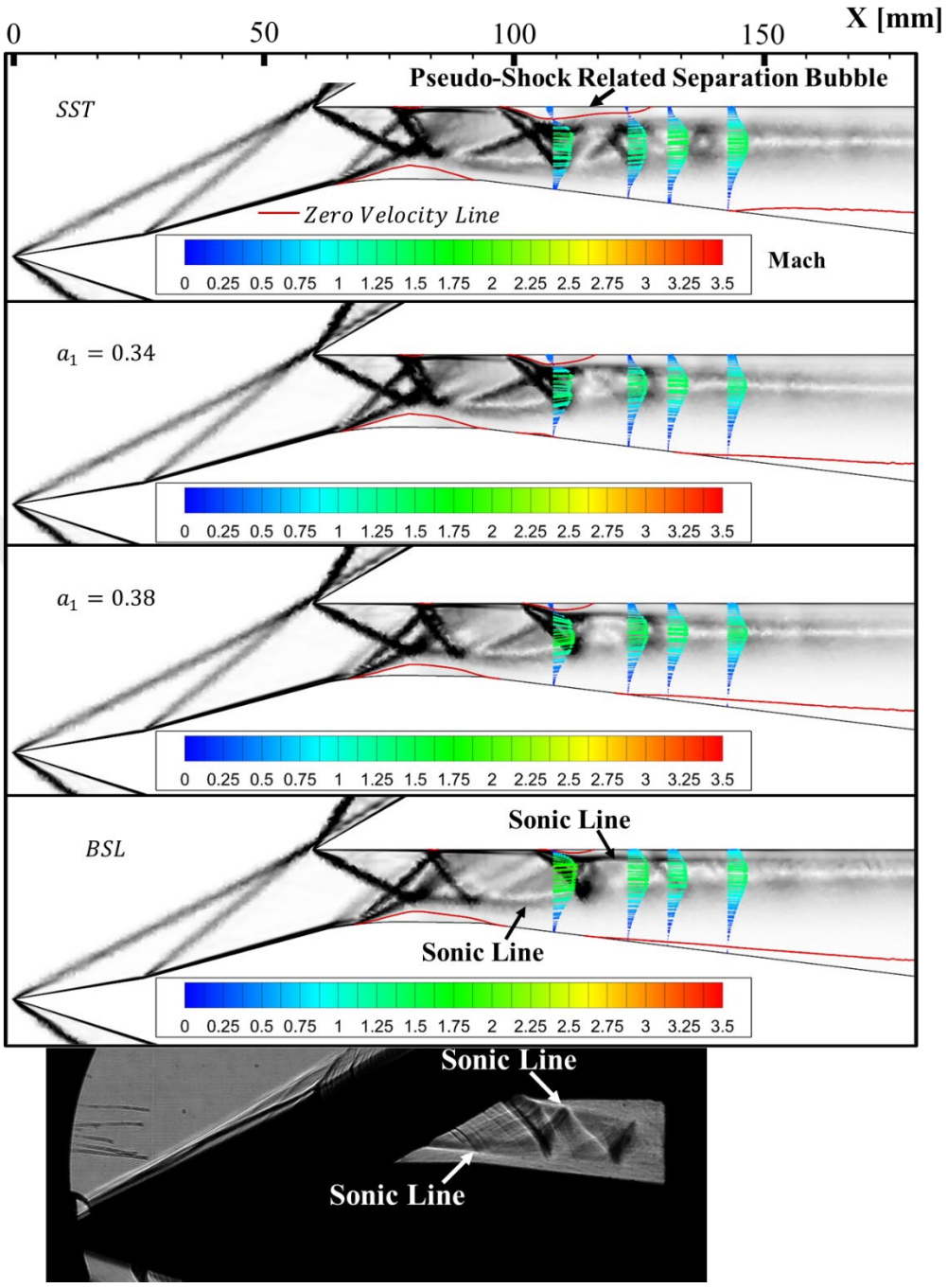


Figure 4-42. Density gradient magnitude contours with velocity vectors and zero velocity lines for the numerical simulation and the shadowgraph image corresponding to Mach = 3 without bleed (Test 4372) at VPN 18.

4.5.2.3 Mach = 2.63 with Bleed (Test 4340)

Numerical simulations were performed for Mach = 2.63 with bleed case (Test 4340) at VPNs 1, 15, 18, 19, and 20. The results for VPN 1 were already presented in section 4.5.1, and this section covers the results for the other valve positions according to the matrix of simulations.

4.5.2.3.1 VPN 15

Numerical simulations were conducted for Test 4340 at valve position number 15 using both SST and BSL models according to the matrix of simulations. However, the intended convergence could not be achieved with the SST model, and noticeable pressure oscillations were observed along the intake, which is atypical for most of the simulations conducted for the present study. It is also worth noting that as the a_1 coefficient is increased, the amount of oscillations decreased however convergence could not be achieved. The obtained results with BSL model are given in Appendix G.

4.5.2.3.2 VPN 18

Figure 4-43 displays the Mach number contours, revealing that the orientation of the pseudo-shock differs between the SST and BSL models. Furthermore, increasing the a_1 coefficient in the SST simulations leads to a thicker or a less confined pseudo-shock structure. Figure 4-44 compares the pressure distribution along the intake, indicating that the pressures on the ramp side and cowl side are compatible, yet some conceptual differences exist. Specifically, the simulation with the BSL model results in a fluctuating change of pressure along the cowl side, and a more monotonic increase on the ramp side, opposite of the SST models' results. Additionally, if the pressure in the vicinity of D2 tap is examined, it is seen that the BSL model predicts the starting point of pressure rise on the cowl side to be 9 mm downstream.

Conversely, the SST model with original coefficients and $a_1 = 0.34$ captures the pressure rise point and provides a better estimate. However, the estimated pressures from the SST model with original coefficients are slightly lower than the experimental data. Overall, the SST model with $a_1 = 0.34$ provides the most compatible results in terms of pressure distribution along the intake.

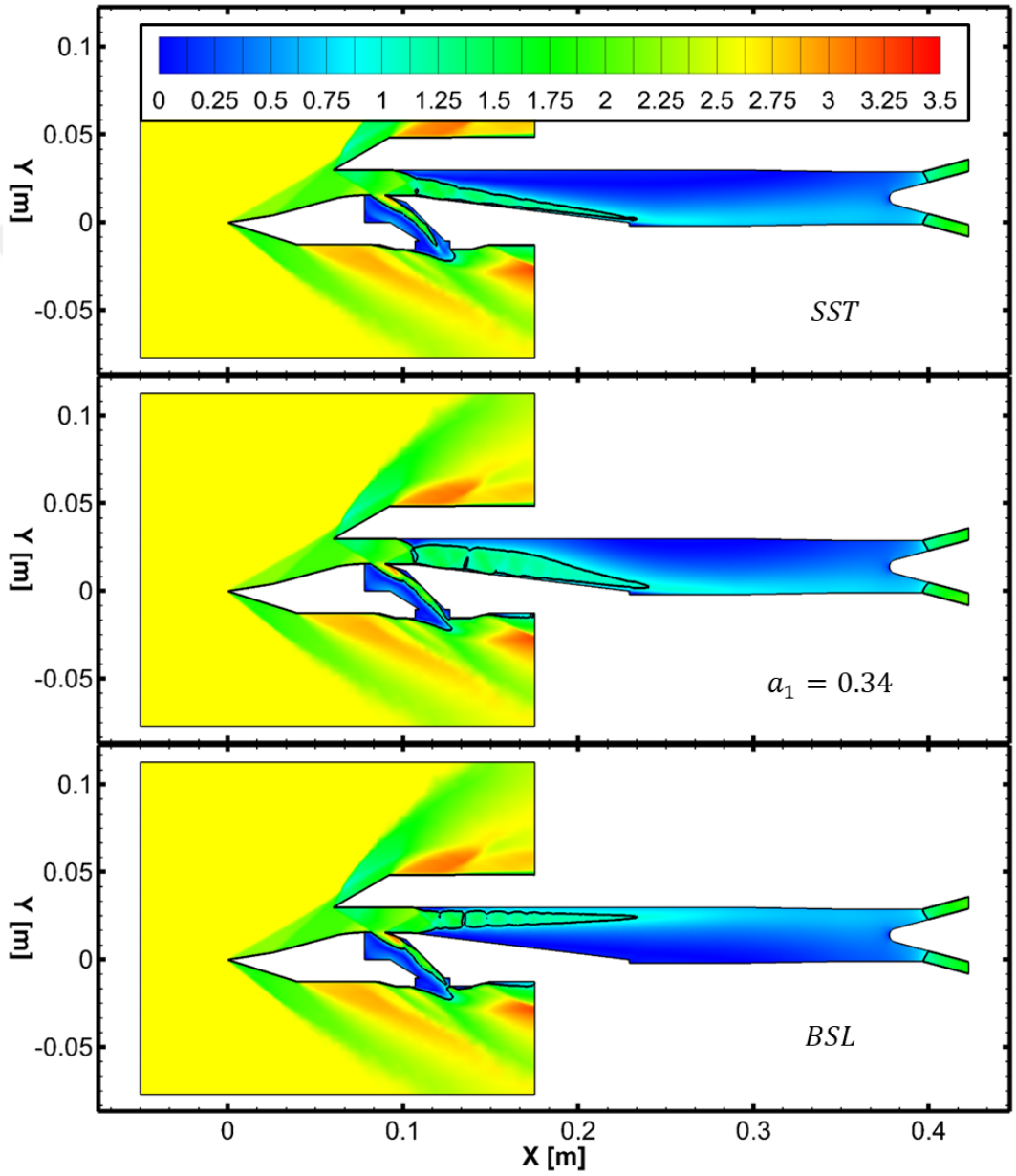


Figure 4-43. Mach number contours for the numerical simulations corresponding to Mach = 2.63 with bleed (Test 4340) at VPN 18.

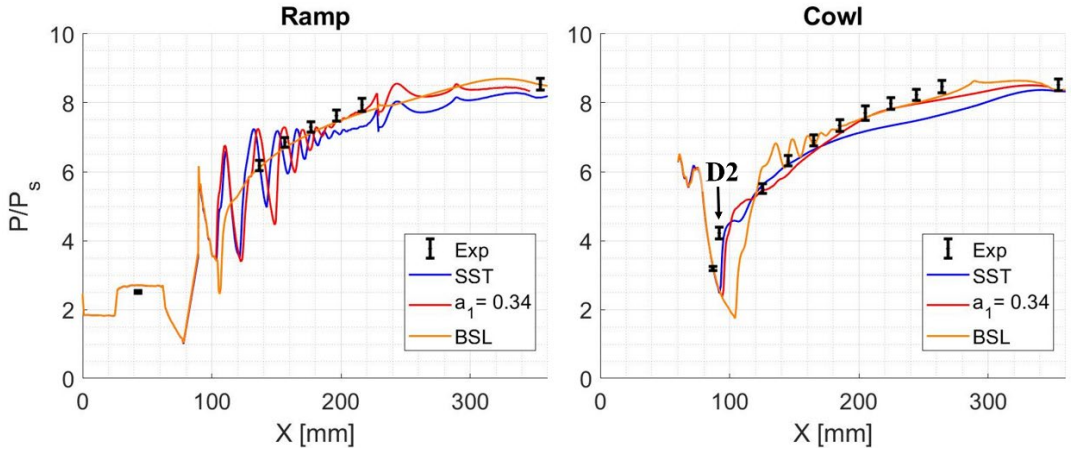


Figure 4-44. Comparison of pressure distribution along the intake between numerical and experimental data for Mach = 2.63 with bleed (Test 4340) at VPN 18.

Comparing the shock structures in Figure 4-45, where the density gradient magnitude contour plot obtained from the numerical simulation with SST for $a_1 = 0.34$ is compared with a shadowgraph image at the instant when the pseudo-shock is at downstream position during the oscillation at VPN 18, reveals that the shock structures are very similar. The sonic line's shape on the cowl side and the separation shock's location on the cowl side are also similar. Furthermore, the numerical simulation captures a brief separation of the sonic line on the ramp side due to the pseudo-shock. Both structures show X-type interaction. Figure 4-46 provides velocity vectors and zero velocity lines for a detailed examination of the numerical results. The formation of separation bubbles due to the pseudo-shock is visible on both the ramp and cowl sides, but the separation bubble on the ramp side is minor and results in a nearly attached sonic line. On the cowl side, the larger separation bubble directs the shock-train and sonic line towards the ramp, resulting in a fully detached sonic line. Additionally, the velocity vectors show that the thickness of the sonic layer increases on both the cowl and ramp sides, but the cowl side's increase is much more effective in confining the pseudo-shock.

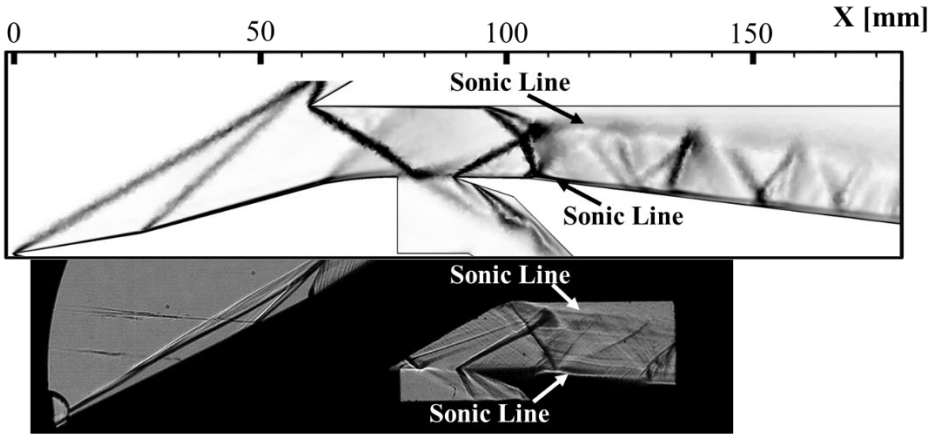


Figure 4-45. Numerical density gradient magnitude contour and experimental shadowgraph image for Mach = 2.63 with bleed (Test 4340) at VPN 18.

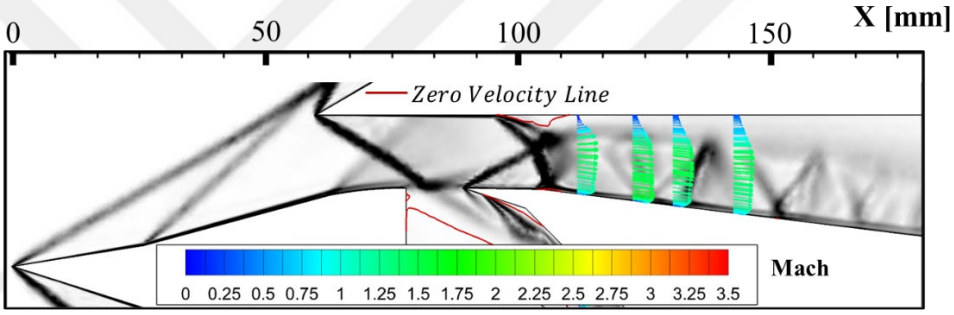


Figure 4-46. Density gradient magnitude contour with velocity vectors and zero velocity line for the numerical simulation corresponding to Mach = 2.63 with bleed (Test 4340) at VPN 18.

Another point of comparison can be made by examining the pressure distribution at the exit of the intake, as presented in Figure 4-47. The results obtained are generally similar, except for those obtained with the BSL model, which show an inverse pattern due to the different orientation of the pseudo-shock. This difference is also evident in the distribution of Mach number. Additionally, increasing the value of a_1 for the SST model, slightly improves the prediction of exit pressure when compared to the experimental data.

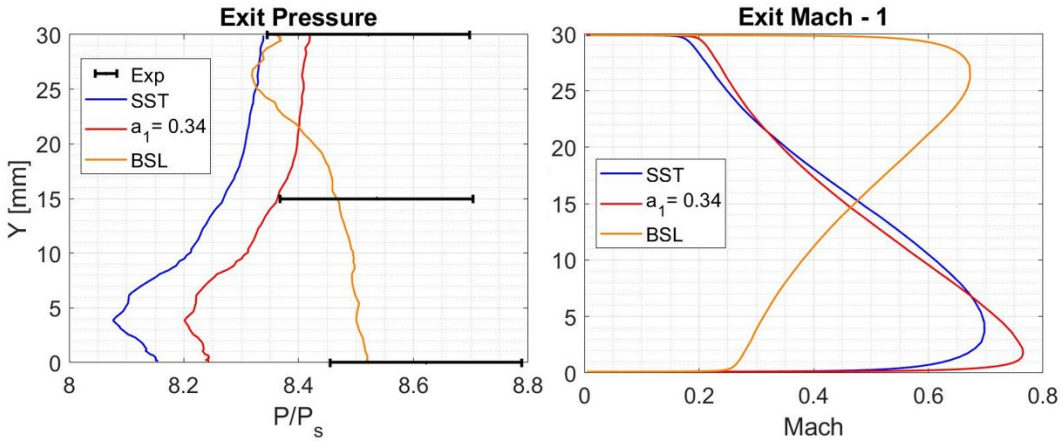


Figure 4-47. Comparison of pressure distribution and Mach number at the exit of the intake for Mach = 2.63 with bleed (Test 4340) at VPN 18.

4.5.2.3.3 VPN 19

Numerical simulations were conducted for Test 4340 at valve position number 19 using both SST and BSL models based on the matrix of simulations. However, convergence could not be achieved with the SST model using the original coefficients. Nonetheless, increasing the a_1 coefficient to 0.34 resulted in the elimination of pressure oscillations through iterations. Therefore, the results obtained using SST with $a_1 = 0.34$ and BSL models are presented for valve position number 19 in Appendix G.

4.5.2.3.4 VPN 20

Figure 4-48 illustrates the Mach number contours, indicating that a much shorter pseudo-shock is obtained in comparison to previous valve positions. The orientation of the pseudo-shock is consistent across all simulations for VPN 20. Increasing the a_1 coefficient in the SST simulations results in the disappearance of the supersonic-tongue structure, while the use of the BSL model produces a slightly longer pseudo-shock structure.

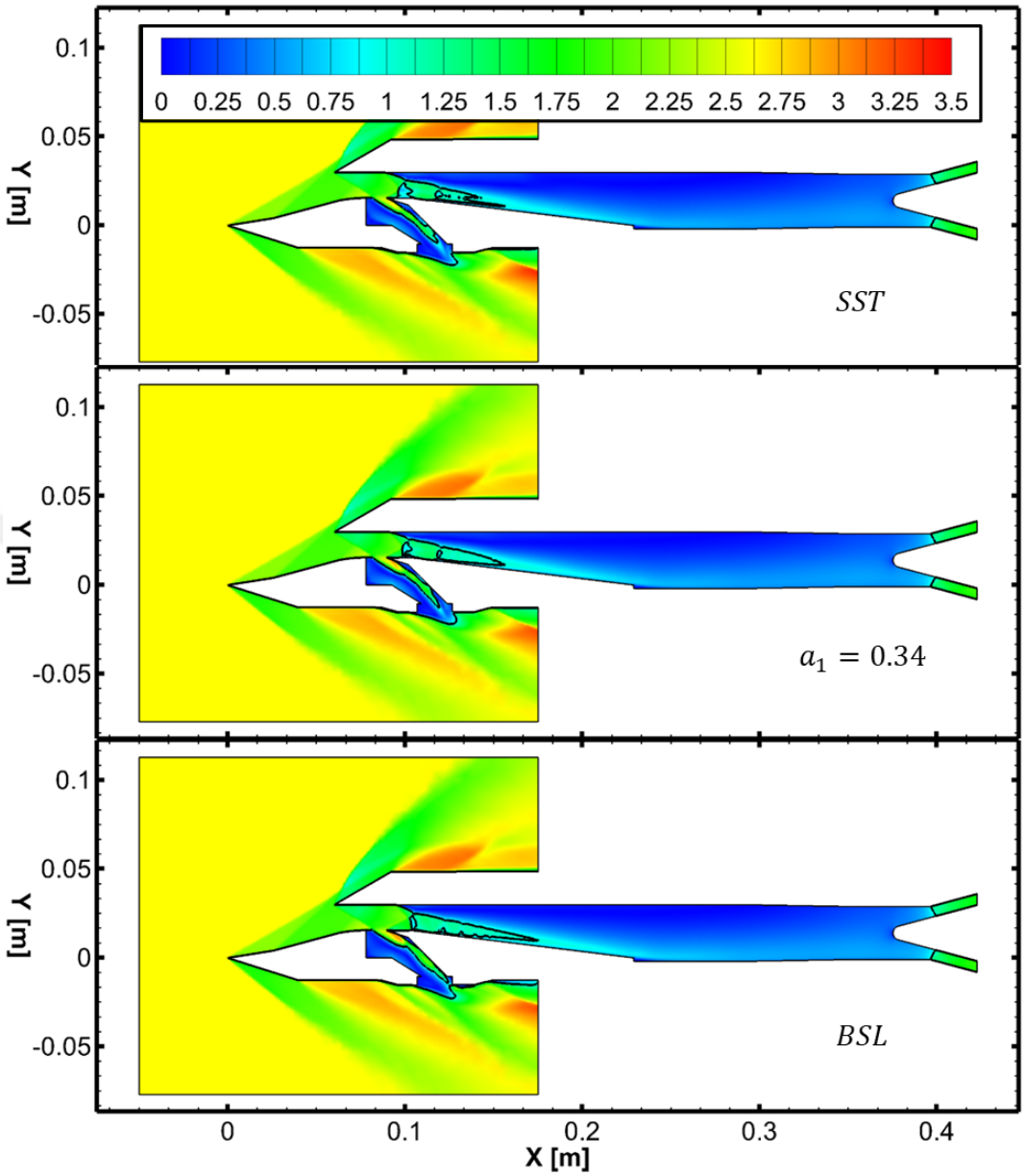


Figure 4-48. Mach number contours for the numerical simulations corresponding to Mach = 2.63 with bleed (Test 4340) at VPN 20.

Figure 4-49 compares the pressure distribution along the intake, revealing that numerical simulations provide similar results to each other, except for the point where the pressure rise of the pseudo-shock begins. The results are compatible with the experiment on the ramp side and on the cowl side upstream of the D8 tap. However, the SST models are better suited for estimating the pressure rise point and rising characteristics in the vicinity of the D1 and D2 taps. The difference between

the points calculated with the SST model with original coefficients and the BSL model is 6 mm. On the cowl side downstream of the D8 tap, numerical simulations slightly underpredict the pressure, but the results become closer to the experimental data at the exit. The pressure distribution at the exit is analyzed in detail in Figure 4-50, which demonstrates that the numerical simulations yield results that are consistent with the experimental data. Additionally, the figure indicates that the Mach number distribution is comparable across the simulations, although a slightly higher Mach number is observed with the BSL model.

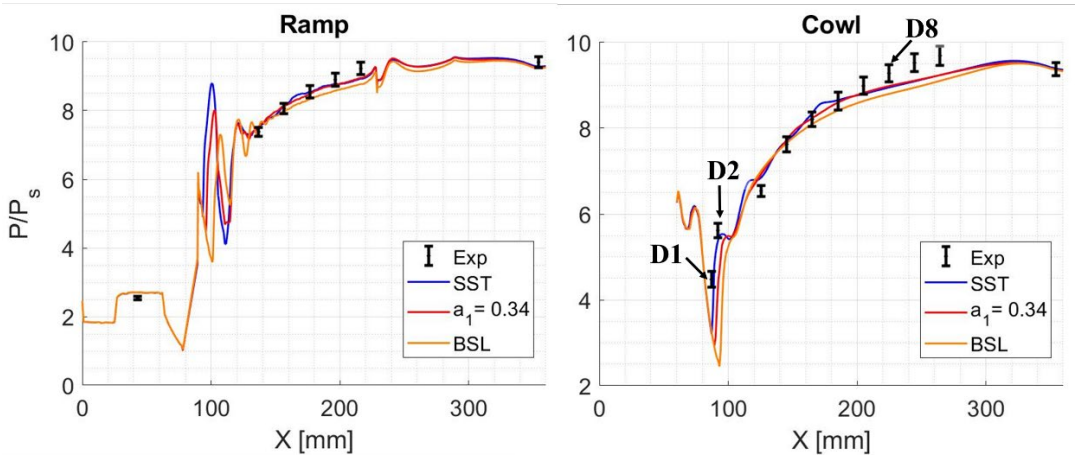


Figure 4-49. Comparison of pressure distribution along the intake between numerical and experimental data for Mach = 2.63 with bleed (Test 4340) at VPN 20.

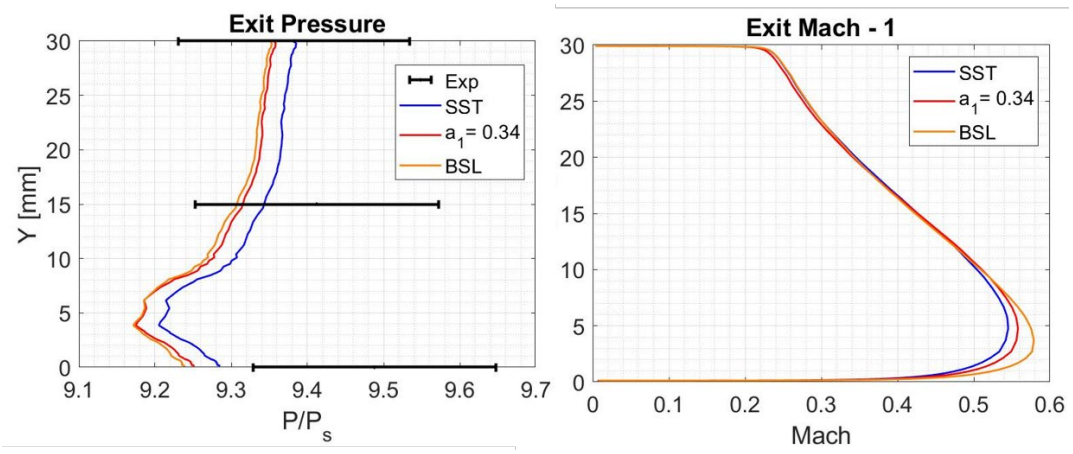


Figure 4-50. Comparison of pressure distribution and Mach number at the exit of the intake for Mach = 2.63 with bleed (Test 4340) at VPN 20.

Visual comparison can be made using the images provided with Figure 4-51, which compares the density gradient magnitude contour plot obtained from the result of the numerical simulation with the SST model using original coefficients and the shadowgraph image at the instant where the pseudo-shock is at downstream position during oscillations occurs dwell time at VPN 20. The results indicate that the shock structures are similar, with similar observed features such as the locations of separation shocks on the cowl and ramp side, the orientation of the shock-train, and the formation of the Mach stem. The zero velocity lines and flow vectors reveal that the larger separation bubble on the cowl side causes the pseudo-shock to orient towards the ramp side, resulting in a thicker subsonic layer and confining the pseudo-shock.

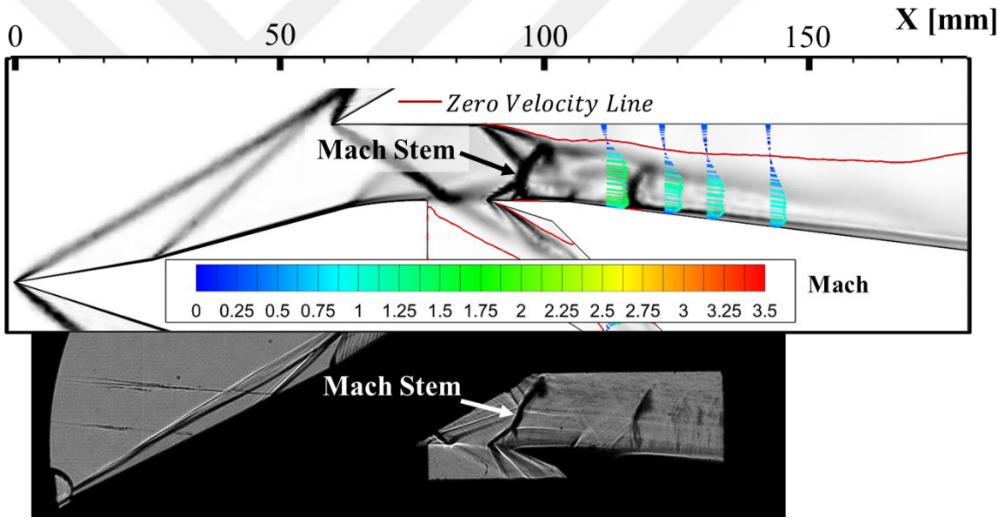


Figure 4-51. Numerical density gradient magnitude contour with velocity vectors and experimental shadowgraph image for Mach = 2.63 with bleed (Test 4340) at VPN 20.

4.5.2.4 Mach = 2.63 without Bleed (Test 4373)

Numerical simulations were performed for Mach = 2.63 without bleed case (Test 4373) at VPNs 1, 15 and 18. The results for VPN 1 were already presented in section 4.5.1, and this section covers the results for the other VPNs.

4.5.2.4.1 VPN 15

Figure 4-52 presents a comparison for the Mach number contours for VPN 15. The impact of increasing the a_1 coefficient on the length of the pseudo-shock is seen, as the contours show a reduction in length. This finding is consistent with Test 4331 and 4372 at VPN 15, and the BSL model exhibits the shortest pseudo-shock.

Figure 4-53 compares the pressure data obtained from numerical simulations and experiments at VPN 15. The SST model with original coefficients shows the largest deviation from the experimental data, while the SST model with $a_1 = 0.38$ and the BSL model show better agreement. However, both on the ramp and cowl side, after the pseudo-shock starts or downstream of D3 tap, the experimental data show a steeper change in the pressure, which results in underestimated pressures upstream of D7. Furthermore, the estimated shock structures are different from the experiment, as seen in the comparison given in Figure 4-54. The density gradient magnitude contour plot in the figure is obtained with the solution of the simulation using the SST model with original coefficients. The orientation of the shock-train is different, and there is a brief separation of the sonic line on the cowl side seen in the numerical simulation, whereas in the experiment, it is much clearer, and the sonic line goes away from the cowl side. Additionally, the location at which the sonic line separation starts on the cowl is different and more downstream in the numerical simulation.

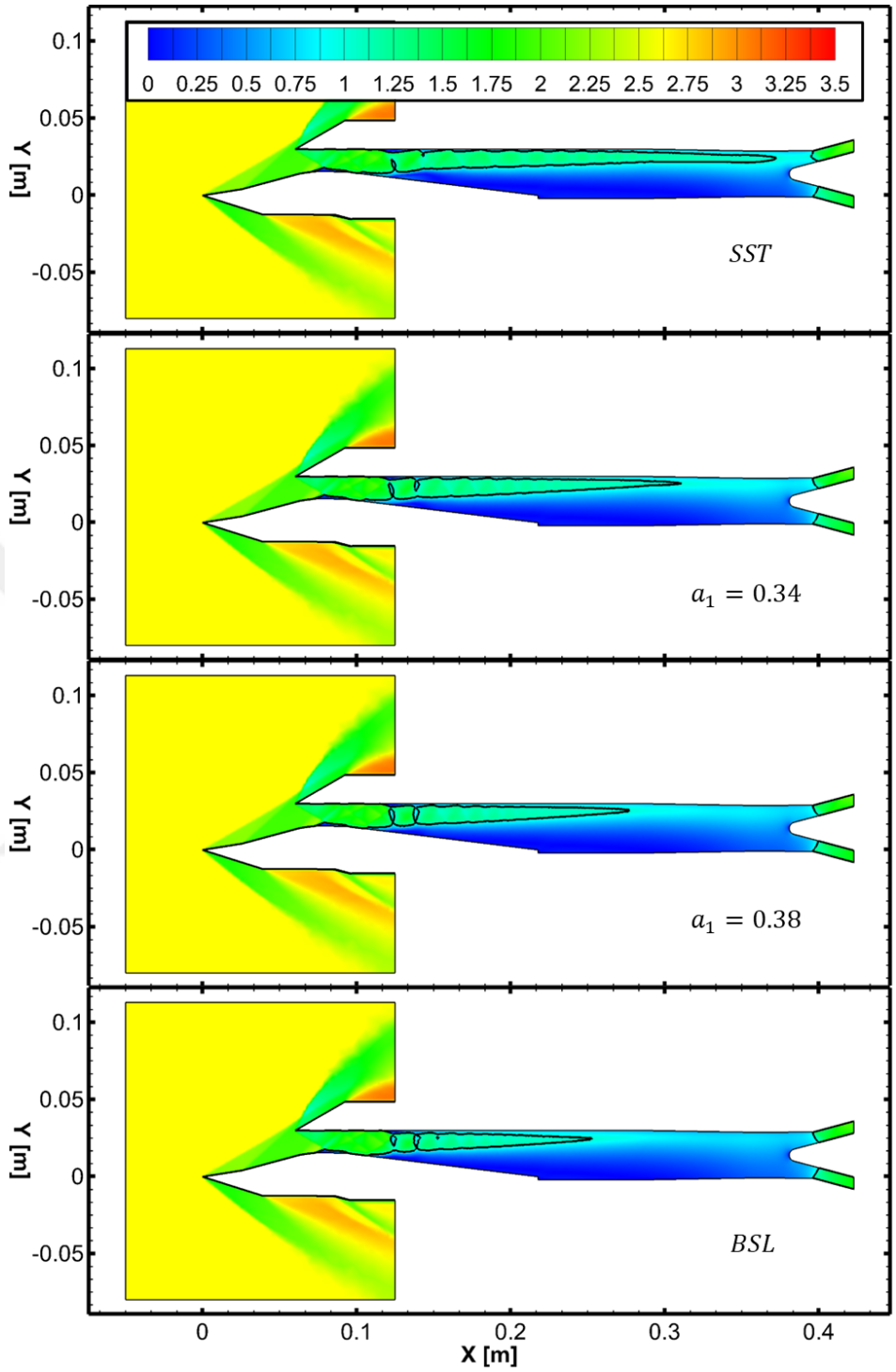


Figure 4-52. Mach number contours for the numerical simulations corresponding to Mach = 2.63 without bleed (Test 4373) at VPN 15.

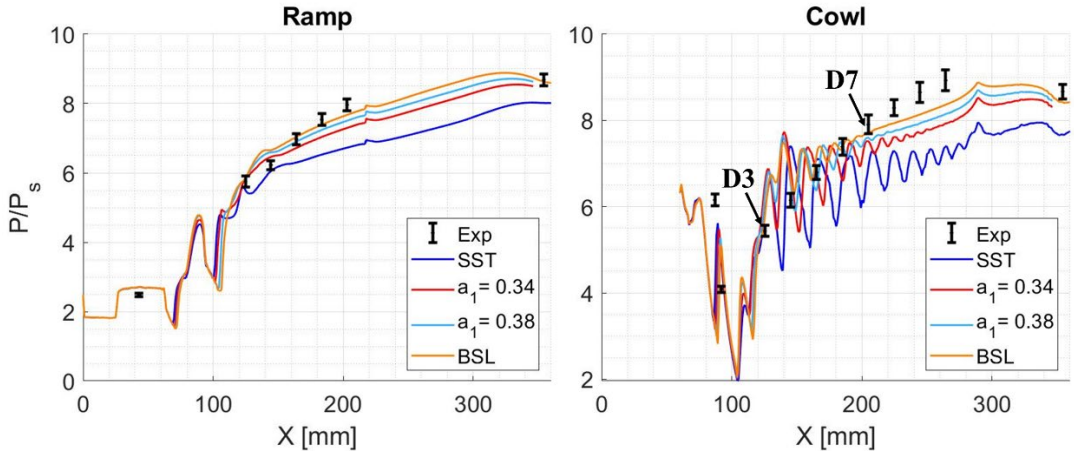


Figure 4-53. Comparison of pressure distribution along the intake between numerical and experimental data for Mach = 2.63 without bleed (Test 4373) at VPN 15.

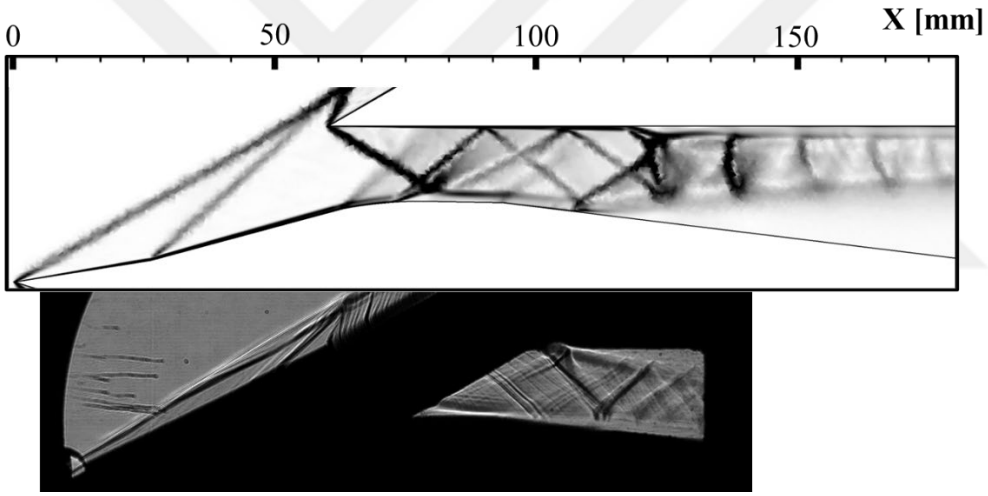


Figure 4-54. Numerical density gradient magnitude contour and experimental shadowgraph image for Mach = 2.63 without bleed (Test 4373) at VPN 15.

The examination of pressure distribution at the exit in Figure 4-55 shows that exit pressure is better estimated with $a_1 = 0.38$ and BSL model. Moreover, examination of Mach number distribution shows that as the a_1 increases, the maximum Mach number decreases, and a more homogeneous distribution is obtained. The simulation with BSL results in the most homogeneous distribution.

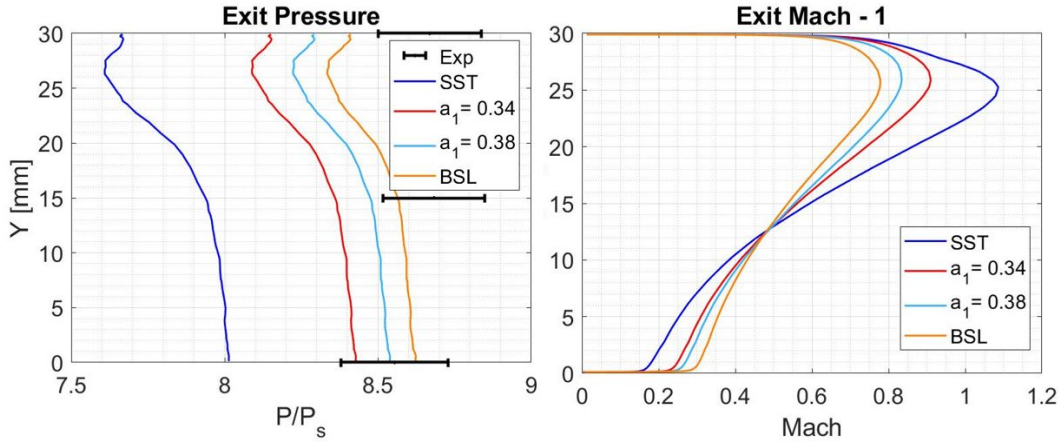


Figure 4-55. Comparison of pressure distribution and Mach number at the exit of the intake for Mach = 2.63 without bleed (Test 4373) at valve position 15.

4.5.2.4.2 VPN 18

Figure 4-56 shows a comparison of Mach number contours at VPN 18, indicating a slight reduction in the length of the pseudo-shock as the a_1 coefficient increases for the SST model. The simulations with BSL model result in a similar length to the SST model. It should be noted that the orientation of the pseudo-shock is the same for all simulations. However, the differences in shock structures can be observed more closely in Figure 4-57. There are differences in the size of the separation bubble on the cowl side that affects the pseudo-shock. The simulations with SST using original coefficients predict the largest bubbles, while all simulations predict the characteristics seen in the experiment, such as the merging of the sonic region due to the separation bubble of the cowl tip shock and of the pseudo-shock on the ramp side. The shapes of the sonic line on the ramp side are considered similar to the experiment.

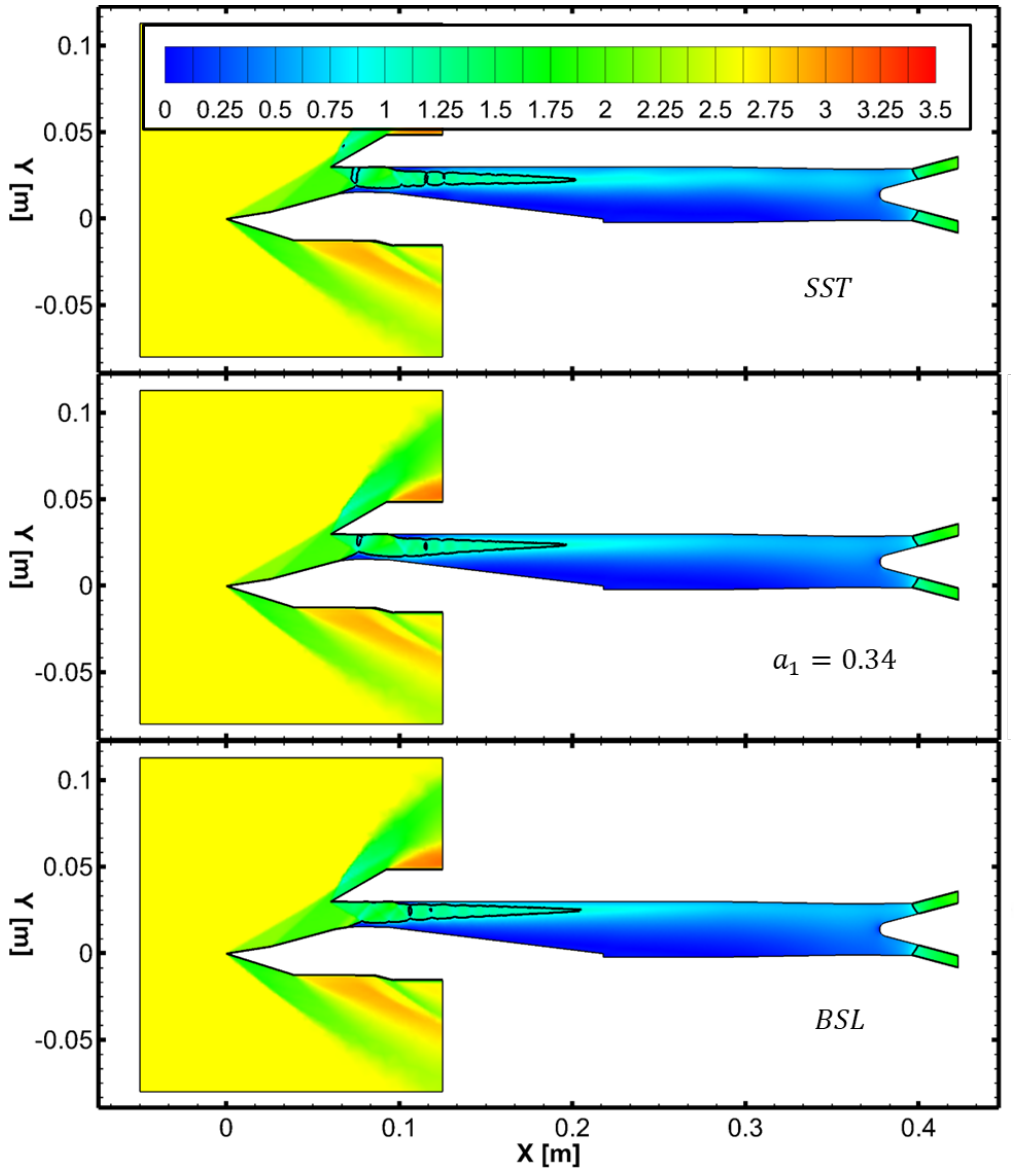


Figure 4-56. Mach number contours for the numerical simulations corresponding to Mach = 2.63 without bleed (Test 4373) at VPN 18.

Figure 4-58 presents a comparison of the pressure distribution along the intake. The numerical results exhibit relatively small differences among the different models. However, the simulations using the $a_1 = 0.34$ coefficient and the BSL model show a better agreement with the experimental data in terms of pressure distribution. It is worth noting that there is a slight underestimation of pressure upstream of 120 mm from the intake tip. Nevertheless, the trend of the variation is consistent with the experimental data. Furthermore, the calculated pressure at the exit is in good

agreement with the experimental measurement. A more detailed examination of the pressure distribution at the exit is shown in Figure 4-59. The results using the $a_1 = 0.34$ coefficient and the BSL model are similar to each other and agree well with the experimental data. On the other hand, the simulations using the original coefficients of the SST model result in a slightly underpredicted pressure. The Mach number distribution at the exit is also similar among the models, with the maximum Mach number being slightly higher and the distribution being more heterogeneous in the simulations using the original coefficients of the SST model.

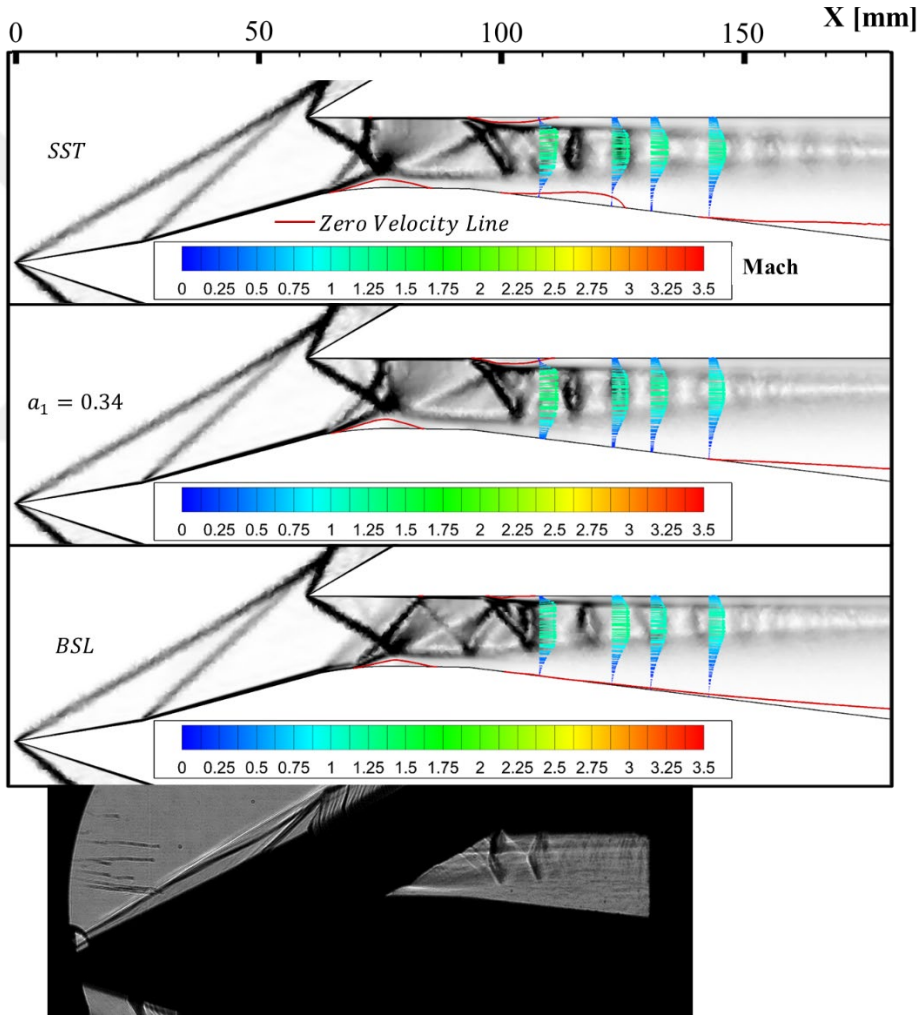


Figure 4-57. Density gradient magnitude contours with velocity vectors and zero velocity line for the numerical simulation and the shadowgraph image corresponding to Mach = 2.63 without bleed (Test 4373) at VPN 18.

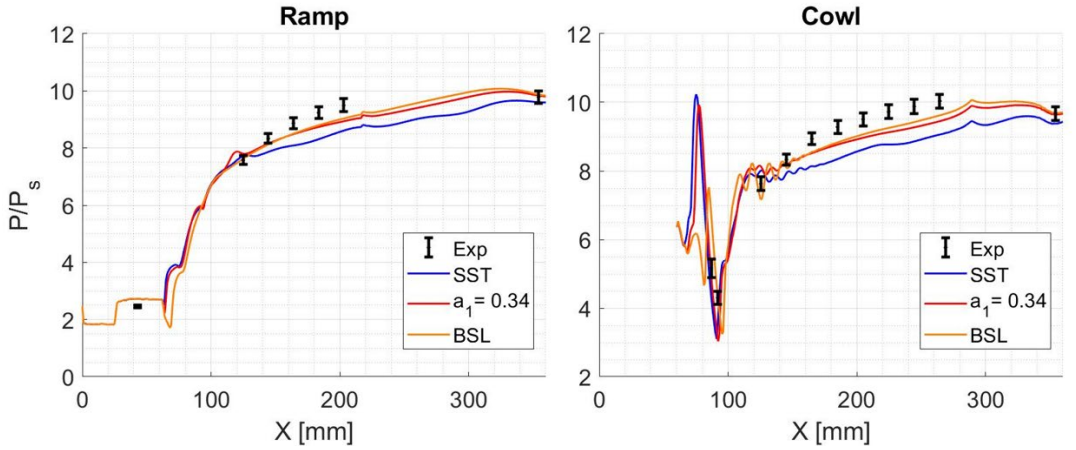


Figure 4-58. Comparison of pressure distribution along the intake between numerical and experimental data for Mach = 2.63 without bleed (Test 4373) at VPN 18.

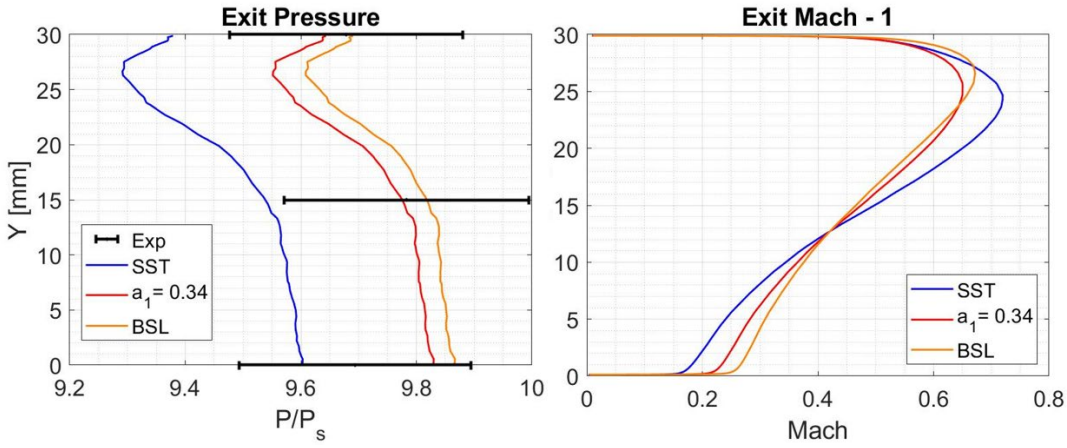


Figure 4-59. Comparison of pressure distribution and Mach number at the exit of the intake for Mach = 2.63 without bleed (Test 4373) at VPN 18.

SUMMARY AND CONCLUDING REMARKS

In this thesis, the focus is on investigating pseudo-shock structures in a mixed compression, rectangular, supersonic intake for different bleed configurations; with and without bleed. The examinations were conducted for two different Mach numbers: on design (Mach = 3) and below design (Mach = 2.63). The objectives were to analyze the change of shock structures under different back pressure throttling, and explore the hysteresis behavior and study the fluctuations of the pseudo-shock through experimental investigations. Additionally, numerical simulations are conducted using the SST and BSL k-ω turbulence models and the results of numerical simulations were utilized to gain further insights into the flow characteristics within the intake.

In this chapter, the concluding remarks and observations derived from both the experimental and numerical studies conducted in this thesis are presented. Furthermore, it provides suggestions for future research.

Summary Experimental Observations:

Abrupt changes in the shock structures during the valve motion or just after settling are observed, leading to the separation of the attached sonic line on the cowl side and attachment to the ramp side or vice versa. The maximum and minimum measured durations for these changes are 4.250 ms and 0.75 ms, respectively. During the tests conducted using the test item with bleed, the bleed wedge shock hits to cowl surface and establishes a location susceptible to separation. With the effect of the back pressure, the separation bubble on the cowl side thickens, leading to a bigger separation bubble and complete separation of the sonic line from the cowl side. The separation shocks due to back pressure tending to sit near the impact point of the other oblique shocks. In the tests without the bleed, the cowl shock generates a separation bubble on the ramp side. With an increase in back pressure, the pseudo-shocks begin to influence the separation bubble formed due to the cowl shock,

resulting in a detached sonic line on the ramp side. This detachment can alter the orientation of the pseudo-shock structure, causing a complete change in its direction.

At the operational points where there is a sudden and significant change in shock structures due to changes in back pressure, hysteresis characteristics are observed with respect to throttling direction. As the catastrophe theory suggests, the shock structures tend to maintain their previous form.

The use of image averaging technique has provided insights into the effects of the pseudo-shock on the flow structure and allowed identification of the areas in which the pseudo-shock is most prominent. Examining the instantaneous shadowgraph images has revealed the oscillatory nature of the pseudo-shocks. The experiments involving bleed have shown that these oscillations can result in significant changes in position, up to 12.9 mm, corresponding to a displacement amplitude of 45% relative to the throat height of the intake. However, when the pseudo-shock interacts with the bleed region, a relatively stable position is observed with a displacement during oscillations less than 2.5 mm. For the tests without bleed, the maximum observed change in position during the oscillations is 7.6 mm, and after the formation of structures related to λ-type shocks, there is a consistent decrease in displacement of the shock down to 4.5 mm.

In the conducted tests using the item with bleed, it was observed that at higher throttled conditions, when the first shock of the pseudo-shock on the ramp side reaches the diffuser section with a lower angle, oscillations result in not only changes in the shock position but also alternating switches between X and λ-type shock structures. Furthermore, when the back throttling is increased further, and the first shock of the pseudo-shock on the ramp side remains on the diffuser section with a lower angle during the oscillations, the λ-type shock is predominant. This shift in shock structure was observed at both Mach numbers of 2.63 and 3, suggesting that the impact of the diffuser angle might be more significant than that of the pre-shock Mach number.

Moving averaged data of the traced position revealed that, the mean position of the first separation shock of the pseudo-shock moves toward upstream as the back pressure increases. Moreover, the most upstream and downstream positions of the leading shocks of the pseudo-shock during the oscillations move upstream.

Pressure measurements together with the shadowgraph images reveal that, an attached sonic line on both ramp and cowl side, results in a pseudo-shock structure capable of compressing the flow in a shorter distance. The length of the pseudo-shock is not always shorter at higher throttling conditions, as it depends on factors such as the separation characteristics and related shock structures.

The experiments show that the maximum achievable pressure recovery is %56 at Mach = 2.63 and %45 at Mach = 3 without bleed. However, when bleed is employed, the maximum pressure recovery increases to %67 at Mach = 2.63 and %56 at Mach = 3. As expected, the use of bleed results in a decrease in the mass flow ratio. The highest measured supercritical mass flow ratios for the tests at Mach = 3 are 0.98 without bleed and 0.93 with bleed, whereas at Mach = 2.63, the maximum measured supercritical mass flow ratios are 0.87 without bleed and 0.77 with bleed. It is worth noting that the cowl shock hits the bleed channel at a more upstream position, resulting in higher air loss due to bleed at Mach = 2.63.

The interaction between the shock structure and bleed region are analyzed by examining the flow field within the bleed channel. The oscillation of shock structures during the dwell time can result in oscillation of the operational mode, particularly at points close to the critical operation mode. However, calculated mass flow rate using the measured pressure reveals that, from an operational perspective, a significant change in the mass flow ratio can only be observed with further back throttling.

Summary of Observations Regarding the CFD Simulations and Comparison with the Experimental Data

The experiments and numerical simulations of the test item without bleed showed that as the back pressure increases, the subsonic region inside the separation bubble formed by the cowl shock merges with the subsonic region caused by the pseudo-shock on the ramp side. Although the flow downstream of the separation bubble reattaches, the sonic line remains detached due to the thickening of the boundary layer, resulting in the thickening of the sonic layer. As a result, the thickness of the sonic layer increases and further confines the pseudo-shock.

The orientation of the pseudo-shock is influenced by the relative sizes of the separation bubbles on the cowl and ramp side. The shock-train has a tendency to attach to the side where the separation bubble is smaller in size. Moreover, orientation of the pseudo-shock has a significant impact on the Mach number distribution at the exit of the intake.

For the case with bleed, all of the simulations produce compatible results with each other and with experiments upstream of pseudo-shock. However, for the cases without bleed, formation of cowl shock related separation bubble leads some differences between the simulations. SST with original coefficients is better in estimating the separation bubble due to cowl shock. Moreover, increasing the a_1 results in calculation of the separation bubble starting at slightly downstream. Calculations with BSL shows a more noticeable downstream shift in the separation bubble. Onset of the pseudo-shock related pressure rise can be calculated slightly different with SST and BSL models. The range of difference observed in this study changes between 3 to 9 mm.

At lower throttled conditions, there is a noticeable difference between the SST and BSL models. The a_1 parameter has a significant effect on the results. The BSL model and the SST model with higher a_1 value provides a better estimation of the pressure rise due to the pseudo-shock and the exit pressure. However, as the throttling increases and the mode of operation approaches to critical, the difference between

the models decreases. Additionally, for higher throttled conditions, the SST model with its original coefficients provides a better estimation of the pressure distribution due to its ability to better estimate the location of separations.

Concluding Remarks

In the content of pseudo-shock structures in a mixed compression rectangular supersonic intake, the concluding remarks are as follows:

-The undisturbed locations of the oblique shocks and their impact points on the walls, as well as the formation of separation bubbles due to the oblique shocks, have significant effect on the location of the onset, orientation, and oscillation characteristics of the pseudo-shock. Moreover, they significantly influence the pseudo-shock's orientation at operational points, where abrupt changes and hysteresis phenomena are observed.

-The orientation of the pseudo-shock is influenced by the relative sizes of the separation bubbles formed by the leading shocks on the cowl and ramp sides. The shock-train has a tendency to attach to the side with a smaller separation bubble.

-Oscillatory behavior of the pseudo-shock can lead to substantial position changes, up to 12.9 mm, representing a displacement amplitude of 45% relative to the intake's throat height. However, stability is observed when the pseudo-shock interacts with the bleed region.

-At operational points where significant changes in shock structures occur due to variations in back pressure, hysteresis characteristics are observed, consistent with the catastrophe theory's suggestion that shock structures tend to retain their previous form.

-When predicting flow using CFD with the RANS approach, particularly with Menter’s SST and BSL models, careful attention should be given to turbulence modeling. The BSL model and the SST model with a higher a_1 value provide better estimations of pressure rise due to the pseudo-shock and exit pressure at lower throttled conditions. For higher throttled conditions, the SST model with its original

coefficients delivers better estimations of pressure distribution due to its improved ability to estimate separation locations.

Suggestions for Future Research

To better characterize the oscillatory behavior of the pseudo-shock in supersonic intakes, it is recommended to conduct experiments using high-speed pressure sensors. By analyzing the high-frequency pressure data, the effect of pseudo-shock oscillation on pressure oscillation and the magnitude of pressure changes due to the oscillations can be determined. Although visual examination of the shocks during the reopening of the valve was not possible in the present study due to memory limitations of the high-speed camera, it is proposed to capture the shape of the shock structures using high-speed shadowgraphy during both the closing and opening of the back pressure valve. This will allow for a visual examination of the hysteresis behavior and its effects. Performing the numerical simulations that requires high computational power and utilizing anisotropic turbulence models such as EARSM-based models [97] or hybrid models like SUQ-SST [98], which combine the equations of EARSM and SST, would be beneficial. Additionally, conducting the simulations with higher computational power using the unsteady RANS equations has the potential to generate data that can help understand the unsteady behavior of the pseudo-shock in supersonic intakes.

REFERENCES

[1] R. S. Fry, "A Century of Ramjet Propulsion Technology Evolution," *Journal of Propulsion and Power*, vol. 20, no. 1. American Institute of Aeronautics and Astronautics Inc., pp. 27–58, 2004.

[2] J. Anderson, *Fundamentals of Aerodynamics*, Sixth Edition.

[3] *Air Intakes for High Speed Vehicles*. Advisory Group for Aerospace Research & Development (AGARD), 1991.

[4] C. Bauer and G. Kurthy, "Importance of the bleed system on the overall air intake performance," in *47th AIAA/ASME/SAE/ASEE Joint Propulsion Conference and Exhibit 2011*, 2011.

[5] G. Kurth and C. Bauer, "Air Intake Development for Supersonic Missiles," 2008.

[6] J. Ekermo, "Validation and Parametric Study of Supersonic Air Intake," Master's Thesis in Applied Mechanics, Chalmers University of Technology, 2018.

[7] Vignesh Ram, Petha Sethuraman, and Heuy Dong Kim, "Characteristics of Shock Train Flow in Divergent Channels," in *Lecture Notes in Mechanical Engineering - Recent Asian Research on Thermal and Fluid Sciences*, A. Suryan Deog Hee Doh Minoru Yaga Guang Zhang, Ed., Springer Nature Singapore, 2018, pp. 353–364.

[8] F. Gnani, H. Zare-Behtash, and K. Kontis, "Pseudo-shock waves and their interactions in high-speed intakes," *Progress in Aerospace Sciences*, vol. 82, pp. 36–56, Apr. 2016.

[9] M. Sajben, J. Donovan, and M. Morris, "Experimental Investigation of Terminal Shock Sensors in Mixed-Compression Inlets," in *AIAA/SAE/ASME/ASEE 26th Joint Propulsion Conference*, 1990.

[10] D. Herrmann and A. Gülhan, “Experimental analyses of inlet characteristics of an airbreathing missile with boundary-layer bleed,” *J Propuls Power*, vol. 31, no. 1, pp. 170–179, Jan. 2015.

[11] D. Herrmann, F. Siebe, and A. Gülhan, “Pressure fluctuations (buzzing) and inlet performance of an airbreathing missile,” *J Propuls Power*, vol. 29, no. 4, pp. 839–848, 2013.

[12] D. Herrmann, S. Blem, and A. Gülhan, “Experimental study of boundary-layer bleed impact on ramjet inlet performance,” *J Propuls Power*, vol. 27, no. 6, pp. 1186–1195, 2011.

[13] M. R. Soltani, A. Daliri, and J. S. Younsi, “Effects of shock wave/boundary-layer interaction on performance and stability of a mixed-compression inlet,” *Scientia Iranica B*, vol. 23, no. 4, pp. 1811–1825, 2016.

[14] N. Khobragade *et al.*, “Characterization of bleedless shockwave-boundary layer interactions for high-speed intakes,” in *AIAA Scitech 2020 Forum*, American Institute of Aeronautics and Astronautics Inc, AIAA, 2020, pp. 1–20.

[15] A. C. Calvin, N. Khobragade, S. Unnikrishnan, and R. Kumar, “Computational and Experimental Evaluation of Unstart Characteristics of a Mixed-Compression Intake,” in *AIAA AVIATION 2022 Forum*, American Institute of Aeronautics and Astronautics Inc, AIAA, 2022.

[16] H. J. Lee, B. J. Lee, S. D. Kim, and I. S. Jeung, “Investigation of the pseudo-shock wave in a two-dimensional supersonic inlet,” *J Vis (Tokyo)*, vol. 13, no. 1, pp. 25–32, Feb. 2010.

[17] A. Kantrowitz and C. D. Donaldson, *Preliminary Investigation of Supersonic Diffusers*. Natonal Advisory Committee for Aeronautics, 1945.

[18] S. J. das K Prasad, “Starting characteristics of a rectangular supersonic air-intake with cowl deflection,” *The Aeronautical Journal*, vol. 114, 2010.

[19] A. K. Flock and A. Gülhan, “Modified Kantrowitz starting criteria for mixed compression supersonic intakes,” *AIAA Journal*, May 2019.

[20] T Cain, *Ramjet Intakes*. NATO STO, 2010.

[21] H. Ran, R. Denney, and D. N. Mavris, “Determination of the Terminal Shock in Two-Dimensional Supersonic Inlets,” *J Aircr*, vol. 49, no. 5, pp. 1532–1535, 2012.

[22] F. Gnani, H. Zare-Behtash, C. White, and K. Kontis, “Effect of Back-pressure Forcing on Shock Train Structures in Rectangular Channels,” *Acta Astronaut*, vol. 145, pp. 471–481, 2018.

[23] R. L. Klomparens, J. F. Driscolly, and M. Gambaz, “Response of a shock train to downstream back pressure forcing,” in *54th AIAA Aerospace Sciences Meeting*, American Institute of Aeronautics and Astronautics Inc, AIAA, 2016.

[24] K. Matsuo, Y. Miyazato, and H.-D. Kim, *Progress in Aerospace Sciences 25 - Shock train and pseudo-shock phenomena in internal gas flows*, vol. 35. Elsevier Science Ltd., 1999.

[25] John J. Mahoney, *Inlets for Supersonic Missiles*. AIAA, 1990.

[26] J. Sepahi-Younsi, B. Forouzi Feshalami, S. R. Maadi, and M. R. Soltani, “Boundary layer suction for high-speed air intakes: A review,” *Proceedings of the Institution of Mechanical Engineers, Part G: Journal of Aerospace Engineering*, vol. 233, no. 9. SAGE Publications Ltd, pp. 3459–3481, Jul. 01, 2019.

[27] M. R. Soltani, J. S. Younsi, and M. Farahani, “Effects of boundary-layer bleed parameters on supersonic intake performance,” *J Propuls Power*, vol. 31, no. 3, pp. 826–836, 2015.

[28] S. Trapier, S. Deck, and P. Duveau, “Delayed detached-eddy simulation and analysis of supersonic inlet buzz,” *AIAA Journal*, vol. 46, no. 1, pp. 118–131, Jan. 2008.

[29] N. D. Domel, D. Baruzzini, and D. N. Miller, “A perspective on mixed-compression inlets and the use of cfd and flow control in the design process,” in *50th AIAA Aerospace Sciences Meeting Including the New Horizons Forum and Aerospace Exposition*, 2012.

[30] J. Délery and J. P. Dussauge, “Some physical aspects of shock wave/boundary layer interactions,” *Shock Waves*, vol. 19, no. 6, pp. 453–468, 2009.

[31] N. D. Sandham, *Shock-Wave/Boundary-Layer Interactions*. NATO STO, 2011.

[32] M. Sajben, T. J. Bogar, and J. C. Kroutil, “Experimental Study of Flows in a Two-Dimensional Inlet Model,” in *AIAA 21st Aerospace Sciences Meeting*, 1983.

[33] N. Khobragade and R. Kumar, “Control of shock wave/boundary layer interactions in a supersonic air intake using a modified backward-facing step,” *Shock Waves*, vol. 32, no. 6, pp. 467–483, Sep. 2022.

[34] H. Babinsky and J. K. Harvey, *Shock Wave-Boundary Layer Interactions*. Cambridge University Press, 2011.

[35] Barry Edney, “Anomalous Heat Transfer And Pressure Distributions On Blunt Bodies At Hypersonic Speeds In The Presence Of An Impinging Shock,” 1968.

[36] T. Ikui, K. Matsuo, and K. Sasaguchi, “Modified Diffusion Model of Pseudo-Shock Waves Considering Upstream Boundary Layers,” *Bulletin of the Japan Society of Mechanical Engineers*, 1981.

[37] T. Ikui, K. Matsuo, and M. Nagai, “The Mechanism of Pseudo-Shock Waves,” *Bulletin of the Japan Society of Mechanical Engineers*, 1974.

[38] L. Q. Sun and K. Fukuda, “Numerical and Experimental Investigations on the Mach 2 Pseudo-Shock Wave in a Square Duct,” *J Vis (Tokyo)*, vol. 6, no. 4, pp. 363–370, 2003.

[39] Vignesh Ram, Petha Sethuraman, Abhilash Suryan, and Heuy Dong Kim, “Pseudo Shock Wave in a Slotted Duct of Constant Area,” in *Lecture Notes in Mechanical Engineering - Recent Asian Research on Thermal and Fluid Sciences*, A. Suryan Deog Hee Doh Minoru Yaga Guang Zhang, Ed., Springer Nature Singapore, 2018, pp. 341–352.

[40] T. Tamaki, Y. Tomita, and Y. Ryuichiro, “A Study of Pseudo-Shock (1st Report, X-Type Pseudo-Shock),” vol. 14, no. 74, 1971.

[41] T. Tamaki, Y. Tomita, and R. Yamane, “A Study of Pseudo-Shock (1st Report, λ-Type Pseudo-Shock),” *Bulletin of the JSME*, vol. 13, no. 55, 1970.

[42] R. L. Hunt and M. Gamba, “Shock train unsteadiness characteristics, oblique-to-normal transition, and three-dimensional leading shock structure,” *AIAA Journal*, vol. 56, no. 4, pp. 1569–1587, 2018.

[43] Y. Jin, Y. Zhang, X. Li, H. Tan, and S. Sun, “Suppression of flow response hysteresis in the throttling/unthrottling process for supersonic inlet,” *Acta Astronaut*, vol. 202, pp. 34–47, Jan. 2023.

[44] X. Jiao, J. Chang, Z. Wang, and D. Yu, “Hysteresis phenomenon of hypersonic inlet at high Mach number,” *Acta Astronaut*, vol. 128, pp. 657–668, Nov. 2016.

[45] T. Cui, S. Tang, C. Zhang, and D. Yu, “Hysteresis phenomenon of mode transition in ramjet engines and its topological rule,” *J Propuls Power*, vol. 28, no. 6, pp. 1277–1284, 2012.

[46] T. Cui and S. Tang, “Geometry rule of combustor-inlet interaction in ramjet engines,” *J Propuls Power*, vol. 30, no. 2, pp. 449–460, 2014.

[47] Y. Jin, S. Sun, H. Tan, Y. Zhang, and H. Huang, “Flow response hysteresis of throat regulation process of a two-dimensional mixed-compression supersonic inlet,” *Chinese Journal of Aeronautics*, vol. 35, no. 3, pp. 112–127, Mar. 2022.

[48] M. S. Ivanov, G. Ben-Dor, T. Elperin, A. N. Kudryavtsev, and D. V. Khotyanovsky, “Flow-Mach-number-variation-induced hysteresis in steady shock wave reflections,” *AIAA Journal*, vol. 39, no. 5, pp. 972–974, 2001.

[49] G. Ben-Dor, T. Elperin, and E. I. Vasiliev, “Flow-Mach-number-induced hysteresis phenomena in the interaction of conical shock waves - A numerical investigation,” *J Fluid Mech*, vol. 496, pp. 335–354, Dec. 2003.

[50] X. Zhang *et al.*, “Experimental study of hysteresis and catastrophe in a cavity-based scramjet combustor,” *Chinese Journal of Aeronautics*, vol. 35, no. 10, pp. 118–133, Oct. 2022.

[51] J. Chang, L. Wang, W. Bao, Q. Yang, and J. Qin, “Experimental investigation of hysteresis phenomenon for scramjet engine,” *AIAA Journal*, vol. 52, no. 2, pp. 447–451, Feb. 2014.

[52] C. Tao, Y. Daren, C. Juntao, and B. Wen, “Topological geometry interpretation of supersonic inlet start/unstart based on catastrophe theory,” *J Aircr*, vol. 45, no. 4, pp. 1464–1468, 2008.

[53] C. Tao, Y. Daren, C. Juntao, and B. Wen, “Catastrophe model for supersonic inlet start/unstart,” *J Aircr*, vol. 46, no. 4, pp. 1160–1166, 2009.

[54] E. C. Zeeman, “Catastrophe Theory,” *Sci Am*, vol. 234, no. 4, pp. 65–83, 1976.

[55] G. Ben-Dor, “Hysteresis phenomena in shock wave reflections in steady flows,” in *FIFTH INTERNATIONAL CONGRESS ON SOUND AND VIBRATION* , 1997.

[56] W. Shi, J. Chang, J. C. Ma, Y. Wang, L. Gao, and W. Bao, “Path dependence characteristic of shock train in a 2D hypersonic inlet with variable background waves,” *Aerosp Sci Technol*, vol. 86, pp. 650–658, Mar. 2019, doi: 10.1016/j.ast.2019.02.001.

[57] B. F. Carroll and J. C. Dutton, “Characteristics of multiple shock wave/turbulent boundary-layer interactions in rectangular ducts,” *J Propuls Power*, vol. 6, no. 2, pp. 186–193, 1990.

[58] T. Oka, D. Ono, and Y. Miyazato, “Study of shock trains and pseudo-shock waves in constant area ducts,” in *52nd AIAA Aerospace Sciences Meeting - AIAA Science and Technology Forum and Exposition, SciTech 2014*, American Institute of Aeronautics and Astronautics Inc., 2014.

[59] B. F. Carroll and J. C. Dutton, “Multiple normal shock wave/turbulent boundary-layer interactions,” *J Propuls Power*, vol. 8, no. 2, pp. 441–448, 1992.

[60] B. F. Carroll and J. C. Dutton, “Turbulence phenomena in a multiple normal shock wave/turbulent boundary-layer interaction,” *AIAA Journal*, vol. 30, no. 1, pp. 43–48, 1992.

[61] H. Sugiyama, K. Fukuda, K. Mizobata, L. Sun, and R. Minato, “Experimental Investigation on Shock Wave and Turbulent Boundary Layer Interactions in a Square Duct at Mach 2 and 4,” in *Proceedings of the International Gas Turbine Congress*, 2003.

[62] H. Sugiyama, Y. Tsujiguchi, and T. Honma, “Structure and Oscillation Phenomena of Pseudo-Shock Waves in a Straight Square Duct at Mach 2 and 4,” in *AIAA International Space Planes and Hypersonic Systems and Technologies Conference*, 2008.

[63] C. Wang, C. Cheng, K. Cheng, and L. Xue, “Unsteady behavior of oblique shock train and boundary layer interactions,” *Aerosp Sci Technol*, vol. 79, pp. 212–222, Aug. 2018, doi: 10.1016/j.ast.2018.05.054.

[64] K. Matsuo, H. Mozhizuki, Y. Miyazato, and M. Gohya, “Oscillatory characteristics of a pseudo-shock wave in a rectangular straight duct,” *JSME International Journal*, vol. 36, no. 2, 1993.

[65] T. Ikui, K. Matsuo, M. Nagai, and M. Honjo, “Oscillation phenomena of pseudo-shock waves,” *Bulletin of the JSME*, vol. 17, no. 112, 1974.

[66] H. Sugiyama, H. Takeda, J. Zhang, K. Okuda, and H. Yamagishi, “Locations and oscillation phenomena of pseudo-shock waves in a straight rectangular duct,” *JSME International Journal*, 1987.

[67] J. K. James, P. S. Vignesh Ram, and H. D. Kim, “Characteristics of self-excited shock wave oscillations in a supersonic isolator with exit duct configurations,” *Acta Astronaut*, vol. 203, pp. 1–15, Feb. 2023, doi: 10.1016/j.actaastro.2022.11.029.

[68] V. R. Petha Sethuraman, T. H. Kim, and H. D. Kim, “Effects of back pressure perturbation on shock train oscillations in a rectangular duct,” *Acta Astronaut*, vol. 179, pp. 525–535, Feb. 2021, doi: 10.1016/j.actaastro.2020.11.057.

[69] L. Lu, Y. Wang, X. qiang Fan, G. wei Yan, and J. wen Pan, “Numerical investigation of shock train unsteady movement in a mixing duct,” *Aerosp Sci Technol*, vol. 81, pp. 375–382, Oct. 2018, doi: 10.1016/j.ast.2018.08.027.

[70] V. R. Petha Sethuraman, T. H. Kim, and H. D. Kim, “Control of the oscillations of shock train using boundary layer suction,” *Aerosp Sci Technol*, vol. 118, Nov. 2021, doi: 10.1016/j.ast.2021.107012.

[71] P. S. V. Ram and H. D. Kim, “The characterization of pseudo-shock wave in various ducts with constant area,” *Journal of Mechanical Science and Technology*, vol. 35, no. 10, pp. 4503–4510, Oct. 2021.

[72] J. K. James and H. D. Kim, “Study on Multiple Shock Wave Structures in Supersonic Internal Flow,” *Journal of the Korean Society of Propulsion Engineers*, vol. 24, no. 3, pp. 31–40, Jun. 2020, doi: 10.6108/kspe.2020.24.3.031.

[73] J. Zhang, H. Yuan, Y. Wang, and G. Huang, “Experiment and numerical investigation of flow control on a supersonic inlet diffuser,” *Aerosp Sci Technol*, vol. 106, Nov. 2020.

[74] M. Fujii, S. Ogura, T. Sato, H. Taguchi, A. Hashimoto, and T. Takahashi, “Effect of angle of attack on the performance of the supersonic intake for High Mach Integrated Control Experiment (HIMICO),” *Aerosp Sci Technol*, vol. 127, Aug. 2022, doi: 10.1016/j.ast.2022.107687.

[75] D. Herrmann and K. Triesch, “Experimental investigation of isolated inlets for high agile missiles,” *Aerosp Sci Technol*, vol. 10, no. 8, pp. 659–667, Dec. 2006, doi: 10.1016/j.ast.2006.05.004.

[76] M. Farahani, A. Daliri, and J. S. Younsi, “Supersonic inlet buzz detection using pressure measurement on wind tunnel wall,” *Aerosp Sci Technol*, vol. 86, pp. 782–793, Mar. 2019, doi: 10.1016/j.ast.2019.02.002.

[77] S. Ogura *et al.*, “Experimental study of high-speed air intake performance by side clearance,” *Aerosp Sci Technol*, vol. 123, Apr. 2022, doi: 10.1016/j.ast.2022.107439.

[78] Y. J. Wang, Y. P. Zhao, H. Wu, and Y. Jin, “A real-time online unstart prediction approach for supersonic inlet,” *Aerosp Sci Technol*, vol. 130, Nov. 2022, doi: 10.1016/j.ast.2022.107883.

[79] J. Sepahi-Younsi, “Effects of boundary-layer bleed parameters on supersonic intake buzz,” *Aerosp Sci Technol*, vol. 120, Jan. 2022, doi: 10.1016/j.ast.2021.107246.

[80] I. T. Karpuzcu, Ü. Poyraz, E. Anık, U. Olgun, H. Tabanlı, and K. B. Yüceil, “Wind tunnel tests of rectangular supersonic air inlet at itu,” in *AIAA Propulsion and Energy Forum and Exposition, 2019*, American Institute of Aeronautics and Astronautics Inc, AIAA, 2019.

[81] M. Winroth, “Pressure measurements in pulsating flows,” 2014.

[82] I. Bajsic, J. Kutin, and T. Zagar, “Response time of a pressure measurement system with a connecting tube,” *Instrum Sci Technol*, vol. 35, no. 4, pp. 399–409, Jul. 2007.

[83] J. Canny, “A Computational Approach to Edge Detection,” *IEEE Trans Pattern Anal Mach Intell*, vol. PAMI-8, no. 6, pp. 679–698, 1986, doi: 10.1109/TPAMI.1986.4767851.

[84] C. Wang, L. Xue, and X. Tian, “Experimental characteristics of oblique shock train upstream propagation,” *Chinese Journal of Aeronautics*, vol. 30, no. 2, pp. 663–676, Apr. 2017, doi: 10.1016/j.cja.2017.02.004.

[85] M.-S. Liou, “Progress Towards an Improved CFD Method: AUSM+,” 1995.

[86] “Imperial College TS4 Supersonic Wind Tunnel Data Sheet,” *National Wind Tunnel Facility United Kingdom*.

[87] “ANSYS Fluent Theory Guide,” 2017. [Online]. Available: http://www.ansys.com

[88] “ANSYS Fluent User’s Guide,” 2017.

[89] F. R. Menter, “Two-equation eddy-viscosity turbulence models for engineering applications,” *AIAA Journal*, vol. 32, no. 8, pp. 1598–1605, 1994, doi: 10.2514/3.12149.

[90] F. Menter, R. Sechner, A. A. Germany GmbH Matyushenko, and S. Petersburg, “Best Practice: RANS Turbulence Modeling in Ansys CFD.”

[91] K. Boychev, G. N. Barakos, and R. Steijl, “Flow physics and sensitivity to RANS modelling assumptions of a multiple shock wave/turbulent boundary layer interaction,” *Aerosp Sci Technol*, vol. 97, Feb. 2020.

[92] A. Erb and S. Hosder, “Analysis of turbulence model uncertainty for shock-wave/boundary-layer interaction simulations,” *J Spacecr Rockets*, vol. 57, no. 6, pp. 1264–1283, 2020.

[93] J. Schaefer, S. Hosder, T. West, C. Rumsey, J. R. Carlson, and W. Kleb, “Uncertainty quantification of turbulence model closure coefficients for transonic wall-bounded flows,” in *AIAA Journal*, American Institute of Aeronautics and Astronautics Inc., 2017, pp. 195–213. doi: 10.2514/1.J054902.

[94] A. Erb and S. Hosder, “Uncertainty analysis of turbulence model closure coefficients for shock wave-boundary layer interaction simulations,” in *AIAA Aerospace Sciences Meeting, 2018*, American Institute of Aeronautics and Astronautics Inc, AIAA, 2018. doi: 10.2514/6.2018-2077.

[95] F. zhi Zeng, J. ping Li, Y. Wang, M. Sun, and C. Yan, “Parametric uncertainty quantification of SST turbulence model for a shock train and pseudo-shock phenomenon,” *Acta Astronaut*, vol. 196, pp. 290–302, Jul. 2022, doi: 10.1016/j.actaastro.2022.05.002.

[96] N. J. Georgiadis and D. A. Yoder, “Recalibration of the shear stress transport model to improve calculation of shock separated flows,” in *51st AIAA Aerospace Sciences Meeting including the New Horizons Forum and Aerospace Exposition 2013*, American Institute of Aeronautics and Astronautics Inc., 2013. doi: 10.2514/6.2013-685.

[97] Gatski T B and Speziale C G, “On explicit algebraic stress models for complex turbulent flows,” *J. Fluid Mech*, vol. 254, pp. 59–77, 1993.

[98] P. Raje and K. Sinha, “Anisotropic SST turbulence model for shock-boundary layer interaction,” *Comput Fluids*, vol. 228, Oct. 2021, doi: 10.1016/j.compfluid.2021.105072.

APPENDICES

A. Calculated Distances Using the Tracer Lines for Different Tests and VPNs

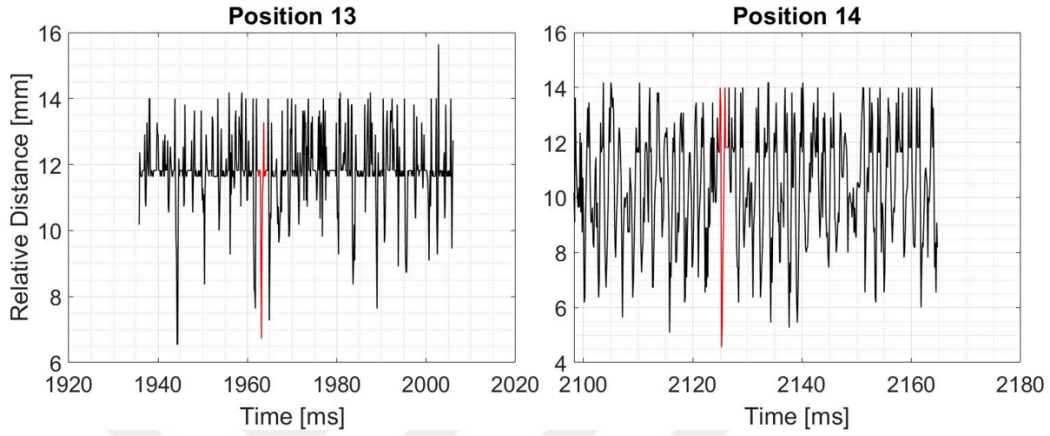


Figure A 1. Calculated distances at VPNs 13 and 14 for Mach = 3 with bleed (Test 4331).

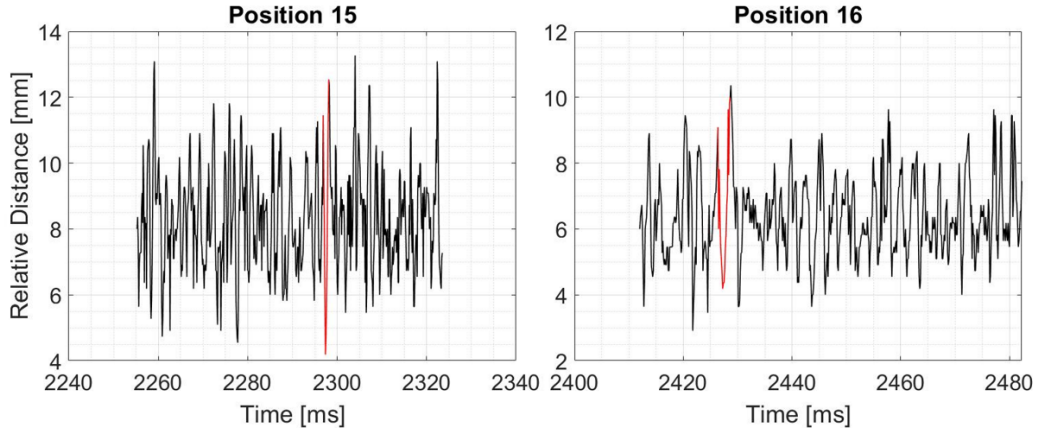


Figure A 2. Calculated distances at VPNs 15 and 16 for Mach = 3 with bleed (Test 4331).

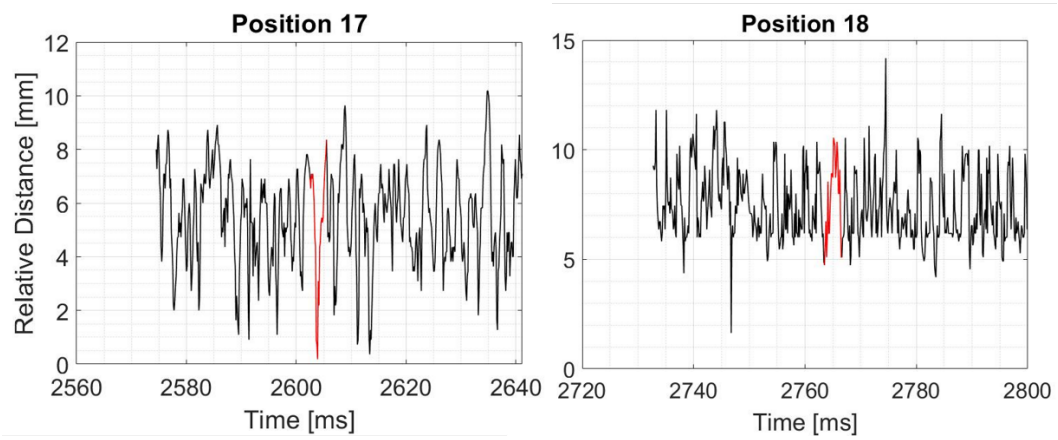


Figure A 3. Calculated distances at VPNs 17 and 18 for Mach = 3 with bleed (Test 4331).

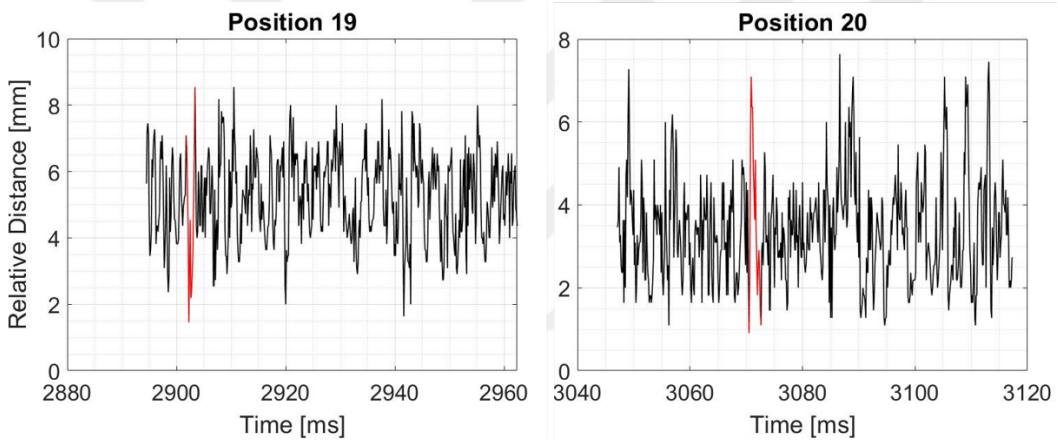


Figure A 4. Calculated distances at VPNs 19 and 20 for Mach = 3 with bleed (Test 4331).

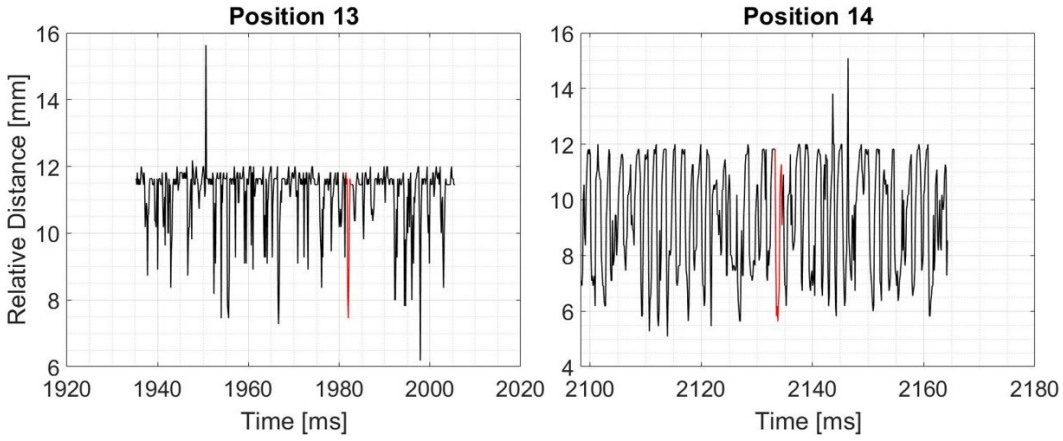


Figure A 5. Calculated distances at VPNs 13 and 14 for Mach = 2.63 with bleed (Test 4340).

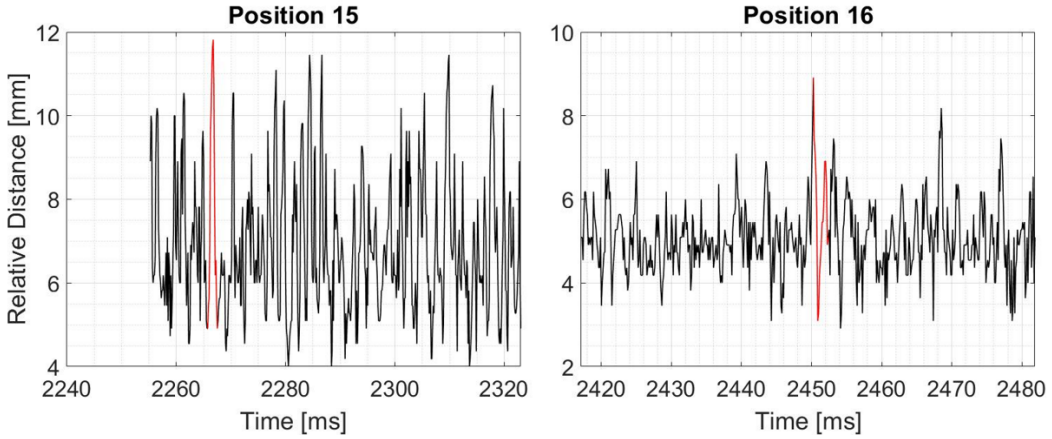


Figure A 6. Calculated distances at VPNs 15 and 16 for Mach = 2.63 with bleed (Test 4340).

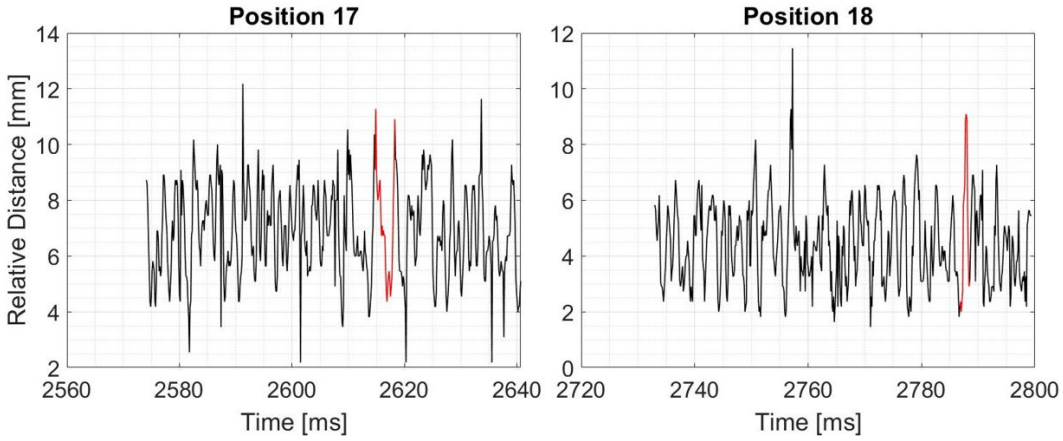


Figure A 7. Calculated distances at VPNs 17 and 18 for Mach = 2.63 with bleed (Test 4340).

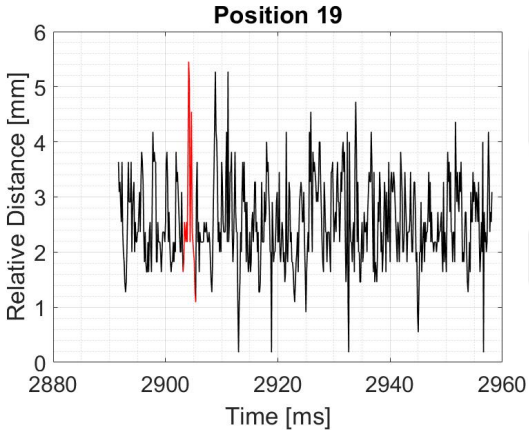


Figure A 8. Calculated distances at VPN 19 for Mach = 2.63 with bleed (Test 4340).

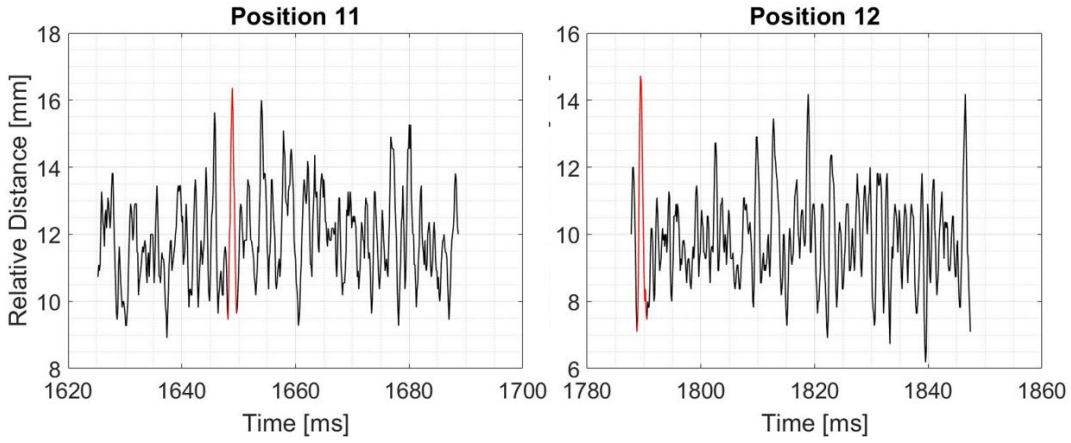


Figure A 9. Calculated distances at VPNs 11 and 12 for Mach = 3 without bleed (Test 4372).

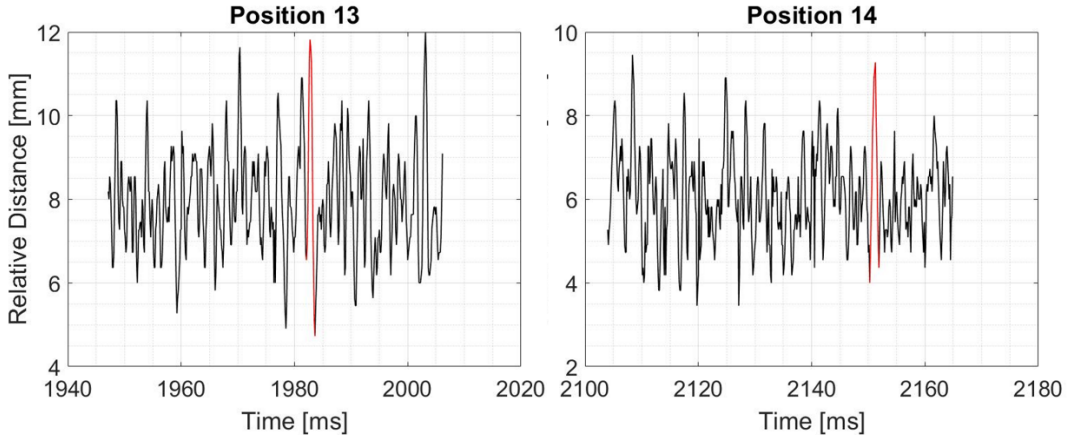


Figure A 10. Calculated distances at VPNs 13 and 14 Mach = 3 without bleed (Test 4372).

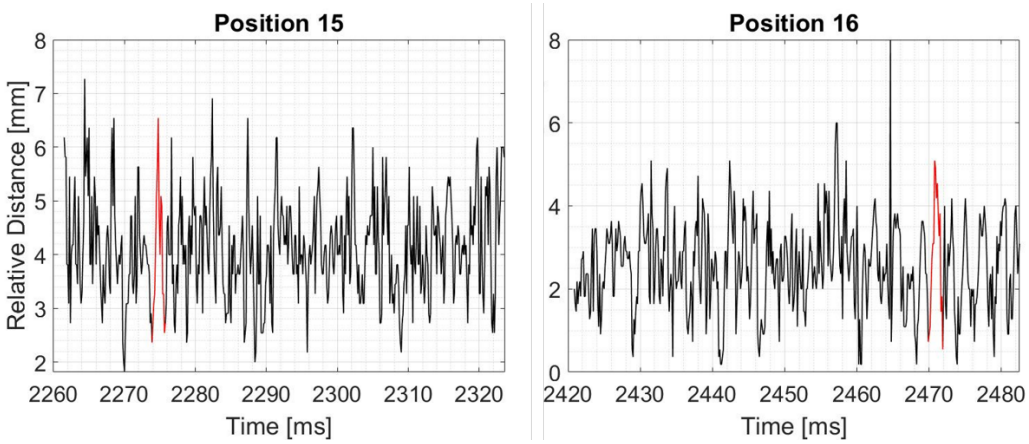


Figure A 11. Calculated distances at VPNs 15 and 16 for Mach = 3 without bleed (Test 4372).

B. Oscillation of Shock Patterns for Different Tests and VPNs

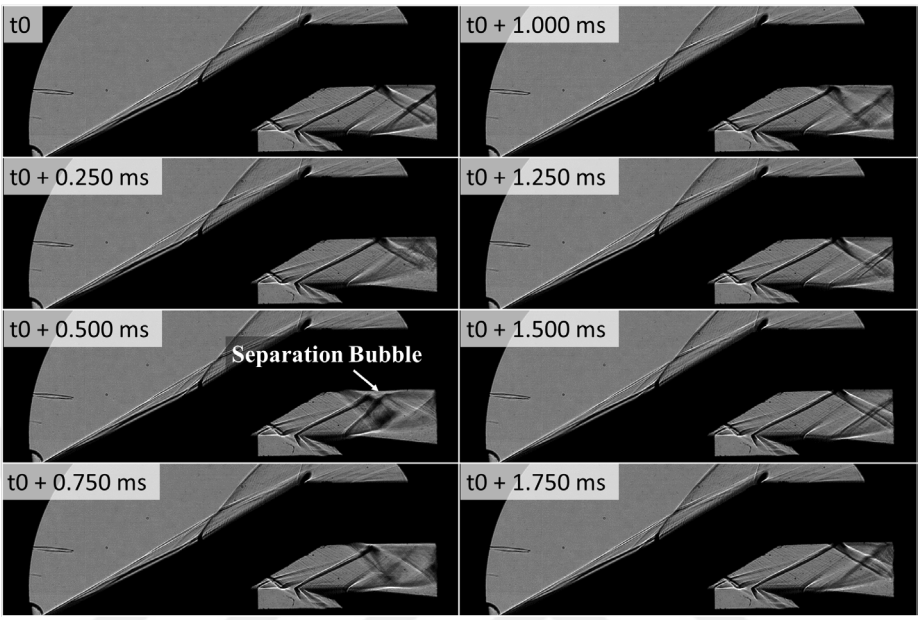


Figure B 1. Oscillation of shock patterns at VPN 14 for Mach = 3 with bleed (Test 4331).

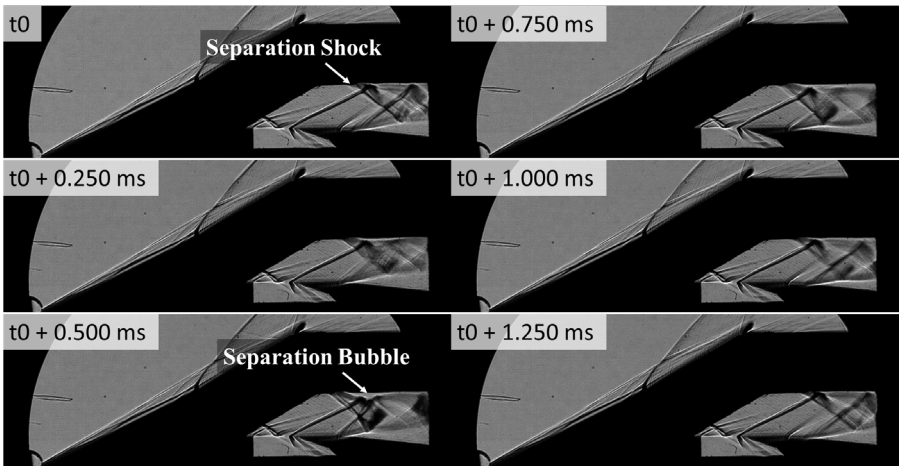


Figure B 2. Oscillation of shock patterns at VPN 15 for Mach = 3 with bleed (Test 4331).

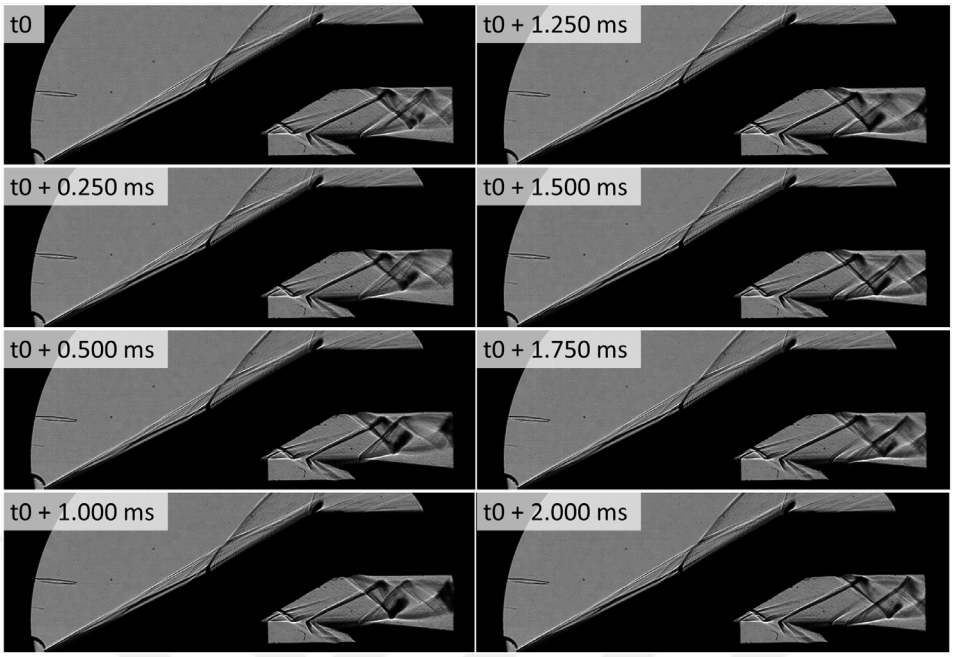


Figure B 3. Oscillation of shock patterns at VPN 16 for Mach = 3 with bleed (Test 4331).

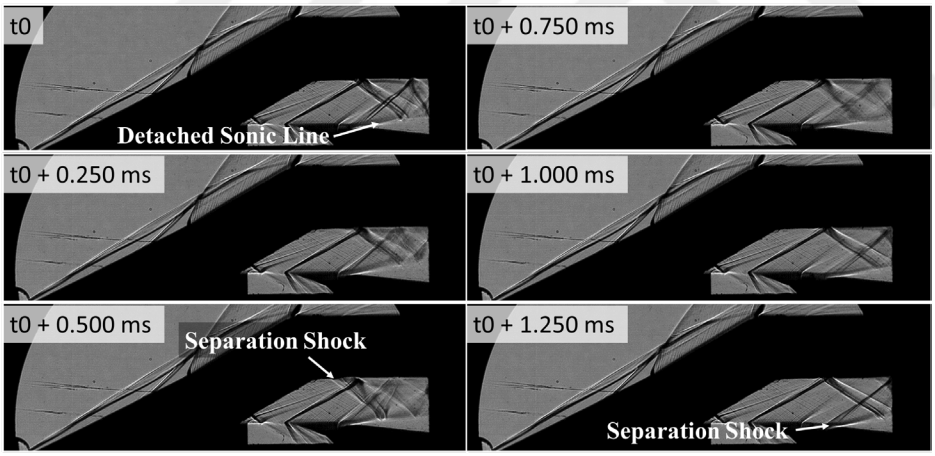


Figure B 4. Oscillation of shock patterns at VPN 13 for Mach = 2.63 with bleed (Test 4340).

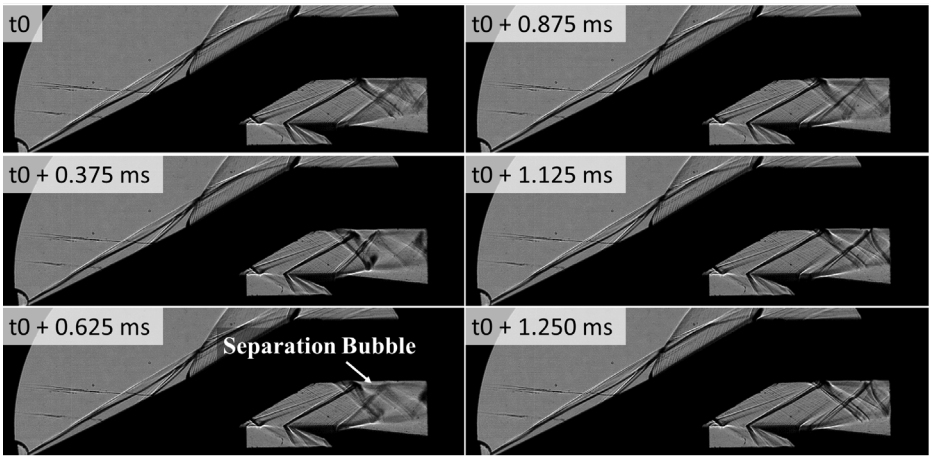


Figure B 5. Oscillation of shock patterns at VPN 14 for Mach = 2.63 with bleed (Test 4340).

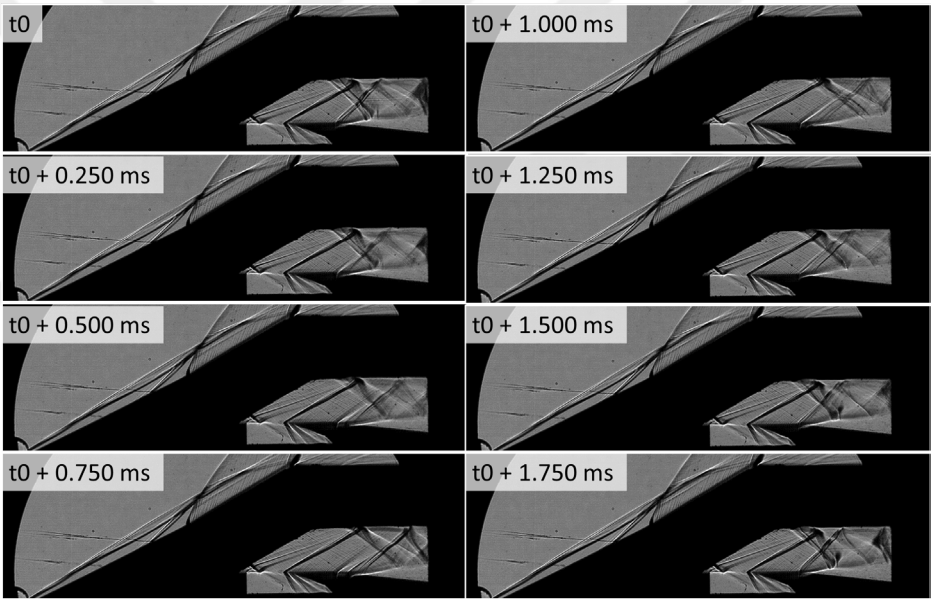


Figure B 6. Oscillation of shock patterns at VPN 15 for Mach = 2.63 with bleed (Test 4340).

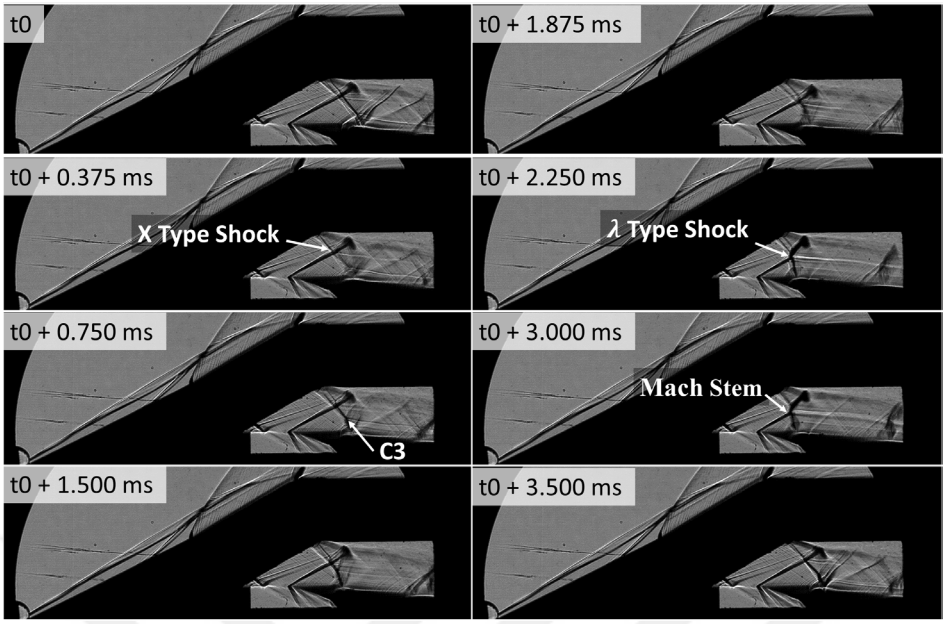


Figure B 7. Oscillation of shock patterns at VPN 17 for Mach = 2.63 with bleed (Test 4340).

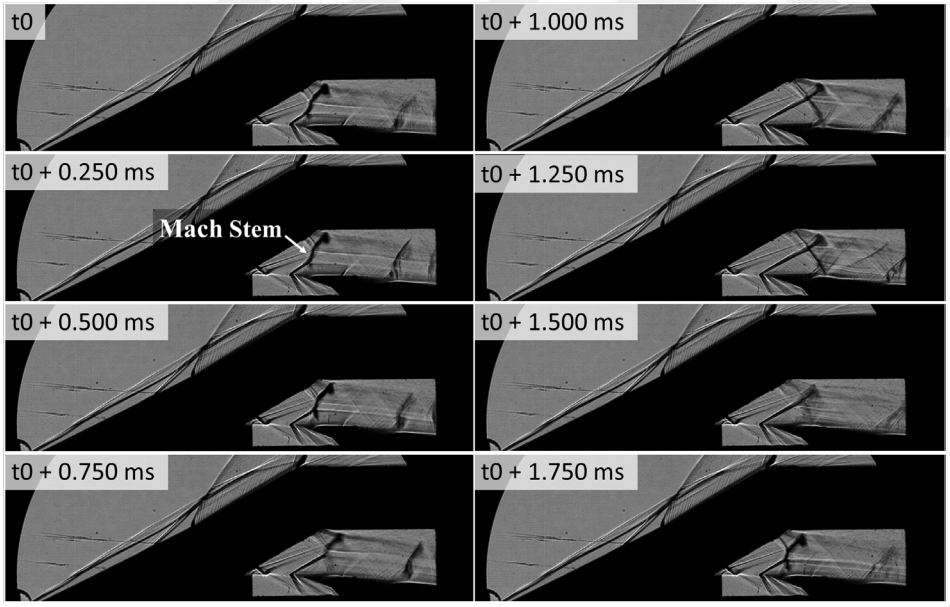


Figure B 8. Oscillation of shock patterns at VPN 18 for Mach = 2.63 with bleed (Test 4340).

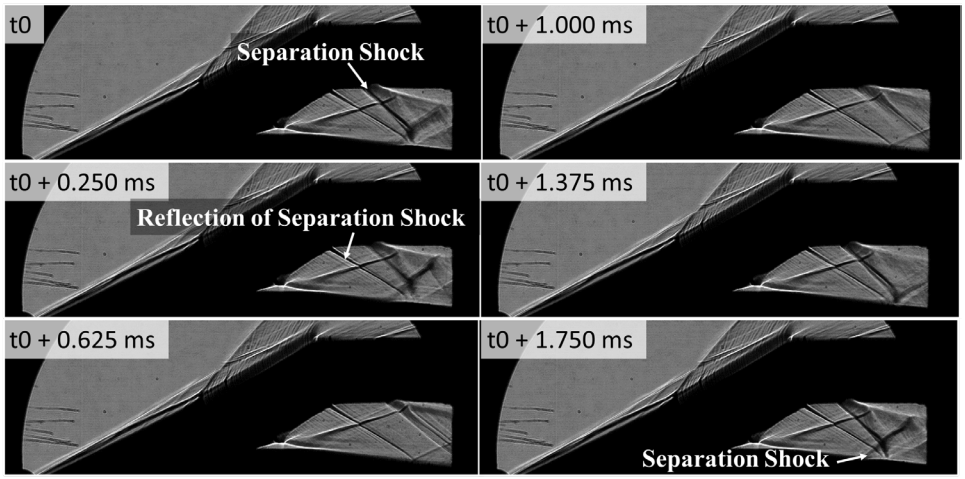


Figure B 9. Oscillation of shock patterns at VPN 12 for Mach = 3 without bleed (Test 4372).

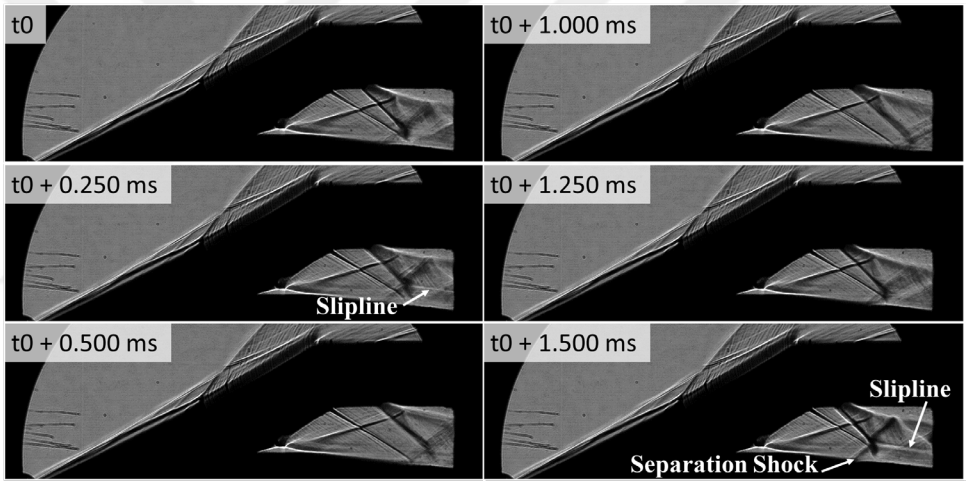


Figure B 10. Oscillation of shock patterns at VPN 13 for Mach = 3 without bleed (Test 4372).

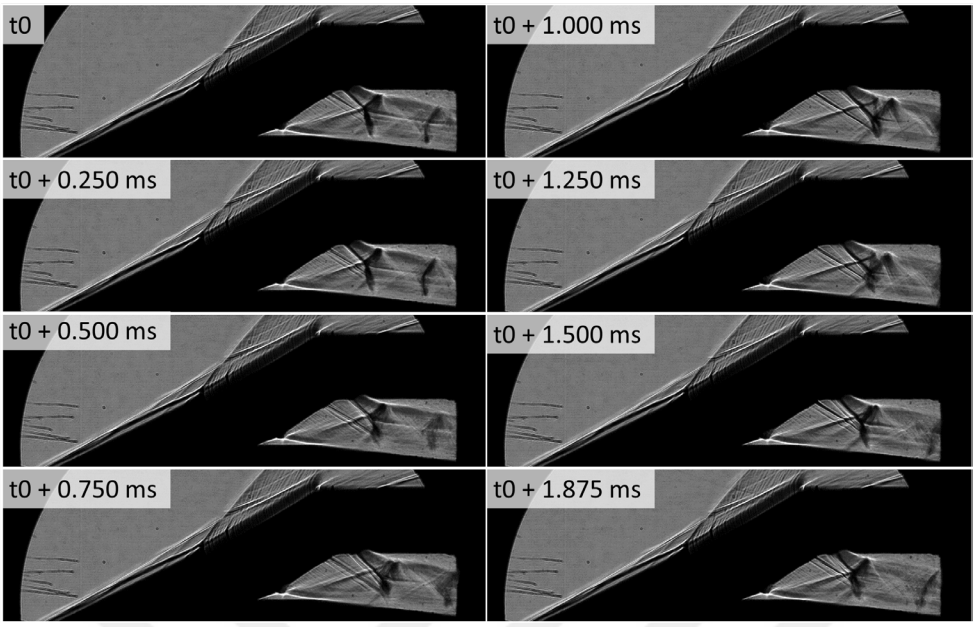


Figure B 11. Oscillation of shock patterns at VPN 16 for Mach = 3 without bleed (Test 4372).

C. Change in the Shock Structures During Back Pressure Transitions

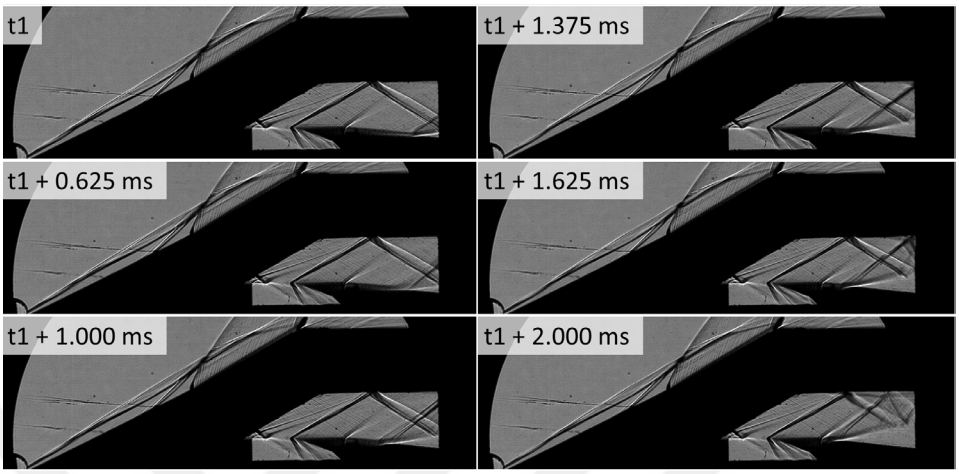


Figure C 1. Change of the shock structures between VPNs 11 and 12 for Mach = 2.63 with bleed (Test 4340).

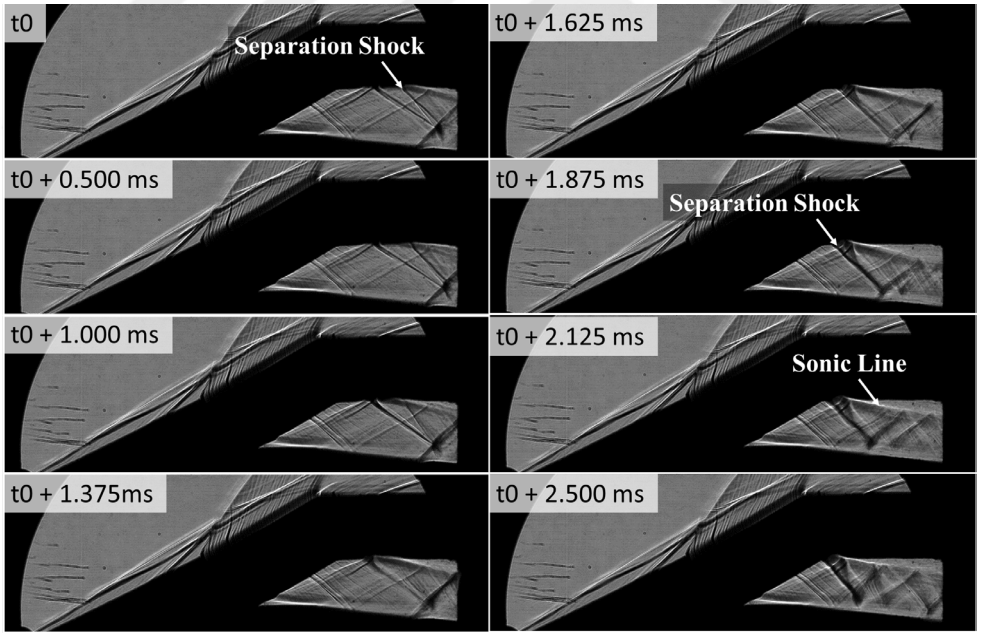


Figure C 2. Change of the shock structures between VPNs 13 and 14 for Mach = 2.63 without bleed (Test 4373).

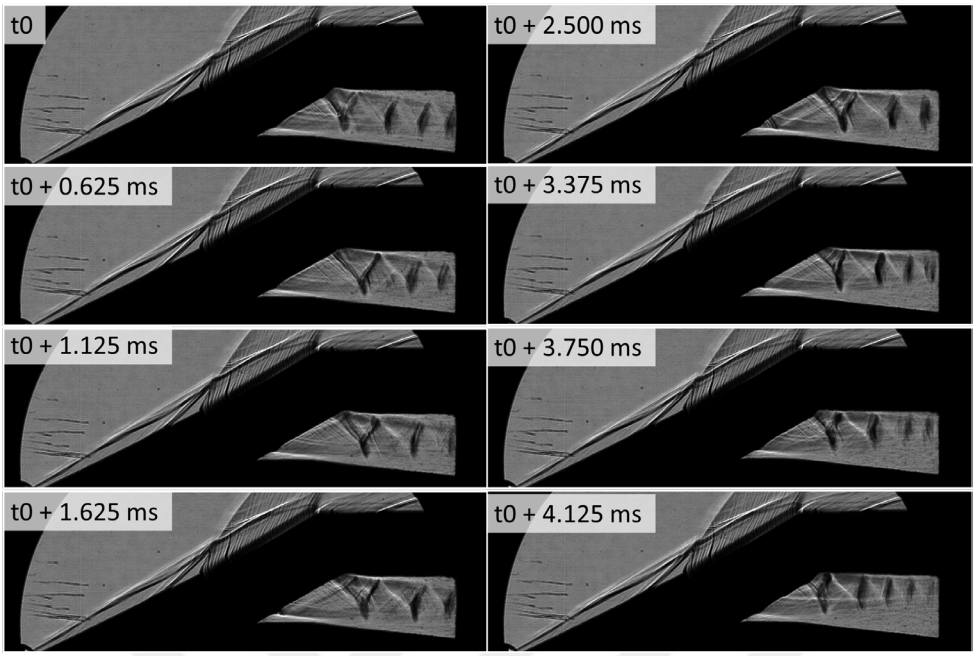


Figure C 3. Change of the shock structures between VPNs 17 and 18 for Mach = 2.63 without bleed (Test 4373).

D. Change of Shock Structures During Buzz

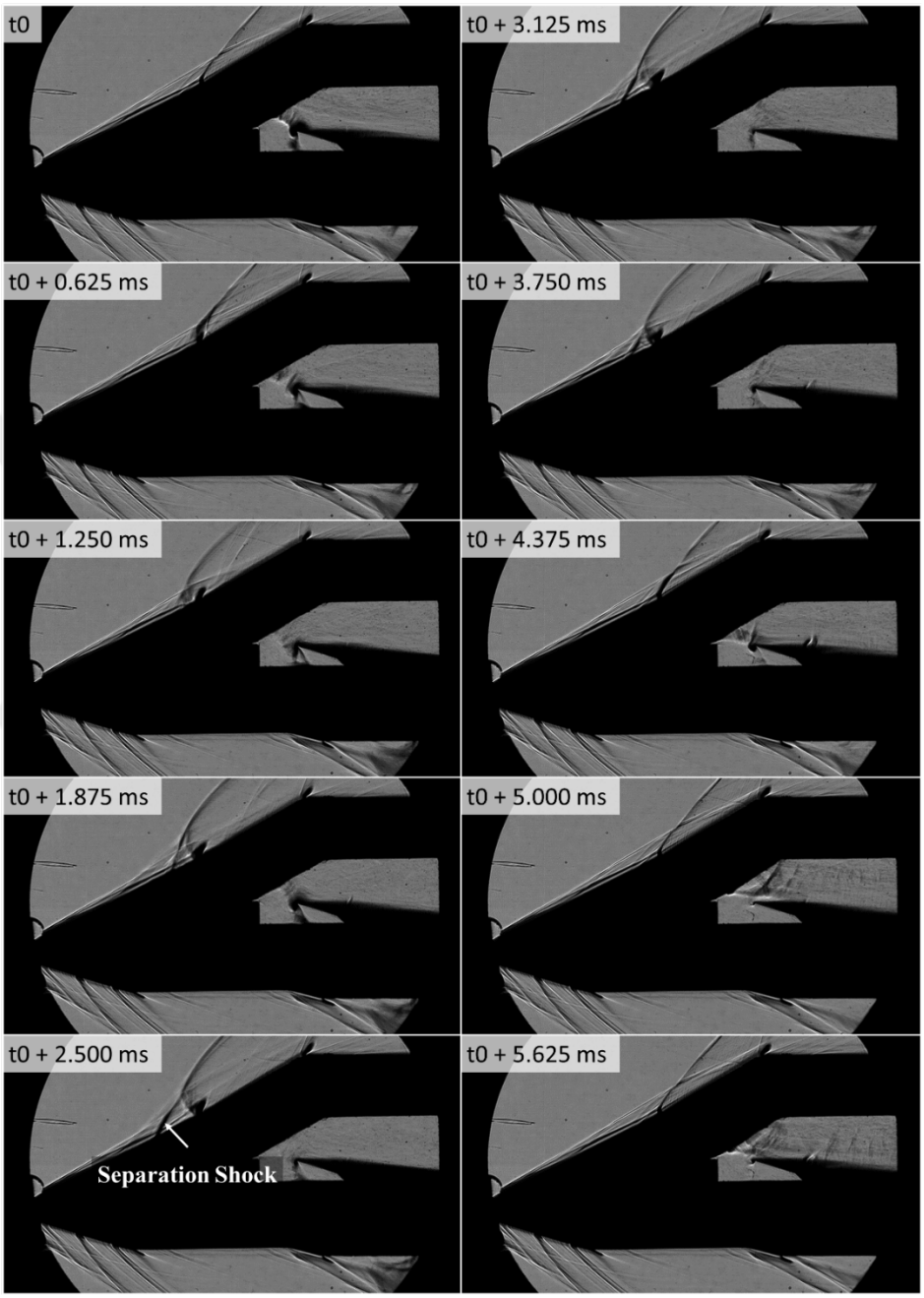


Figure D 1. Change of shock structures and small buzz at the VPN 31 for Mach = 3, with bleed (Test 4331).

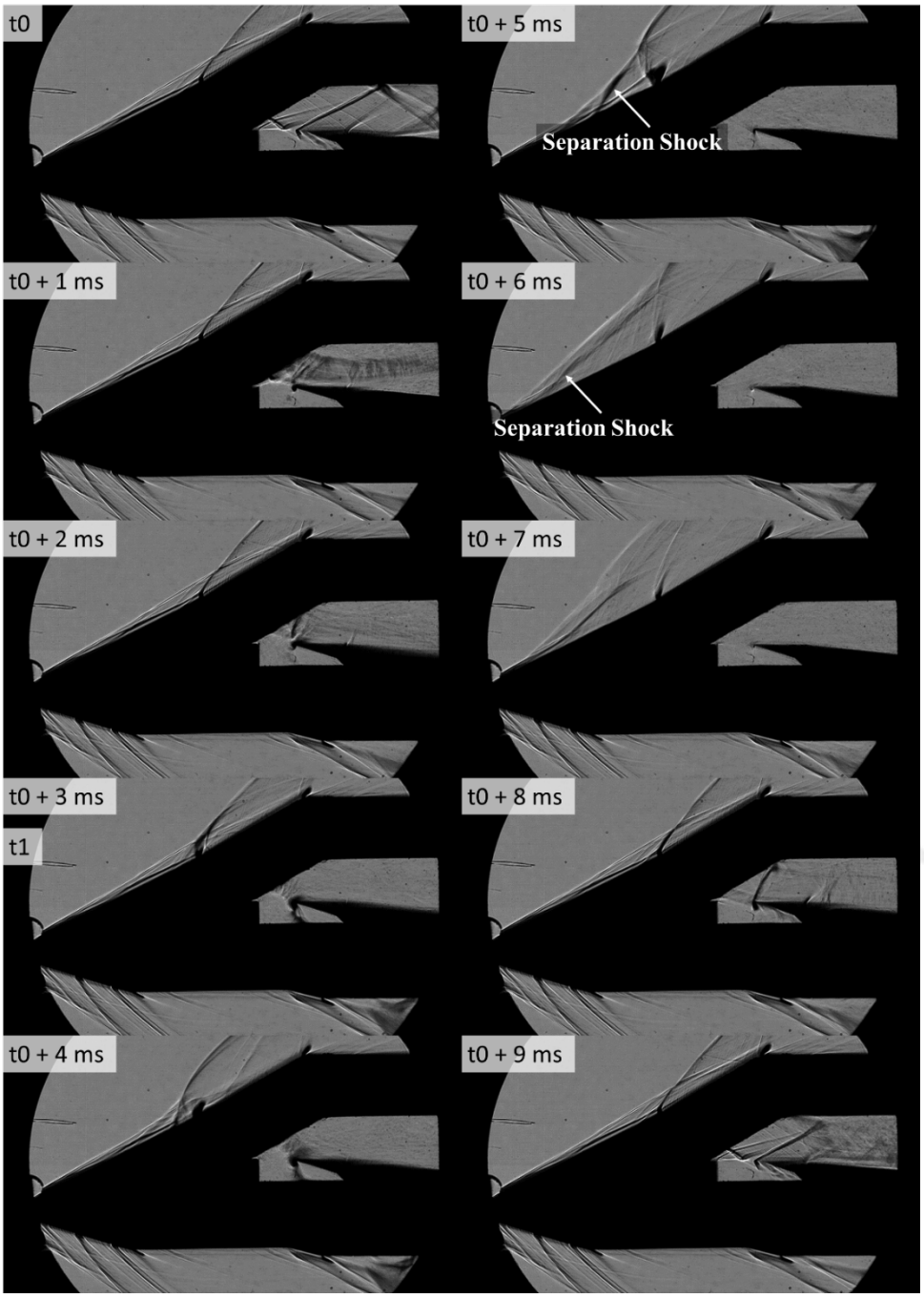


Figure D 2. Change of shock structures and big buzz at the VPN 32 for Mach = 3, with bleed (Test 4331).

E. Pressure Data of the Repatability Tests

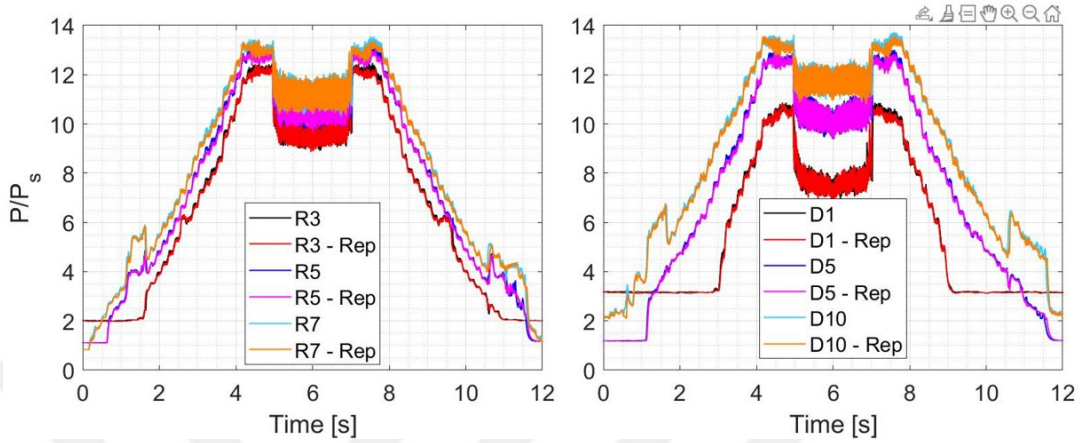


Figure E 1. Variation of pressure with respect to valve position for Mach = 2.63, with bleed (Test 4339 and 4339-rep).

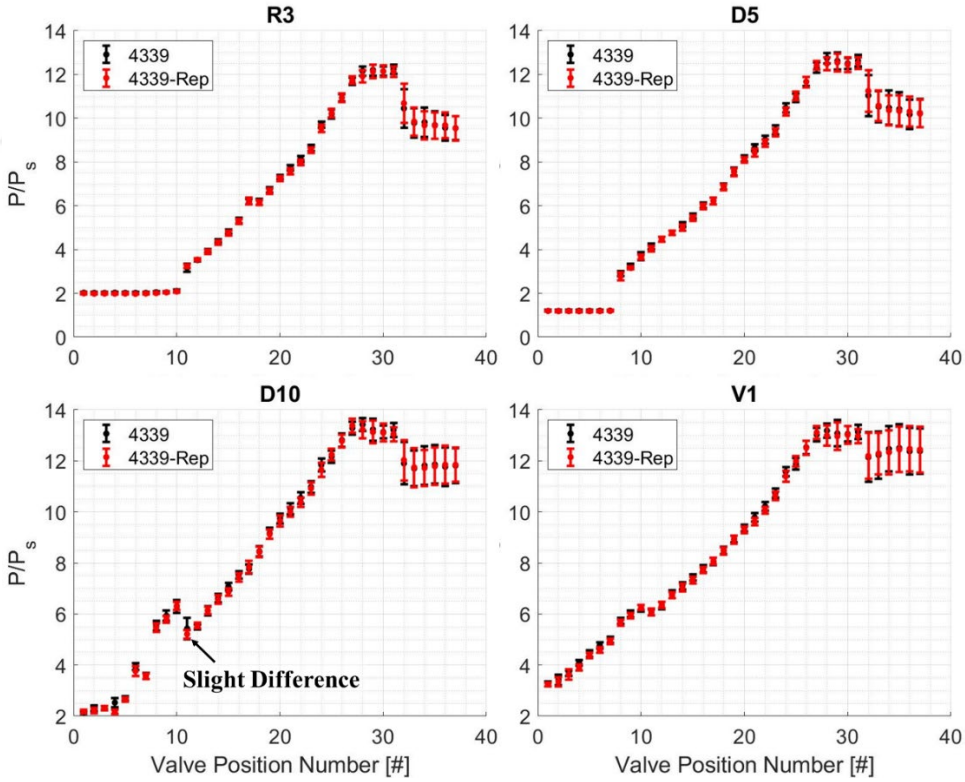


Figure E 2. Variation of pressure with respect to VPN for Mach = 2.63, with bleed (Test 4339 and 4339-rep).

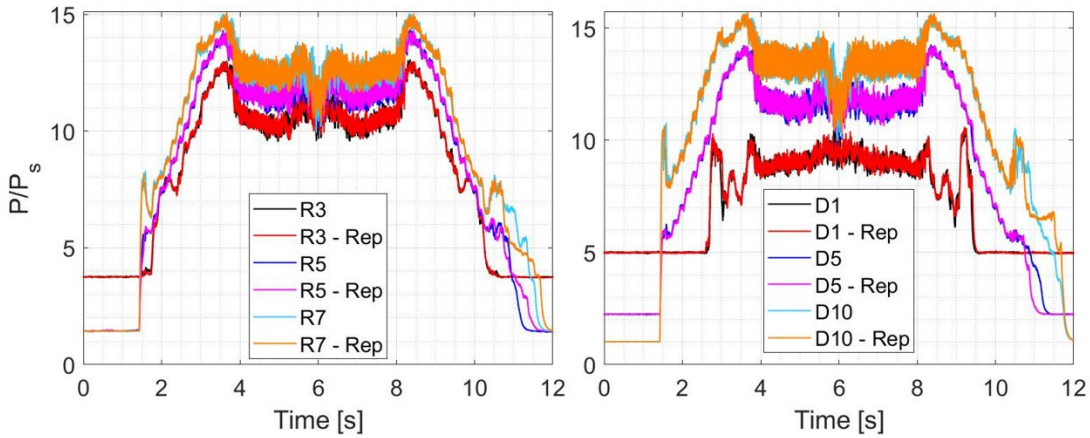


Figure E 3. Variation of pressure with respect to valve position for Mach = 3, without bleed (Test 4372 and 4372-rep).

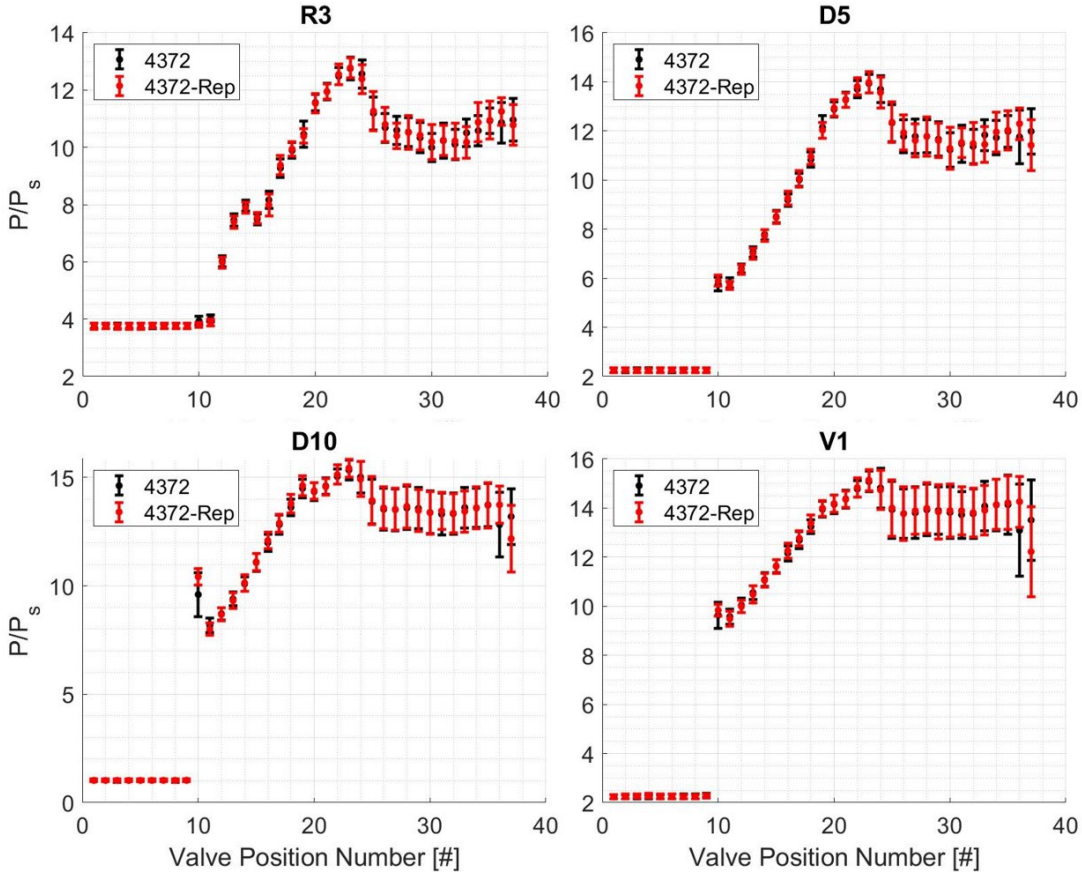


Figure E 4. Variation of pressure with respect to VPN for Mach = 3, without bleed (Test 4372 and 4372-rep).

F. Change of Pressure Along the Intake for Different Tests and VPNs

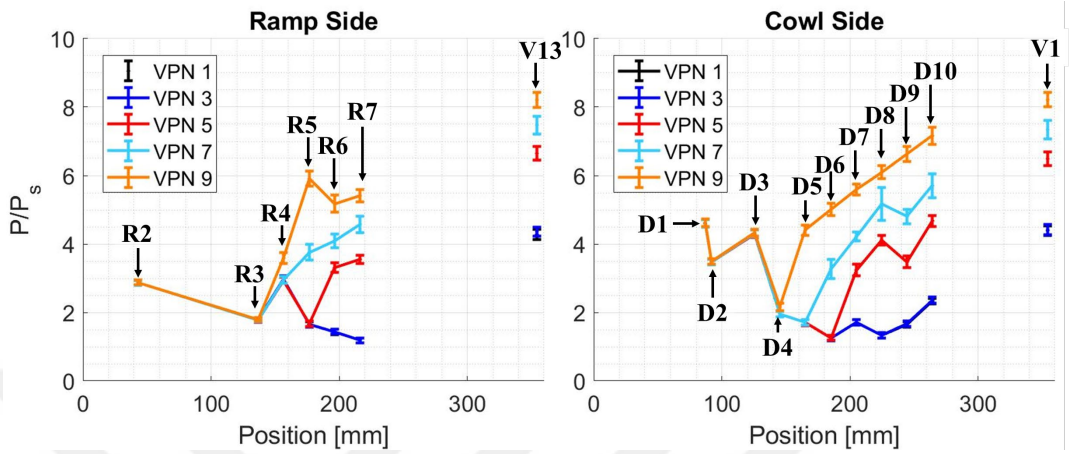


Figure F 1. Change of pressure along the intake at VPNs between 1 and 9 for Mach = 3 with bleed (Test 4331).

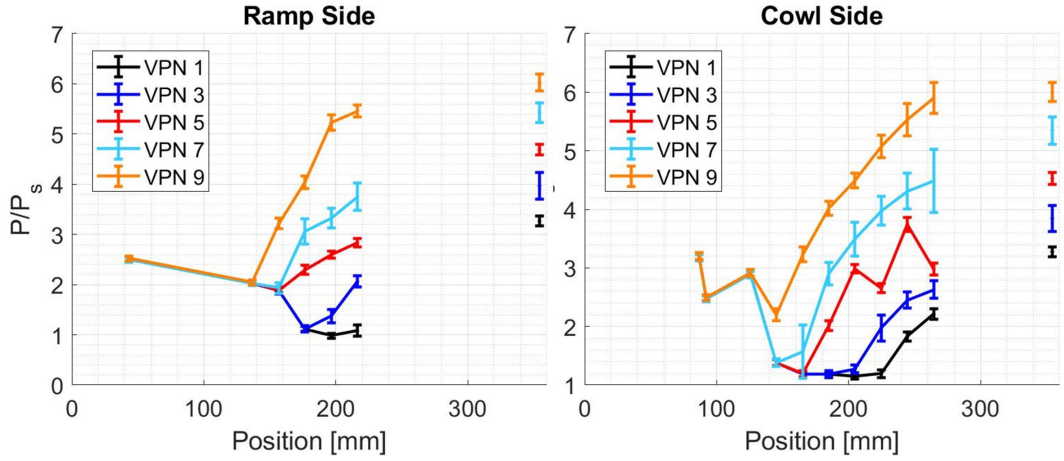


Figure F 2. Change of pressure along the intake at VPNs between 1 and 9 for Mach = 2.63 with bleed (Test 4340).

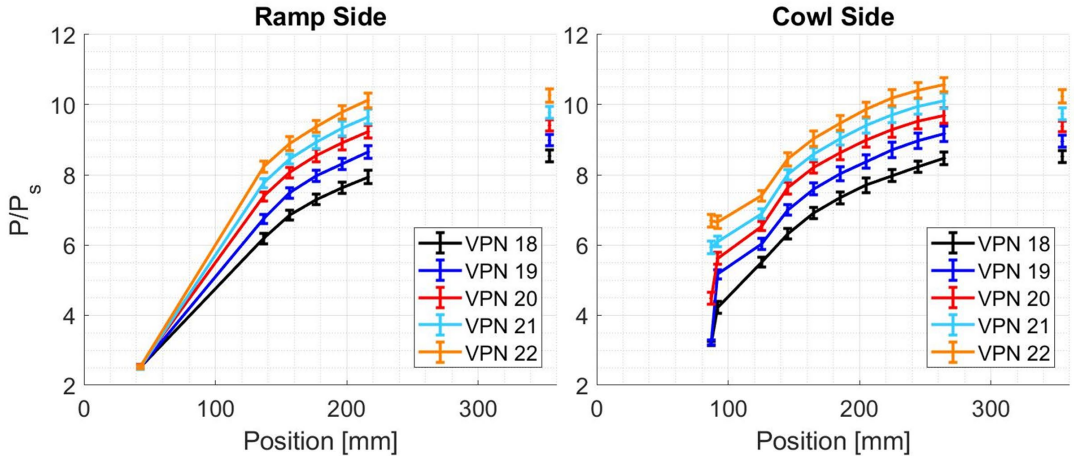


Figure F 3. Change of pressure along the intake at VPNs between 18 and 22 for Mach = 2.63 with bleed (Test 4340).

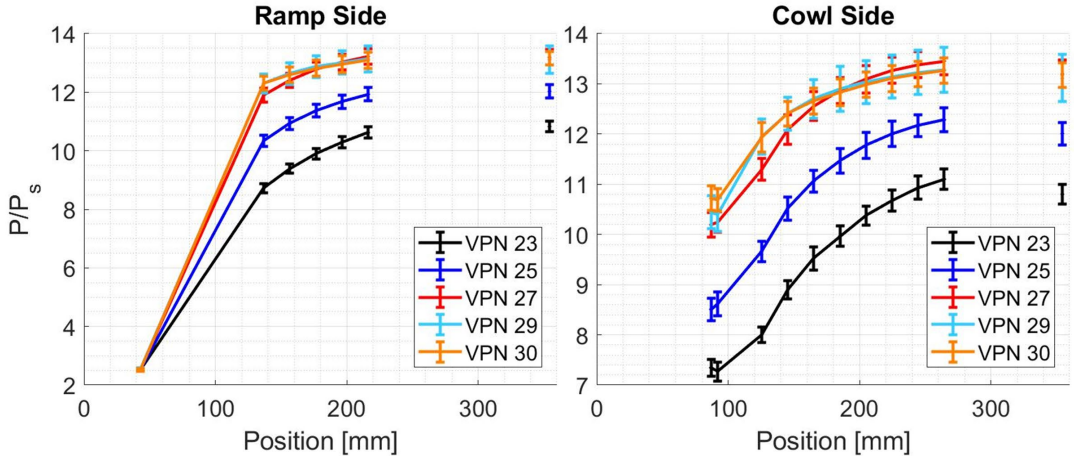


Figure F 4. Change of pressure along the intake at VPNs between 23 and 30 for Mach = 2.63 with bleed (Test 4340).

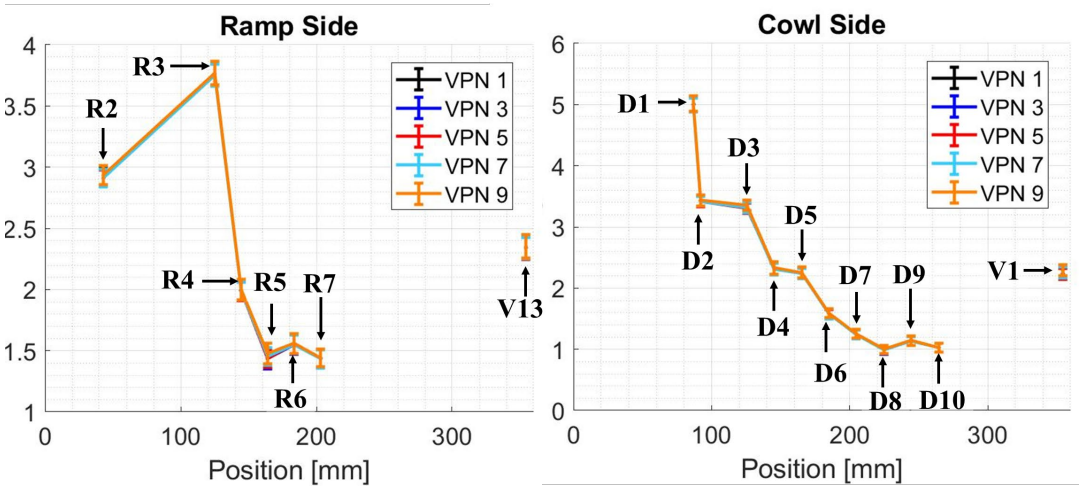


Figure F 5. Change of pressure along the intake at VPNs between 1 and 9 for Mach = 3 without bleed (Test 4372).

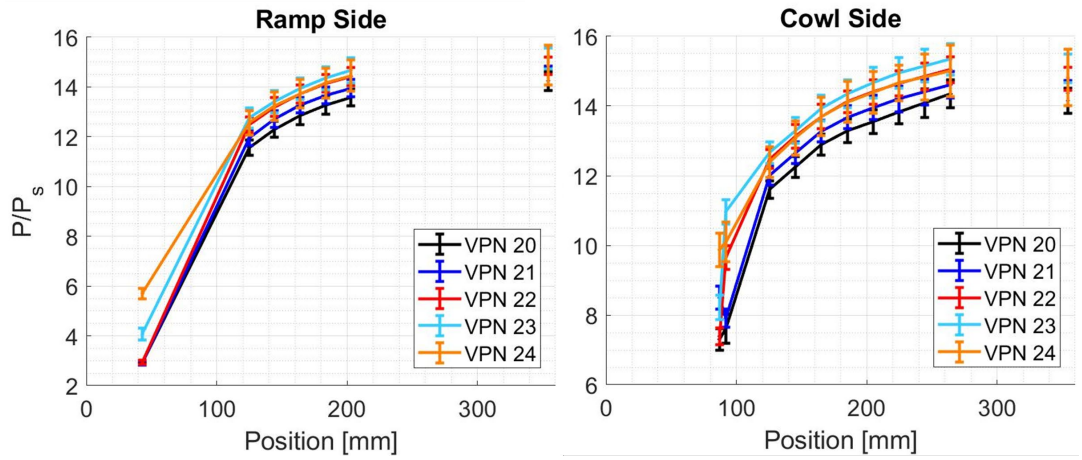


Figure F 6. Change of pressure along the intake at VPNs between 20 and 24 for Mach = 3 without bleed (Test 4372).

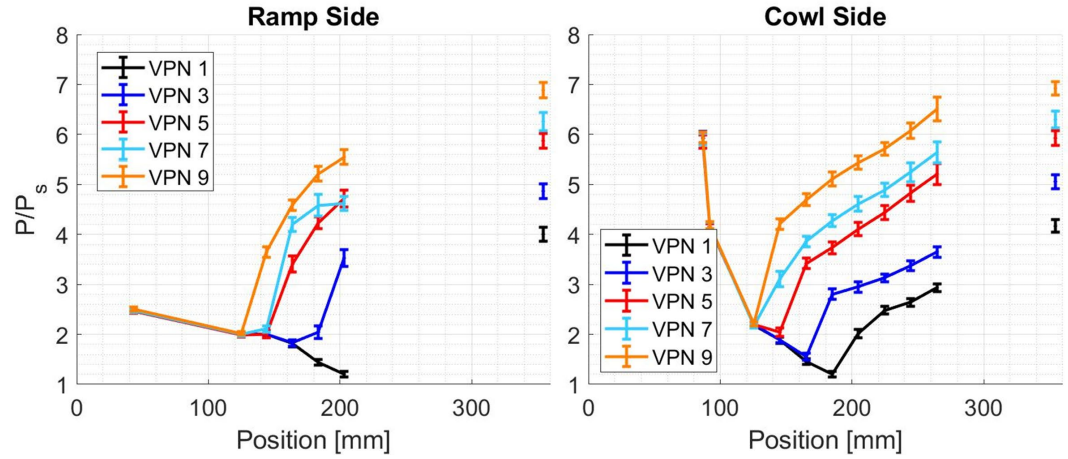


Figure F 7. Change of pressure along the intake at VPNs between 1 and 9 for Mach = 2.63 without bleed (Test 4373).

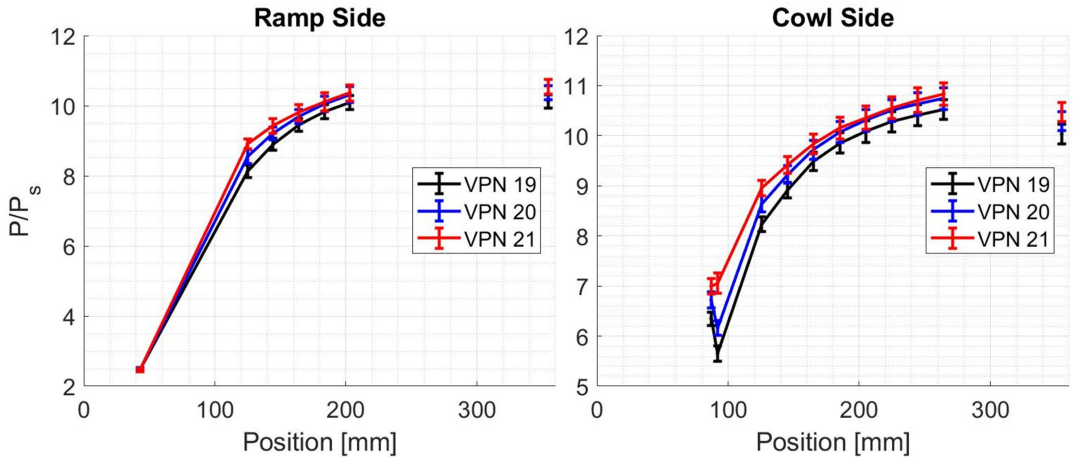


Figure F 8. Change of pressure along the intake at VPNs between 19 and 21 for Mach = 2.63 without bleed (Test 4373).

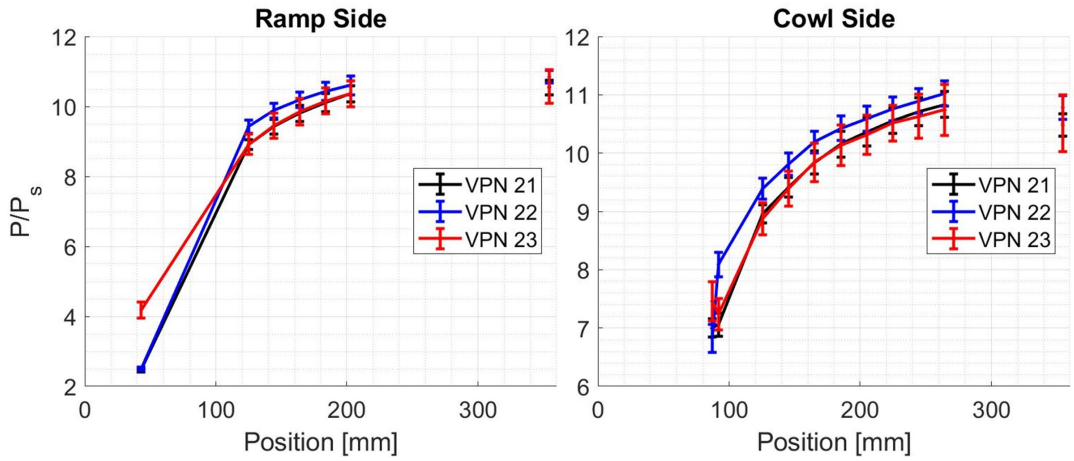


Figure F 9. Change of pressure along the intake at VPNs between 21 and 23 for Mach = 2.63 without bleed (Test 4373).

G. Mach Number Contour Plots and Pressure Data Obtained from the Numerical Simulations

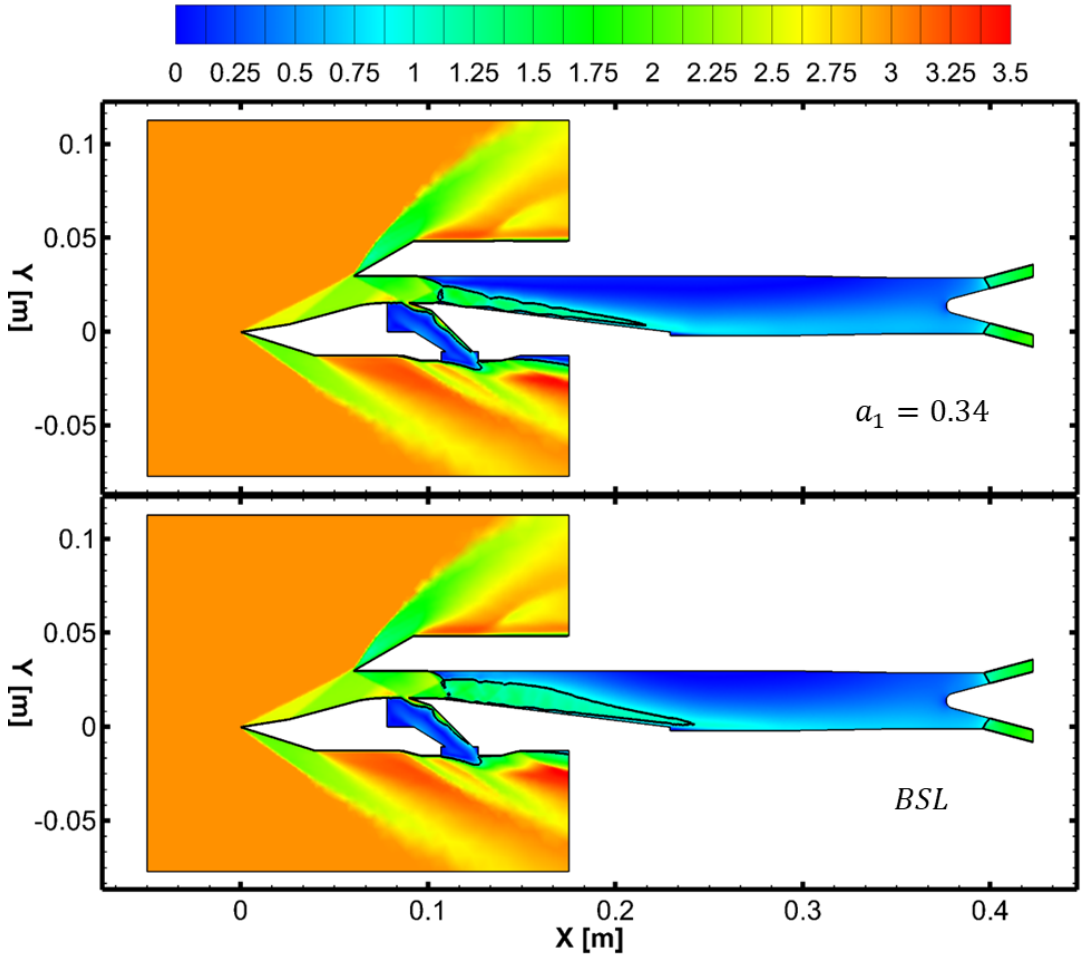


Figure G 1. Mach number contours for the numerical simulations corresponding to Mach = 3 with bleed (Test 4331) at VPN 19.

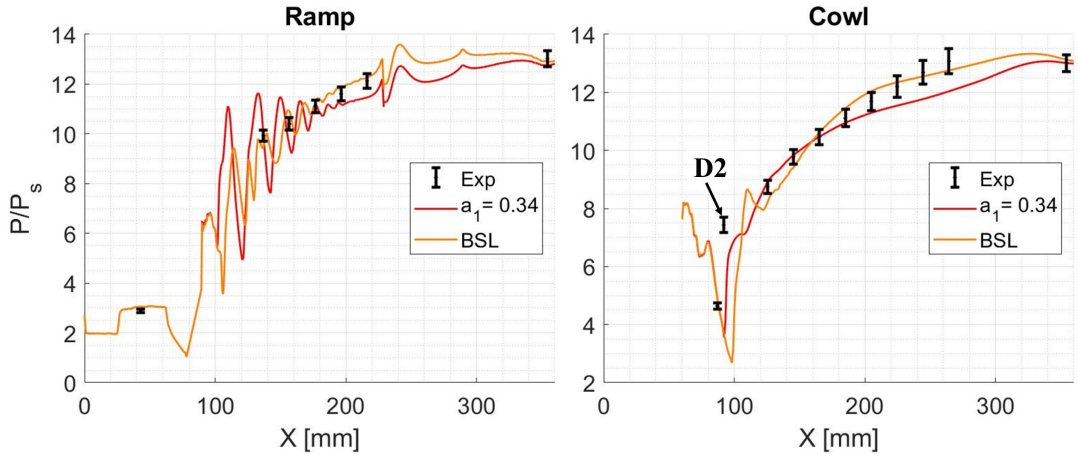


Figure G 2. Comparison of pressure distribution along the intake between numerical and experimental data for Mach = 3 with bleed (Test 4331) at VPN 19.

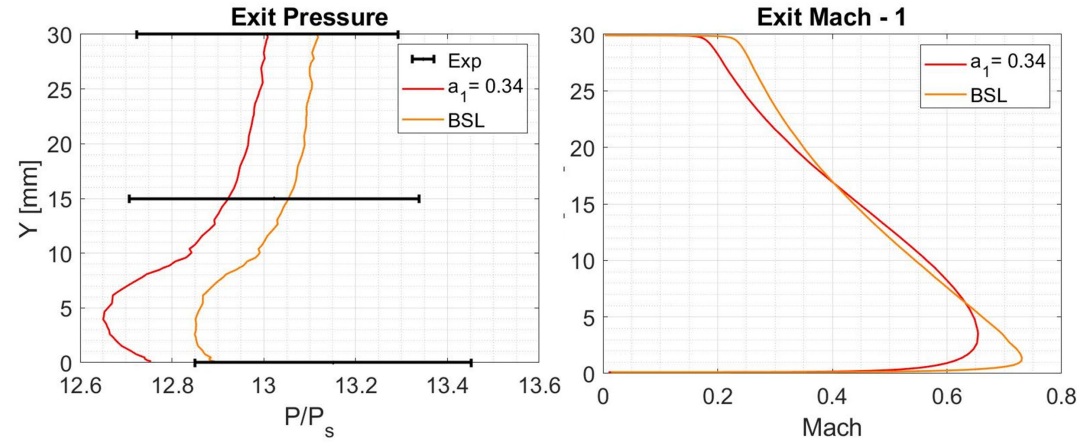


Figure G 3. Comparison of pressure distribution and Mach number at the exit of the intake for Mach = 3 with bleed (Test 4331) at VPN 19.

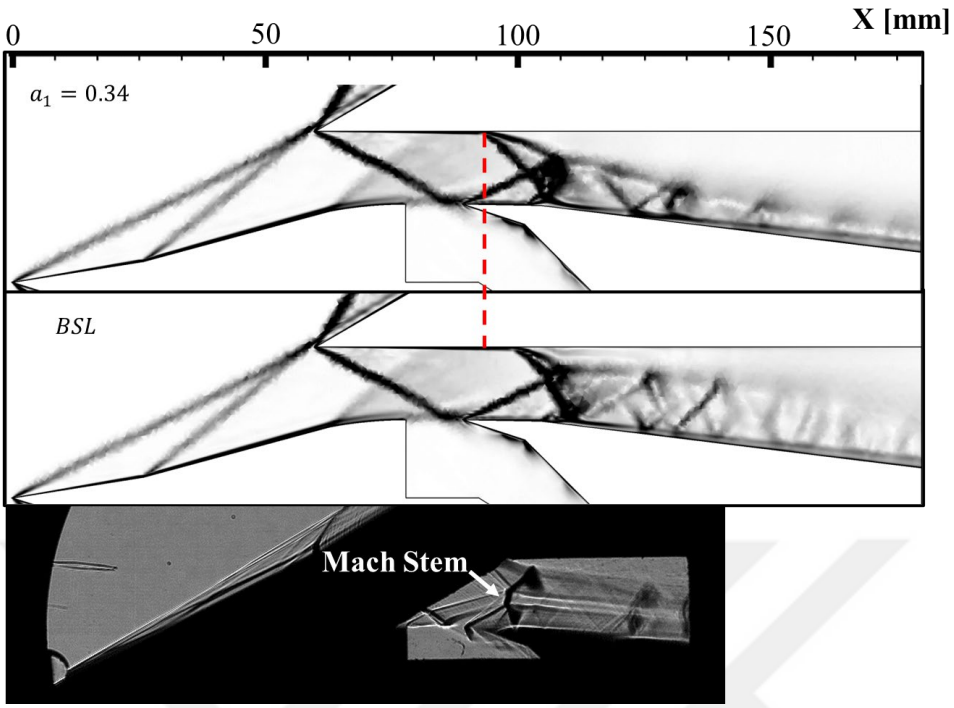


Figure G 4. Comparison of pressure distribution and Mach number at the exit of the intake for Mach = 3 with bleed (Test 4331) at VPN 19.

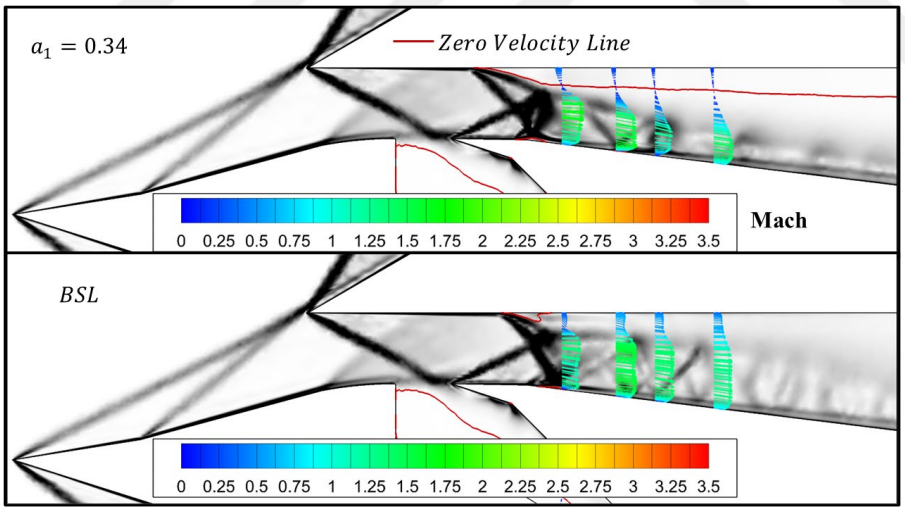


Figure G 5. Density gradient magnitude contours with velocity vectors and zero velocity line for the numerical simulation corresponding to Mach = 3 with bleed (Test 4331) at VPN 19.

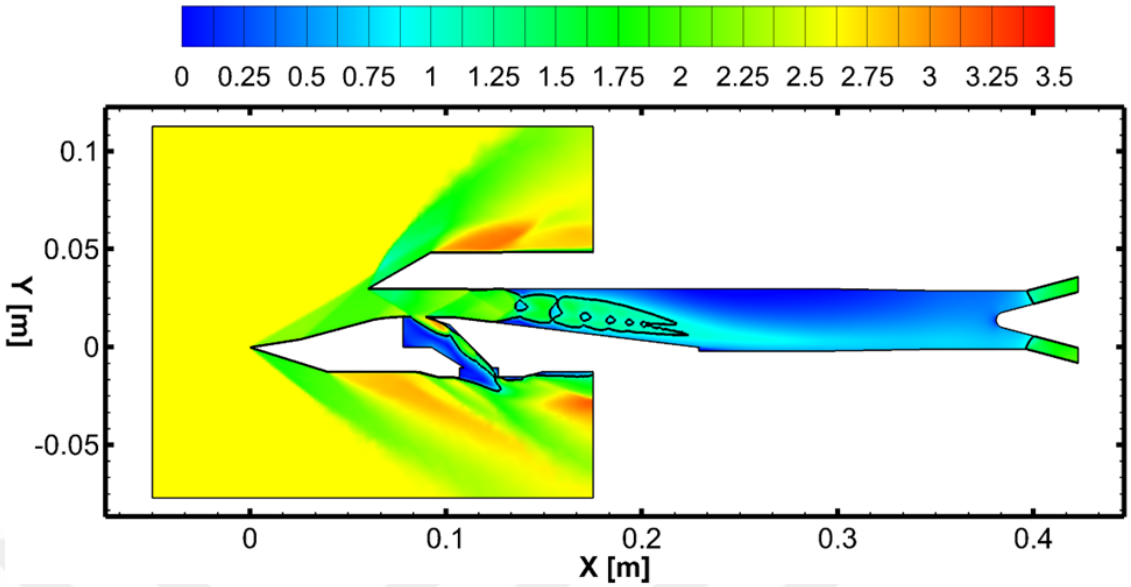


Figure G 6. Mach number contour for the numerical simulation corresponding to Mach = 2.63 with bleed (Test 4340) at VPN 15.

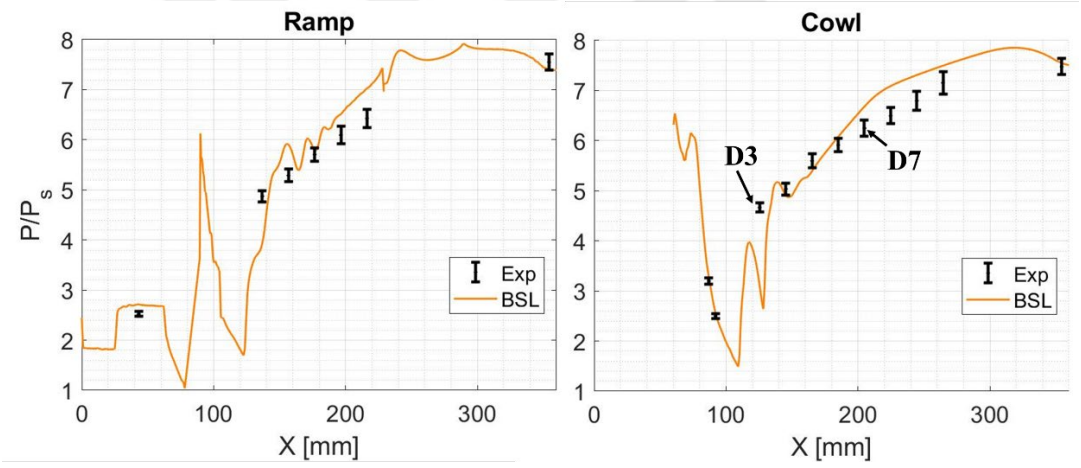


Figure G 7. Comparison of pressure distribution along the intake between numerical and experimental data for Mach = 2.63 with bleed (Test 4340) at VPN 15.

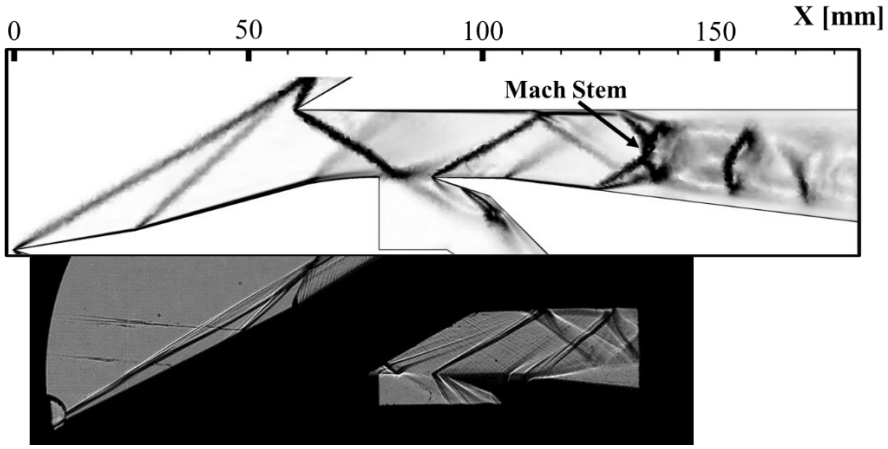


Figure G 8. Numerical density gradient magnitude contour and experimental shadowgraph image for Mach = 2.63 with bleed (Test 4340) at VPN 15.

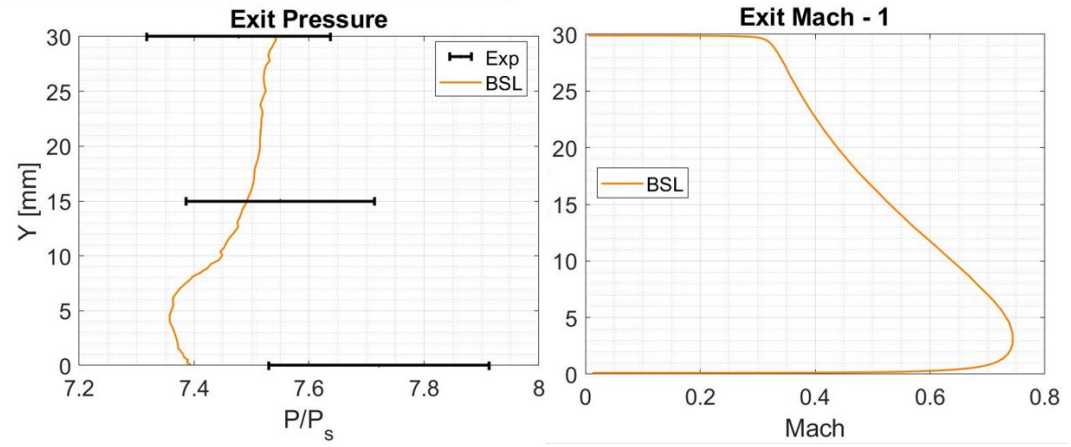


Figure G 9. Comparison of pressure distribution and Mach number at the exit of the intake for Mach = 2.63 with bleed (Test 4340) at VPN 15.

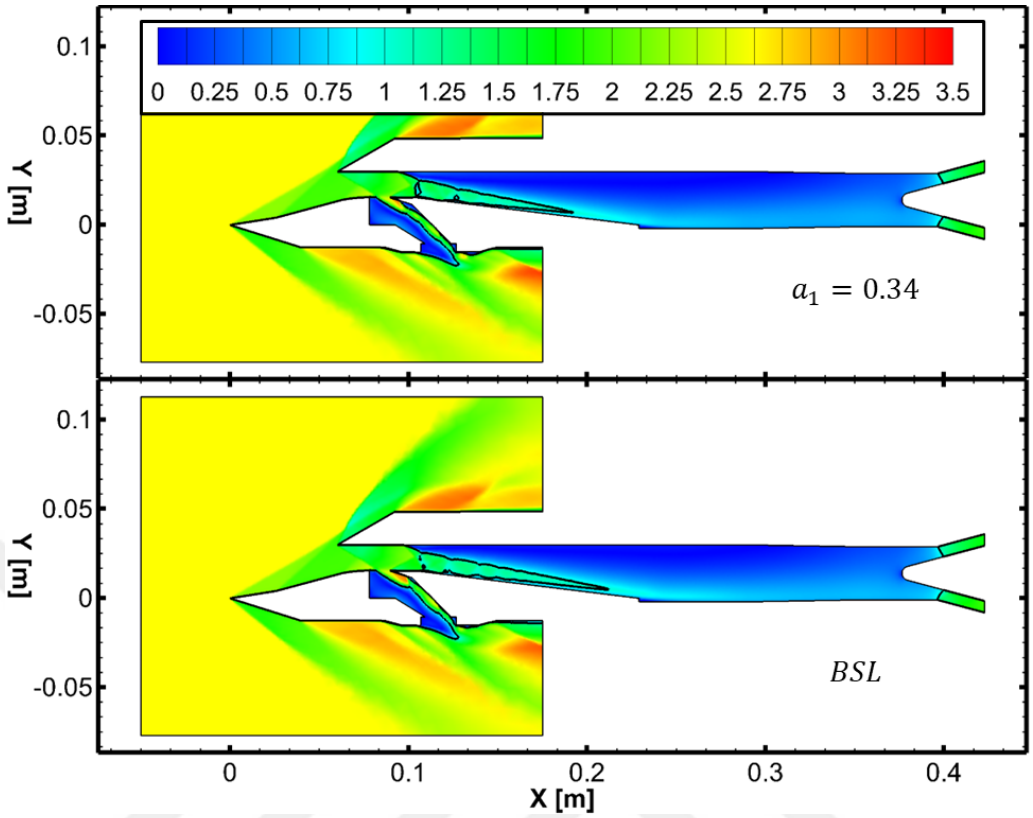


Figure G 10. Mach number contours for the numerical simulations corresponding to Mach = 2.63 with bleed (Test 4340) at VPN 19.

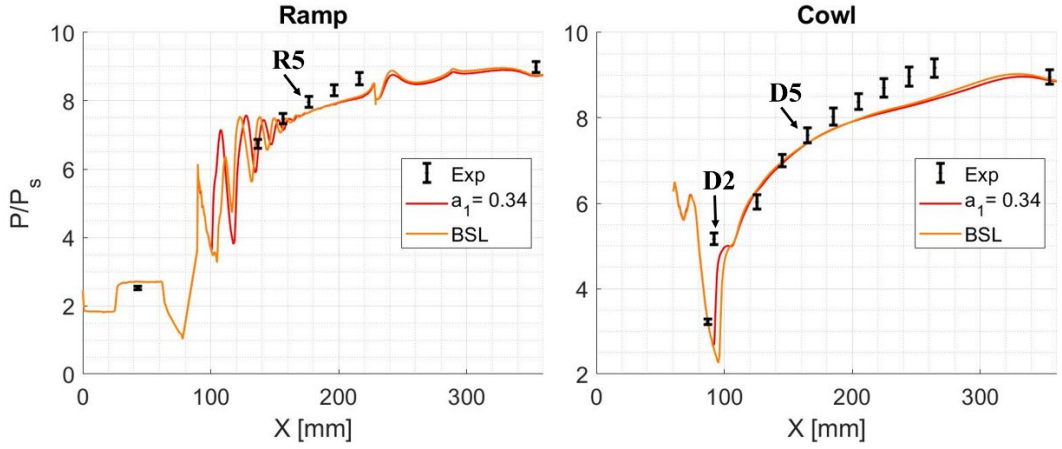


Figure G 11. Comparison of pressure distribution along the intake between numerical and experimental data for Mach = 2.63 with bleed (Test 4340) at VPN 19.

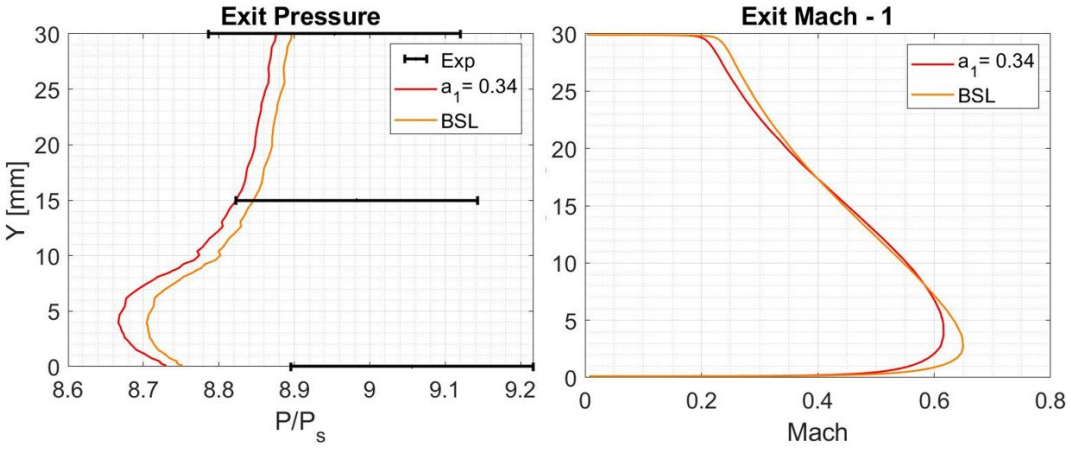


Figure G 12. Comparison of pressure distribution and Mach number at the exit of the intake for Mach = 2.63 with bleed (Test 4340) at VPN 19.

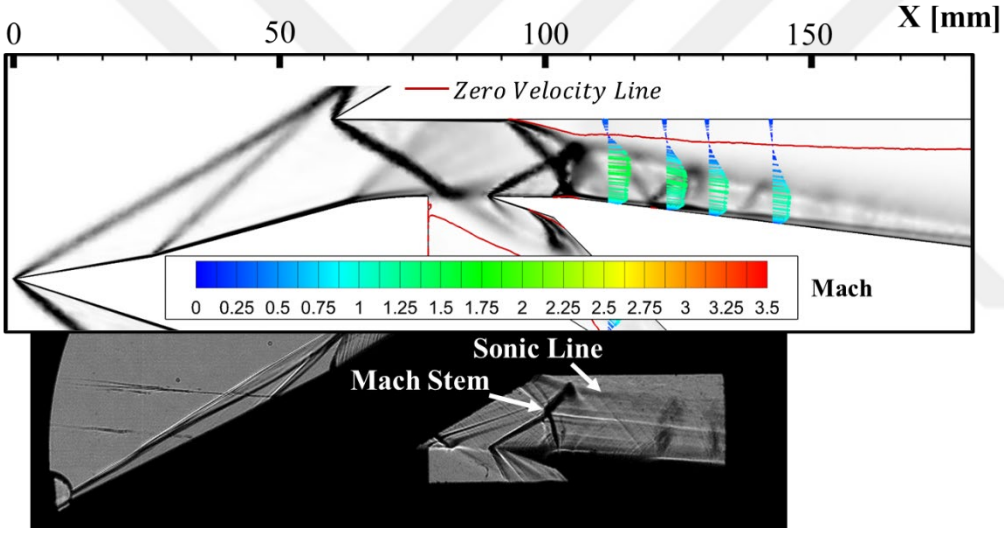


Figure G 13. Numerical density gradient magnitude contour with velocity vectors and experimental shadowgraph image for Mach = 2.63 with bleed (Test 4340) at VPN 19.

CURRICULUM VITAE

Surname, Name: Özer, Ali Can

EDUCATION

Degree	Institution	Year of Graduation
MS	METU Aerospace Engineering	2015
BS	METU Aerospace Engineering	2012
High School	Arı Fen Lisesi	2007

EXPERIENCE

2012 - 2013	TEI	Rig Test Design Engineer
2013 - 2021	TÜBİTAK-SAGE	Chief Research Engineer
2021 - 2021	ROKETSAN	Lead Engineer
2021 - present	TÜBİTAK-SAGE	Chief Research Engineer

PUBLICATIONS

A.C. Özer, B. Sümer, Y. Özyörük "Examination of Flow Field Inside Grain Port and Grain Regression Characteristics of a Nozzleless Solid Propellant Rocket Motor", in AIAA Propulsion and Energy Forum, 2019.

L.Ç. Öz, A.C. Özer, B. Sümer "Evaluation of an Augmented Spark Igniter's Flame Length and Comparison of Numerical and Experimental Investigations" in AIAA Propulsion and Energy Forum, 2019.

A.C. Özer and Y. Özyörük "Application of the Universal Expression for Erosive Burning to Nozzleless Solid Propellant Rocket Motors", in 53rd AIAA/SAE/ASEE Joint Propulsion Conference, 2017.

A.C. Özer and Y. Özyörük "Performance Prediction of Nozzleless Solid Propellant Rocket Motors" in AIAC 2015 Conference.